Long Term Aerosol Composition Measurements at the CESAR Tower at Cabauw, NL

Patrick Schlag

Energie & Umwelt / Energy & Environment
Band / Volume 251
ISBN 978-3-95806-037-1

JÜLICH
FORSCHUNGSZENTRUM

Schriften des Forschungszentrums Jülich
Reihe Energie & Umwelt / Energy & Environment Band / Volume 251

Forschungszentrum Jülich GmbH
Institut für Energie- und Klimaforschung
Troposphäre (IEK-8)

Long Term Aerosol Composition Measurements at the CESAR Tower at Cabauw, NL

Patrick Schlag

Schriften des Forschungszentrums Jülich
Reihe Energie & Umwelt / Energy & Environment Band / Volume 251

ISSN 1866-1793 ISBN 978-3-95806-037-1

Bibliographic information published by the Deutsche Nationalbibliothek.
The Deutsche Nationalbibliothek lists this publication in the Deutsche Nationalbibliografie; detailed bibliographic data are available in the Internet at http://dnb.d-nb.de.

Publisher and Distributor: Forschungszentrum Jülich GmbH
Zentralbibliothek
52425 Jülich
Tel: +49 2461 61-5368
Fax: +49 2461 61-6103
Email: zb-publikation@fz-juelich.de
www.fz-juelich.de/zb

Cover Design: Grafische Medien, Forschungszentrum Jülich GmbH

Printer: Grafische Medien, Forschungszentrum Jülich GmbH

Schriften des Forschungszentrums Jülich
Reihe Energie & Umwelt / Energy & Environment, Band / Volume 251

D 38 (Diss., Köln, Univ., 2014)

ISSN 1866-1793
ISBN 978-3-95806-037-1

The complete volume is freely available on the Internet on the Jülicher Open Access Server (JuSER) at www.fz-juelich.de/zb/openaccess.

Abstract

In this work, intensive mass spectrometric measurements of PM_1 aerosol size distribution and chemical composition were performed at Cabauw, the Netherlands, using a High Resolution Time-of-Flight Aerosol Mass Spectrometer (HR-ToF-AMS), an Aerosol Chemical Speciation Monitor (ACSM), a Thermal-Desorption Proton-Transfer-Reaction Time-of-Flight Mass Spectrometer (TD-PTR-ToF-MS), and supplementary instruments. The field campaigns took place in November 2011, during May to July 2012 (both periods with the AMS and the collocated TD-PTR-MS) and between July 2012 and June 2013 (ACSM). Average total aerosol mass loadings of 9.26 µg m^{-3}, 6.40 µg m^{-3}, and 9.50 µg m^{-3} were observed during the campaign periods, respectively. Within the ACSM campaign, 12 exceedances of the $PM_{2.5}$ daily mean limit, established by the World Health Organization (WHO), were observed. In almost all campaigns, the highest contribution to total mass were seen by nitrate (21 % - 39 %, mainly as ammonium nitrate) and organic compounds (23 % - 33 %) on average, especially in periods with relatively high total mass loadings (> 25 µg m^{-3}). The presence of organic nitrate and excess ammonium indicate the high impact of nitrogen containing compounds on the formation and composition of ambient aerosols in Cabauw. Factor analysis was applied to organic aerosols (OA) for all data sets. AMS and ACSM data showed that secondary organic aerosols (SOA, 53 % - 84 % average contribution to OA) dominated the organic fraction throughout all campaigns. A factor which is attributed to humic-like substances (HULIS) was identified as a highly oxidised background aerosol in Cabauw. Primary organic aerosols (POA) were mainly emitted by traffic (8 % - 35 % average contribution to OA) and biomass burning (8 % - 23 %). A first approach of the application of factor analysis to TD-PTR-MS data was performed in this work, showing good agreement with factors obtained from the collocated AMS. The dominance of secondary aerosol in PM_1 shows the high importance of atmospheric ageing processes of aerosol concentration at this rural site. Due to the large secondary fraction of aerosol reduction of particulate mass is challenging on a local scale.

Kurzzusammenfassung

In dieser Arbeit wurden massenspektrometrische Messungen zur Untersuchung der Größenverteilung und chemischen Zusammensetzung von PM_1 Aerosolen in Cabauw in den Niederlanden durchgeführt. Dabei wurden ein Flugzeit-Aerosol-Massenspektrometer (HR-ToF-AMS), ein Messgerät zur chemischen Bestimmung von Aerosolen (ACSM) und ein Protonen-Transfer-Reaktions-Flugzeit-Massenspektrometer, gekoppelt mit einem Thermo-Desorptions-Einlasssystem (TD-PTR-[ToF]-MS) eingesetzt. Die AMS- und TD-PTR-MS-Feldmesskampagnen fanden im November 2011 und zwischen Mai und Juli 2012 statt. Das ACSM war zwischen Juli 2012 und Juni 2013 in Cabauw in Betrieb. Während der Kampagnen wurden mittlere Partikelmassenbeladungen von jeweils 9.26 µg m^{-3}, 6.40 µg m^{-3} und 9.50 µg m^{-3} gemessen. In der ACSM-Messzeit wurde der $PM_{2.5}$ Tagesmittelgrenzwert der Weltgesundheitsorganisation (WHO) 12 mal überschritten. In fast allen Zeitperioden, vor allem in Zeiten hoher Aerosolbeladungen (> 25 µg m^{-3}), waren der Nitrat- (21 % - 39 %) und der Organik-Anteil (23 % - 33 %) im Durchschnitt dominierend, wobei Nitrat hauptsächlich als Ammoniumnitrat vorlag. Das Vorkommen von partikulären Organonitraten und überschüssigem Ammonium verdeutlicht die wichtige Rolle von stickstoffhaltigen Bestandteilen für die Bildung und Zusammensetzung der in Cabauw gemessenen Partikel. Der organische Anteil aus allen Datensätzen wurde mittels Faktorenanalyse untersucht. Dabei bildeten die sekundären organischen Aerosole (SOA) in allen Datensätzen die größte Fraktion mit durchschnittlich 53 % - 84 % Anteil an der Gesamtorganik (OA). Die Hauptemittenten von primären organischen Aerosolen wurden dem Straßenverkehr (8 % - 35 % relativer Anteil an OA) und Verbrennungsprozessen von biologischem Material (8 % - 23 % relativer Anteil an OA) zugeordnet. Zusätzlich wurde ein besonders hochoxygenierter Anteil, HULIS genannt, gefunden. Dieser Anteil wurde huminstoffhaltigen Substanzen zugeordnet und als regionales Hintergrund-Aerosol identifiziert. Eine erste Faktorenanalyse von TD-PTR-MS Daten ergab gute Übereinstimmungen mit Faktoren, die aus entsprechenden Analysen der zu derselben Zeit gemessenen AMS-Daten erhalten wurden. Die Dominanz von sekundärem Aerosol im PM_1 Anteil zeigt die hohe Relevanz von atmosphärisch-chemischen Prozessen für die Bildung von Partikeln im Vergleich zu direkten Aerosolemissionen. Dieser Umstand erschwert die lokale Reduktion von Partikelbeladungen im ländlich gelegenen Cabauw.

Contents

1. Introduction **1**

2. Experimental section **9**

2.1. The Aerosol Mass Spectrometer 10
2.1.1. Quantification with the AMS 13
2.1.1.1. Mass concentration measurement and ionization efficiency calibration 16
2.1.1.2. AMS fragmentation table 18
2.1.1.3. Particle size measurement and calibration 18
2.1.1.4. Elemental analysis of HR-ToF-AMS data 19
2.1.1.5. Inorganic and organic nitrate fractions 20
2.1.1.6. Aerosol ion balance 21
2.2. The Aerosol Chemical Speciation Monitor 21
2.2.1. Quantification with the ACSM 24
2.2.1.1. ACSM fragmentation table 26
2.2.1.2. Aerosol ion balance 28
2.3. The TD-PTR-ToF-MS 28
2.3.1. TD-PTR-ToF-MS data treatment 31
2.3.1.1. Elemental analysis of TD-PTR-MS data 34
2.4. Measurement site: Cabauw, NL 34
2.4.1. The Cabauw Experimental Site for Atmospheric Research (CESAR) tower 35
2.4.1.1. Supplementary instruments at the CESAR tower 38
2.4.2. Experimental set-ups of the HR-ToF-AMS at the CESAR tower . . 38
2.4.2.1. November 2011 38
2.4.2.2. May to July 2012 39
2.4.3. Experimental set-up of the TD-PTR-MS at the CESAR tower . . . 40
2.4.4. Experimental set-up of the ACSM at the CESAR tower 40
2.5. Statistical methods of organic aerosol data analysis 40
2.5.1. Application of PMF to AMS data 44

2.5.2. Application of PMF/ME-2 to ACSM data . . . 45
2.5.3. Application of PMF to TD-PTR-ToF-MS data . . . 46

3. Observations **49**
3.1. AMS Campaign 2011 . . . 49
3.1.1. Meteorological conditions and aerosol composition as observed with the AMS . . . 49
3.1.1.1. Inorganic and organic nitrate fractions . . . 56
3.1.1.2. Aerosol ion balance and Excess-NH_4 . . . 57
3.1.1.3. Chemical size distribution . . . 59
3.1.2. Comparison of measurements of total PM_1 mass . . . 60
3.1.3. Comparison of organic aerosol mass measurements . . . 62
3.2. AMS Campaign 2012 . . . 65
3.2.1. Meteorological conditions and aerosol composition as observed with the AMS . . . 65
3.2.1.1. Inorganic and organic nitrate fractions . . . 70
3.2.1.2. Aerosol ion balance and Excess-NH_4 . . . 71
3.2.1.3. Chemical size distribution . . . 73
3.2.2. Comparison of measurements of total PM_1 mass . . . 73
3.2.3. Comparison of inorganic aerosol mass . . . 75
3.2.4. Comparison of organic aerosol mass measurements . . . 77
3.3. ACSM campaign 2012-2013 . . . 79
3.3.0.1. Aerosol ion balance . . . 84
3.3.1. Comparison of measurements of total PM_1 mass . . . 85
3.3.2. Comparison of inorganic aerosol mass . . . 87
3.3.3. Comparison of measurements of PM_1 chemical contribution . . . 89

4. Discussion **93**
4.1. Analysis of organic aerosol . . . 93
4.1.1. PMF results for AMS data in 2011 . . . 93
4.1.2. PMF results for AMS data in 2012 . . . 97
4.1.3. PMF results for TD-PTR-MS data . . . 102
4.1.3.1. Campaign 2011 . . . 103
4.1.3.2. Campaign 2012 . . . 107
4.1.4. Factor analysis of ACSM data . . . 112
4.1.5. Summary and conclusions from organic aerosol analysis . . . 120
4.2. Aerosol composition during specific periods . . . 124
4.2.1. High mass periods . . . 124

4.2.2. Precipitation events . . . 127
4.3. Organic nitrates . . . 130
4.4. Excess ammonium . . . 131

5. Summary and Outlook **137**

A. Appendix **171**
A.1. AMS calibration results and data analysis: November 2011 . . . 171
A.1.1. Calibration results . . . 171
A.1.2. Data analysis . . . 172
A.2. AMS calibration results and data analysis: May to July 2012 . . . 174
A.2.1. Calibration results . . . 174
A.2.2. Data analysis . . . 175
A.3. Detection limits of the AMS and the ACSM . . . 177
A.4. TD-PTR-MS data analysis . . . 178
A.5. Observations . . . 206
A.5.1. Campaign 2011 . . . 206
A.5.2. Campaign 2012 . . . 210
A.5.3. ACSM campaign 2012 - 2013 . . . 214
A.5.4. PMF results for AMS data in 2011 . . . 219
A.5.5. PMF results for AMS data in 2012 . . . 221
A.5.6. PMF results for TD-PTR-MS data 2011 . . . 224
A.5.7. PMF results for TD-PTR-MS data 2012 . . . 225
A.5.8. PMF/ME2 results for ACSM data 2012 - 2013 . . . 226
A.5.9. Aerosol composition during special events . . . 227

1. Introduction

Per definition aerosols are a suspension of solid or liquid particulate matter (PM) in a surrounding gas. Though, aerosols are usually referred to as the particulate phase in the literature. In the atmosphere, aerosol particles typically have the highest contributions in the troposphere, with still significant concentrations in the stratosphere.

Most important properties of aerosols are their size, shape and chemical composition. Particle sizes are mainly expressed in diameters, which range from nanometers to tens of micrometers in the atmosphere. Atmospheric aerosols are usually classified into nucleation ($\approx$ 2 nm - 20 nm), accumulation ($\approx$ 20 nm - 1 µm), and coarse mode ($>$ 1 µm) (*Hinds*, 1999). Particles with diameters of more than a few micrometers have a short atmospheric lifetime due to deposition on the ground. Particulate mass (PM) concentration is commonly reported as PM_1, $PM_{2.5}$, and PM_{10}, i.e. the particle mass concentration of all particles with diameters of up to 1 µm, 2.5 µm, and 10 µm, respectively.

Aerosols influence the global climate directly and indirectly. The direct effect includes scattering and absorbing long and short wave radiation, depending on the optical properties of the particles. Besides the resulting impact on the visibility (*Ramanathan et al.*, 2007; *Romanou et al.*, 2007), this can have a cooling or heating effect on the atmosphere. The aerosol indirect climate effect refers to the impact of particles on cloud formation and their properties. This and the resulting increased cloud lifetime have an overall cooling effect (*Albrecht*, 1989). Figure 1.1 illustrates the net radiative forcing of anthropogenic emitted atmospheric compounds. For the aerosol fraction, a net cooling effect on the climate is seen, but corresponding error bars indicate the large uncertainty, especially for the estimation of the aerosol indirect effect on climate (*IPCC*, 2013).

In addition to climate effects, particles can impact adversely on human health by increasing the probability of cardiopulmonary and lung cancer mortality (*Pope et al.*, 2002). The World Health Organization (WHO) recently estimated, that globally, 3.7 million deaths were attributable to ambient air pollution in both cities and rural areas in 2012[1]. This mortality is reported to be due to exposure to small particulate matter (PM_{10}), which causes cardiovascular and respiratory disease, and cancers. Therefore, a number of institutions established air quality standards to limit particulate matter. The WHO

[1] http://www.who.int/phe/health_topics/outdoorair/databases/en/

and the European Union set annual and daily limits for both $PM_{2.5}$ and PM_{10} mass concentrations in the atmosphere. Details for the $PM_{2.5}$ limits are given in subsection 4.2.

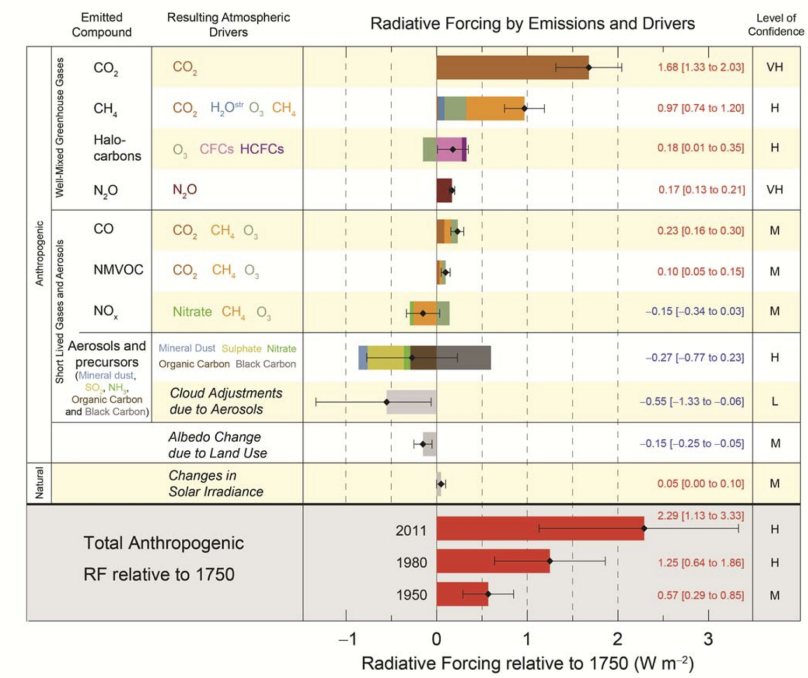

Figure 1.1.: Global mean radiative forcings and their 65% uncertainty range in 2011 with respect to 1750 for various agents and mechanisms. Figure taken from *IPCC* (2013).

All effects mentioned above are not only depending on the particle number concentration and size, but also on their chemical composition. As indicated in figure 1.1, the net climate effects of different aerosol components differ largely. While most aerosol constituents cause atmospheric cooling, black carbon (BC) shows a heating effect due to its high ability to absorb light. Yet the determination of aerosol composition is still challenging. In fact, the lack of knowledge on aerosol composition is mainly responsible for the large uncertainty of the total anthropogenic radiative forcing given in figure 1.1 (*IPCC*, 2013).

Besides particulate water, atmospheric aerosols consist mainly of nitrate, sulphate, ammonium, chloride, minerals and carbonaceous materials *Seinfeld and Pandis* (2006). The last include black carbon and organic compounds, which are usually referred to as organic matter (OM) (*Rogge et al.*, 1993). Figure 1.2 shows the average total mass and chemical composition of PM_1 at a number of measurement sites across the Northern Hemisphere, performed by aerosol mass spectrometry (AMS). It includes OM (or Org, green colours) and the inorganic components nitrate (NO_3, blue), sulphate (SO_4, red), ammonium (NH_4,

orange), and chloride (Chl, purple). The organics are typically further distinguished via factor analysis methods (*Paatero and Tapper*, 1994; *Paatero*, 1997; *Ulbrich et al.*, 2009). As illustrated by the pie charts, the average fractional abundances of these compounds, further referred to as aerosol species, vary largely throughout the sites, where OM contributes significantly to total mass within all measurements (*Jimenez et al.*, 2009).

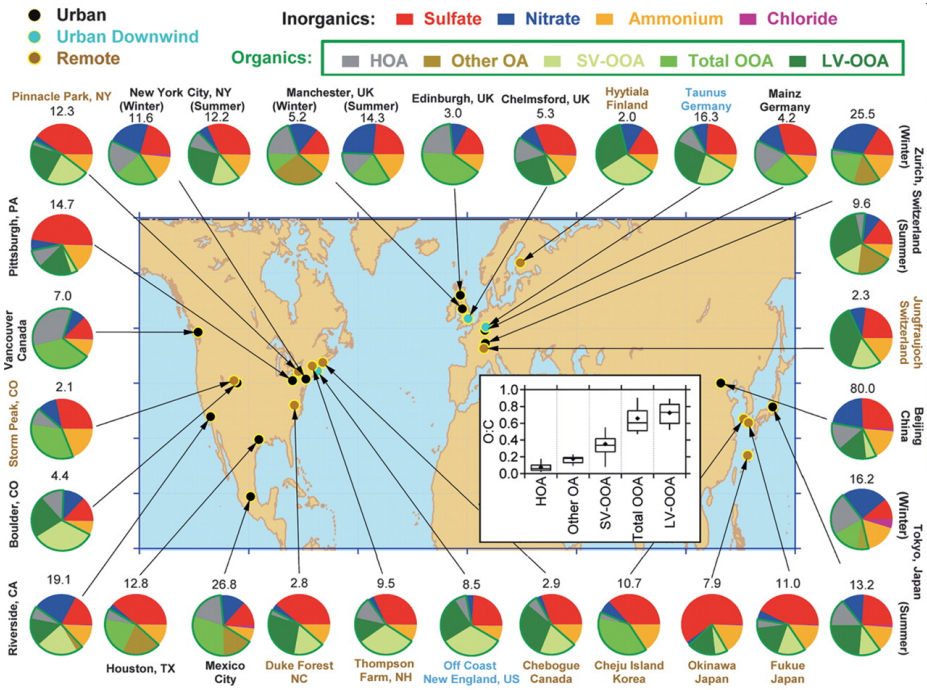

Figure 1.2.: Total mass concentration (in µg m^{-3}) and mass fractions of non-refractory inorganic species and organic components in submicrometer aerosols measured with the AMS. The organic components were obtained with factor analysis methods (see section 2.5). Figure taken from *Jimenez et al.* (2009).

To explain this variability, the sources of particles have to be explored. A first classification of aerosols is performed by the distinction into primary aerosols (PA) and secondary aerosols (SA) (*Seinfeld and Pandis*, 2006). PA are directly emitted (e.g. dust, sea spray, or soot from incomplete combustions) and can be of anthropogenic or biogenic origin. SA on the other hand is formed from atmospheric chemical conversion of gaseous precursors to low-volatile oxidation products and gas to particle conversion. Both inorganic and organic aerosol components can be of secondary origin.

Tropospheric sulphate originates mainly from atmospheric oxidation of sulphur containing gas phase components. A major contributor is sulphur dioxide (SO_2), which is largely emitted by anthropogenic sources such as traffic and industry. According to equation

R1.1 and R1.2, SO_2 is oxidised predominantly in the atmosphere by OH radicals to form SO_3, which converts in the presence of water vapour to sulphuric acid (H_2SO_4). M represents a so called collision partner. Sulphuric acid can either form new particles, called nucleation, or condense on pre-existing aerosols. Since the main source of OH radicals is the photo-induced reaction of water vapour and oxygen, the oxidation of SO_2 is almost exclusively relevant at day-time. However, recent studies reported another pathway, where SO_2 may be significantly oxidised to H_2SO_4 by organic compounds via so called stabilized Criegee intermediates (*Sarwar et al.*, 2013). The importance of this reaction scheme is still very uncertain, since reaction rate constants depend on a number of factors such as ambient temperature and humidity and the structure of the respective Criegee intermediate (*Sarwar et al.*, 2014; *Berndt et al.*, 2014).

Dimethyl sulphide (DMS) is an example of a biogenic source for particulate sulphate and organic sulphates. It is mainly released from the ocean into the atmosphere (*Chasteen and Bentley*, 2004), where it is oxidised to sulphuric acid and/or sulphur containing organics like methanesulfonic acid (CH_3SO_3H, MSA), which may condense on pre-existing particles. The atmospheric oxidation of DMS takes mainly place by the reaction with OH radicals at day-time.

$$SO_2 + OH + O_2 + M \longrightarrow SO_3 + HO_2 + M \quad \text{(R1.1)}$$

$$SO_3 + H_2O + M \longrightarrow H_2SO_4 + M \quad \text{(R1.2)}$$

Likewise sulphate, nitrate is also appearing as inorganic or organic nitrate. The first step in forming inorganic nitrate is the oxidation of gaseous nitrogen dioxide (NO_2), as part of NO_x (= NO + NO_2), which is strongly attributed to anthropogenic sources (*Finlayson-Pitts and Pitts*, 2000). Mainly OH radicals or ozone (O_3) act as oxidants for NO_2. At day-time the reaction with OH is most important (see equation R1.3), resulting in nitric acid (HNO_3). The last has a sufficient low vapour pressure to condense on pre-existing particles.

$$NO_2 + OH + M \longrightarrow HNO_3 + M \quad \text{(R1.3)}$$

In the absence of OH, the oxidation with ozone (O_3), which can be found significantly both at day and night, becomes more relevant, leading to NO_3 radicals (equation R1.4).

This reaction represents the only direct source for NO_3 radicals in the atmosphere (*Seinfeld and Pandis*, 2006). In case of high NO_3 radical concentrations, a further reaction with NO_2 takes place (equation R1.5), resulting in N_2O_5, which decomposes in case of NO_3 depletion or undergoes heterogeneous hydrolysis with water vapour (equation R1.6). During day-time NO_3 radicals photolyze rapidly by sunlight and react with NO, with average lifetimes of approximately 5 seconds at noon-time (*Seinfeld and Pandis*, 2006).

$$NO_2 + O_3 \longrightarrow NO_3 + O_2 \tag{R1.4}$$

$$NO_3 + NO_2 + M \longleftrightarrow N_2O_5 + M \tag{R1.5}$$

$$N_2O_5 + H_2O(l) \longrightarrow 2HNO_3(aq) \tag{R1.6}$$

Atmospheric organic nitrates ($RONO_2$) are predominantly formed by the oxidation of volatile organic compounds (VOC's) with NO_3 radicals, produced by reaction R1.4 (*Neff et al.* (2002) and references therein). An additional pathway is the reaction of RO_2 radicals with NO (*Roberts*, 1990). RO_2 radicals are formed by the oxidation of VOC's with OH radicals and oxygen. While the reaction of VOC's with OH radicals is the most important oxidative process at day-time, the NO_3 radical is the dominant oxidant during night-times due to the absence of OH radicals. On the other hand, this dominance is also dependent on the concentration of ozone (*Perring et al.*, 2013). Because of the functionalization of VOC's the resulting organic nitrate molecules have likely a lower vapour pressure than their precursors and may condense on pre-existing particles (*Farmer et al.*, 2010).

Since particulate nitrate and sulphate are formed by (photo-induced) chemical reactions in the atmosphere, they are considered as secondary aerosols. In the presence of ammonia (NH_3), both H_2SO_4 and HNO_3 are neutralized to their ammonium salts and form ammonium sulphate ($(NH_4)_2SO_4$) and ammonium nitrate (NH_4NO_3), respectively. According to their low- and semi-volatile character, respectively, and their hygroscopicity (the affinity to absorb water vapour), these compounds condense on pre-existing aerosols, depending on ambient temperature and humidity (*Seinfeld and Pandis*, 2006). The major sources for ammonia are the agricultural use of nitrogen containing fertilizers and emissions from animal livestocks, especially from chicken, pig and cattle farms (*van der Hoek*, 1998). Due to its high water solubility and reactivity with acids, the reactions to $(NH_4)_2SO_4$ and NH_4NO_3 are the most important sinks for NH_3 rather than the reaction with OH radicals, which is relatively slow (*Seinfeld and Pandis*, 2006).

Particulate chloride can originate from sea spray (including e.g. sodium chloride) or from the neutralization of HCl vapours, formed e.g. by waste incinerators or power

stations (*Seinfeld and Pandis*, 2006). The neutralization of HCl again takes mainly place by ammonia, resulting in particulate ammonium chloride (NH_4Cl). Overall, particulate ammonium exists mainly in form of $(NH_4)_2SO_4$, NH_4NO_3, and NH_4Cl. If particles consist of less NH_4 than expected for the neutralization of these inorganic species, the aerosols are considered to be acidic. If more NH_4 is found, then so called excess ammonium (Excess-NH_4) is present. Details are given in subsection 2.1.1.6.

In contrast to inorganic species, the organic fraction may consist of up to hundreds of thousands of different molecules (*Goldstein and Galbally*, 2007). Thus, a direct identification or source apportionment for all individual organic compounds is not feasible. Similar to inorganics mentioned above, organic aerosols are separated into primary organic aerosols (POA) and secondary organic aerosols (SOA), depending on their formation processes. POA, including also BC, are emitted directly into the atmosphere, either by biogenic (e.g. plant debris) or anthropogenic sources (e.g. combustion processes). SOA are formed by gas to particle conversion of atmospherically oxidised semi- and low- volatile VOC's. *Guenther et al.* (1995) estimated a global VOC budget in the order of 1150 Tg carbon per year. Biogenic VOC's (BVOC's) contribute approximately 90 %, including isoprene (50 % of total BVOC's), monoterpenes (15 %), sesquiterpenes (3 %) (*Guenther et al.*, 2012). In turn, 10 % of emitted VOC's are of anthropogenic origin, including e.g. alkanes, alkenes, benzene and toluene.

The atmospheric oxidation of VOC's takes place by the reaction with OH radicals, ozone and nitrate radicals. As indicated above, the OH concentration is driven by its photochemically induced formation, while NO_3 radicals rapidly photolyze by sunlight. Thus, OH radicals represent the main oxidant during day-time, while NO_3 radicals reach significant oxidation potential in the night. Ozone on the other hand is found at significant concentrations both at day- and night-time. *Hallquist et al.* (2009) suggests, that SOA contributes 70 % to organic aerosol mass, and that 90 % of SOA includes atmospherically oxidised compounds.

The investigation of the aerosol composition is critical for the development of climate models, since the composition influences important particle properties. The least well characterized aerosol fraction in this regard is the organic fraction. Figure 1.3 shows the dependence of the aerosol hygroscopicity (κ) and the particle growth factor on the atomic O/C ratio of the organic fraction of a number of chamber and ambient measurements. A higher O/C ratio likely increases the polarity and thus the hygroscopicity. *Jimenez et al.* (2009) stated that „a more hygroscopic particle of a given size will grow more under humid conditions, scattering more incident light; it will also be more likely to form cloud droplets. Both phenomena strongly influence the radiative forcing of climate through the direct and indirect effects of aerosols“.

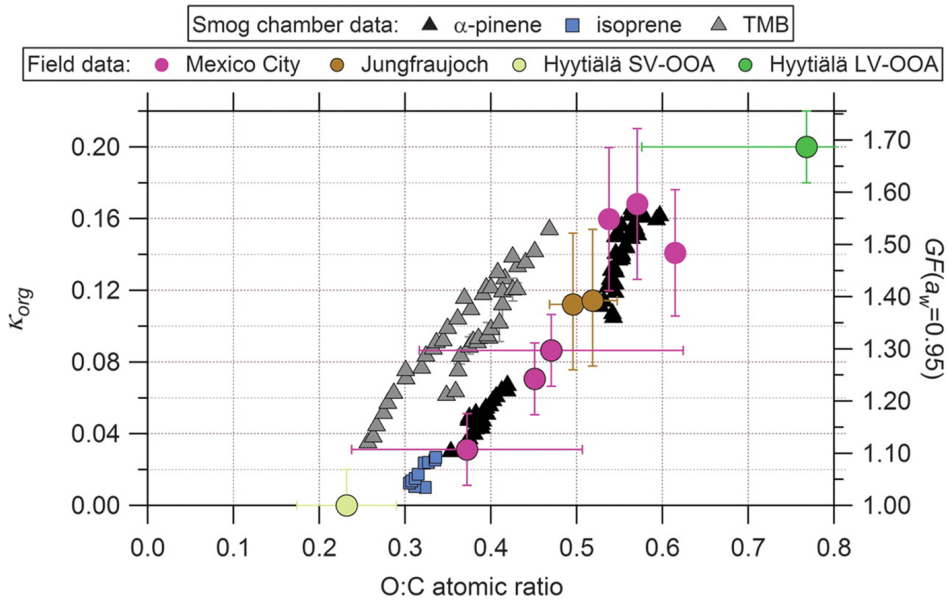

Figure 1.3.: Relationship between O/C and hygroscopicity (κ, or equivalently the particle growth factor at 95% relative humidity) of OA for several field data sets (a high-altitude site at Jungfraujoch, Switzerland; above Mexico City, a polluted mega city; and at the forested site of Hyytiälä, Finland) and for laboratory smog chamber SOA. TMB: trimethylbenzene. Error bars represent the uncertainties in O/C and κ_{Org} (Org: organic) and are shown for only a few data points to reduce visual clutter. GF: growth factor; a_w: water activity. Figure taken from *Jimenez et al.* (2009).

The inorganic fraction plays also an important role for the formation of atmospheric aerosols, especially with the presence of ammonium nitrate and ammonium sulphate. During the last decade, significant reductions were achieved for the emission of SO_2 in Europe (*Vestreng et al.*, 2007; *Monks et al.*, 2009), which diminishes the role of sulphate aerosol but increases the availability of ammonia to form ammonium nitrate (*Schaap et al.*, 2011). Due to its semi-volatile character, NH_4NO_3 is neglected in most global models up to now. The inability to accurately model semi-volatile, especially nitrogen containing compounds is likely to be a significant deficiency in attempts to constrain the direct radiative forcing by aerosols (*Morgan et al.*, 2010). By the implementation of these compounds, the discrepancies between measured and modelled SA budgets (*Kanakidou et al.*, 2005; *Morgan et al.*, 2010) might be reduced. To evaluate models which estimate the efficiencies of aerosol reduction scenarios, data from aerosol measurements are needed from laboratory and chamber experiments, as well as from field observations.

North-Western Europe is characterized as polluted region affected by substantial agricultural emissions. A representative measurement site for North-Western Europe is the Cabauw Experimental Site for Atmospheric Research (CESAR) Tower in Cabauw, the Netherlands, characterized by relatively high OM and ammonium nitrate concentrations

(*Morgan et al.*, 2010; *Schaap et al.*, 2011; *Mensah et al.*, 2012).

This work presents results and conclusions from long term aerosol composition measurements at the CESAR site by aerosol mass spectrometric instruments. The three instruments used, their set-up at the measurement site, and the data analysis procedures applied are described in chapter 2. Observations of particle composition for each campaign are described in chapter 3, together with results from intercomparison with collocated instruments. In the discussion (chapter 4) it is shown that SA dominates aerosol mass. SA in turn had the highest contributions from inorganic secondary aerosols comparing to their organic counterpart. This is also a result of the high gaseous ammonia concentration in Cabauw, leading to high particulate inorganic ammonium salts and even to the neutralization of organic acids by ammonia.

The findings give conclusions on the nature and relevance of sources of organic and inorganic aerosols for this rural region over the whole year. This data set provides the basis to establish efficient strategies for local particle mass reduction.

2. Experimental section

The classical investigation of aerosol composition is performed by collecting particles on filter samples and analysing these filters later with classical analytical methods (*Subramanian et al.*, 2004; *Viana et al.*, 2006, 2007). These so called offline techniques have several disadvantages. Offline measurements can only reach time resolutions from hours to days. The disadvantage of a low time resolution becomes clear when considering that, depending on the investigated site and actual meteorological situation, the atmospheric composition can change on shorter time scales, which is not detectable using offline techniques. Furthermore, filter samples have to be stored before their analysis, which can lead to evaporation of volatile and semi-volatile particle compounds, contaminations, and ageing due to chemical reactions. The analysis itself can be a source of uncertainties as well, especially when there is the need of a high amount of analytical steps. Examples for such sources are the extraction of the sampled particles with solvents followed by a clean-up of the eluent, before analysis using chromatographic procedures and/or mass spectrometric detection devices.

The development of online aerosol sampling and composition measurement techniques during the last decades enhanced the possibilities to investigate aerosol chemical composition in real-time, that means instantaneously after sampling, minimizing the artefacts and shortcomings from offline types mentioned above.

The following sections describe three different online aerosol measurement instruments which were used in this work: the High Resolution Time-of-Flight Aerosol Mass Spectrometer (HR-ToF-AMS), the Aerosol Chemical Speciation Monitor (ACSM), and the Thermal-Desorption Proton-Transfer-Reaction Time-of-Flight Mass Spectrometer (TD-PTR-ToF-MS). They feature a relatively high time resolution which amounts within this work to seven, thirty, and ninety minutes for the AMS, ACSM, and TD-PTR-MS, respectively. All three instruments use mass spectrometry as detection method, but different aerosol sampling and ionization techniques. Next, the measurement site and the experimental set-up at the CESAR tower in Cabauw, NL, are described. This is followed by an introduction into the statistical data analysis methods Positive Matrix Factorization (PMF) and Multilinear Engine 2 (ME-2), including their application to AMS, ACSM and TD-PTR-MS data used within this work.

2.1. The Aerosol Mass Spectrometer

The Aerodyne High Resolution Time-of-Flight Aerosol Mass Spectrometer (HR-ToF-AMS) is a commercially available instrument for realtime determination of the chemical composition and the vacuum aerodynamic diameter D_{va} of the non-refractory (NR) fraction of aerosols (*Jayne et al.*, 2000; *Jimenez et al.*, 2003; *DeCarlo et al.*, 2006). The AMS was already used in a large number of laboratory and short and long term field studies (*Canagaratna et al.*, 2007; *Zhang et al.*, 2007). It can distinguish between the total organic fraction (Org) and the inorganic compounds particulate water (H_2O), ammonium (NH_4), nitrate (NO_3), sulphate (SO_4), and chloride (Chl). The time resolution can reach seconds or minutes per data point.

Figure 2.1 shows a schematic drawing of a HR-ToF-AMS. The set up can be divided into the particle inlet, the differentially pumped sizing chamber, and the particle composition detection section.

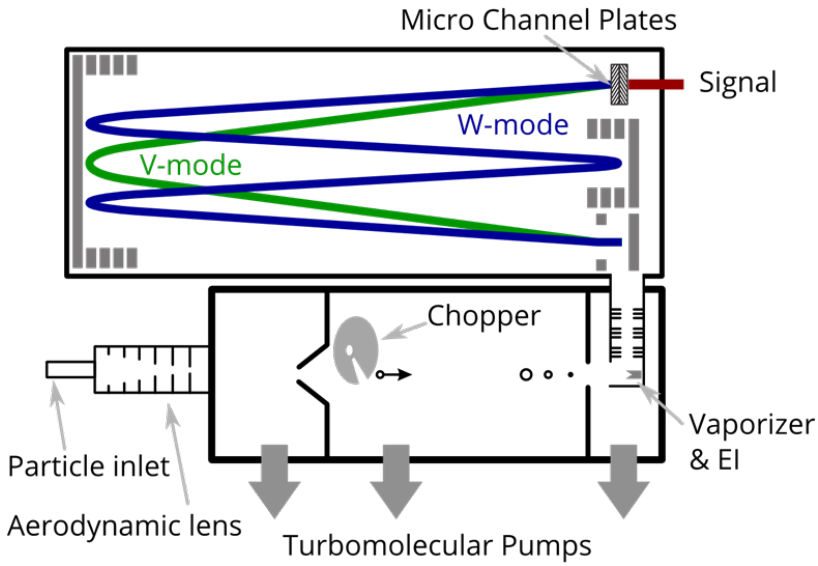

Figure 2.1.: Schematic drawing of the HR-ToF-AMS. Adopted from *DeCarlo et al.* (2006)

The particle inlet contains a critical orifice with a diameter of 100 µm which limits the sample flow into the instrument to approximately 80 cm^3 min^{-1}. Due to the typically low aerosol concentration in respect to gas phase molecules it is necessary to enhance this concentration before the actual analysis of the particles. This is done by the combination of an aerodynamic lens (*Liu et al.*, 1995a,b) and a set of turbomolecular pumps of the following vacuum chamber, resulting in an enrichment of aerosols in the detection region

by a factor of 10^7 compared to ambient concentration. However, sufficient signals from the most prominent gas phase molecules like N_2, O_2, CO_2, and Argon (Ar) are still detected. The sum of all signals originating from gas phase molecules measured by the AMS is called the Air Beam (AB). The AB serves as internal standard to track AMS instrument performances.
The aerodynamic lens focuses the sub-micron aerosols on a narrow beam with a diameter $< 1\,\text{mm}$. The transmission efficiency of particles with diameters between 70 nm and 500 nm reaches 100 %, with still substantially efficiencies for size ranges of 30 nm to 70 nm and 500 nm to 2500 nm (*Canagaratna et al.*, 2007; *Liu et al.*, 2007). Thus, the AMS is referred to as a PM_1 instrument, reflecting its transmission efficiency of approximately 50 % at a particle size of 1 µm. The more divergent expanding, non-focused gas is mainly pumped away in the first part of the following vacuum chamber, called the aerosol sizing chamber, where the pressure is decreased to 10^{-2} Pa. In the next two sections, the particle sizing chamber and the vaporization/ionization region, the pressure decreases further to 10^{-3} Pa and 10^{-5} Pa, respectively.
The particles are accelerated when exiting the aerodynamic lens. Smaller particles reach higher velocities than larger ones. This fact is used to determine the particle aerodynamic diameter. A chopper can be moved into the aerosol beam to modulate it and to cut the beam into defined aerosol packages. This chopper position is referred to as „chopped“ position. An optosensor registers when the particle beam is passing the chopper through one of the slits. This defines the starting time of the aerosol package. By measuring the Particle Time of Flight (PToF) needed for the well known distance between the chopper to the detection region, the aerodynamic diameter can be calculated using calibration parameters derived from PToF measurements with particles of defined diameters (see subsection 2.1.1.3). This mode of the AMS is called the PToF mode.
Besides the chopped position, the chopper can also be moved to the „opened“ position, where the aerosol beam passes to the detection region completely unhindered. In the „closed“ position the beam is totally blocked and therefore only background signals deriving from inside the vacuum chamber are measured. By subtracting the signals of the mass spectra recorded during the closed period from those of the opened period, the differential spectra of the so called MS mode are achieved. The differential MS mode signal thus excludes possible internal contaminations.

In the detection region, the aerosol beam impacts on a conic porous tungsten surface, called the vaporizer, which is resistively heated up to 600°C. Components, which are non-refractory at this temperature, are flash vaporized. The evaporated molecules are then immediately ionized by electrons with an energy of 70 eV emitted by a nearby located filament. The resulting positively charged ions are transferred by an ion op-

tic into the ion chamber of the Time-of-Flight Mass Spectrometer. Here, the ions are pulsed extracted onto two possible ion flight paths until they reach a set of multichannel plates (MCP), where the ions generate a measurable electron signal. Unlike earlier AMS versions, equipped with a Quadrupole Mass Spectrometer (thus named Q-AMS), an HR-ToF-AMS is able to acquire a complete mass spectrum (MS) during one single ion extraction, with an acquiring frequency of the order of tens of kHz (*DeCarlo et al.*, 2006). Ions are separated according to their mass to charge ratio (m/z) in the time-of-flight mass spectrometer. Smaller m/z are more accelerated than larger m/z, causing a shorter ion time of flight. According to equation 2.1 the MS resolution (R) for a given m/z is defined here as the ratio of the respective nominal mass m and the full-width of the peak at half maximum Δm (FWHM) (*Todd*, 1995).

$$R = \frac{m}{\Delta m} \tag{2.1}$$

The mass resolution achievable in the ToF-MS depends on the length of the flight path, on which the mass separation takes place. With a longer path the ions have more time to get separated. One possible path is highlighted in green in Figure 2.1 and is formed like the letter V due to a single reflection. Hence it is called the V-mode. In the W-mode, highlighted in blue in Figure 2.1, the ions are send to a triple reflection path, which has an approximately doubled ion flight path compared to the V-mode. This is why the mass resolution of the W-mode (FWHM; approximately 4000 at m/z 200) is about twice the mass resolution of the V-mode (FWHM; approximately 2000 at m/z 200) (*DeCarlo et al.*, 2006). Due to the longer ion flight path the period between two ion extractions has to be longer (50 µs) in the W-mode than in the V-mode (30 µs) (*DeCarlo et al.*, 2006). Together with the fact that the ion beam is divergent, this results in approximately 20 times lower sensitivity of the W-mode compared to the V-mode. Hence in this work, the W-mode is used for qualitative questions, while the here presented quantitative results derive from V-mode measurements.

The 70 eV Electron Impact (EI) ionization is a standard ionization technique used in most commercially available mass spectrometers. The high energy of the emitted electrons causes high fragmentation of the ionized molecules. Since the fragmentation pattern of a given parental ion into fragment ions is specific for the used ionization energy, mass spectra acquired by this method are generally comparable. Reference spectra of many compounds can be obtained from the National Institute for Standards and Technology (NIST). Due to the flash evaporation of the aerosols in the AMS the molecules receive additional energy compared to standard EI applications, because of which the fragmentation pattern shifts slightly towards smaller fragments. Nevertheless, assuming constant vaporization and

ionization conditions, the fragmentation pattern in the AMS remains constant. Hence, AMS mass spectra are comparable with other AMS reference spectra and, with some limitations, with spectra from the NIST data base.

2.1.1. Quantification with the AMS

This subsection describes the theory underlying the data processing and evaluation of AMS data. For this work, standard AMS software (SQUIRREL v1.53G and PIKA v1.12G)[1] within Igor Pro 6.2.3 (Wave Metrics, Lake Oswego, OR) was used.

The AMS measures signal as an ion rate I [s^{-1}]. With this rate the mass concentration C [µg m^{-3}] can be calculated by equation 2.2 (*Jimenez et al.*, 2003; *Allan et al.*, 2003, 2004), where MW represents the average molecular weight in µg mol^{-1} of the respective ion, CE the collection efficiency, IE the ionization efficiency, N_A the Avogadro constant, and Q the volumetric flow rate in m^3 s^{-1} into the instrument.

$$C = \frac{I \cdot MW}{CE \cdot IE \cdot Q \cdot N_A} \tag{2.2}$$

Each ionized molecule has a specific fragmentation pattern depending on the ionization technique. The mass concentrations of each aerosol species is determined by summing up the mass concentrations calculated from every molecule and its fragments, which contribute to that particular species. This leads to equation 2.3, where the mass concentration for a specific species s is calculated from ion signals of each of its mass spectral fragments i_s ($I_{i,s}$), using the species specific molecular weight MW_s and ionization efficiency IE_s. The number of individual ions and fragments, which contribute to the inorganic species NH_4, NO_3, SO_4, and Chl, is much lower than the number of ions that originated from the ambient organic aerosol fractions. Organic fragments are found at nearly every m/z acquired by the mass spectrometer, potentially interfering with inorganic fragments.

$$C_s = \frac{MW_s}{CE \cdot IE_s \cdot Q \cdot N_A} \sum_{i_s} I_{i,s} \tag{2.3}$$

The collection efficiency is a dimensionless factor between 0 and 1, expressing the ratio of the mass which is actually detected to the aerosol mass introduced into the instrument. It accounts mainly for three effects that cause signal loss in the AMS (*Huffman et al.*, 2005):

[1] http://cires.colorado.edu/ jimenez-group/wiki/index.php/ToF-AMS_Analysis_Software

(i) The effect of the Liu-type aerodynamic lens, leading to loss during the particle transmission (*Liu et al.*, 1995a,b, 2007).

(ii) The particle shape can lead to a $CE < 1$, because non spherical particles cause the particle beam to broaden, resulting again in a lower transmission (*Jayne et al.*, 2000).

(iii) Effect of the particle phase. This includes the probability of solid particles to reflect off the vaporizer prior to complete evaporation (*Canagaratna et al.*, 2007; *Alfarra et al.*, 2004) and is called particle bouncing.

Every effect, and thus the collection efficiency itself, is largely depending on the aerodynamic diameter. Collection efficiencies can be determined for example by comparisons of the AMS total mass loadings with observations from instruments like a Scanning Mobility Particle Sizer (SMPS). Several studies indicate that CE is dominated by the effects depending on the physical state. This means that the CE is a function of mainly ambient humidity and particle chemical composition. High aerosol acidities result in higher collection efficiencies (Quinn et al., 2006), as well as high mass fractions of ammonium nitrate do (*Crosier et al.*, 2007; *Mensah et al.*, 2012). The amount of particulate water is depending on the relative humidity (RH). When the RH reaches so called RH_{Del}, solid particles become spherical due to deliquescence, meaning that the particle compounds are dissolved in the absorbed water to form a solution. This allows the particles to be more efficiently focused by the aerodynamic lens inlet system. RH_{Del} in turn is a function of the chemical composition. *Middlebrook et al.* (2012) evaluated a parametrization of the AMS CE based on the aerosol composition and sampling line relative humidity with a 30 % (2σ) uncertainty. This was done by comparing AMS data with data from independent measurements of fine particle volume and Particle-Into-Liquid Sampler (PILS) ion chromatography measurements. The CE which is determined by this algorithm is called Composition Dependent Collection Efficiency (CDCE) and is explained below (equation 2.7 and 2.8). The CDCE is supposed to be applied to ambient AMS measurements rather than the previously recommended constant CE value of 0.5, especially in areas where high ammonium nitrate or high acidities are observed. The Middlebrook algorithm was used to calculate the CE for all AMS ambient measurements presented in this work.

In general, the CDCE is not determined as an average for a whole data set, but time resolved and applied individually to each data point using the respective composition and relative humidity, with the acidity and the ammonium nitrate mass fraction as the important parameters.

The level of particle acidity is estimated with the following considerations: A theoretically predicted ammonium ($NH_{4,pred}$), which is needed to neutralize all inorganic anion mass concentrations when forming the corresponding ammonium salts is calculated using equation 2.4. The ratio of actually measured NH_4 concentration to $NH_{4,pred}$ serves as

indicator for particle acidity. The ammonium nitrate mass fraction ($ANMF$) in turn is determined by equation 2.5. For ratios of NH_4/ $NH_{4,pred}$ below 0.75, the CDCE is calculated by equation 2.6. If NH_4/ $NH_{4,pred}$ is between 0.75 and 1, CDCE is a function of $ANMF$ using equation 2.7.

$$\mathrm{NH}_{4,pred} = 18 \cdot ((\mathrm{NH}_4/96) \cdot 2 + \mathrm{NO}_3/62 + \mathrm{Chl}/35.45) \tag{2.4}$$

$$ANMF = \frac{80/62 \cdot \mathrm{NO}_3}{(\mathrm{NH}_4 + \mathrm{SO}_4 + \mathrm{NO}_3 + \mathrm{Chl} + \mathrm{Org})} \tag{2.5}$$

$$CE_{dry} = 1 - 0.73 \cdot (\frac{\mathrm{NH}_4}{\mathrm{NH}_{4,pred}}) \tag{2.6}$$

$$CE_{dry} = 0.0833 + 0.9167 \cdot ANMF \tag{2.7}$$

In both cases, the minimum CE is defined to 0.45. In addition, it can be referred to as dry CE or CE_{dry}, since high relative humidities are not taken into account. Laboratory and ambient measurements suggest, that at $RH > 80\,\%$, CE_{dry} should be modified to CE_{wet} by equation 2.8 (*Middlebrook et al.*, 2012).

$$CE_{wet} = (5 \cdot CE_{dry} - 4) + (1 - CE_{dry})/20 \cdot RH \tag{2.8}$$

In general, the ionization efficiency IE is the ratio of detected ions to the amount of evaporated molecules and has to be calibrated periodically (see subsection 2.1.1.1). In principle, the IE calibration has to be done for every aerosol species which is measured by the AMS in order to calculate each individual mass concentration. In practice this is not feasible, especially in case of the ambient organic fraction, because this fraction is the sum of up to hundreds of thousands of different molecules, which have different molecular weights and different IE's. Instead, an IE calibration for nitrate is performed to determine $IE_{\mathrm{NO_3}}$. For all other aerosol species, the relative ionization efficiency (RIE), that means relative to the $IE_{\mathrm{NO_3}}$ and specified for each species s is used, which results in equation 2.9. Inserting equation 2.9 into 2.2 results in equation 2.10.

$$\frac{IE_s}{MW_s} = RIE_s \cdot \frac{IE_{\mathrm{NO_3}}}{MW_{\mathrm{NO_3}}} \tag{2.9}$$

$$C_s = \frac{I \cdot MW_{\mathrm{NO_3}}}{CE \cdot RIE_s \cdot IE_{\mathrm{NO_3}} \cdot Q \cdot N_A} \tag{2.10}$$

The $IE_{\mathrm{NO_3}}$ calibration and the determination of the species RIE's are described in detail in subsection 2.1.1.1

2.1.1.1. Mass concentration measurement and ionization efficiency calibration

Each aerosol species has a known specific ionization pattern due to the constant vaporization and ionization conditions, which means that for example nitrate, NO_3, mainly fragments into the ions NO^+ and $NO_2{}^+$. To calculate the total mass concentration of a certain species using equation 2.3, the sum of the ion rates of all ions, which are contributing to this species have to be taken into account, as well as the individual ionization efficiency and molecular weight. For the example of nitrate this leads to equation 2.11.

$$C_{\mathrm{NO_3}} = \frac{MW_{\mathrm{NO_3}}}{CE \cdot IE_{\mathrm{NO_3}} \cdot Q \cdot N_A} \cdot \sum_{i,\mathrm{NO_3}} (I_{i,\mathrm{NO_3}}) \tag{2.11}$$

For the calibration of the ionization efficiency IE of nitrate, the so called mass based method was applied in this work (*Jayne et al.*, 2000). For this, solutions with different concentrations of ammonium nitrate (NH_4NO_3) are nebulized by a constant output atomizer (TSI 3076), dried by a diffusion dryer and size selected by a Differential Mobility Analyser (DMA). The produced particles are measured by the AMS and a Condensation Particle Counter (CPC, TSI 3022a) in parallel. Knowing the number concentration and the size of the aerosols, the total aerosol mass introduced in the AMS can be calculated, using the bulk density of NH_4NO_3 of $1.77\,\mathrm{g\ cm^{-3}}$. After comparing the calculated mass with the sum of the signals of all nitrate ions, measured by the AMS, a linear regression leads to a scaling factor which represents IE and is in the order of 10^{-7} ions per molecule. That means that one molecule out of a million is actually detected as an ion.

This procedure assumes that all particles are spherical and have a CE of 1. This is justified considering that sub-micron aerosols of pure NH_4NO_3 are known to be liquid or metastable liquid droplets (*Matthew et al.*, 2008), which do not tend to bounce off the vaporizer and are well focused by the aerodynamic lens.

As already mentioned, the V-mode has a higher sensitivity than the W-mode, which means that both modes have also different ionization efficiencies. In practice, an actual IE calibration is only done for the V-mode (IE_V). For the calculation of the corresponding W-mode value (IE_W), the signal of the air beam, measured in both modes (AB_V, AB_W) is taken into account. Assuming a constant concentration of N_2 in the sampled air over time, IE_W is calculated via equation 2.12. The uncertainties deriving from this simplified way to calculate IE_W is acceptable, since the W-mode is mainly used to answer qualitative questions. In the following, the ionization efficiency IE is referred to as the value determined from the calibration in V-mode, if not further specified.

$$IE_W = IE_V \cdot \frac{AB_W}{AB_V} \tag{2.12}$$

Instead of performing a mass calibration for every aerosol species, the relative ionization efficiency (RIE) is used according to equation 2.10. The RIE of ammonium is determined directly from each IE_{NO_3} calibration and resulted in an averaged value of 4.65 ± 0.21 and 4.24 ± 0.14 in this work, assuming that NH_4NO_3 particles produced from aqueous solutions are fully neutralized. That means, that IE_{NH_4} is approximately four to five times higher than IE_{NO_3}.

During the campaigns at the CESAR tower in Cabauw in 2011 and 2012, IE_{NO_3} calibrations of the AMS and the determination of RIE_{NH_4} were done weekly. Table 2.1 shows the averaged calibration results and used RIE's from each species. These values are used for the evaluation of mass concentrations for the data set. Since it would have been too complex to determine the RIE's for the organics, sulphate, chloride, and particulate water, specific for the AMS used in this work, the RIE values of 1.4, 1.2, 1.3, and 2, respectively, were taken from the literature (*Alfarra et al.*, 2004; *Canagaratna et al.*, 2007; *Mensah et al.*, 2011). The value of 1.1 for nitrate arises from the fact that in IE calibrations, only the signals from the NO^+ and $NO_2{}^+$ ions are accounted for the nitrate mass in the AMS, which contribute approximately 90 % of the total ion signal from the NO_3 group. Detailed calibration results are provided in the appendix (A.1.1 and A.2.1):

The detection limits (DL, 3σ) of each species were determined by using the standard deviation (σ or SD) of all mass concentrations measured from particle free ambient air. An overview of the DL's for each campaign is given in the appendix (table A.13).

Table 2.1.: Summary of averaged calibration results and RIE's used for the AMS data during the campaigns in Cabauw in November 2011 and from May to July 2012, respectively. RIE_{NH_4} is directly calculated during IE calibrations, the RIE values of nitrate, sulphate, organics, and chloride were taken from *Alfarra et al.* (2004) and *Canagaratna et al.* (2007). RIE_{H_2O} was determined by *Mensah et al.* (2011).

	November 2011	May to July 2012
IE_V	$1.10{\cdot}10^{-7}$	$9.16{\cdot}10^{-8}$
IE_W	$2.98{\cdot}10^{-9}$	$5.96{\cdot}10^{-9}$
RIE_{NH_4}	4.65 ± 0.21	4.24 ± 0.14
RIE_{NO_3}	1.1	1.1
RIE_{SO_4}	1.2	1.2
RIE_{Org}	1.4	1.4
RIE_{Chl}	1.3	1.3
RIE_{H_2O}	2	2

2.1.1.2. AMS fragmentation table

The determination of mass concentration of each species requires the unambiguous assignment of ion signals to an aerosol compound. The mass resolution of the HR-ToF-AMS, either in V- or W-mode, is sufficient enough to separate and quantify most ions within the whole acquired mass spectra. However, some ions can have different sources, including the air beam signal. The CO_2^+ ion for example can originate from gaseous CO_2 in the sample air or from the fragmentation of organic molecules. Also the H_2O^+ ion can originate from the air beam, particulate water, or the fragmentation of organics or sulphuric acid. To account for that, *Allan et al.* (2004) introduced the so called fragmentation table. This table is a matrix which defines qualitatively and quantitatively, how the signal of such ions is distributed to each possible origin. For initial assumptions, results from laboratory experiments and known fragmentation patterns are taken into account. For example, in case of sulphate, the contribution to the H_2O^+ ion signal is calculated via the signal intensities of the SO^+ and SO_2^+ ions. However, if possible, the entries in the fragmentation table have to be individually adjusted for a particular data set to account for the specific environmental and instrumental conditions. For example, the contributions of the gas phase to a specific ion is determined by measuring particle free sampling air. This is done by using a High Efficiency Particulate Air filter (HEPA-filter) in the inlet line. If supplementary measurements of gas phase compounds like CO_2 or the relative humidity (RH) are available, time dependent corrections can be done additionally for these entries. All adjustments on the AMS fragmentation table values done in this work are summarized in appendix (tables A.6 and A.12).

2.1.1.3. Particle size measurement and calibration

As mentioned above, the measurement of the particle size distribution in the PToF-mode needs to be calibrated. This is done by determining the time of flight, that particles with known diameters and narrow size distributions need for the known distance l_c between the chopper and the vaporizer. Since the combination of vaporization, ionization and acquisition of the ion signals are in general much faster, these processes are considered to happen without any delay after particles are impacting on the vaporizer.

In the presented work the PToF calibrations were done by introducing spherical Polystyrene Latex spheres (PSL, Thermo Scientific) of monodisperse diameters between 80 nm and 600 nm and a constant density of 1.05 g cm^{-3} into the instrument. Suspensions of the PSL's are nebulized by a constant output atomizer (TSI 3076) and the generated particles are dried with a diffusion dryer containing silica gel. Because of the thermal stability of the PSL material the AMS vaporizer temperature has to be increased to 900°C. The cal-

ibration of the vacuum aerodynamic diameter D_{va} with the flight velocity v is performed by equation 2.13, developed by *Jayne et al.* (2000).

$$v = \frac{l_c}{t_p} = v_l + \frac{v_g - v_l}{1 + (\frac{D_{va}}{D^*})^b} \tag{2.13}$$

In this equation, t_p is the measured particle time of flight, v_l the velocities inside and v_g after the aerodynamic lens. D^* and b are calibration parameters and, as well as v_l and v_g , are determined when the plot of the velocities versus the aerodynamic diameters is fitted. A summary of PSL standards used in this work and results from particle size calibrations are presented in tables A.3 and A.9.

2.1.1.4. Elemental analysis of HR-ToF-AMS data

The Time-of-Flight detector resolves and identifies almost all organic fragments containing C-, H-, and O- atoms in various amounts. In a mass spectrum acquired by the AMS, the signal intensity I_i, as well as the elemental composition of each ion i are known. The mass fraction F_E of each element E can therefore be calculated for each ion. By summing up these mass fractions $F_{E,i}$, weighted by the respective signal intensity I_i, for all ions across the whole mass spectrum, the relative mass concentration M_E of E for a given organic spectrum can be obtained using equation 2.14 (*Aiken et al.*, 2007).

$$M_E = \sum_{i=m/z_{min}}^{m/z_{max}} I_i \cdot F_{E,i} \tag{2.14}$$

Dividing the relative mass concentrations by the corresponding molar weight MW_E of the element E results in the relative atomic fraction N_E (equation 2.15).

$$N_E = \frac{M_E}{MW_E} \tag{2.15}$$

Divisions of the respective atomic fractions are done to obtain elemental ratios like O/C, H/C, N/C, and S/C. *Aiken et al.* (2007) and *Aiken et al.* (2008) established correction factors for each elemental ratio by comparing results from laboratory experiments to theoretically calculated elemental ratios of various standards measured by the AMS. The correction factors, which are also used in this work, are 0.75, 0.91, and 0.96 with uncertainties of 31 %, 10 %, and 22 % for O/C, H/C and N/C, respectively. A potential correction factor for S/C was not published yet. Therefore the calculated S/C ratios in this work can only be used qualitatively. These elemental ratios are suitable parameters to estimate and describe atmospheric organic aerosol chemistry like the degree of oxidation of hydrocarbons or the degree of ageing.

2.1.1.5. Inorganic and organic nitrate fractions

Particulate nitrate measured by the AMS can be of organic ($OrgNO_3$) or inorganic (mainly NH_4NO_3) origin. Nitrate is mainly detected on its major fragments NO^+ (m/z 30) and NO_2^+ (m/z 46). Several studies reported, that the fragmentation pattern of nitrate is depending on its origin (*Alfarra et al.*, 2004). The NO_2^+/NO^+ ratio of purely organic nitrates (R_{OrgNO_3}) was found to be approximately 0.1 in chamber experiments, measuring SOA from the reactions of BVOC's with NO_3 with an HR-ToF-AMS (*Fry et al.*, 2009; *Mensah*, 2011; *Fry et al.*, 2011). The corresponding ratio for pure NH_4NO_3 (R_{calib}) was observed to be around 0.4 within the IE calibrations during all AMS campaigns presented in this work. Using these threshold values of both extremes, the fraction of organic nitrates to total measured nitrate $OrgNO_{3_{frac}}$ can be determined by the equation 2.16, adopted from *Farmer et al.* (2010).

$$OrgNO_{3_{frac}} = \frac{(1 + R_{OrgNO_3}) \cdot (R_{meas} - R_{calib})}{(1 + R_{meas}) \cdot (R_{OrgNO_3} - R_{calib})} \tag{2.16}$$

Here, R_{meas} is the measured intensity ratio of NO_2^+ and NO^+ ions as a function of time. Multiplying $OrgNO_{3_{frac}}$ with the total nitrate mass concentration $NO_{3_{total}}$ results in the $OrgNO_3$ mass concentration, according to equation 2.17.

$$OrgNO_{3_{mass}} = OrgNO_{3_{frac}} \cdot NO_{3_{total}} \tag{2.17}$$

Note, that this value represents only the mass of the NO_3 fragment of $OrgNO_3$ and does not include the mass from the varying organic fragments of $OrgNO_3$.

Knowing the organic nitrate fraction, the mass concentration of the inorganic nitrate fraction ($InOrgNO_{3_{mass}}$) can be determined by equation 2.18.

$$InOrgNO_{3_{mass}} = NO_{3_{total}} - OrgNO_{3_{mass}} \tag{2.18}$$

Potential interferences on the NO_2^+/NO^+ ratio originate from other inorganic nitrate salts like $Mg(NO_2)_2$, $NaNO_3$, or $Ca(NO_3)_2$, whose NO_2^+/NO^+ ratios are reported to be 0.09, 0.03, and 0.02, respectively (*Alfarra*, 2004). The contribution and relevance of these salts are estimated by MARGA (Monitor for Aerosol and Gases, see subsection 2.4.1) measurements of particulate Mg, Na, and Ca, done in 2012 and 2013.

2.1.1.6. Aerosol ion balance

An important aerosol property is the acidity, that means the concentration of H^+ ions. The concentration of H^+ ions can be determined directly using the ion balance of all inorganic compounds measured by the AMS. The sensitivity of the AMS for salts containing alkali metal or alkaline earth metals cations is very low due to the high evaporation temperature of these salts. Thus it is acceptable to consider only the main inorganic aerosol anions NO_3^-, SO_4^{2-}, and Cl^- and the cation NH_4^+. In case of nitrate, only the inorganic nitrate ($InOrgNO_3$) ions are used for this ion balance, since organic nitrates are already neutralized by their organic fragments. The determination of inorganic nitrate mass concentrations is described in subsection 2.1.1.5.

If less of the aerosol species NH_4 is measured than necessary to neutralize all anions to form NH_4NO_3, $(NH_4)_2SO_4$, and NH_4Cl, remaining anions are considered to be neutralized by H^+ ions, assuming that aerosols are generally neutral. On the other hand, a higher NH_4 contribution than needed for neutralizing the negative ions indicates the presence of so called excess ammonium (Excess-NH_4). Its mass concentration (e_{NH_4}) is calculated by equation 2.19, where MW_{NH_4} represents the molecular weight of NH_4 and n_i the molar concentration of species i.

$$e_{NH_4} = MW_{NH_4} \cdot [n_{NH_4} - (n_{NO_3} + n_{Chl} + 2 \cdot n_{SO_4})] \tag{2.19}$$

Excess-NH_4 was observed in several periods of both AMS campaigns and is discussed in chapter 4.

2.2. The Aerosol Chemical Speciation Monitor

Though the Aerosol Mass Spectrometer (AMS) is a powerful instrument to measure ambient aerosol chemical composition with high time and mass resolution, it requires a high amount of maintenance from skilled and trained personnel due to its complexity. In addition, the costs of the instrument and its operation are relatively high. That is why measurement campaigns using an AMS are usually not exceeding one or two months (*Sun et al.*, 2012). The Aerodyne Aerosol Chemical Speciation Monitor (ACSM) built upon AMS is specially designed for long-term continuous measurements of mass concentrations and composition of NR-PM_1 species (*Ng et al.*, 2011b), including the organic fraction (Org), particulate water (H_2O), ammonium (NH_4) nitrate (NO_3), sulphate (SO_4), and chloride (Chl). Recent studies showed good agreements of ACSM data with data from other aerosol instruments like HR-ToF-AMS in ambient measurement campaigns, even in highly polluted areas like Beijing (*Sun et al.*, 2011, 2012). An intercomparison of two

collocated ACSM's resulted in strong correlations ($r^2 = 0.8$) and agreements within 27 % (*Budisulistiorini et al.*, 2013). These results indicate that the ACSM can be used as a suitable and cost-effective alternative for aerosol composition measurements due to its capability of stable and reproducible operation. A schematic scheme of the ACSM is given in figure 2.2.

Compared to the AMS the ACSM uses the same aerosol sampling, vaporization, and ionization modules. That includes an identical particle inlet, a Liu-type PM_1 aerodynamic lens, and a vaporizer operated at 600°C, where NR-PM_1 components are flash vaporized and ionized by 70 eV electron impact (see also section 2.1). Due to the same critical orifice of a diameter of 100 µm, a similar inlet flow of approximately 80 cm^3 min^{-1} is achieved. Differences arise from the fact that the ACSM is not equipped with a spinning chopper wheel. Hence, it is not possible to determine particle size information. Since no PToF measurements are performed, there is no need for a long sizing chamber. Because of that, the ACSM chamber has only 2/3 of the length of the AMS, and needs therefore only three turbomolecular pumps instead of five to be evacuated. On the other hand this causes higher air beam concentrations and lower signal-to-noise ratios (SNR). To achieve reliable data, acquired mass spectra are therefore averaged to a time resolution of 30 minutes.

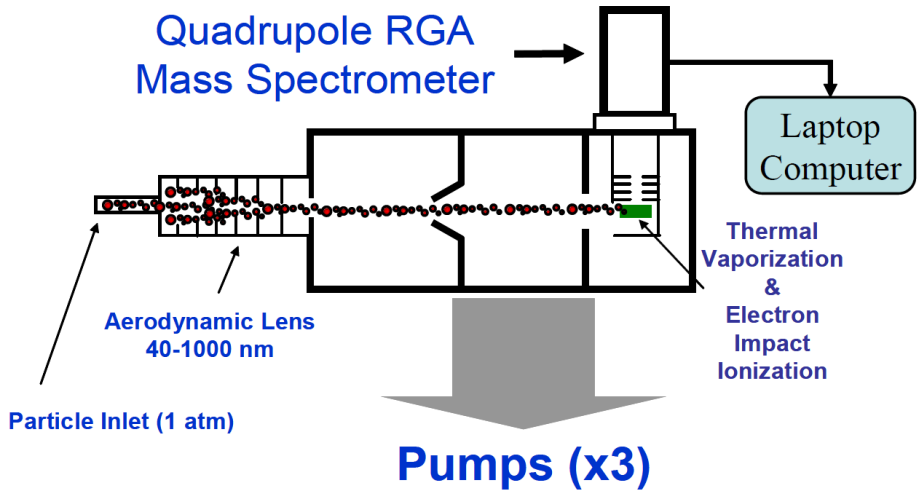

Figure 2.2.: Schematic drawing of the ACSM. Sub-micron particles that enter the aerodynamic lens are focused into a narrow beam that impacts a hot vaporizer. The resulting vapour is ionized with electron impact and chemically characterized with an RGA quadrupole mass spectrometer. Adopted from (*Ng et al.*, 2011b)

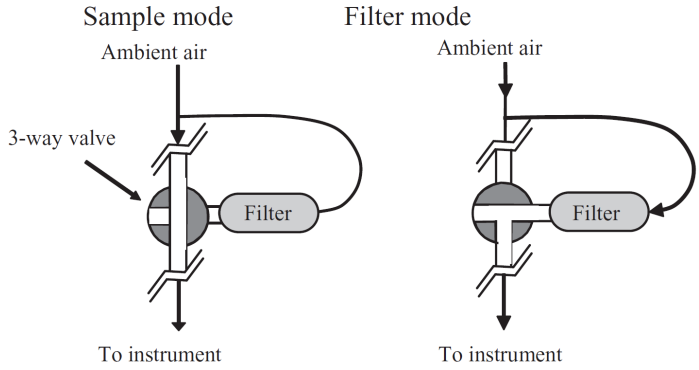

Figure 2.3.: The 3-way valve system is alternately switched between filter position and sample position at the completion of each full mass scan. This results in a "particle" mass spectrum and a "particle free" mass spectrum. The difference between these two spectra contains the particle composition information; Picture is taken from *Ng et al.* (2011b)

The second function of the chopper wheel in an AMS, namely blocking the aerosol beam to obtain background measurements, is replaced by an automated zeroing system as shown in Figure 2.3.

It consists of an automated 3-way valve system placed in the ACSM inlet line. It switches frequently between the sample mode, where the sample air is directly sent into the instrument, and the filter mode, in which particles are removed by a HEPA-filter to gain particle free sample air measured by the ACSM. Similar to the AMS, differential spectra are obtained by subtracting spectra acquired with filtered sample air from spectra of unfiltered air. Using this procedure the resulting differential spectra already exclude signals deriving from internal background and gas phase molecules in combination, so that additional frequent particle free measurements acquired with a HEPA-filter, like in case of the AMS, are not necessary.

Instead of a Time-of-Flight Mass Spectrometer, a commercial grade Quadrupole Residual Gas Analyser (RGA) is employed in the ACSM. It provides unit mass resolution (UMR) mass spectra by scanning consecutively a defined range of m/z (usually up to 200 amu) in a given time. The applied scan rate of the ACSM is chosen to be much slower (0.5 s amu^{-1}) compared to a Quadrupole AMS (Q-AMS; 1 ms amu^{-1}). In general, the sensitivity of the RGA type analyser is approximately ten times lower compared to the high-performance quadrupole used in Q-AMS instruments and a hundred times lower than in ToF-AMS systems (*Ng et al.*, 2011b). This is another reason for choosing a time resolution of 30 minutes in ACSM measurements. The RGA is known to have a mass dependent ion transmission efficiency. To correct for that, an internal calibration source containing an effusive source of naphthalene is located nearby the vaporization/ionization region. Thus, naphthalene signal is always present in the mass spectra acquired from

both the filtered and unfiltered air. The NIST data base provides reference 75 eV electron impact mass spectra of naphthalene. By comparing the fragments of naphthalene measured with the ACSM with the reference fragmentation pattern, the transmission efficiency can be determined as a function of m/z. During data analysis the mass spectra are corrected using this function for the varying ion transmission efficiency. In addition, the parent peak of naphthalene on m/z 128 is used as a reference for the m/z calibration and, assuming constant naphthalene concentration in the detection region, to account for the degradation of the detector (*Ng et al.*, 2011b; *Sun et al.*, 2012).

The detection limits (3σ) for each species are reported to be 0.148 µg m^{-3}, 0.284 µg m^{-3}, 0.012 µg m^{-3}, 0.024 µg m^{-3}, 0.011 µg m^{-3} for organics, ammonium, nitrate, sulphate, and chloride, respectively, at an averaging time of 30 minutes (*Ng et al.*, 2011b). A comparison of AMS and ACSM detection limits is given in the appendix (table A.13).

2.2.1. Quantification with the ACSM

Since the ACSM is a modification of the AMS and has the same principles in terms of aerosol sampling, vaporization/ionization and detection techniques, the determination of mass concentrations of each aerosol species is similar to procedures described in subsection 2.1.1.

Due to the slower detection electronics (no capability to time resolve single ions) of the ACSM, the calibration is based on determining the instrument response factor, RF using NH_4NO_3 as calibration substance (*Ng et al.*, 2011b). The measured RF_{NO_3} in units of amps of NO_3 signal (sum of NO^+ and $NO_2{}^+$) per µg m^{-3} of sampled aerosol is proportional to the ionization efficiency of NO_3 (IE_{NO_3}, in ions/molecule), when normalized to the volumetric sample flow rate Q_{cal} [cm^3 s^{-1}] and multiplier gain G_{cal} (typically approximately 20000) via equation 2.20, again with the Avogadro constant N_A and the specific molecular weight of nitrate MW_{NO_3}. The RF_{NO_3} calibration procedure itself is adopted from the IE calibration with the AMS, as described in subsection 2.1.1.1. Briefly, monodisperse ammonium nitrate particles are generated with an atomizer and passed through a diffusion dryer. The particles are then size selected with a DMA (320 nm) and delivered into both a CPC and the ACSM, where the sum of the ion signals representing the NO_3 moiety is recorded. Knowing particle size and number concentrations of the particles, the mass of the particles can be calculated (*Jayne et al.*, 2000; *Jimenez et al.*, 2003).

$$IE_{NO_3} = \frac{N_A}{MW_{NO_3}} = \frac{RF_{NO_3}}{Q_{cal} \cdot G_{cal}} \tag{2.20}$$

The RF value for each species s is then determined in form of relative ionization efficiencies RIE_s according to 2.1.1.1. RIE_{NH_4} is again deriving from each calibration. In

contrast to the AMS campaigns, the relative ionization efficiency of sulphate (RIE_{SO_4}) was measured during the ACSM campaign in this work. Through measurements of pure ammonium sulphate particles, directly after a calibration using NH_4NO_3, the relative ionization efficiency for sulphate relative to ammonium (RIE_{SO_4/NH_4}) is calculated. Since the RIE of NH_4, relative to NO_3 (RIE_{NH_4/NO_3}), is known, the RIE of SO_4, relative to NO_3 (RIE_{SO_4/NO_3}) is achieved by equation 2.21.

$$RIE_{SO_4/NO_3} = \frac{RIE_{SO_4/NH_4}}{RIE_{NH_4/NO_3}} \tag{2.21}$$

Table 2.2 shows the averaged calibration results during the ACSM campaign from July 2012 to June 2013 at the CESAR Tower in Cabauw. These values are used for the evaluation of mass concentrations for the whole data set. Although the ACSM has in great parts a similar design and similar modules like the AMS, the ACSM has a few significant conceptional differences. These may result in a not full suitability of the calibration procedure, used in this work, for this relatively new instrument. For example, the ACSM is not equipped with a chopper, which blocks the aerosol beam in the particle chamber of an AMS. In addition, the ACSM filter cycle was not used during the RF and RIE calibrations with generated NH_4NO_3 and $(NH_4)_2SO_4$ particles. This made it impossible to account for instrument and also gas phase background signals. During calibration, pure $(NH_4)_2SO_4$ particles showed to produce a high and long-lasting SO_4 background signal inside the instrument, which would potentially result in too low determined relative ionization efficiencies of SO_4 (RIE_{SO_4}) and therefore low reported mass concentrations for this compound.

Table 2.2.: Summary of averaged calibration results and RIE's used for the ACSM data during the campaigns in Cabauw from July 2012 to June 2013. While RIE_{NH_4} and RIE_{SO_4} is directly calculated during the RF calibrations, the same RIE values of nitrate, organics, and chloride were chosen as used for AMS data sets.

RF_{NO_3}	$2.74{\cdot}10^{-11}$
RIE_{NH_4}	7.53 ± 0.21
RIE_{NO_3}	1.1
RIE_{SO_4}	0.81 ± 0.1
RIE_{Org}	1.4
RIE_{Chl}	1.3
RIE_{H_2O}	2

Taking the correction for the m/z dependent ion transmission efficiency of the quadrupole RGA ($T_{m/z}$) into account, mass concentrations for each species s can be calculated using equation 2.22 (*Ng et al.*, 2011b).

$$C_s = \frac{CE}{T_{m/z}} \frac{1}{RIE_s} \frac{Q_{cal} \cdot G_{cal}}{RF_{NO_3}} \frac{1}{Q \cdot G} \sum_{i_s} I_{i,s} \tag{2.22}$$

In practice, Q and G during operation are set to their corresponding values during the RF_{NO_3} calibrations. Hence, these variables effectively cancel out each other.

Despite the smaller vacuum chamber, the effects and component parameters, which influence the collection efficiency CE, are the same for the ACSM and the AMS. Thus, a time resolved CE correction using the algorithm developed by *Middlebrook et al.* (2012) (see subsection 2.1.1) was tested for this particular data set, but was found to be not suitable here. The reason is, that in the ACSM data set, the ratio $NH_4/\ NH_{4,pred}$ is seen to be around 0.75 in some periods. In the Middlebrook algorithm, this value is defined as the threshold, at which the algorithm changes between two different equations to determine the CE, resulting in large jumps of CE values during the mentioned periods, and in consequence, unreasonable jumps in aerosol mass concentrations. Previous campaigns using a HR-ToF-AMS at the CESAR tower in Cabauw, published by *Mensah et al.* (2012), developed a site specific CE correction algorithm, using SMPS data as reference. If the mass fraction of nitrate MF_{NO_3} is below or equal to 0.3, the CE is set to 0.5, the former recommended constant value for ambient AMS measurements. If MF_{NO_3} is above or equal to 0.78, CE is set to 1.0, in respect to pure ammonium nitrate particles. At nitrate mass fractions between 0.3 and 0.78, equation 2.23 is used to determine time resolved CE.

$$CE = 0.1875 + 1.0417 \cdot MF_{NO_3} \tag{2.23}$$

Since this algorithm produced more appropriate results, it was used to provide a time resolved CE correction of the mass concentrations from this campaign.

All ACSM data processing and analysis within this work was performed using software provided by Aerodyne Research (ACSM Local, version 1.531)[2] within IGOR Pro version 6.2.3.

2.2.1.1. ACSM fragmentation table

In contrast to high resolution AMS, the RGA detector of the ACSM acquires only UMR mass spectra. That means, the ACSM is not able to resolve contributions of different molecular ions to the total signal of a certain nominal m/z within the recorded mass spectra. As an example, signals from m/z 43 and m/z 44, measured by different AMS models, are shown in figure 2.4, taken from *DeCarlo et al.* (2006).

[2] https://sites.google.com/site/ariacsm

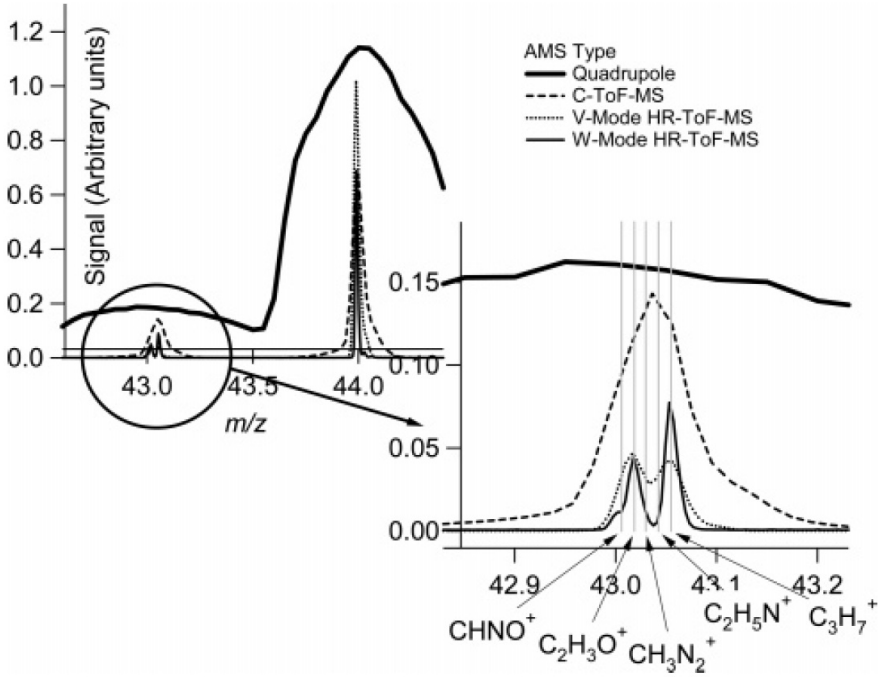

Figure 2.4.: Mass spectrometric signals at m/z 43 (and m/z 44) acquired from different AMS types, where the Q-AMS signals (straight line) can be seen as a representative for ACSM signals. Taken from *DeCarlo et al.* (2006)

The mass resolution of a RGA detector is in the same range as the mass resolution of a Q-AMS. While the HR-ToF-AMS, either operating in V-mode or in W-mode, clearly separates the most prominent individual ions contributing to m/z 43, the limited mass resolution of a unit mass resolution instrument is not able to resolve these ions. That is why an elemental analysis like the determination of O/C and H/C ratios (*Aiken et al.*, 2008) cannot be achieved with ACSM mass spectra. In addition, ions contributing to a certain species can interfere with ion signals from gas phase or from other species. For example, the following ions contribute most likely to the total signal at m/z 16: O^+, NH_4^+, and CH_4^+ . The last two derive from NH_4 and organics, respectively. The O^+ ion may be a fragment of sampled gas phase O_2 or H_2O, but is also formed in minor concentrations from particulate organics, water, and sulphate. Such interferences occur at many m/z $<$ 100. Thus, an UMR version of the already mentioned fragmentation table (subsection 2.1.1.2), introduced by *Allan et al.* (2004), has to be applied and individually adjusted to a specific data set. Again, this table defines the distribution of the ion signals measured at each m/z to the individual species.

In contrast to the AMS UMR fragmentation table, an older version, as described by

Allan et al. (2004), was used due to the restrictions of the ACSM software (see subsection 2.5.2). Due to the automated zeroing system used for the ACSM within this work (section 2.2), adjustments of the fragmentation table entries concerning interferences from air beam molecules are not needed (*Ng et al.*, 2011b). Other adjustments were not possible since the ACSM software does not support proper changes of the fragmentation table.

2.2.1.2. Aerosol ion balance

Similar to AMS data, the aerosol acidity and/or the presence of Excess-NH_4 was determined for ACSM data using the equations described in subsection 2.1.1.6. Different to the AMS, all measured nitrate anions were used for the ion balance and not only the inorganic nitrate fraction, since no certain determination of this fraction could be achieved.

In principle, it is possible to determine time resolved $OrgNO_3$ (see subsection 2.1.1.5) using UMR AMS data (*Mensah*, 2011), resulting in a higher ambiguity due to the interference of both the NO^+ (m/z 30) and NO_2^+ (m/z 46) ion with organic fragments on these nominal masses. An average 46/30 ratio of approximately 0.2 was found for pure NH_4NO_3 particles used at ACSM IE calibrations during the presented campaign. This is significantly lower than observed with the AMS (0.4) in this work. It indicates that the use of a R_{OrgNO_3} value of 0.1 would result in a too high uncertainty for the determination of the organic nitrate fraction from ACSM data, which was therefore not performed in this work.

2.3. The TD-PTR-ToF-MS

The Thermal-Desorption Proton-Transfer-Reaction Time-of-Flight Mass Spectrometer (TD-PTR-ToF-MS) is a modified version of a commercially available PTR-TOF8000 instrument (Ionicon Analytik GmbH, Austria, further referred to as 'PTR-MS'). It is able to detect quantitatively organic compounds alternately from gas and aerosol phase and was already used in several campaigns (*Holzinger et al.*, 2010a, 2013).

A full description of a PTR-MS and its functionality is given elsewhere (*Jordan et al.*, 2009; *Graus et al.*, 2010). Briefly, this instrument allows for precise measurements of volatile organic compounds (VOC) in air or nitrogen. The soft chemical ionization using H_3O^+ ions to protonate VOC's is a proven technique of ionization with limited fragmentation. In the ion source region of the instrument, water molecules are ionized to form H_3O^+. These ions are extracted to the so called drift tube where proton transfer reactions take place with gas molecules from sampled air, according to equation R2.7 and resulting in ions with $(m/z)_{AH^+} = (m/z)_A + 1$. Proton transfer occurs only on analytes (A), if A

has a higher proton affinity (PA) than water (PA_{H_2O} = 691 kJ mol^{-1}, *Hunter and Lias* (1998)), which is not the case for the main components of ambient air. On the other hand, most of the common VOC's have higher proton affinities than water (*Hansel et al.*, 1998; *Lindinger et al.*, 1998), meaning that the PTR-MS ionizes selectively the compounds of interest in this work. As the difference of PA_{H_2O} and PA_A is usually small, little energy is available in proton transfer reactions, which results in low fragmentation and a high abundance of protonated parent ions AH^+.

$$A + H_3O^+ \longrightarrow AH^+ + H_2O \tag{R2.7}$$

The generated analyte ions (AH^+) are then transferred to the Time-of-Flight Mass Spectrometer (ToF-MS), where they are separated by their mass to charge ratio and detected by a Multichannel Plate (MCP). The working principle of a ToF-MS is described in section 2.1. The version used here allows high mass resolutions up to 4000 (FWHM).

The modification of the TD-PTR-MS consists of an additional dual aerosol inlet which was operated as described in (*Holzinger et al.*, 2010b). Centrepiece of each of both aerosol inlets is a Collection Thermal Desorption cell (CTD, Aerosol Dynamics, Berkeley, CA, USA), on which humidified ambient particles of a size range between 70 nm to 2 µm are collected by impaction onto a stainless steel collection surface using a sonic jet impactor. The humidification to approximately 70 % is achieved by a Nafion based humidifier and reduces particle rebound. A schematic drawing is presented in figure 2.5.

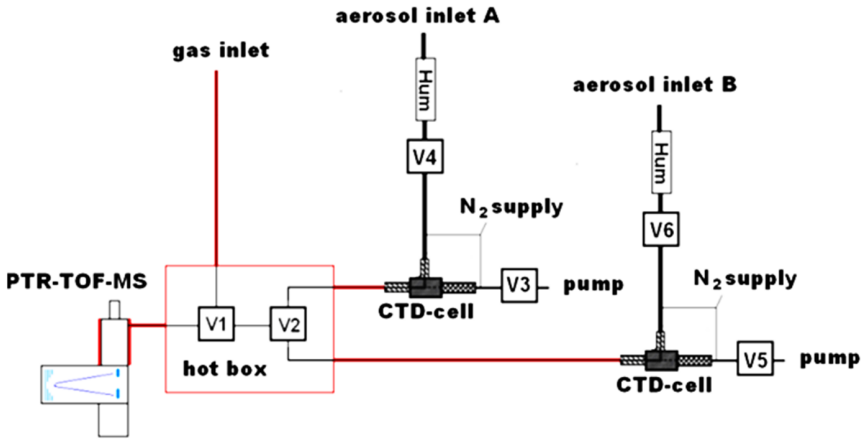

Figure 2.5.: Schematic drawing of the TD-PTR-MS, taken from *Holzinger et al.* (2013)

After collection, the particles are immediately desorbed by heating up the CTD cell in steps of 50°C for a duration of 3 minutes, starting at 50°C and going up to 350°C. A flow of nitrogen (8 mL min^{-1}, standard conditions) transfers the desorbed species to the PTR-MS. The transfer lines and the PTR-MS drift tube are heated to 200°C to prevent semi-volatile compounds from condensing on the walls inside the instrument. As a result a thermogram is obtained, defined as measured mixing ratio profile over a range of temperatures. Figure 2.6 shows example time series of the total product ion signal at m/z 59.049 (protonated acetone) over a full measurement cycle including gas phase and aerosol background measurements for one aerosol inlet, derived from *Holzinger et al.* (2013). This cycle was also applied in the presented campaigns with minor differences. Since the TD-PTR-MS is equipped with two aerosol inlets (Inlet A and B), it is possible to collect particles with one inlet, while the particles sampled from the second one are analysed at the same time, enhancing the time resolution by a factor of two in comparison of using only one aerosol inlet. Background measurements were done by passing ambient air through a Teflon membrane filter located in the system (one filter per inlet). The filters were changed once per week during the campaign. Background signals can originate from contamination from semi-volatile air beam components sticking at the CTD cell or instrumental background contamination (*Holzinger et al.*, 2013).

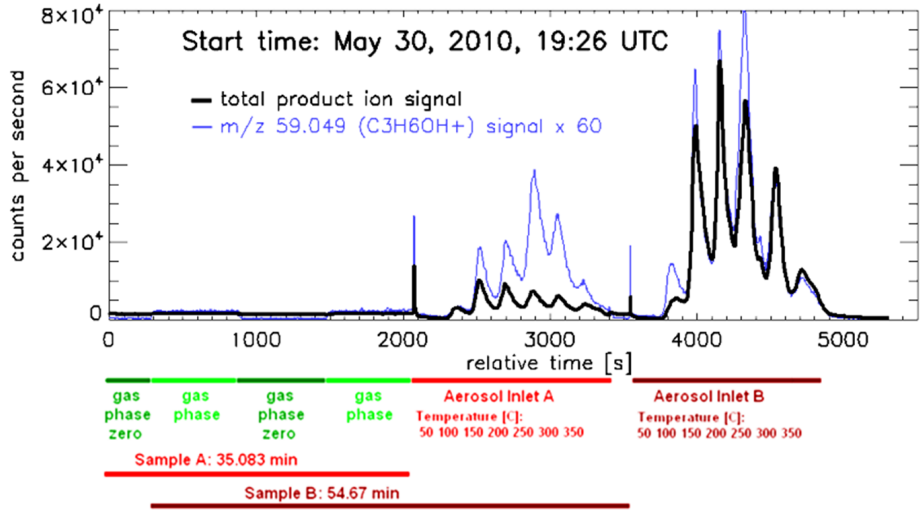

Figure 2.6.: Part of a time series of the total product ion signal at m/z 59.049 (protonated acetone). The inlet A sampled through a particle filter while inlet B samples unfiltered ambient air, taken from *Holzinger et al.* (2013)

The sampling time during the campaigns described here were approximately 40 minutes and 60 minutes, collecting 217 L and 300 L of sample air for inlet A and B, respectively.

The resulting time resolution for organic aerosol measurement using both aerosol inlets was approximately 105 minutes.

2.3.1. TD-PTR-ToF-MS data treatment

The performance of the measurement and the data collection itself during the campaigns in Cabauw in 2011 and 2012 were not part of this work, but the processing and evaluation of the achieved data. This was done with Interactive Data Language (IDL, version 8.2, ITT Visual Information Solutions), using custom made routines described by *Holzinger et al.* (2010a). There, a so called „unified mass list“ was created, containing a list of high resolution ions, which are present in each mass spectrum and detected within the limits of the instrument precision. Based on analysis of the whole datasets from the Cabauw campaigns in 2011 and 2012, all m/z < 40 were excluded, because of high instrument contaminations and/or interferences with inorganic ions (J. Timkovsky and R. Holzinger; personal communications). Exceptions are m/z 27.023 ($C_2H_3^+$), m/z 28.039 ($HCNH^+$), m/z 31.017 (CH_2OH^+), and m/z 33.032 (CH_4OH^+). Additionally, m/z values associated with inorganic ions and higher water clusters of H_3O^+ (NO_2^+ and $(H_2O)_2H_3O^+$, respectively) were excluded. After these corrections, the ion mass list contained 648 ions with the highest mass at m/z 1143, and 296 ions with the highest mass at m/z 283 for 2011 and 2012, respectively. The full lists of ions used for data analysis including most probable assignments of sum formulas is given in appendix (see subsection A.4). The discrepancy between 2011 and 2012 can be explained by the use of a degraded MCP inside the TD-PTR-MS in 2012, which was not able to detect ions with m/z higher than 283 with a sufficient signal-to-noise (SNR) ratio.

Since it is not feasible to calibrate the instrument for every organic compound x occurring in ambient aerosols, the volume mixing ratios VMR_x (in nmol mol^{-1}) were calculated according to equation 2.24 (*Holzinger et al.*, 2010b).

$$VMR_x = \frac{S_x}{(S_{H_3O^+} \cdot k_{H_3O^+} + S \cdot k_{(H_2O)_2H^+}) \cdot t_r \cdot N} \cdot 10^9 \tag{2.24}$$

Here, S_x, $S_{H_3O^+}$, and $S_{(H_2O)_2H^+}$ are the ion count rate (in s^{-1}) of compound x, H_3O^+, and $(H_2O)_2H^+$. $k_{H_3O^+}$ and $k_{(H_2O)_2H^+}$ are the reaction rate constants (in cm^{-3} s^{-1} molecule^{-1}) of compound x with H_3O^+, and $(H_2O)_2H^+$, respectively. The protonated water dimer $(H_2O)_2H^+$ was taken into account as second primary ion, since its signal intensity can reach up to 20 % of the H_3O^+ signal (*Holzinger et al.*, 2010b). Reaction rate constants are reported to be in a range of 1.7 to 2.5$\cdot$ 10^{-9} cm^{-3} s^{-1} molecule^{-1} for most of the organic compounds of interest (*Zhao and Zhang*, 2004). Within this work, a standard reaction

rate constant of $2{\cdot}10^{-9}\,\mathrm{cm^{-3}\ s^{-1}\ molecule^{-1}}$ was used. Furthermore, t_r represents the residence or reaction time of H_3O^+ in the drift tube (typically $9.5{\cdot}10^{-5}\,\mathrm{s}$) and N is the number density of the sample gas in the drift tube (typically $1.35{\cdot}10^{16}$ molecules $\mathrm{cm^{-3}}$).

The mixing ratio of each detected ion was calculated separately for the different desorption temperatures (50°C, 100°C, 150°C, 200°C, 250°C, 300°C, and 350°C), sample types (filtered or unfiltered), and inlets (A or B) in respective matrices where one dimension represents time and the other dimension represent the mass to charge ratio. The aerosol signals were computed by subtracting the signals of filtered sample periods (background) from signals of unfiltered sample periods. The background signals were taken from the nearest measurement of the corresponding unfiltered sample measurement. In contrast to *Holzinger et al.* (2013), all aerosol signals were considered. Also negative values were allowed for the mixing ratios that were sometimes obtained after background subtraction.

The corresponding error value matrices, which were used later for Positive Matrix Factorization (PMF, see section 2.5), were calculated as follows: First, the standard deviation $SD_{BG,i_{T,I}}$ as the median of all background measurements of the whole particular campaign is determined for each ion (i) signal at each desorption temperature T and inlet I. These standard deviations were combined with the corresponding statistical errors $E_{stat,i_{T,I}}$ via error propagation to form the „final error“ $E_{i_{T,I}}$ (equation 2.25).

$$E_{i_{T,I}} = \sqrt{(E_{stat,i_{T,I}})^2 + (SD_{BG,i_{T,I}})^2} \tag{2.25}$$

The statistical error associated with the count rates is obtained from equation 2.26, using the mean signal of a given ion i (mS_i, in $\mathrm{s^{-1}}$) and the dwell time DT in seconds, which is the time spent counting at ion i (*Hayward et al.*, 2002).

$$E_{stat,i} = \frac{mS_i}{\sqrt{mS_i \cdot DT}} \tag{2.26}$$

To convert the volume mixing ratio values ($VMR_{i_{T,I}}$, in nmol $\mathrm{mol^{-1}}$), measured by the PTR-MS, into mass concentrations ($C_{i_{T,I}}$, in µg $\mathrm{m^{-3}}$), the corresponding molecular weight ($M_{i_{T,I}}$, in g $\mathrm{mol^{-1}}$) of the ion i, the flow through the CTD cell during desorption (F_{inlet}, typically 8 mL $\mathrm{min^{-1}}$), the sampled volume (S, in $\mathrm{m^3}$), and the duration of a single temperature step (t, typically 3 minutes) have to be taken into account, resulting in equation 2.27. This was done for the data matrices, containing the mixing ratios from background subtracted aerosol signals, as well as for the error matrices.

$$C_{i_{T,I}} = \frac{VMR_{i_{T,I}} \cdot F_{inlet} \cdot t \cdot M_{i_{T,I}}}{22.4 \cdot S \cdot 1000} \tag{2.27}$$

From the data matrices for each desorption temperature and each inlet, containing the

mass concentrations, new matrices, called summed matrices SM_I, were obtained. The mass concentrations of each ion from a given time point and inlet was summed up over every thermal desorption temperature, using equation 2.28.

$$C_{i_I} = \sum_T C_{i_{T,I}} \tag{2.28}$$

For comparisons with other instruments like the AMS and ACSM, the total organic aerosol (OA_{total}) mass concentrations at a given time point and inlet ($C_{Total,I}$) were determined by summing up the mass concentrations C_{i_I} from the summed matrices SM_I of all ions measured at that time point (equation 2.29). Since the PTR-MS usually measured the aerosol signals from inlet A and B alternately, OA_{total} data sets from both inlets were combined and the data points were sorted by their acquisition date and time, to gain a higher time resolution of 105 minutes.

$$C_{Total,I} = \sum_i C_{i_I} \tag{2.29}$$

In order to perform the analysis based on different classes of chemical compounds, the detected mass peaks were associated with molecular formulas based on the mass library developed by *Holzinger et al.* (2010a, 2013). It contains hydrocarbon molecules with up to 8 atoms of oxygen, including also their corresponding ^{13}C isotopes, and up to 2 atoms of nitrogen. An empirical formula was attributed to a mass peak, when the difference between its exact mass to the measured m/z was less than 2σ. The whole signal at a given m/z was ascribed to one sum formula. In case multiple formulas were plausible for a given ion mass, the following rules were used to prioritize and ascribe signal to one ion for the presented data sets:

1. The formula containing two N atoms is not attributed.

2. A possible ^{13}C ion is only attributed, if the corresponding ^{12}C isotope is detected and attributed, and the signal of the ^{13}C ion reaches at least 50 % of the total signal at the respective m/z. This rule was also applied, when a ^{13}C isotope is the only possible formula to be associated.

3. Since the PTR-MS is more sensitive to organics with lower O/C ratio, the formula containing less oxygen atoms is favoured.

4. In all cases, if several formulas passed criteria were available, the formula with the smallest deviation from the considered mass was chosen.

2.3.1.1. Elemental analysis of TD-PTR-MS data

The elemental analysis of TD-PTR-MS data sets were done similar as described in subsection 2.1.1.4 for AMS data, except that in case of the TD-PTR-MS no correction factors were used to determine the elemental ratios O/C, H/C and N/C, since potential necessary corrections were not investigated yet for the TD-PTR-MS.

2.4. Measurement site: Cabauw, NL

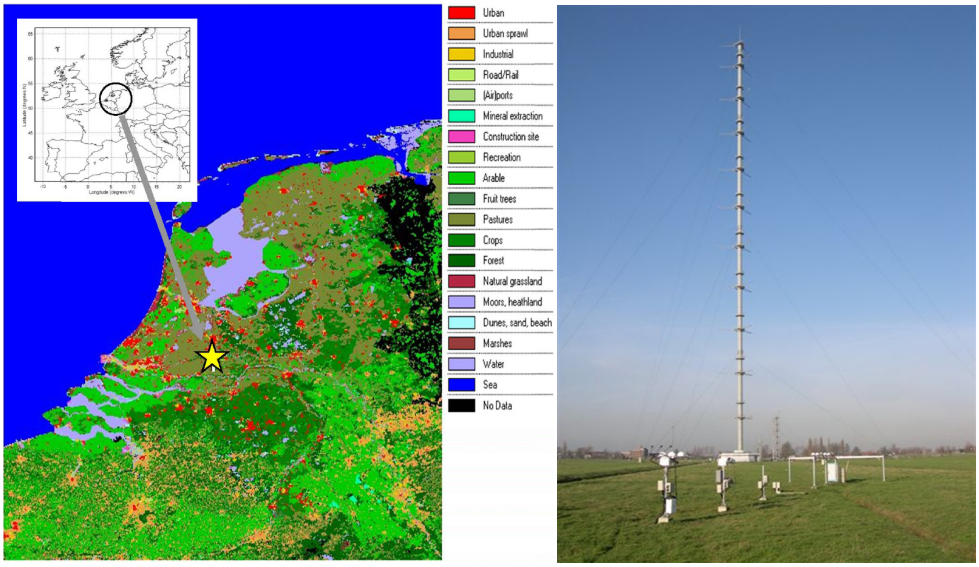

Figure 2.7.: Left: Measurement location; colours define different land use; taken from *Vermeulen et al.* (2011); Right: Picture of CESAR tower

The CESAR tower is about 220 m high and managed and operated by the Royal Netherlands Meteorological Institute (KNMI). It is located in a rural site (51.970°N, 4.926°E), about 20 km south-west of the city of Utrecht in the Netherlands and about 45 km south east of the Dutch North Sea cost, while the direct surroundings of the tower have a relatively low population density. The site conditions are typical for North Western Europe. They can either be maritime or continental, depending on the wind direction. The nearby region is used mainly by agriculture, with a mixture of intensively and extensively managed grassland (see Figure 2.7). These are used also for animal keepings like cattle and sheep, besides nearby located chicken farms. The surface elevation changes in the surrounding are at most a few meters over 20 km. Because the tower ground is approximately

0.7 m below sea level, the diurnal variation of the temperature is relatively stable (*Vermeulen et al.*, 2011).

2.4.1. The Cabauw Experimental Site for Atmospheric Research (CESAR) tower

Two intensive measurement campaigns of aerosol composition were performed at the Cabauw Experimental Site for Atmospheric Research (CESAR) Tower in Cabauw, using a HR-ToF-AMS. The first campaign took place from 08.11. to 01.12.2011, the second from 11.05. to 17.07.2012. During these periods, a collocated TD-PTR-MS was operated by the Institute for Marine and Atmospheric research Utrecht (IMAU, Utrecht University, The Netherlands). Finally, an ACSM, provided also from IMAU, was measuring between 11.07.2012 to 03.06.2013, meaning six days of temporal overlap with the AMS and TD-PTR-MS.

Additionally, data from collocated aerosol instruments, which are deployed at the CESAR tower for routine measurements, are presented and compared to data from the instruments mentioned above: a Monitor for Aerosol and Gases (MARGA, Applikon Analytical BV), a Multi-Angle Absorption Photometer (MAAP, Thermo Scientific Model 5012), both operated by the Energy Research Centre of the Netherlands (ECN) and a Scanning Mobility Particle Sizer (SMPS, TSI 3034), operated by the Netherlands Organisation for Applied Scientific Research (TNO). Figure 2.8a shows a detailed overview of the data coverage of each aerosol instrument.

The MARGA measures water soluble components of both the gas and aerosol phase simultaneously, including the aerosol species nitrate, ammonium, sulphate, and chloride. It uses a Wet Annular Denuder (WAD) followed by a Steam Jet Aerosol Collector (SJAC). The operational and calibration procedures, as well as details of the data analysis are given by *Trebs et al.* (2004). It was collecting alternately the PM_1 and $PM_{2.5}$ fraction of ambient particles at ambient *RH* and temperature, each fraction sampled hourly with a measurement error smaller than 10 % (*Schaap et al.*, 2011). The MARGA inlet was equipped with a PM_{10} size selective head (Rupprecht and Pataschnick, R&P), placed on the roof of the CESAR tower building at approximately 5 m height. The sample air is sucked into the instrument within a polyethylene („Polyflo“) tube with an inner diameter of 0.5” (= 1.27 cm) and a sample flow of 1 m^3 h^{-1}. To compare with the PM_1 instruments AMS and ACSM, only MARGA data containing PM_1 composition is considered within this work.

The MAAP instrument has been introduced by *Petzold and Schönlinner* (2004) and *Petzold et al.* (2005) for the determination of the so called black carbon (BC) fraction

of PM_1 particles. It measured simultaneously the radiation penetrating through and scattered back from a particle-loaded fibre filter. The definition of BC is still ambiguous. *Petzold et al.* (2013) proposed to distinguish between different kinds of BC according to the method of measurement. According to *Petzold et al.* (2013), BC determined by MAAP is referred to as so called equivalent black carbon. Here, it is assumed, that this fraction, further referred to as BC, cannot be not measured by the AMS, ACSM or TD-PTR-MS and can have several origins, most likely incomplete combustion of fossil fuels and biomass burning. During the presented campaigns the MAAP was connected to the common aerosol inlet sampling at 60 m height (see subsection 2.4.2.1), achieving a time resolution of 5 minutes with an uncertainty of 12 % (*Petzold and Schönlinner*, 2004).

The SMPS was also connected to the 60 m sampling line. As a sequential combination of an impactor, neutralizer, Differential Mobility Analyser (DMA) and a Condensation Particle Counter (CPC), it determined the size distribution of particles in a range of 9.37 nm to 515.6 nm. The DMA classified the sampled particles according to their electrical mobility, while the CPC measures the number concentration of each size. The number concentrations were converted into volume distributions, from which the aerosol mass concentration was calculated. For this purpose, the particle density has to be determined, using the aerosol composition information derived from the AMS/ACSM and the MAAP at each data point. Assuming spherical particles, the total density is computed by using the densities of the aerosol species, weighted by their mass fractions. Bulk densities of NH_4NO_3 (1.72 g cm^{-3}) and $(NH_4)_2SO_4$ (1.77 g cm^{-3}), and the density of organics (1.4 g cm^{-3}, *Hallquist et al.* (2009)) were taken into account. Inorganic salts containing chloride are likely not detected by AMS and ACSM systems due to their low capability to flash vaporize these salts, meaning that most of the AMS/ACSM chloride originates from organic chlorides. Considering its low fractional abundance (usually 1 % to 3 % at this site, *Mensah et al.* (2012)) and therefore its low influence on the total particle density, it is acceptable to set the density for chloride to 1 g cm^{-3}. Finally, a density of 2 g cm^{-3} for BC (*D'Almeida et al.*, 1991) was used for the determination of SMPS total aerosol mass concentration.

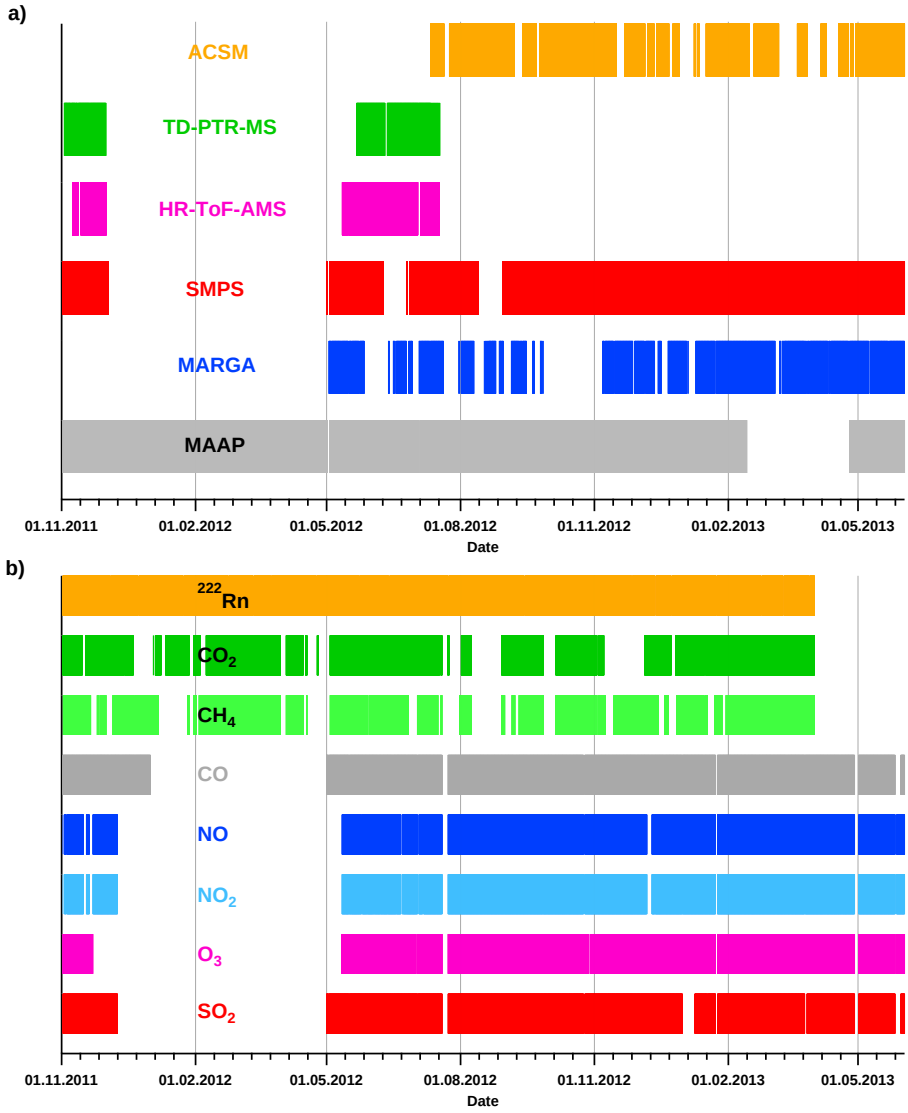

Figure 2.8.: Data coverage from a) aerosol and b) gas phase instruments deployed at the CESAR tower

2.4.1.1. Supplementary instruments at the CESAR tower

The CESAR tower is equipped with external platforms and booms at 2 m, 10 m, 20 m, 40 m, 80 m, 140 m, and 200 m. At all these levels, meteorological observations of standard parameters like wind speed, wind direction, dew point temperature, and ambient temperature are routinely performed (*Ulden and Wieringa*, 1996). These data sets are available at the CESAR data base[3]. In addition, other meteorological data like precipitation, radiation and remote sensing are acquired at the tower and submitted to the CESAR data base. Meteorological data at 60 m height was obtained by averaging measured data at 40 m and 80 m. Also concentrations of gaseous compounds, including greenhouse gases, are monitored at CESAR (*Russchenberg et al.*, 2005; *Vermeulen et al.*, 2011). The National Institute for Public Health and the Environment (RIVM, the Netherlands) provided hourly data from CO, NO, NO_2, SO, SO_2, and O_3, but also daily PM_1 measurements. Data of ambient CO_2, CH_4 (both measured at 20 m, 60 m, 120 m, and 200 m height), and Radon 222 (^{222}Rn, measured at 20 m and 200 m height) is determined by ECN on a time scale of 30 minutes. Figure 2.8b gives an overview of the available data of gas tracers used within this work.

The following subsections explain the sampling conditions and the experimental set-ups for the AMS, ACSM, and TD-PTR-MS during the respective measurement campaign at the CESAR tower.

2.4.2. Experimental set-ups of the HR-ToF-AMS at the CESAR tower

Because the exact location of the AMS and the used sampling inlets differed between the campaigns in 2011 and 2012, the descriptions regarding the AMS are given separately for each campaign.

2.4.2.1. November 2011

During the campaign in November 2011, the AMS was located in the basement of the tower building and connected to the common aerosol inlet which samples at 60 m height. This inlet consisted of four PM_{10} size selective heads at the top, followed by a Nafion dryer to keep the relative humidity (RH) of the sample air below 40 %. The stainless steel pipe, ranging from the aperture at 60 m to the basement, has an inner diameter of 0.5" (= 1.27 cm) and ends in a manifold, where the sampled air is distributed to a variety of different instruments, each with its own sample flow. An overall sample flow

[3] http://www.cesar-database.nl

of 60 L min^{-1} was adjusted inside the 60 m pipe, assuring laminar conditions. The AMS, the MAAP and the SMPS were connected to this manifold, together with instruments providing temperature and *RH* data. For the AMS, the sample air was piped through 3 m of a stainless steel tube (6 mm inner diameter), before reaching a remote controlled 4-port valve to switch between measurements of sample air directly and particle free air by using 2 HEPA filters in a row. Behind the valve, the remaining inlet was shared by the AMS and a Butanol CPC (TSI 3022a), which data was acquired directly with the AMS data acquisition software (DAQ[4], version 3.1.0). Furthermore, a Vaisala HMP 235 was installed in-line between the remote valve and the CPC and provided temperature and *RH* information of the sample air in the basement, again acquired directly with the AMS DAQ. The CPC was equipped with an external pump to maintain an overall sample flow of 380 mL min^{-1} within the whole inlet system between the manifold and the two instruments. The total residence time of the sample air within this set-up was approximately 84 seconds. The AMS acquired MS data using V- and W-mode alternately, in addition to the determination of the size distribution in V-mode. Regarding the V-mode only, a time resolution of 7 minutes was achieved. Measurements of filtered air were performed every 2 to 3 days at different day and night times to determine representative gas phase background, acquiring 4 to 5 data points of both MS modes. AMS calibration intervals and results for 2011 and 2012 are described in subsection 2.1.1.

Very recent investigations showed that aerosol measurements through the 60 m sampling line underestimate each aerosol species by approximately 33 %, most likely due to wall losses and/or evaporation (Alex Vermeulen, ECN, personal communication). Therefore, aerosol species and total masses obtained from this sampling line are divided by a factor of 0.66 to account for these losses. This is done for all data derived from the MAAP and SMPS, as well as AMS data from 2011.

2.4.2.2. May to July 2012

In contrast to 2011, the AMS was placed next to the MARGA and the TD-PTR-MS in the tower ground level during the 2012 campaign, sharing the MARGA inlet (see subsection 2.4.1). Close to the MARGA entry of the polyethylene tube, a tee was installed with an additional 50 cm long stainless steel tube (6 mm inner diameter) towards the AMS remote valve mentioned in subsection 2.4.2.1. The residence time was approximately 20 seconds. Besides a different CPC model (here, a TSI 3786 was used), the set-up and all measuring conditions remained the same as described in subsection 2.4.2.1. CPC data acquisition was performed with the Aerosol Instrument Manager (AIM, TSI, version 7.0).

[4]https://sites.google.com/site/tofamsdaq/

2.4.3. Experimental set-up of the TD-PTR-MS at the CESAR tower

During the campaigns in 2011 and 2012, the TD-PTR-MS was located beside the MARGA and sampled ambient aerosol and gas phases with separated inlets on the roof of the tower building next to the MARGA inlet aperture at 5 m height. Each aerosol inlet head was equipped with a $PM_{2.5}$ cyclone (URG-2000-30EN, URG Corporation, Chapel Hill, USA) to remove coarse mode particles. Ambient aerosols are sucked through 10 m long non-insultated copper lines with an inner diameter (ID) of 6.5 mm to the CTD collection device. The sample flow of each aerosol inlet was maintained at 8 L min^{-1}. The gas phase inlet was located next to the aerosol inlet and consisted of a 10 m PEEK tubing (ID = 1 mm), which was heated to a temperature of 150°C. From the sample flow of the gas inlet (50 mL min^{-1}) the PTR-MS sub-sampled at a rate of 8 mL min^{-1} (standard conditions). Using this set-up, residence times of approximately 10 and 38 seconds for each aerosol inlet and the gas phase inlet, respectively, were achieved.

2.4.4. Experimental set-up of the ACSM at the CESAR tower

Between July 2012 and June 2013, the ACSM was also located near the MARGA and its sampling line was equal to the aerosol sampling set-up of the TD-PTR-MS. It used also a $PM_{2.5}$ cyclone and a 10 m long copper line (ID = 6.5 mm) with a sample flow of 9 L min^{-1} within this line, achieved by a bypump. From this flow, a subsample flow of 1 L min^{-1} was diverted to a Nafion dryer and again splitted, resulting in a flow of approximately 80 mL min^{-1} introduced into the ACSM. This resulted in a total residence time of approximately 18 seconds. The calibration procedures and results are stated in subsection 2.2.1. As mentioned in section 2.2, the gas phase and instrument background were excluded using an automated zeroing system (figure 2.3).

2.5. Statistical methods of organic aerosol data analysis

Ambient aerosols contain up to hundreds of thousands of different organic molecules, which makes it impossible to distinguish between all these compounds using mass spectra acquired either by the AMS, ACSM or TD-PTR-MS. Over the past years, the statistical tool called Positive Matrix Factorization (PMF, *Paatero and Tapper* (1994); *Paatero* (1997)) has been successfully used in ambient studies apportioning the measured organic mass spectra in terms of source/process-related components (*Zhang et al.*, 2011). PMF assumes, that the original data set, containing variable mass spectra over time, is a linear combination of a given number of so called factors, each with a constant mass spectrum, but varying contributions over time. A scheme explaining the PMF factorization is shown

in figure 2.9. These factors are attributed to different sources or processes for interpretation of ambient observations. Especially in the AMS/ACSM community, PMF has been established and applied in numerous chamber (e.g. *Chhabra et al.* (2010); *Craven et al.* (2012)) and ambient investigations (e.g. *Aiken et al.* (2009); *Ulbrich et al.* (2009); *Mohr et al.* (2012)) of organic aerosols as a source apportionment technique, since these instruments produce large data sets with high numbers of variables, precisely m/z. PMF is a bilinear model, using a least squares algorithm. It does not need a priori information, except that the variables have to be non-negative, representing real data sets.

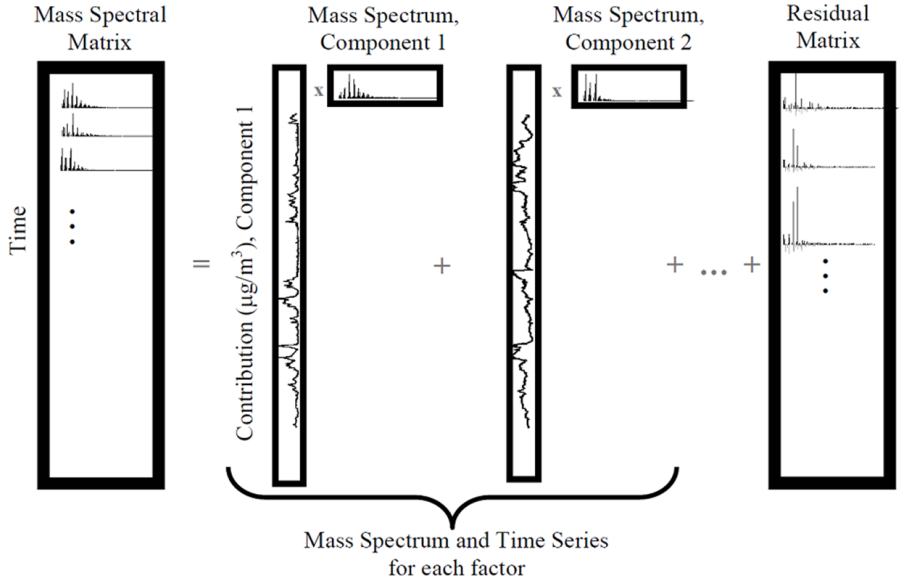

Figure 2.9.: Scheme of Positive Matrix Factorization, applied to AMS/ACSM/TD-PTR-MS data sets; taken from *Ulbrich et al.* (2009)

All three aerosol instruments mentioned above produce data sets of averaged mass spectra, varying between each time point. This can be expressed by a matrix X_{ij} where the columns j are the variables (here the m/z) and each row i represents one averaged data point (here a time point). In PMF X_{ij} is approximated by the product of the matrices G_{ip} and F_{pj}, in addition to a matrix E_{ij} as the model residual (equation 2.30). Each column j of the matrix G represents the time series of a factor, and each row i of F represents the profile (mass spectrum) of this factor. p is then defined as the number of factors of the chosen model.

$$X_{ij} = G_{ip} \cdot F_{jp} + E_{ij} \tag{2.30}$$

The elements of G and F are fitted by iteratively minimizing the quality of fit parameter Q, calculated by equation 2.31.

$$Q = \sum_{i=1}^{m} \sum_{j=1}^{n} (\frac{e_{ij}}{\sigma_{ij}})^2 \tag{2.31}$$

Here, e_{ij} are the elements of the $m \cdot n$ residual matrix E and σ_{ij} are the respective uncertainty (or error) values, containing the measurement and model uncertainty. If all points in the residual matrix are fit to within their expected error, then abs $(e_{ij}/\sigma_{ij}) \approx 1$ and the expected Q_{exp} equals the degrees of freedom of the fitted data $(m \cdot n - p \cdot (m+n))$ (*Paatero et al.*, 2002). In case of the AMS and ACSM data sets, the product of the matrix dimensions $m \cdot n$ are much higher than the term $p \cdot (m+n)$, meaning that Q_{exp} is approximated by $m \cdot n$, the number of points in the data matrix X. As a result, the ratio Q/Q_{exp} should be around 1, assuming accurate error estimation (*Ulbrich et al.*, 2009). If $Q/Q_{exp} \gg 1$, the errors are underestimated or the degree of freedom, i.e. the number of factor profiles, is chosen too low. An overestimation of the errors or overfitting by too many factors is indicated by values $Q/Q_{exp} \ll 1$. In practice, error estimations are difficult to perform in case of aerosol measurements. Therefore, instead of just gaining a Q/Q_{exp} value of 1 as quality parameter for the PMF analysis, the relative change of this ratio is investigated across different model runs to choose a proper and reasonable PMF solution by means of a relatively low Q/Q_{exp} value and other criteria, which will be discussed below. On the other hand, it is possible, that multiple local minima of Q/Q_{exp} exist. To find the global minimum, so called seed runs, that means additional solutions, can be explored by starting the PMF2 algorithm from different pseudorandom values (*Ulbrich et al.*, 2009).

In this work, the PMF2- and the Multilinear Engine 2 (ME-2) solver (*Paatero*, 1999) were used to solve the PMF algorithm. Neither the PMF nor the ME-2 solver gives independently the one and only „right“ or „wrong“ solution. In fact, the user has to determine a suitable and reasonable solution, including a proper number of factors. Choosing too few factors may not explain every possible source or process by one factor (here a MS), but may merge these information in one factor. When too many factors are chosen, „true“ factors may be split into two or more factors, which seem to have the same source or cannot be assigned to known specific sources. In general, a higher number of factors means a higher degree of freedom and thus, a lower quality parameter Q. But a strong decrease of Q/Q_{exp} after the addition of another factor indicates that a high amount of unexplained variation is now embedded within the factors of the particular solution. That means, that the minimization of the residual values, or in other words the unexplained variations are used as another metric to determine a proper solution.

Furthermore, PMF solutions are not unique due to rotational ambiguity (*Paatero et al.*, 2002). For these rotations, Q stays invariant with respect to rotations in space (explained in equations 2.32, where T is a transformation matrix and T^{-1} is its inverse).

$$GF = G \cdot T \cdot T^{-1} \cdot F \tag{2.32}$$

There are two possibilities to reduce the ambiguity. A user-specific parameter called FPEAK, denoted by φ for the global control of such approximate rotations (*Ulbrich et al.*, 2009; *Paatero and Hopke*, 2009), should be explored. FPEAK allows for examining approximate or "distorted" rotations that do not strictly follow equation 2.32. *Reff et al.* (2007) reported, that FPEAK values range between -1 and 1.

Another way to reduce rotational ambiguity is the addition of a priori information into the model in form of constraining one or more profile factors or time series (all with non-negative values), so that it does not rotate and it provides a rather unique solution. This is done within the ME-2 solver (*Paatero*, 1999), which uses also the PMF2 algorithm and provides a more efficient and sensitive exploration of the model space than is possible with the global FPEAK tool. With the ME-2 solver it is possible to introduce a priori information with a user given degree of freedom, defined by the a-value (*Canonaco et al.*, 2013). The a-value determines how much the output factor profiles $f_{j,solution}$ or time series $g_{i,solution}$ are allowed to vary from the reference inputs (f_j, g_i), according to equations 2.33 and 2.34.

$$f_{j,solution} = f_j \pm a \cdot f_j \tag{2.33}$$

$$g_{i,solution} = g_i \pm a \cdot g_i \tag{2.34}$$

A ME-2 approach with all factor profiles (MS) fully constrained, meaning with an a priori a-value = 0, is equal to the so called Chemical Mass Balance (CMB) approach (*Canonaco et al.*, 2013).

Besides the mathematical metrics mentioned above, factors need to be explored and validated by means of their MS characteristics and/or by correlation of the time dependence to so called external tracers, meaning time series of compounds like particulate nitrate, sulphate, ammonium, chloride or black carbon. In addition, meteorological data like temperature and wind direction, as well as gas phase tracers mentioned in subsection 2.4.1 and measured by collocated instruments are taken into account to assign the investigated factors according to their source. As mentioned in chapter 1, the major sources for organic aerosols can be either of primary (POA) or secondary character (SOA). The first group contains directly emitted organic aerosols like hydrocarbon-like (HOA), cooking

(COA, *Mohr et al.* (2012); *Sun et al.* (2013)) or biomass burning organic aerosols (BBOA, *Aiken et al.* (2010)). HOA subclasses are for example fossil fuel combustion or lubricating oil. SOA are usually described by more oxygenated organic aerosols (OOA). The OOA are categorized by their volatility and/or oxidation degree (e.g. O/C ratio), for example into low-volatile OOA (LVOOA) and semi-volatile OOA (SVOOA) (*Jimenez et al.*, 2003; *Lanz et al.*, 2007). Besides, also side specific OA like a methanesulfonic acid containing factor (MSA-OA, *Diesch et al.* (2012); *Schmale et al.* (2013); *Crippa et al.* (2013c)) or very oxidised OOA factors which correspond to humic-like substances (HULIS, *Paglione et al.* (2014)) can be achieved from PMF/ME-2 calculations.

Reference mass spectra for PMF factors are available on the AMS mass spectral data base (*Ulbrich et al.*, 2009; *Crippa et al.*, 2014), which can be used for comparing PMF factor profiles, derived from AMS/ACSM data sets, with mass spectra obtained from laboratory, chamber and ambient studies. Reference mass spectra from this data base are also used as constrained factor profiles within the ME-2 solver in this work. Up to now, no such data base is known for PTR-MS mass spectra.

2.5.1. Application of PMF to AMS data

For the present AMS data sets, the PMF2-solver software PMF Evaluation Tool (PET[5], *Ulbrich et al.* (2009)), version 2.06 beta, was used within Igor Pro 6.2.3.

The data and error matrices were extracted from the AMS high resolution data, evaluated according to subsection 2.1.1, as mass concentrations in µg m^{-3} over time, using PIKA software. Before using the PMF algorithm, the matrices need to be prepared according to *Ulbrich et al.* (2009). Briefly, a minimum counting error of 1 ion is applied, and all isotopes are removed from the m/z list, since they do not contain any additional information. After deleting values equal or below 0, all m/z with a signal-to-noise ratio (SNR) between 0.2 and 2 were downweighted by a factor of 2, while m/z with a SNR below 0.2 were downweighted by a factor of 10 (*Paatero and Hopke*, 2003). The downweighting is performed by multiplying the particular error values with 2 or 10, respectively. Due to the fragmentation table (subsection 2.1.1.2), some information is repeated one or more times. In case of organics, fractions of the concentration on m/z 44 (in high resolution spectra CO_2^+) are also attributed to m/z 16, 17, 18, and 28 (using the fragmentation table from *Aiken et al.* (2008)). Including these ions in PMF therefore gives additional weight to the strong signal at m/z 44. To downweight the columns of these m/z 's, the errors of all mass concentrations on m/z 16, 17, 18, 28 and 44 are multiplied with the square root of 5, so that in total they only contribute the m/z 44 signal once (*Ulbrich et al.*, 2009).

[5]http://cires.colorado.edu/jimenez-group/wiki/index.php/PMF-AMS_Analysis_Guide

The strategy to perform factor analysis and explore PMF solutions on AMS data sets was mainly taken from *Zhang et al.* (2011). Here, solutions with 1 to 10 factors and a FPEAK between -1 and 1 for each number of factors were investigated. After taking all metrics mentioned above into account to find a proper solution, a high number of seed runs (at least 50) is used to find the global minimum of Q/Q_{exp}. The most abundant solution scheme has automatically the highest probability and can therefore be considered as the most likely „true“ solution. Finally, the bootstrapping (BS) method with replacement of MS was used to estimate quantitatively the uncertainty in both the factor mass spectra and time series (*Ulbrich et al.*, 2009). BS is used to detect and estimate disproportionate effects of a small set of observations on the solution and also, to a lesser extent, effects of rotational ambiguity. BS data sets are constructed by randomly sampling blocks of observations from the original data set. As recommended by the PMF manual of the Environmental Protection Agency (EPA[6], USA), at least 100 bootstrapping runs were performed to gain a proper uncertainty estimation.

AMS data sets usually contain a much higher number of both data points and m/z than ACSM data sets for example. Especially the high amount of variables increases the computational time for using the PMF2 algorithm drastically. Because of these reasons, the use of the ME-2 solver for AMS data was not part of this work.

2.5.2. Application of PMF/ME-2 to ACSM data

The extraction of ACSM data and error matrices as mass concentrations in µg m^{-3} over time, as well as their preparation for PMF, was done within the ACSM Local software, version 1.531 within IGOR Pro, version 6.2.3. The preparation procedure was almost equal to that of AMS data sets (subsection 2.5.1). The only difference is due to the use of a slightly different version of the fragmentation table (*Allan et al.*, 2004) in the ACSM software. Here, the information at m/z 44 is repeated only on m/z 16, 17, and 18, and not on m/z 28. That means that in this case the error values of m/z 16, 17, 18, and 44 are multiplied with the square root of 4.

In contrast to AMS PMF, the IGOR Pro based ME-2-solver Source Finder (SoFi, *Canonaco et al.* (2013)), version 4.8, was used to perform the PMF2 algorithm on ACSM data. The overall source apportionment strategy was developed by *Crippa et al.* (2014) and was used here in large parts. Briefly, unconstrained PMF runs were first investigated with 1 to 10 factors and a moderate number of seeds (10 to 15) for each factor number. If POA factor profiles like HOA or BBOA were found, site specific POA mass spectra or spectra derived from the data base were constrained one after another with various

[6]http://www.epa.gov/heasd/documents/PMF_5.0_User_Guide.pdf

a-values. Since SOA factors have much higher variations between measurement sites in terms of their MS than POA, it is not appropriate to constrain SOA factor profiles using reference spectra derived from different locations (*Canonaco et al.*, 2013). The scanning of a-values for each constrained factor is called sensitivity test, where the degree of freedom for each constrained factor is explored, at which reasonable solutions can still be obtained. According to *Crippa et al.* (2014), HOA and COA MS should be more constrained (a-value between 0 and 0.2) than BBOA MS (a $\approx$ 0.3), since the global variation of BBOA by means of its profile is larger. In each step, either in unconstrained or constrained approaches, the following criteria for finding a proper solution were used in this work:

- Q/Q_{exp} was minimized.
- Factor profiles have reasonable mass spectra, as expected for the measurement site.
- Factor time series have high correlations with respective external data sets as described in section 2.5.
- When a proper solution is found, seed runs (typically 50) are necessary to find the global minimum for Q/Q_{exp}.

2.5.3. Application of PMF to TD-PTR-ToF-MS data

Only few studies are reported in the literature, where PMF factor analysis was performed on organic aerosol, measured by other than AMS or AMS based aerosol instruments. *Williams et al.* (2007) and *Williams et al.* (2010b) applied PMF to aerosol composition data derived from the thermal desorption aerosol gas chromatograph (TAG), using standard electron impact ionization similar to AMS. In the context of PMF, PTR-MS data was used by *Slowik et al.* (2010) and *Crippa et al.* (2013a) for combined gas-particle phase source apportionment. For that, a limited number of ion signals, derived from PTR-MS gas phase measurements were implemented into the data/error matrices of a collocated AMS. Factor analysis of these combined matrices provided information about organic aerosol sources and their corresponding precursor VOC. Difficulties arose from the fact, that two different aerosol instruments with different responses on organic compounds were combined. That means that care has to be taken when weighting the uncertainties estimated by each instrument (*Slowik et al.*, 2010).

Due to the unique character of the thermal desorption PTR-MS used in this work, a factor analysis of organic aerosol compounds, measured with proton transfer reaction ionization technique, was not reported so far. There are a number of publications showing reference mass spectra derived from laboratory gas phase measurements with a commercial

PTR-MS (e.g. *Spanel et al.* (2002a,b); *Dryahina et al.* (2004)). Though, it is not certain, to what extend these spectra are comparable with mass spectra, derived from aerosol phase PMF solutions of a TD-PTR-MS.

The values in the data and error matrices were calculated as mass concentrations in µg m^{-3}. Mass concentrations which were obtained at a thermal-desorption temperature of 50°C were completely discarded due to a generally low signal-to-noise ratio at most m/z.

In principle, AMS organic fraction contains all compounds which vaporize at a temperature of 600°C. To compare factor analysis results of AMS and TD-PTR-MS total organic fractions, the PTR-MS mass concentrations of each ion were summed over all thermal-desorption temperatures, derived from one sampling period, but still separated by the inlet. The corresponding errors $e_{ij_{T,I}}$ were combined by error propagation according to equation 2.35.

$$e_{ij_{I,sum}} = \sqrt{\sum_{T}(e_{ij_{T,I}})^2} \tag{2.35}$$

The preparation, performance and investigation of PMF analysis on TD-PTR-MS data was also done with the PMF2-solver software PMF Evaluation Tool (PET, version 2.06 beta). Here, all values equal or below 0 are deleted. After that, all m/z with a signal-to-noise ratio (SNR) between 2 and 0.2 were downweighted by a factor of 2, while m/z with a SNR below 0.2 were deleted. Due to different peak fittings and attributions of formulas to ion signals comparing to AMS data evaluation, ^{13}C isotopes are not removed in TD-PTR-MS matrices. For each approach, PMF solutions with 1 to 15 factors and a FPEAK between -1 and 1 for each number of factors were explored.

3. Observations

In the following sections the observations of the measurement campaigns at CESAR are described separately for the periods November 2011 (section 3.1), May to July 2012 (section 3.2) and the ACSM campaign 2012 to 2013 (section 3.3). The aerosol composition results obtained by the AMS, the ACSM, and the TD-PTR-MS are compared to each other. Furthermore, the observations are compared and related to meteorological events and other collocated instruments mentioned in section 2.4.1. Details on the corresponding calibration results and data analysis are given in the appendix (sections A.1, A.2, and A.4). Times are in UTC (Universal Time, Coordinated), if not otherwise stated.

3.1. AMS Campaign 2011

3.1.1. Meteorological conditions and aerosol composition as observed with the AMS

Figure 3.1 gives an overview of the meteorological conditions during the campaign in November 2011, including wind speed and wind direction (a), temperature (b) and relative humidity (c), measured at both the inlet and at the manifold of the 60 m sample line. The bottom graph (d) displays precipitation (time resolution: 10 minutes) and Radon-222 data.

From 08.11. to 20.11.2011 the air originated mainly from southerly and easterly directions with moderate wind speeds between 0.4 m s^{-1} and 10.2 m s^{-1} (average: 5.0 m s^{-1}). On 20.11. and 21.11.2011, only low wind speed was observed with changing directions, followed by a period which was dominated by southerly and westerly wind directions and wind speeds varying from 5 to 15 m s^{-1}. The temperature and RH at the manifold was obtained with a Vaisala HMP 235 (operated by TNO, The Netherlands), reflecting the actual conditions of the sample air when entering the instruments. Detailed information on the temperatures and relative humidities is presented in table 3.1. At the manifold RH was decreased of approximately 50 % RH by the two Nafion dryers installed in-line the sampling line.

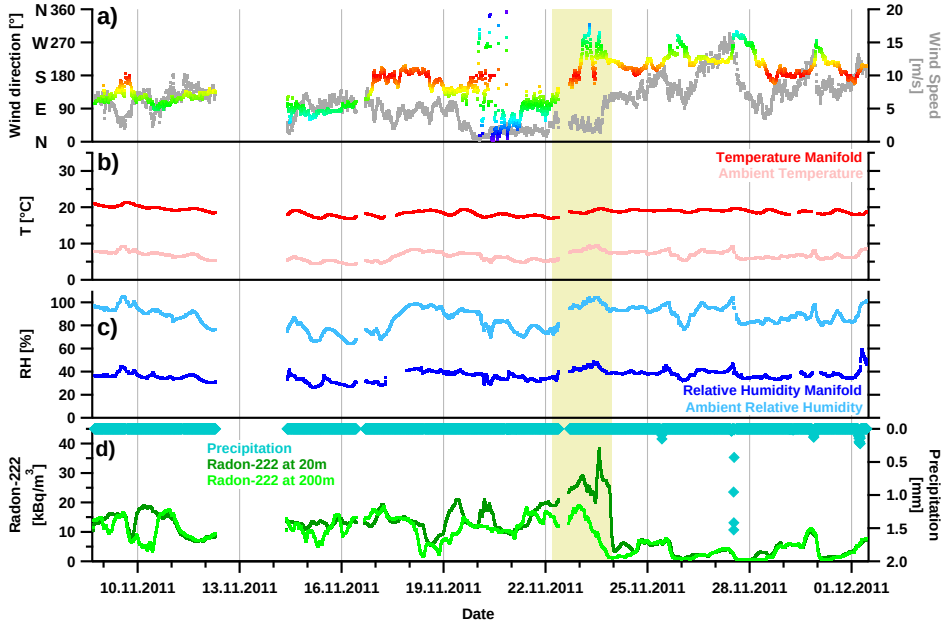

Figure 3.1.: Meteorological overview of the 2011 campaign: a) Wind direction (0°/360°, 90°, 180°, and 270° represent North, East, South, and West, respectively) and wind speed (grey) at 60 m height. b) and c) temperature (red) and relative humidity (blue), measured at the inlet (ambient, dark colours) and at the manifold (light colours) of the 60 m sampling line. d) Precipitation (turquoise) and Radon-222, measured at 20 m (dark green) and 200 m (light green). The period with the highest aerosol mass loading (see below) is highlighted in light green.

Table 3.1.: Overview of the temperatures and relative humidities in 2011, measured at 60 m height and at the sampling line manifold in the basement of the tower.

	Minimum	Maximum	Average
Ambient temperature [°C]	4.2	9.5	6.7
Temperature manifold [°C]	16.9	21.3	18.7
Ambient relative humidity [%]	64.2	104.7	87.1
Relative humidity manifold [%]	26.2	59.3	36.6

The average diurnal variation of both temperatures, the ambient at 60 m and at the manifold (see figure A.1), shows the highest values in the afternoon at around 2 to 3 pm and the lowest at around 4 to 5 am (local time, LT). The difference between the inlet at 60 m and the manifold is approximately 12°C, as also seen in table 3.1.

Vertical profiles of the ambient temperature and relative humidities are routinely measured at the CESAR Tower with a time resolution of 10 minutes. Here, the so called equivalent potential temperature θ was considered, determined according to *Bolton* (1980).

There, θ is defined as the temperature an air parcel would reach if it was brought adiabatically to standard pressure and the water content of the parcel would condense.

The left plot of figure 3.2 illustrates height profiles of θ, obtained during the night to 23.11.2011, the other at 11 am (LT) on 22.11.2011 and at 12 am (LT) on 23.11.2011. The picture on the right shows the CESAR tower at 11 am (LT) on 22.11.2011. The first two profiles show so called temperature inversion. That means, the potential temperature is rising with height, opposite to the expected behaviour. Such profiles were characteristic for this campaign and seen in several periods, mainly in the night-time and mornings. In general, a temperature inversion can be used as an indicator for the height of the so called stable boundary layer (SBL), because an inverted temperature profile prevents mixing of air masses to higher levels (*Stull*, 1988). Details of the SBL and the vertical structure of the atmosphere are given e.g. by *Stull* (1988) and *Wallace and Hobbs* (2006). According to *Wallace and Hobbs* (2006), the observed first two profiles in figure 3.2 indicate that the AMS was sampling within the stable boundary layer. Later during the day of 23.11., the stable layer rose due to radiative heating, and the so called mixed layer grew from the ground to above the 60 m inlet line. This causes the almost invariant temperature profile up to 200 m at 12 am (LT) on 23.11.2011. Similar observations were seen in previous studies at the CESAR tower (*Ulden and Wieringa*, 1996), defining the height of the SBL as done here.

The cloud layer seen in the picture on the right at around 40 m - 80 m may be a visual sign for the transition between the stable boundary layer with the residual layer. A confirmation for the assumption above would be given by remote sensing measurements using LiDAR instruments, which are able to determine the layer heights more precisely (*Seibert et al.* (2000), and references herein). Unfortunately, such data was not available for the observed time periods.

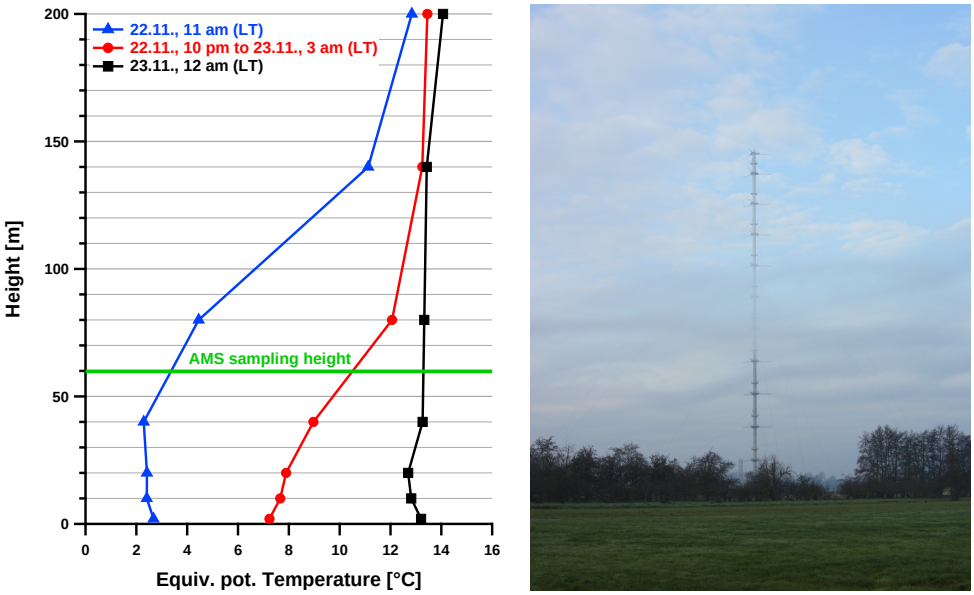

Figure 3.2.: Left: Height profiles of ambient temperature, averaged between 22.11., 10 pm to 23.11., 3 am (LT, red), on 22.11., 11 am (LT, blue), and on 23.11., 12 am (LT, black). Right: Picture of the tower, made on 22.11., 11 am (LT).

Figure 3.3 shows the temporal evolution of mass concentrations (stacked) and mass fractions of black carbon (BC, black), organics (Org, green), nitrate (NO_3, blue), sulphate (SO_4, red), ammonium (NH_4, orange), and chloride (Chl, pink) as measured by the AMS in November 2011. Different meteorological conditions are indicated by different-coloured backgrounds, while precipitation events are displayed through sharp blue rectangles. AMS mass concentrations were determined using the composition dependent collection efficiency (CDCE) correction by *Middlebrook et al.* (2012) and a correction for sampling line losses as described in subsection 2.4.2.1. The AMS collection efficiency as a function of time is given in figure A.4 in the appendix. The average CE over the entire campaign was 0.49. Particulate water is also added to the plot and was calculated using a RIE of 2 (*Mensah et al.*, 2012).

Gaps in the time series are caused by a power supply problem (12.11. and 14.11.) and routine calibrations and maintenance (16.11. and 22.11.). Shorter data gaps occurred because of filter measurements, which data was excluded in all of the following data plots. All time series of data measured from other instruments than the AMS were synchronized to AMS data.

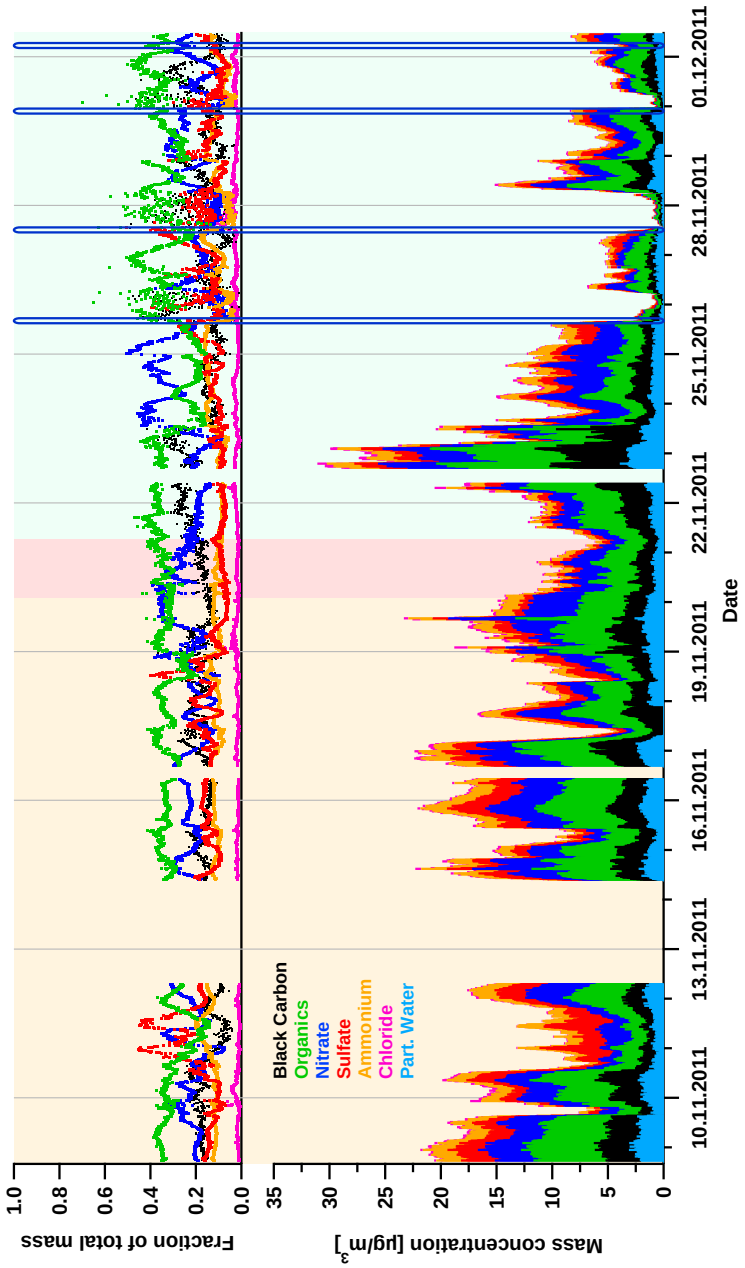

Figure 3.3.: Aerosol composition during the 2011 campaign. Top panel: Time series of mass fractions individual species. Bottom panel: Stacked time series of mass concentrations of aerosol species. Particulate water was not considered for the determination of the total mass and mass fractions due to its large uncertainty. The time period with southerly and easterly wind directions is highlighted in beige. The time of calm northerly winds is indicated by a red background. The period with southerly and westerly wind directions is illustrated in green. The sharp blue rectangles represent precipitation events.

The average fractional abundance of each individual species is displayed on figure 3.4 (a), together with the average diurnal patterns (b). Detailed information about Excess-NH_4 is given in subsection 3.1.1.2. An average total mass concentration of 9.26 µg m^{-3} was observed, dominated by BC and organics, which together contributed 50 %. Note, that particulate water was not considered for the determination of total mass loadings and mass fractions of individual species. The characteristic diurnal behaviour of nitrate (night time maximum) and sulphate (maximum during the day) can be seen, reflecting their different formation and loss mechanisms (see also chapter 1). While SO_4 is produced mainly photochemically from gaseous SO_2, particulate NO_3 is formed by heterogeneous conversion of N_2O_5 in the night and from HNO_3 during day-time. Despite the high volatility of NH_4NO_3, NO_3 did not decrease significantly during the day. This may be due to small differences in temperature between day- and night-time (only $< 1°C$ outside the tower and slightly $> 1°C$ at the manifold). In total, an anti-correlated temporal behaviour of NO_3 and SO_4 is seen, as also shown by the variation of the mass fractions in figure 3.3, upper panel. The diurnal pattern of the total particulate mass, as well as of BC and organics, had maxima during the night and in the morning/noon-time. The maxima of BC can be attributed to traffic (morning and evening rush hours) and biomass burning events (domestic heating in the evenings/nights).

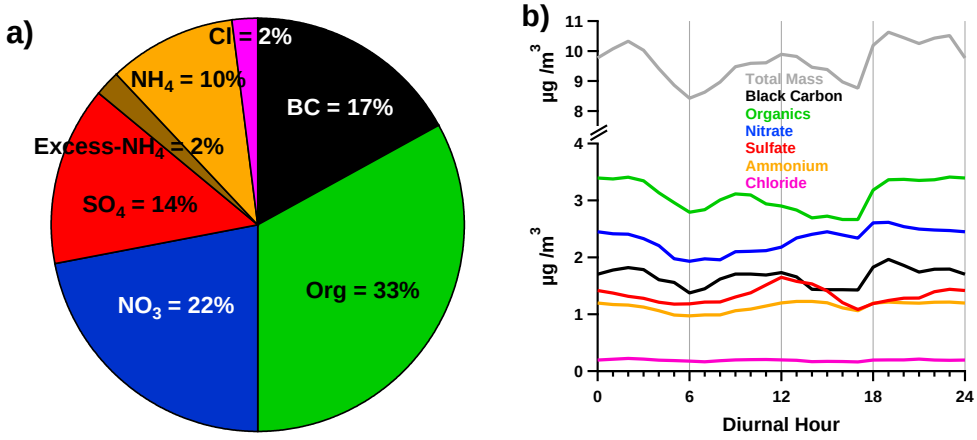

Figure 3.4.: a) Average contributions of aerosol species and b) their diurnal variations (LT) in 2011

Mainly four scavenging precipitation events are identified, which may explain the rapid drops of the particulate masses (down to about 0.4 µg m^{-3}) in the evenings of 25.11., 27.11., and the night of 30.11.2011. High mass loadings (up to approximately 27 µg m^{-3}) were observed between 22.11. to 24.11.2011, corresponding with high concentration of Radon-222 (^{222}Rn), measured at 20 m height (see figure 3.1d). Since soil is known to

be the main source of ^{222}Rn, this inert radioactive compound is commonly used as a tracer for atmospheric vertical mixing (*Williams et al.* (2010a), and references herein). The high ^{222}Rn concentration and large differences between ^{222}Rn values at 20 m and 200 m may therefore be an evidence, that at this time the AMS sampled within the stable boundary layer. Thus, it measured the fresh surface emissions accumulating in the stable boundary layer, resulting in high aerosol mass concentrations. This may explain the high mass loadings found during the nights within the diurnal pattern of the total particle mass and individual species like BC and organics (figure 3.4b). The drop of the total aerosol concentration during the day of 23.11. is accompanied by a large drop of ^{222}Rn concentration at 200 m, emphasizing this assumption. The interim high mass of ^{222}Rn concentration at 20 m during this day may be a result of the rising SBL, transporting air with high ^{222}Rn concentration to the 20 m sampling position. The height profiles of the equivalent potential temperature θ as shown in figure 3.2 suggest this whole scenario as well.

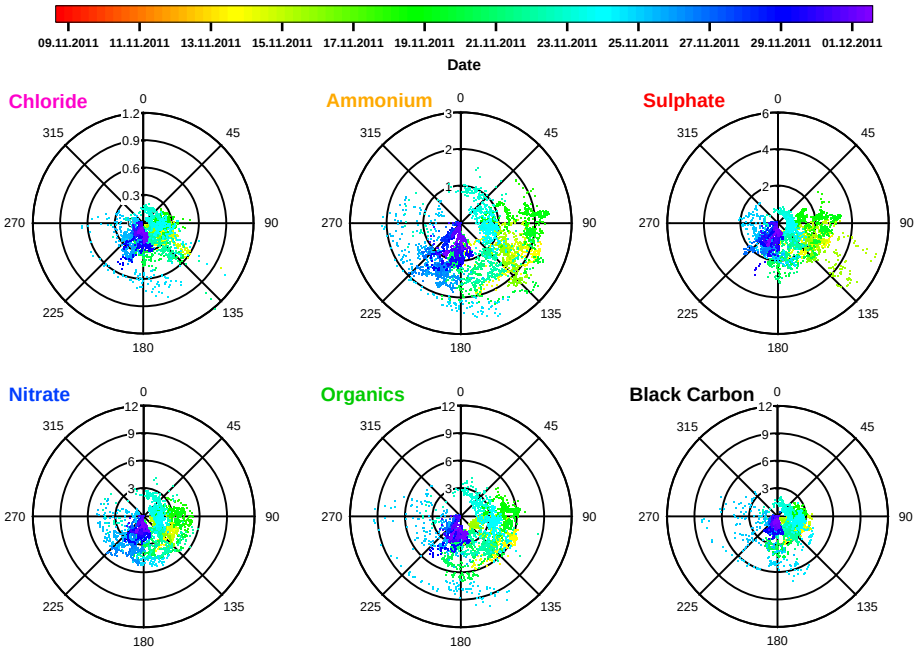

Figure 3.5.: Polar graphs of individual species in 2011, colour-coded by time. The radii represent the respective mass concentration in µg m^{-3}, the angles show the cardinal directions, with the tower in the centre of the plots. Attention should be paid on the different radius scales.

As mentioned, the air masses originated from the West, South, or East during the 2011 campaign. Figure 3.5 shows polar graphs of individual species, illustrating their directional origins, weighted by the respective mass loading. All plots are colour-coded by time. It is not surprising, that the highest average contributions of each compound originated from these three directions (West, South, and East), while SO_4 mass concentrations showed the highest values coming from easterly and southern easterly directions.

3.1.1.1. Inorganic and organic nitrate fractions

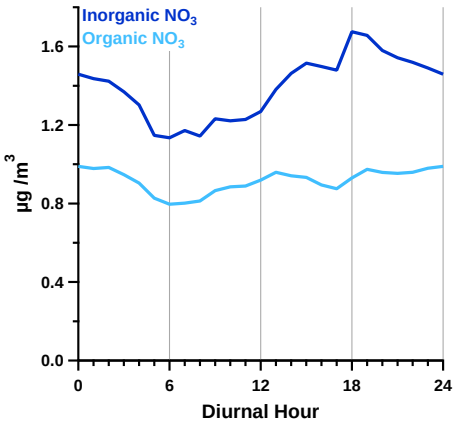

Figure 3.6.: Average diurnal variations (LT) of the AMS organic and inorganic nitrate fraction in 2011.

Following the procedure described in subsection 2.1.1.5, the total NO_3 content was sub-classified to its organic ($OrgNO_3$) and inorganic fraction ($InOrgNO_3$). Figure 3.7 displays the campaign time series of both fractions, figure 3.6 shows their averaged diurnal patterns. An average mass fraction of 40 % was observed for $OrgNO_3$ (average concentration: 0.91 µg m^{-3}) in respect to total NO_3 in November 2011, and in consequence 60 % of total nitrate was inorganic (average concentration: 1.39 µg m^{-3}). Most periods with high total NO_3 mass concentration showed high $InOrgNO_3$ fractions. During precipitation events, the $InOrgNO_3$ concentration decreases to zero, while organic nitrates were still observed (approximately 0.1 µg m^{-3}). This indicates, that inorganic nitrate, which can be assumed to be NH_4NO_3, is more effectively scavenged by precipitation than organic nitrates. Both nitrate fractions show maximum concentration in the afternoon and night-time, followed by a decrease until the morning hours. Note that the decrease of $OrgNO_3$ had a slight delay of one hour compared to the inorganic fraction. Furthermore, an additional maximum of $OrgNO_3$ at around 1 pm was seen.

Unfortunately, no MARGA data was available for November 2011. Therefore, the presence of other inorganic nitrate salts like $Mg(NO_2)_2$, $NaNO_3$, or $Ca(NO_3)_2$ could not be estimated. However, MARGA data from 2012 to 2013 showed only low concentrations of particulate Mg^+, Na^+, and Ca^+ (sum average = 0.1 µg m^{-3}). Thus it can be assumed that these salts do not have a significant influence on the NO_2^+/NO^+ ratio at this site although it could not be excluded explicitly.

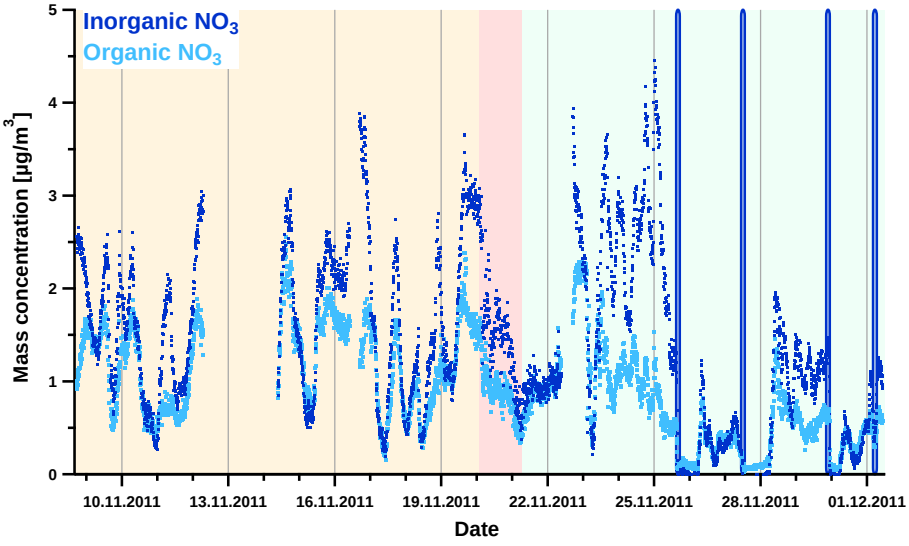

Figure 3.7.: Time series of the AMS organic and inorganic nitrate fraction in 2011. The time period with southerly and easterly wind directions is highlighted in beige. The time of calm northerly winds is indicated by a red background. The period with southerly and westerly wind directions is illustrated in green. The sharp blue rectangles represent precipitation events.

3.1.1.2. Aerosol ion balance and Excess-NH_4

An ion balance of the inorganic aerosol compounds was determined using the equation described in subsection 2.1.1.6. Consequently, only the inorganic nitrate fraction was considered to neutralize NH_4 to NH_4NO_3. In figure 3.9a, the measured NH_4 mass concentration is plotted against the predicted NH_4 concentration resulting from the ion balance. Within the measurement accuracy, a significant excess of NH_4 was obtained during almost the whole campaign. The time series of this Excess-NH_4 is displayed in figure 3.9b and had an average of 0.13 µg m^{-3}. The average contribution to total NH_4 reached 12 %, representing 1 % of the total aerosol mass in November 2011. Figure 3.8 shows a maximum at 7 pm and a minimum at 8 am of the

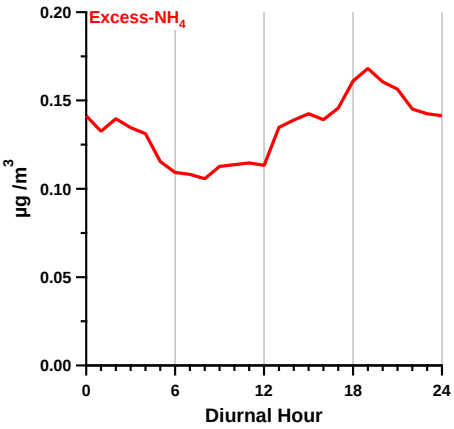

Figure 3.8.: Average diurnal variation (LT) of the Excess-NH_4 mass concentration in 2011.

diurnal variation of Excess-NH_4. Note, that using the total NO_3 for the aerosol ion balance, the predicted NH_4 concentration would exceed the measured NH_4. As shown in the appendix (figure A.2), this would indicate acidic particle conditions almost over the entire campaign. In consequence, no excess ammonium would be obtained in this case.

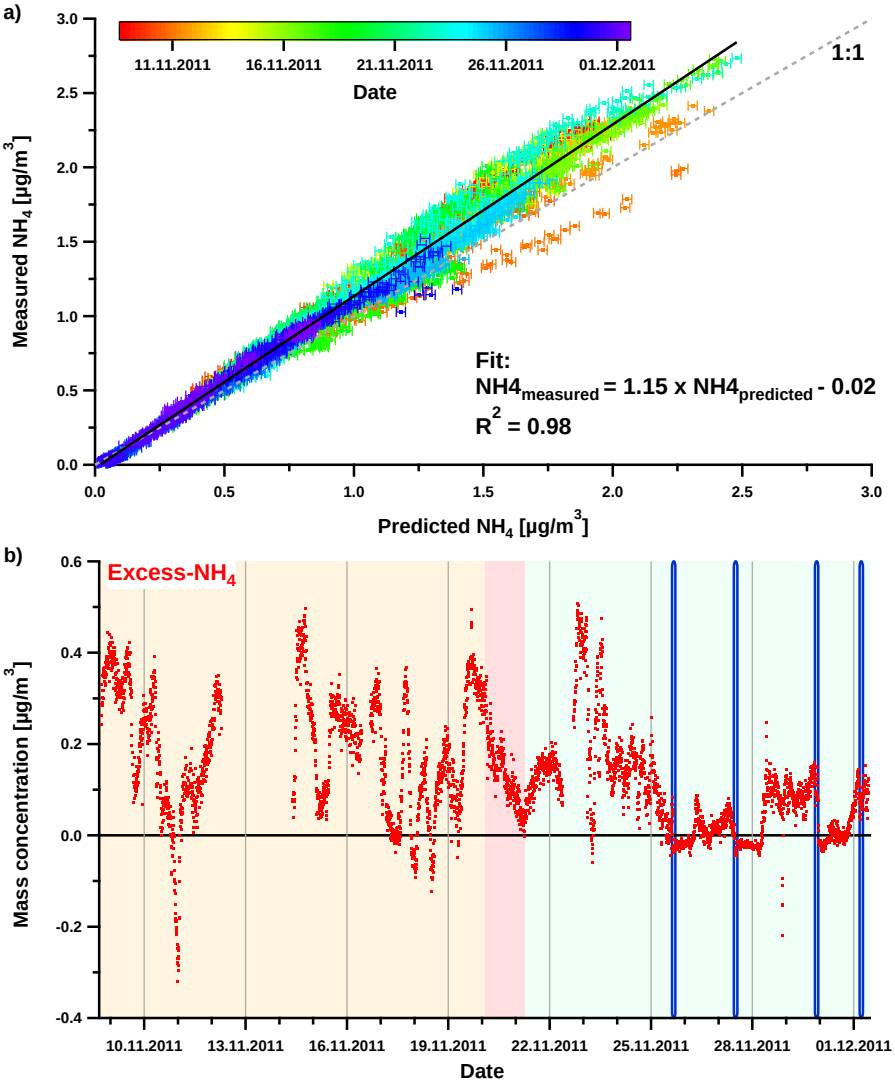

Figure 3.9.: a) Correlation plot of measured against predicted NH_4 in 2011. Error bars represent uncertainties of the NH_4 prediction. A slope of 1.15 ± 0.00 was determined. b) Time series of Excess-NH_4 in 2011. The time period with southerly and easterly wind directions is highlighted in beige. The time of calm northerly winds is indicated by a red background. The period with southerly and westerly wind directions is illustrated in green. The sharp blue rectangles represent precipitation events.

3.1.1.3. Chemical size distribution

Averaged size distribution of each AMS species is shown in figure 3.10. A mode diameter of around 500 nm for all inorganic compounds was found. For unknown reasons, the size distribution of the organic fraction showed a high scattering in most periods of the campaign, as well as for the campaign average. On 08.11. and 09.11.2011, the scattering was less dominant, and therefore the size distribution during this time was used in figure 3.10. The averaged size distribution for organics over the entire campaign is shown in the appendix (figure A.3). The grey line represents the size distribution of the total inorganic signal. In contrast to the inorganics, significant contribution to the organics arose from particles smaller than 100 nm (D_{va}). Below a diameter of 270 nm organics dominated over inorganic contributions. During the period of 08.11. to 09.11.2011, particles with a diameter of 270 nm (D_{va}) were composed of 70 % organic and 30 % inorganic fraction on average.

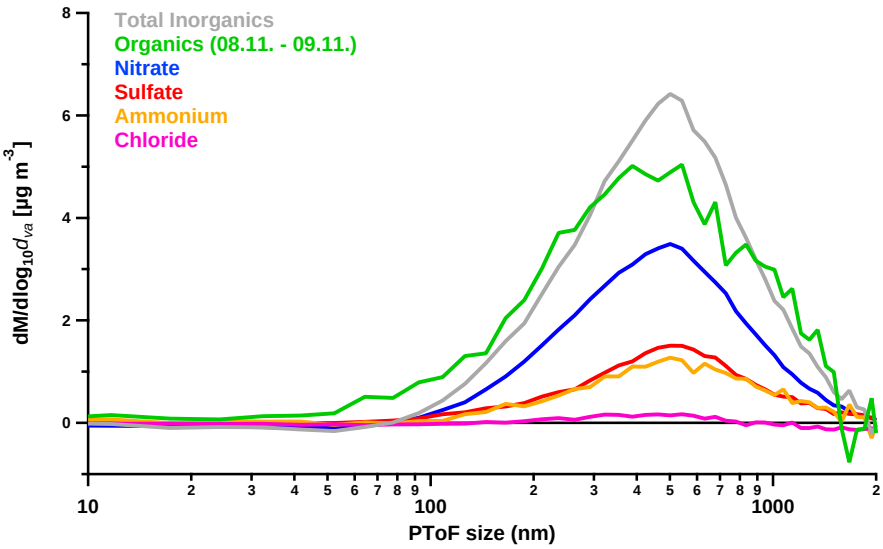

Figure 3.10.: Average size distribution of individual species and the total inorganics, measured by the AMS in November 2011. The green line represents the average for organics on 08.11. and 09.11.2011.

3.1.2. Comparison of measurements of total PM_1 mass

The SMPS system was measuring at the manifold of the 60 m sampling line during the whole campaign in November 2011. Data was processed as described in subsection 2.4.1, including the application of a correction for sampling line losses, mentioned in subsection 2.4.2.1. The time resolved particle density, used for the determination of the SMPS mass concentration, had an average of 1.61 g cm^{-3} and is given in the appendix (figure A.6), as well as the SMPS size distribution (figure A.5).

Over the whole AMS campaign, an average SMPS mass concentration of 17.4 µg m^{-3} was found with a minimum value of 0.46 µg m^{-3} and a maximum of 65.4 µg m^{-3}. Figure 3.11 shows the time series (a) and a correlation plot (b) of the AMS + MAAP and SMPS total aerosol mass.

Though a good correlation is observed ($R^2 = 0.89$), the combined mass concentrations measured by AMS and MAAP, only explains approximately 52 % of the total SMPS observation. The SMPS measured particles with electro-mobility diameters (D_{em}) in the range of 9.4 nm to 516 nm. By definition, the electro-mobility diameter needs to be multiplied with the particle density (ϱ_P) and the particle shape factor (SF) to calculate to corresponding vacuum aerodynamic diameters (D_{va}), according to equation 3.1. This equation is used assuming spherical particles (*DeCarlo et al.*, 2004).

$$D_{va} = D_{em} \cdot \varrho_P \cdot SF \tag{3.1}$$

Using the determined average particle density of 1.61 g cm^{-3} and a shape factor of 1, the D_{va} range of particles measured by the SMPS was between 15 nm to 830 nm. As mentioned in section 2.1, the transmission of the AMS aerodynamic lens was reported to decrease for particles with a D_{va} smaller than 50 nm and larger than 500 nm (*Jayne et al.*, 2000). A specific transmission curve for the aerodynamic lens used in this work was not determined. Further analysis showed that only approximately 50 % of the SMPS total mass originated from aerosols with sizes between 60 nm to 600 nm over the entire campaign. To account for the transmission losses of the AMS, particles outside this size range were excluded from SMPS mass data. The resulting correlation to the AMS, displayed in figure 3.12, shows a high quantitative agreement. This illustrates, that the differences observed between both instruments are most likely due to the different cut-off sizes.

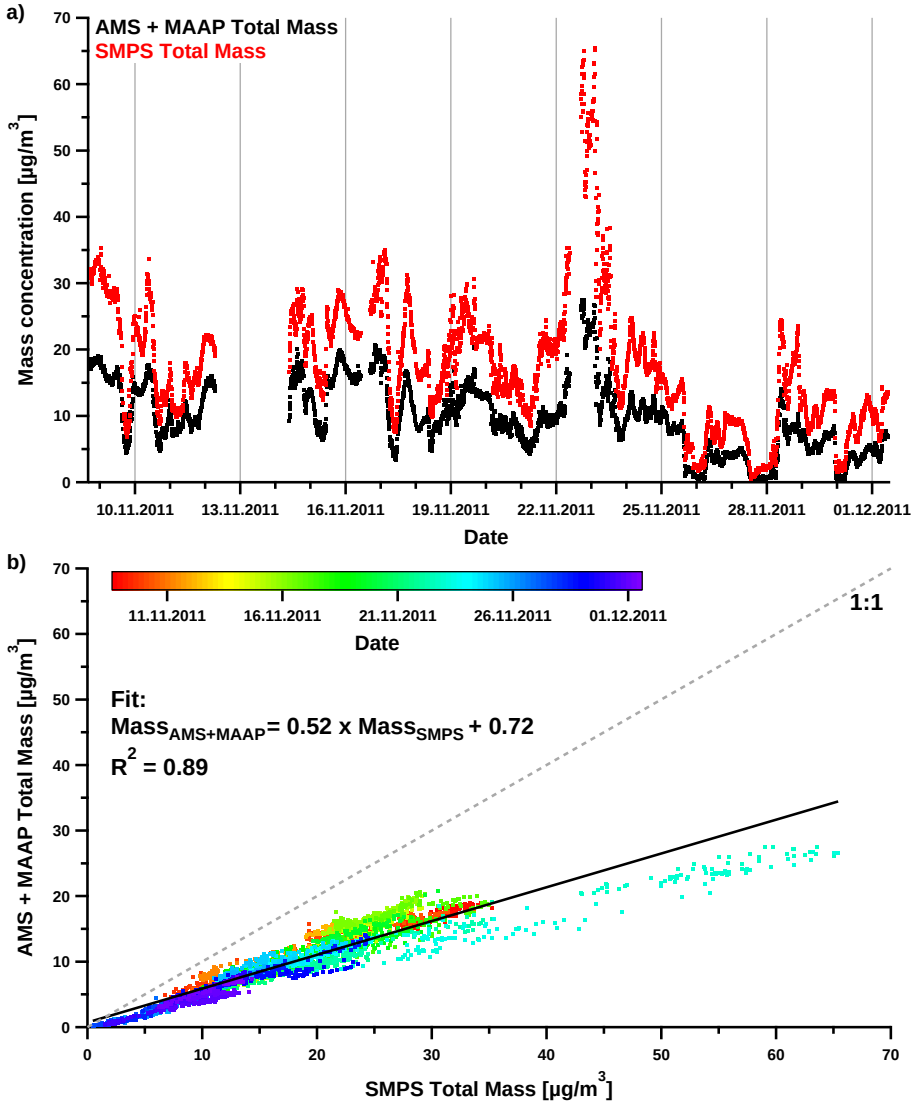

Figure 3.11.: Time series (a) and correlation plot (b) of AMS+MAAP and SMPS mass concentrations in 2011.

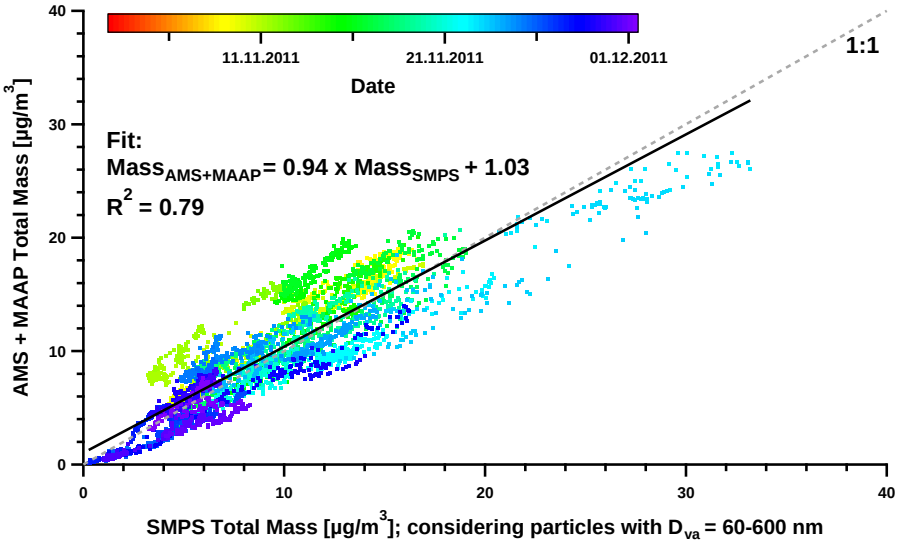

Figure 3.12.: Correlation plot of of AMS+MAAP and SMPS mass concentrations in 2011. Here, only a D_{va} range of 60 nm to 600 nm was considered for the determination of the SMPS mass.

3.1.3. Comparison of organic aerosol mass measurements

Suitable data from the TD-PTR-MS was available from 02.11. to 01.12.2011, where 648 ions with m/z between 27 and 1143 were detected. A list of the detected ions is shown in the appendix (see section A.4). The total signal of organic aerosol was calculated as the sum of all organic ions and is referred to as PTR-OA hereafter. PTR-OA concentrations from both inlets show good agreement (see figure A.7). Thus their time series can be combined, sorted by the acquisition time. The merged PTR-OA showed an average of 0.91 µg m^{-3} over the whole TD-PTR-MS campaign, and an average of 0.86 µg m^{-3}, considering only the time period of the AMS campaign (08.11. to 01.12.). A comparison with AMS-OA is given in figure 3.13.

While an R^2 of 0.70 indicates a good correlation between the two instruments in terms of time trends, the TD-PTR-MS measured only approximately 31 % of the AMS-OA. This is in agreement with previous studies, where the same TD-PTR-MS system was compared with an HR-ToF-AMS in ambient measurements at CESAR in Cabauw 2008 ($R^2 = 0.64$; PTR-OA/AMS-OA $\approx$ 30 % - 85 %; *Mensah et al.* (2012)) and during the CalNex 2010 campaign in Los Angeles, USA ($R^2 = 0.60$; PTR-OA/AMS-OA $\approx$ 50 %; *Holzinger et al.* (2013)).

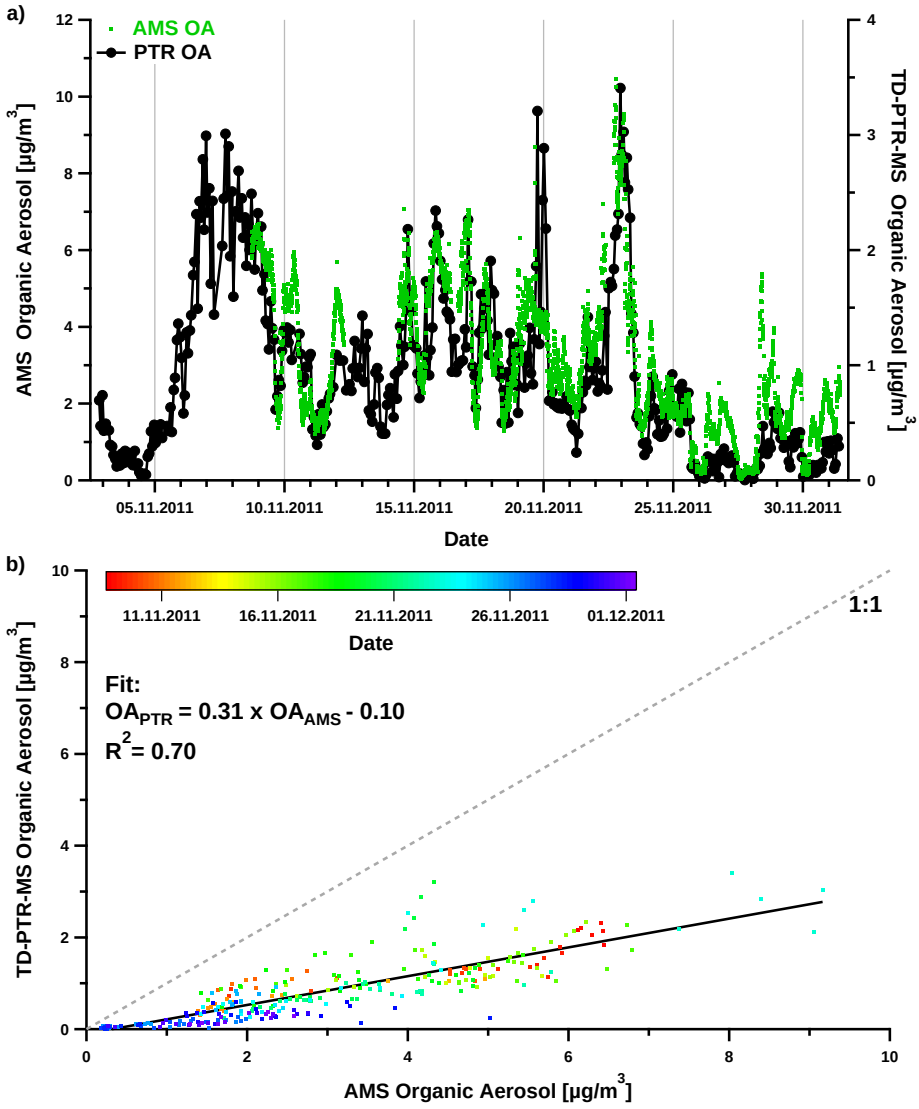

Figure 3.13.: Time series (a) and correlation plot (b) of PTR OA (both inlets combined) and AMS OA mass concentrations in 2011

As discussed in *Holzinger et al.* (2010b) and *Holzinger et al.* (2010a), lower mass concentrations of the TD-PTR-MS can be expected due to the following reasons:

(i) Only detected ions were accounted for the calculation of TD-PTR-MS mass concentrations. In contrast, the AMS data analysis considers the contribution of neutral fragments to the ion signals, based on the well known properties of electron impact ionization.

(ii) While the AMS vaporizer was set to 600°C, the CTD cells of the TD-PTR-MS operated at 350°C, meaning that low-volatile compounds were potentially only partially vaporized by the CTD cell and therefore not detected properly by the PTR-MS.

(iii) Both, the CTD cell and the vaporizer of the AMS produce species like CO_2 and H_2O due to thermal combustion of organic molecules. These can be detected and accounted for as the organic aerosol fraction by the AMS, but not by the TD-PTR-MS.

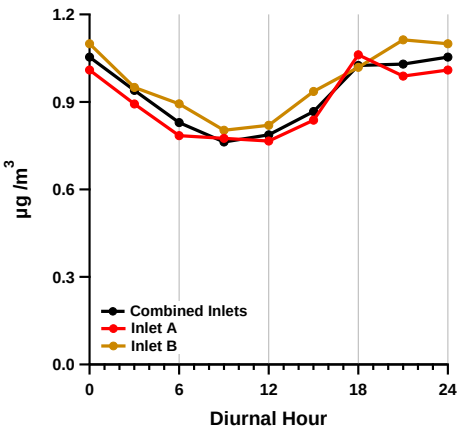

Figure 3.14.: Averaged diurnal variations (LT) of PTR-OA from both inlets and from merged data in 2011. Note that PTR-OA data was pre-averaged to a resolution of 3 hours.

Due to the low time resolution, PTR-OA data was pre-averaged to 3 hours before a determination of the diurnal pattern. Figure 3.14 displays the daily variation, obtained from both inlets separately and from merged data. Similar to their time series, also the averaged variations over the day agree well. PTR-OA shows maxima in the late evening/night-time and minima during the morning/noon-time. The last is in contrast to the AMS-OA diurnal variation, where a second maximum at noon-time was observed. This discrepancy can be used to further investigate which fraction of OA is detected or discriminated by the TD-PTR-MS in more detail in subsection 4.1.3.1.

3.2. AMS Campaign 2012

3.2.1. Meteorological conditions and aerosol composition as observed with the AMS

The meteorological overview in figure 3.15 shows more frequent wind direction changes with longer periods of northerly winds than in 2011, especially from the beginning until 27.06.2012. After that day, southerly and westerly wind directions dominated until the end of the campaign. Wind speeds remain moderate with an average of 4 m s^{-1} and a maximum of 13 m s^{-1}. Ambient humidity and temperature data were obtained at 2 m height, while the inlet was monitored by an in-line installed Vaisala HMP 235. Since the sample air was not dried in 2012, higher RH values than 2011 were measured in the inlet, but still ca. 30 % of RH lower than outside the building, as also seen in table 3.2. This difference is a result of the temperature gradient between both positions of ca. 9°C.

Table 3.2.: Overview of the temperatures and relative humidities in 2012, measured at 2 m height and from the Vaisala HMP 235, connected in-line of the AMS inlet.

	Minimum	Maximum	Average
Ambient temperature [°C]	2.4	28.0	15.3
Temperature AMS inlet [°C]	20.5	29.1	24.0
Ambient relative humidity [%]	30.5	101.3	77.0
Relative humidity AMS inlet [%]	23.0	86.7	47.6

Higher variations of ambient temperature and humidity were observed comparing to 2011, as also seen in the averaged temperature diurnal variation in the appendix (figure A.8). The daily minima and maxima are located as expected. As mentioned in subsection 3.1.1, a vertical temperature inversion is used as an indicator of the stable boundary layer height, as often seen during the 2011 campaign (see figure 3.2). In 2012, only minor differences within the temperature height profiles were found, which means that the ambient air was well mixed at this height at most times. This is also seen in the ^{222}Rn data obtained at 20 m and 200 m height, where ^{222}Rn at 20 m is only rarely higher than the ^{222}Rn at 200 m height.

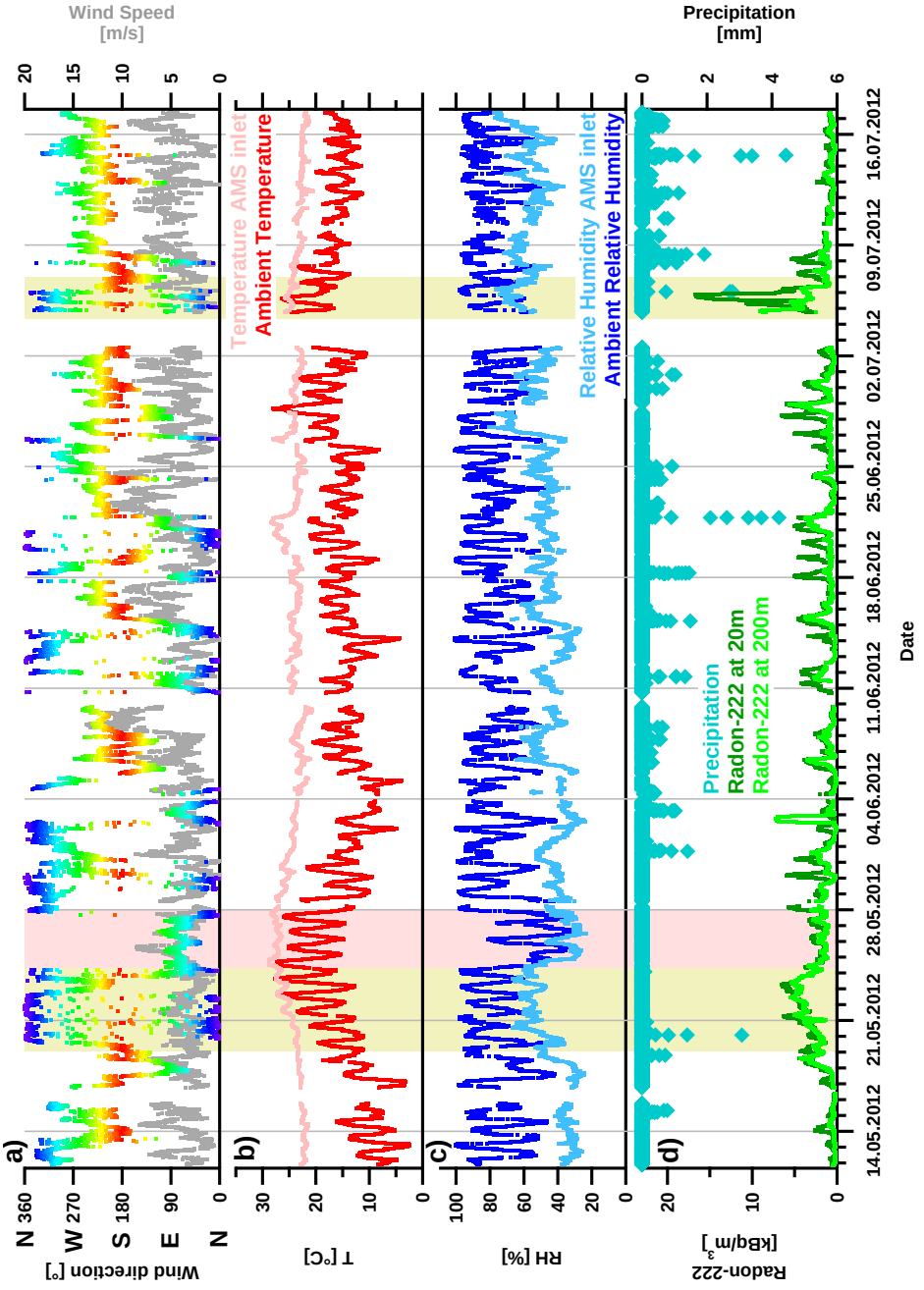

Figure 3.15.: Meteorological overview of the 2012 campaign: a) Wind direction (0°/360°, 90°, 180°, and 270° represent North, East, South, and West, respectively) and wind speed (grey) at 10 m height. b) and c) temperature (red) and relative humidity (blue), measured at 2 m height (ambient, dark colours) and at the AMS inlet (light colours). d) Precipitation (turquoise) and Radon-222, measured at 20 m (dark green) and 200 m (light green). High mass periods are indicated by green backgrounds. The time period with easterly wind directions and high organic contribution is highlighted in red.

Similar to the AMS campaign in 2011, filter measurements, maintenance and calibrations caused data gaps in the 2012 time series from May to July 2012. Furthermore, a power failure prevented measurements from 03.07. to 04.07.2012. Additional gaps occurred due to problems concerning the MARGA, which was sharing the same inlet with the AMS, and a problem with the water-CPC (16.05.). An overview of the aerosol composition, including mass concentrations and mass fractions of individual species is given in figure 3.16. The AMS collection efficiency during this campaign had an average of 0.48, its time series is shown in the appendix (figure A.10). Since the AMS measured at 5 m height in 2012, no correction for sample line losses was applied.

The average total mass concentration in 2012 was 6.40 µg m^{-3}. Several periods with high aerosol mass loadings were observed. Between 20.05. to 23.05. in the afternoon, the total mass concentration increased continuously up to 35.0 µg m^{-3} with an average of 19.0 µg m^{-3}. During this time, northerly and north westerly wind directions dominated and NO_3 and organics were the dominant species. NO_3 and organics also dominated the aerosol composition during the high mass period on 05.07. and 06.07.2012. This period showed high ^{222}Rn, which would argue for a stable boundary layer height of at least 20 m and explain the high mass loadings (see subsection 3.1.1). On the other hand, no significant temperature inversion was seen in any height between 2 m and 200 m at this time. High night-time mass concentrations of NO_3 caused other peaks in mass concentration, like in the nights on 31.05., 15.06, and the nights between 19.06. to 21.06.2012.

During most periods with low mass loadings, the relative abundance of sulphate increased and had sometimes even the highest contributions. The rapid decrease of particle mass on 31.05., 21.06., or 06.07. is correlated with precipitation events (see figure 3.15, bottom graph). The mass concentration drop on 23.05. is most likely due to the change to easterly winds until 28.05.2012. During this period the total mass decreased to an average of 6.60 µg m^{-3}, while the contribution of organics was the highest observed in the entire campaign (average: 60 %, maximum: 78 %).

As seen in figure 3.17a, organics, nitrate and sulphate were the dominant species over the entire campaign in 2012, contributing 32 %, 21 %, and 24 %, respectively. The diurnal variation of NO_3 (figure 3.17b) shows a night-time/morning maximum and low values during the day and in the evening, as a result of the volatility of NH_4NO_3. BC shows a maximum in the morning, while high sulphate concentrations were observed during noon and the afternoon. The variation of the total particulate mass followed largely the pattern of NO_3 and the organics. The polar graphs in figure 3.18 show that high mass concentrations were coming from northerly, westerly and southern westerly directions.

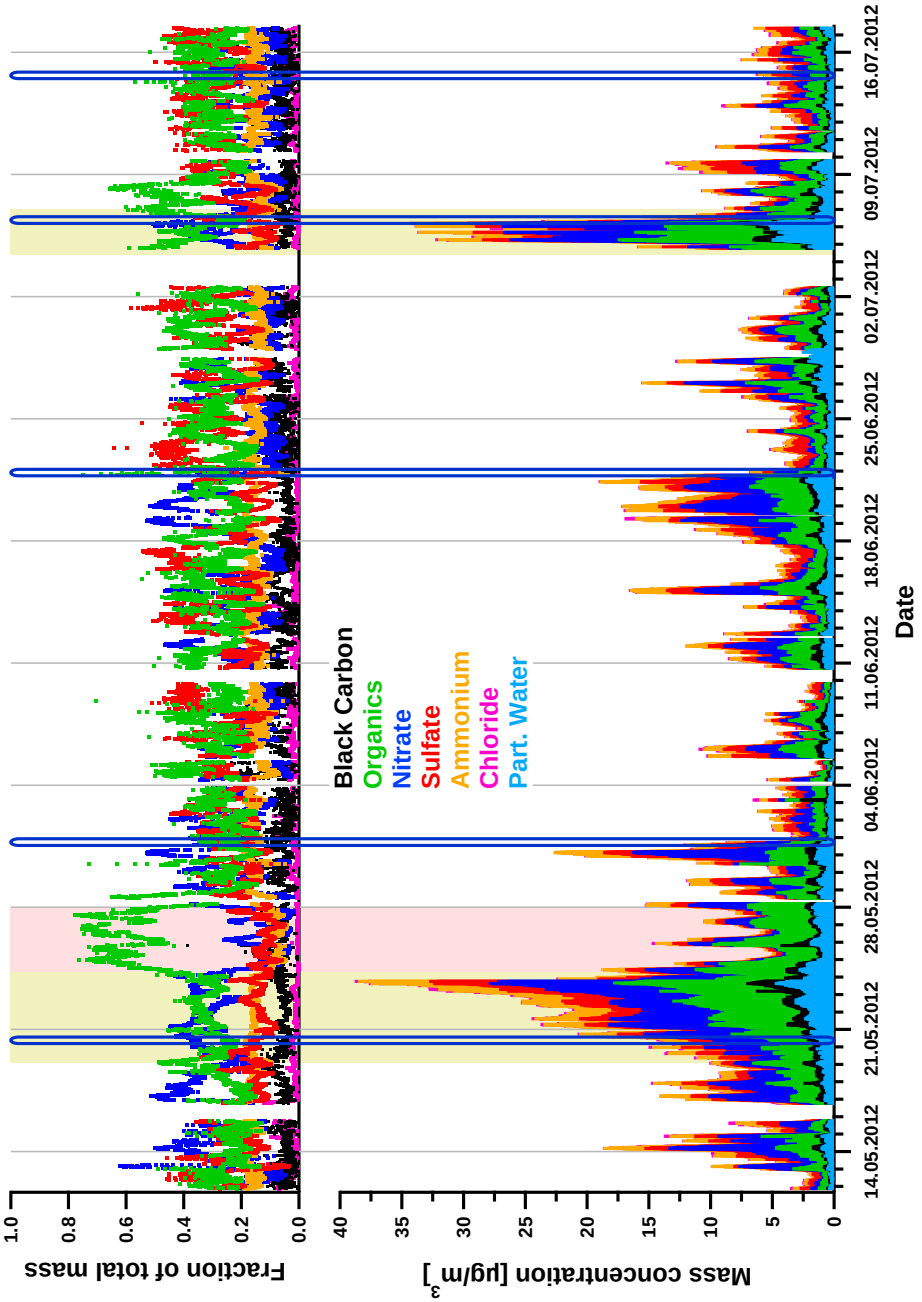

Figure 3.16.: Aerosol composition during the 2012 campaign. Top panel: Time series of mass fractions of BC, Org, NO_3, SO_4, NH_4, Chl, and particulate water. Bottom panel: Stacked time series of mass concentrations of aerosol species. Particulate water was not considered for the determination of the total mass and mass fractions due to its large uncertainty. High mass periods are indicated by light green backgrounds. The time period with easterly wind directions and high organic contribution is highlighted in red. The sharp blue rectangles indicate main precipitation events.

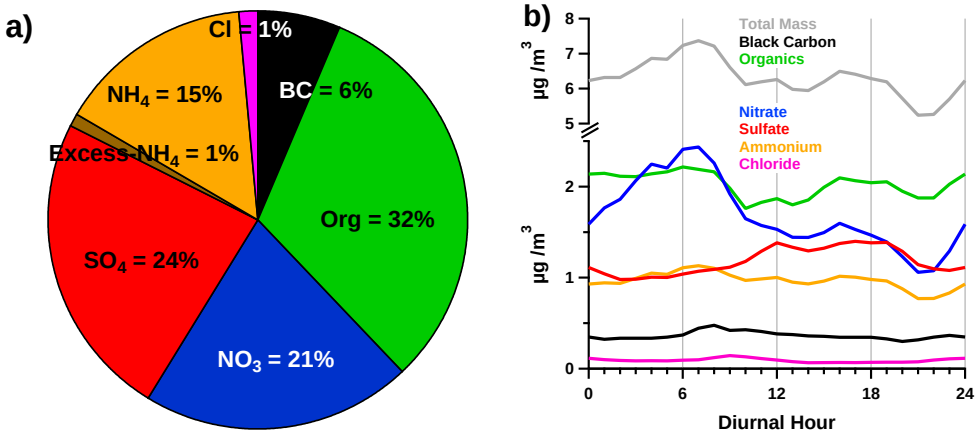

Figure 3.17.: a) Average contributions of aerosol species and b) their diurnal variations (LT) in 2012

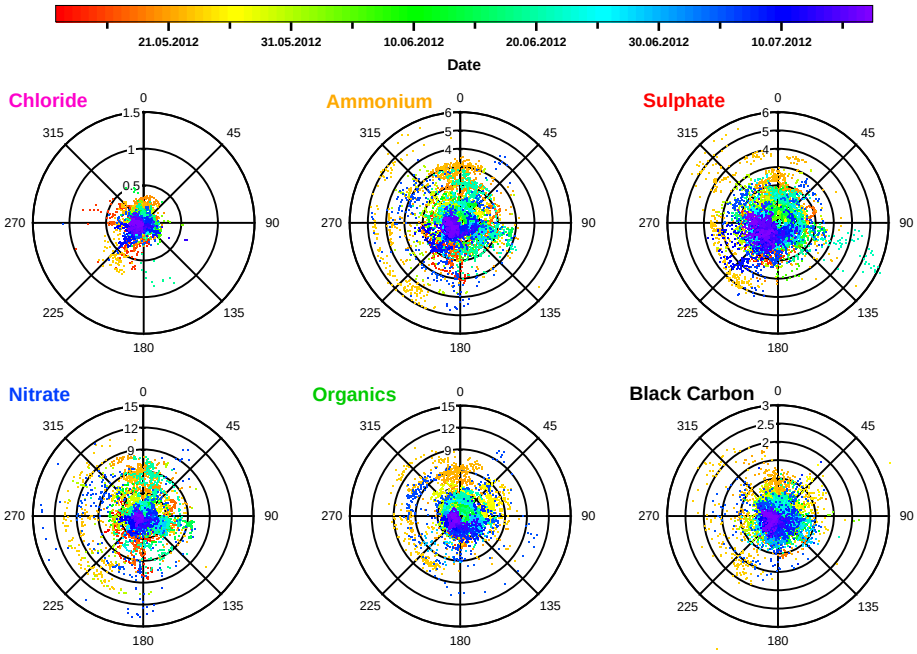

Figure 3.18.: Polar graphs of individual species in 2012, colour-coded by time. The radii represent the respective mass concentration in µg m^{-3}, the angles show the cardinal directions, with the tower in the centre of the plots. Attention should be paid on the different radius scales.

3.2.1.1. Inorganic and organic nitrate fractions

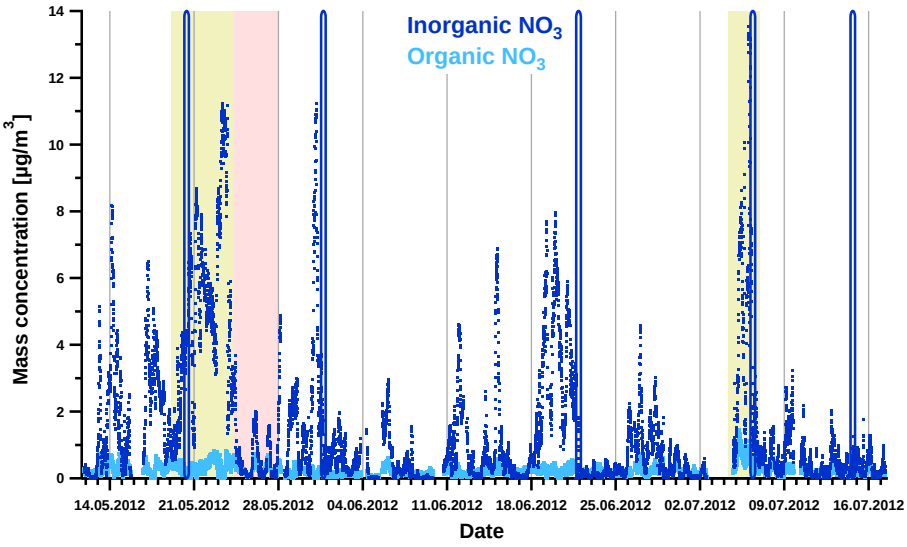

Figure 3.19.: Time series of the AMS organic and inorganic nitrate fraction in 2012. High mass periods are indicated by green backgrounds. The time period with easterly wind directions and high organic contribution is highlighted in red. The sharp blue rectangles represent precipitation events.

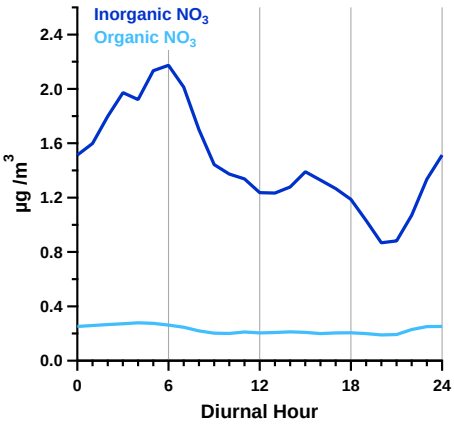

Figure 3.20.: Average diurnal variations (LT) of the AMS organic and inorganic nitrate fraction in 2012

The times series of the organic ($OrgNO_3$) and inorganic nitrate fraction ($InOrgNO_3$) obtained in 2012 can be seen in figure 3.19, the respective average diurnal variation in figure 3.20. An average $OrgNO_3$ mass concentration of 0.22 µg m^{-3} was observed, less than comparing to 2011 (0.91 µg m^{-3}). Simultaneously, the average concentration of $InOrgNO_3$ increased slightly (1.47 µg m^{-3}; 2011: 1.39 µg m^{-3}). This results in a contribution of $OrgNO_3$ to the total NO_3 mass of 13 %, which is much less than seen in 2011 (40 %). As in 2011, periods with high total NO_3 concentrations were dominated by inorganic nitrates. The diurnal variation of $InOrgNO_3$ showed a maximum during the morning hours and minima at noon time and at 7 to 8 pm. Due to the low

mass concentration of $OrgNO_3$, a distinctive diurnal pattern could not be observed.

MARGA PM_1 measurements during May and July 2012 showed, that the sum of Mg, Na, and Ca mass concentrations have low contribution to particulate mass (average sum: 0.09 µg m^{-3}). Thus significant influence of their nitrate salts to total nitrate and the variability on the NO_2^+/NO^+ ratio can be excluded.

3.2.1.2. Aerosol ion balance and Excess-NH_4

Figure 3.22a shows the measured NH_4 mass concentration plotted against the predicted NH_4 concentration resulting from the determined ion balance of all inorganic aerosol species. A slope of 1.05 indicates the presence of Excess-NH_4 in 2012 within the measurement uncertainty. As expressed in figure 3.22b, the highest mass concentration of Excess-NH_4 were observed especially during the high mass periods highlighted in green. An average Excess-NH_4 concentration of 0.05 µg m^{-3} was determined, resulting in average mass fractions of 5 % and 1 % with respect to total NH_4 and total aerosol mass. Excess-NH_4 occurred mainly in during the high mass events from 20.05. to 23.05. and on 05.07. and 06.07.2012. Therefore, a representative diurnal variation could not be achieved (figure 3.21).

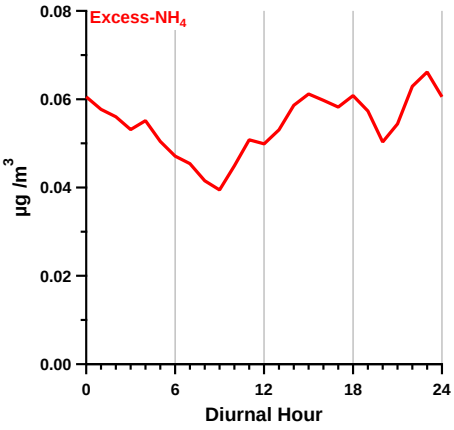

Figure 3.21.: Average diurnal variation (LT) of the Excess-NH_4 mass concentration in 2012.

Due to the low $OrgNO_3$ fraction of 13 % over the entire campaign, the use of the total NO_3 mass for the ion balance instead of the $InOrgNO_3$ concentration (see A.9) did not change the presented results as much as in the 2011 campaign (see subsection 3.1.1.2).

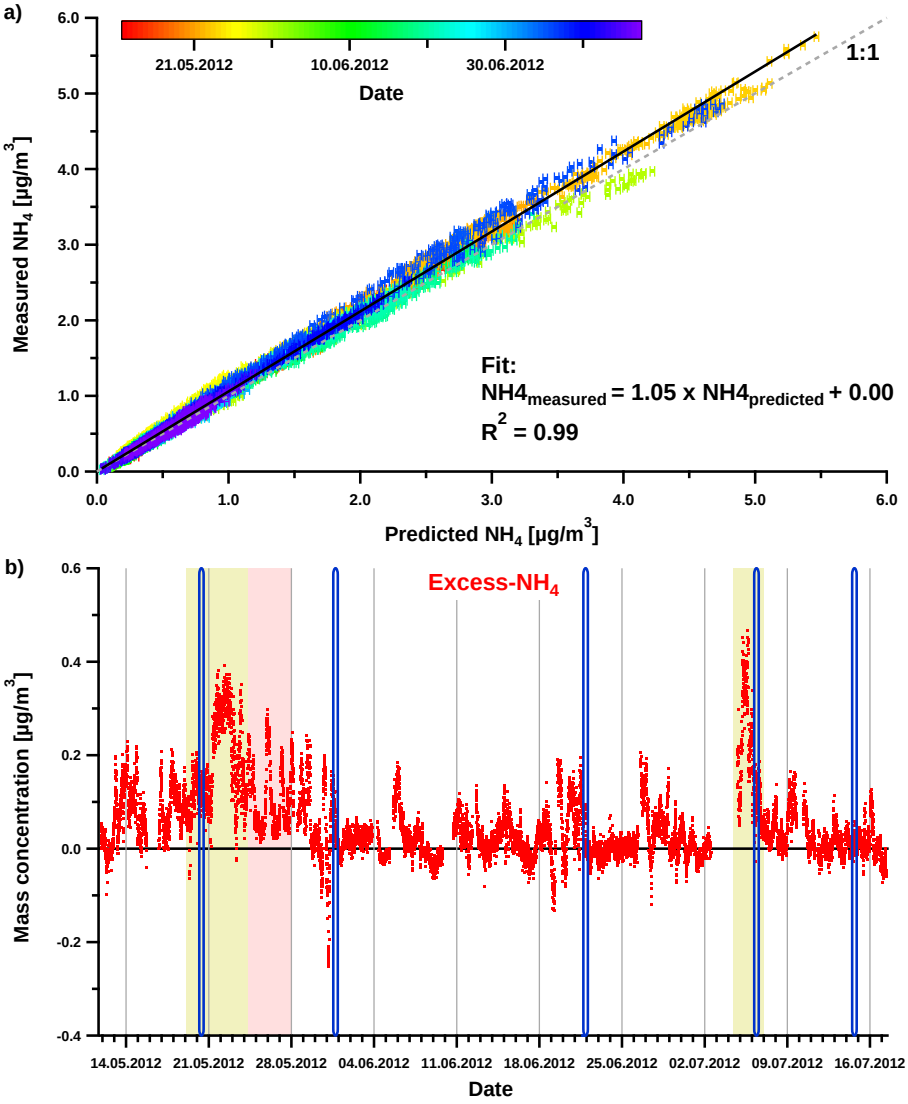

Figure 3.22.: a) Correlation plot of measured against predicted NH_4. Error bars represent uncertainties of the NH_4 prediction. A slope of 1.05 ± 0.00 was determined. b) Time series of Excess-NH_4 in 2012. High mass periods are indicated by green backgrounds. The time period with easterly wind directions and high organic contribution is highlighted in red. The sharp blue rectangles represent precipitation events.

3.2.1.3. Chemical size distribution

Figure 3.23 displays chemically resolved size distributions, measured by the AMS and averaged over the whole campaign. The curve of the total mass, as well as of the organics and SO_4, shows a mode diameter of approximately 460 nm. For NO_3 and NH_4, slightly higher mode diameters are seen (around 490 nm). Organics showed the largest contribution in particles with diameter below 290 nm. Aerosols with diameters $\leq$ 100 nm (D_{va}) consist of at least two thirds of organic mass with minor contributions of inorganics.

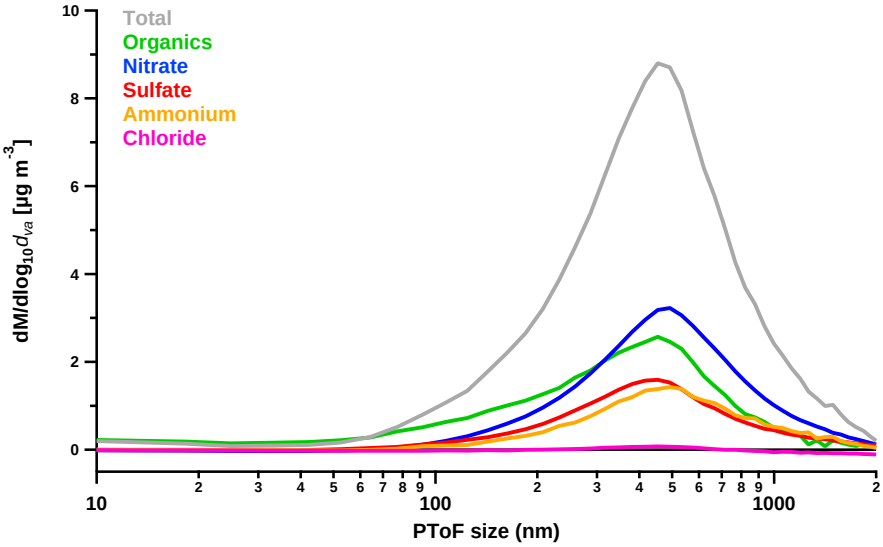

Figure 3.23.: Average size distribution of individual species and the total mass, measured by the AMS from May to July 2012

3.2.2. Comparison of measurements of total PM_1 mass

The time series of the total masses, derived from the SMPS on the one hand and from the sum of aerosol species, measured from the AMS and MAAP, on the other, are displayed in figure 3.24a. The SMPS mass concentration, which was again determined using the AMS particle density (average: 1.64 g cm^{-3}; see figure A.12), had a campaign average of 12.1 µg m^{-3}, a minimum of 0.92 µg m^{-3} and a maximum of 73.6 µg m^{-3}. One should note, that the SMPS was sampling at the 60 m inlet, meaning that its data was again corrected for particle losses at this sampling line. This correction was also done for BC data, but not for AMS mass concentrations, since the last was sampling at 5 m height. Although the instruments were sampling at different heights, the correlation, as shown in figure 3.24b, is in agreement with the comparison between the data sets in 2011. Again,

the combination of AMS and MAAP data resulted in about 52 % of the SMPS mass over the entire campaign, showing a good correlation coefficient (R^2 = 0.85 using 8160 data points). In case when only particles of a D_{va} range from 60 nm to 600 nm are considered for the determination of SMPS mass (see subsection 3.1.2), the comparison between the data sets shows high quantitative agreement over the whole campaign (figure 3.25). Again, this shows the large impact of the different cut-off sizes on this particular correlation.

The SMPS size distribution is shown in figure A.11.

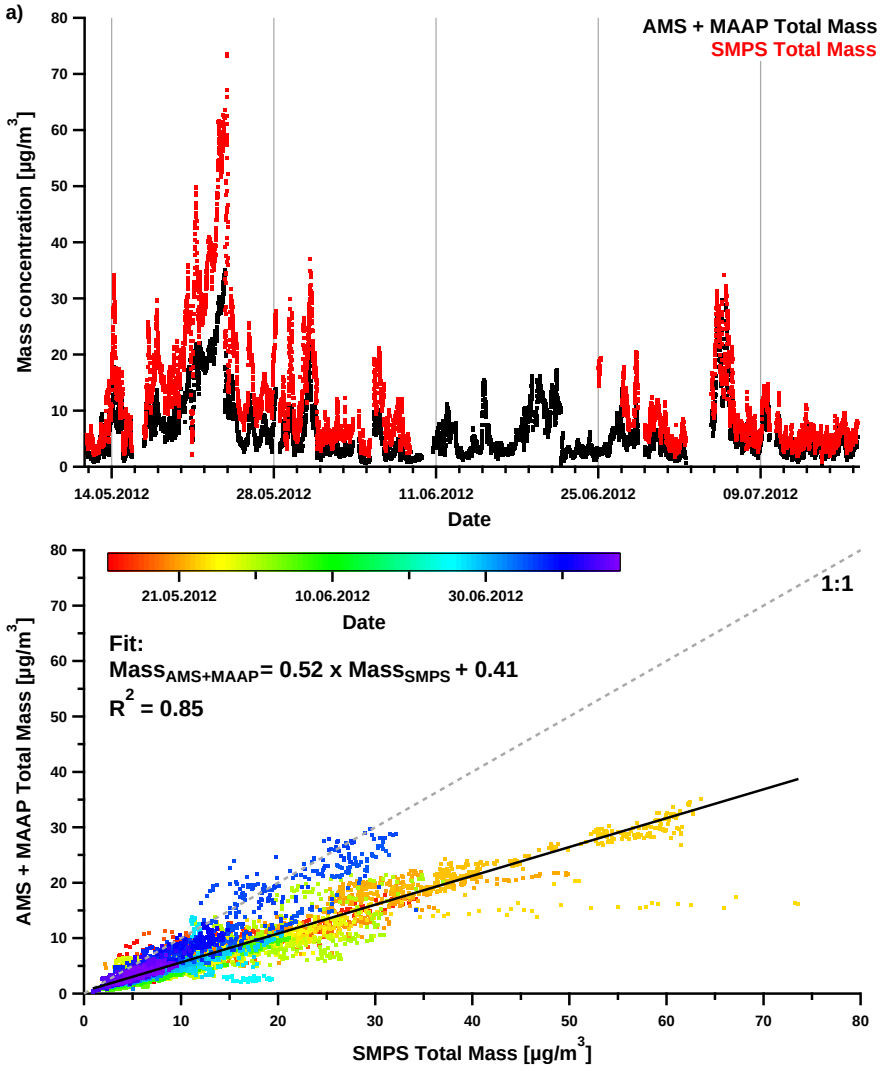

Figure 3.24.: Time series (a) and correlation plot (b) of AMS+MAAP and SMPS mass concentrations in 2012

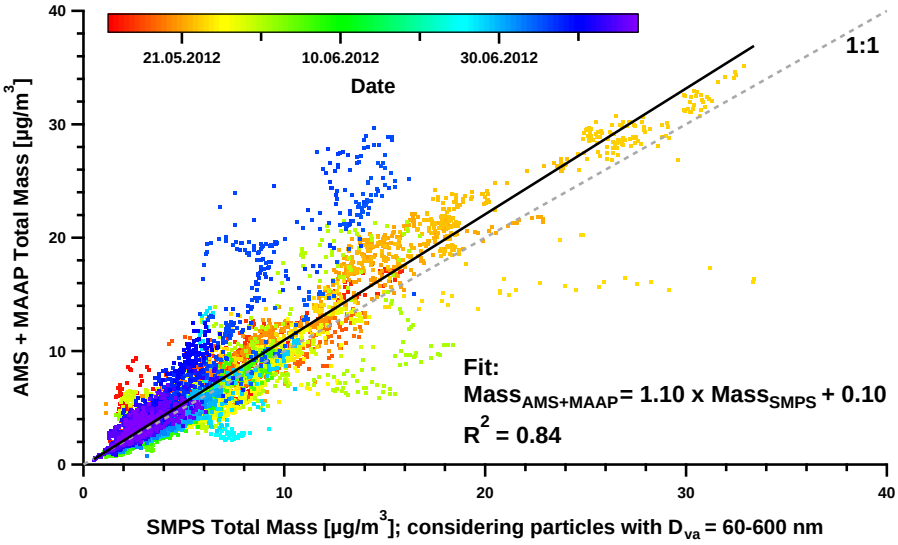

Figure 3.25.: Correlation plot of AMS+MAAP and SMPS mass concentrations in 2012. Here, only a D_{va} range of 60 nm to 600 nm was considered for the determination of the SMPS mass.

3.2.3. Comparison of inorganic aerosol mass

The Monitor for Aerosol and Gases (MARGA) shared the AMS inlet during the whole campaign in 2012, acquiring hourly data alternately with a PM_1 and a $PM_{2.5}$ inlet. Due to technical problems, no MARGA data is available between 26.05.; 9 pm to 12.06.; 2 pm and between 13.06.; 1 am to 15.06.; 11 pm (all in UTC). In this work, only PM_1 MARGA results are presented to compare with AMS data, which is considered a PM_1 instrument. The time series of particulate Chl, NH_4, SO_4, and NO_3 from the MARGA (black lines) and AMS (coloured dots) can be seen in figure 3.26. Table 3.3 shows the slopes, intercepts, and the correlation coefficients (Pearsson R^2) from the comparison of inorganic aerosol species between the AMS and the MARGA. For every comparison, 396 data points were used. The corresponding correlation graphs are given in the appendix (figure A.13). Both instruments showed good qualitative agreement during the whole campaign in case of all four investigated compounds. Comparing to the MARGA, the AMS measured 51 % to 61 % of individual species and 60 % of the total inorganic mass, which is consistent with the comparison between the AMS+MAAP and the SMPS.

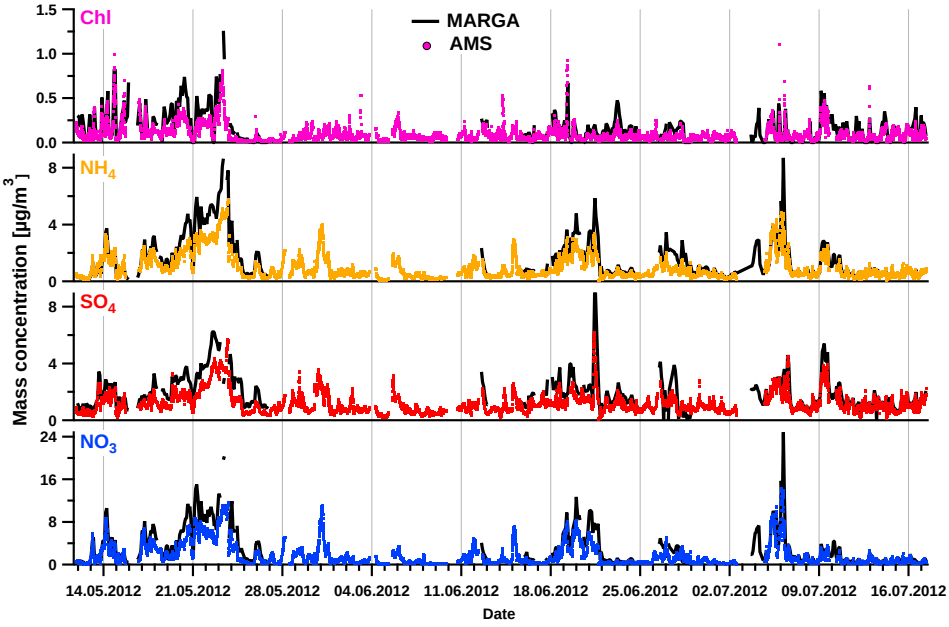

Figure 3.26.: Time series of particulate Chl, NH_4, SO_4, and NO_3, measured by the AMS (coloured dots) and the MARGA (black lines) between May to July 2012

Table 3.3.: Results of the AMS to MARGA comparison from four particulate inorganic species and the total inorganic mass (396 common data points) between May to July 2012

	slope	intercept [µg m^{-3}]	R^2
Chl	0.51	0.02	0.83
NH_4	0.61	0.14	0.93
SO_4	0.55	0.23	0.83
NO_3	0.60	0.09	0.92
Total Inorganics	0.60	0.38	0.92

The quantitative discrepancies between the AMS and the MARGA may be explained by the different measurement techniques themselves. The MARGA detects the water soluble particle components, while the AMS measures the non-refractory fraction. During periods with high particulate water, such as in the end of May and around 05.07. (see figure 3.15), the largest differences in the mass concentrations were observed. Although both instruments are supposed to be PM_1 instruments, size cut-offs are achieved using different modules. The aerodynamic lens is known to have transmission efficiencies significantly lower than 100 % at particle sizes larger than 700 nm (D_{va}). If particles with sizes of 700 nm to 1 µm have high contribution to aerosol mass, this fraction would be un-

derestimated by the AMS. A comparison between MARGA PM_1 and $PM_{2.5}$ data showed higher PM_1 concentration than $PM_{2.5}$ in some periods. That might be due to the different sampling periods, because the MARGA sampled changes hourly between its PM_1 and $PM_{2.5}$ inlet. Alternatively, the PM_1 inlet was not properly characterized and sampled particles larger than 1 µm, which would also explain the discrepancy to AMS data.

Another possible reason arises from the fact, that the AMS inlet was connected to the MARGA inlet with a T-formed connection. Taking into account, that the flow rate into the MARGA is much higher (16.7 L min^{-1}) than within the AMS inlet (AMS+CPC: 380 mL min^{-1}), the AMS may under-sample especially large particles.

3.2.4. Comparison of organic aerosol mass measurements

The TD-PTR-MS was measuring between 21.05. and 17.07.2012, detecting 296 ions with the highest mass at m/z 283. A list of the detected ions is shown in the appendix (see section A.4). Between 11.07. and the end of the campaign, a contamination was observed in one of the inlets (B). Thus, data derived from inlet B during this period was excluded from further analysis. The PTR-OA time series from both inlets are given in the appendix (figure A.14). After exclusion of data containing contaminations, the remaining OA concentrations of both aerosol inlets agree well. Thus, they are merged and displayed in figure 3.28a. From the merged data set, an average PTR-OA mass concentration of 0.24 µg m^{-3}, a maximum of 1.45 µg m^{-3}, and a minimum of 0.02 µg m^{-3} were observed.

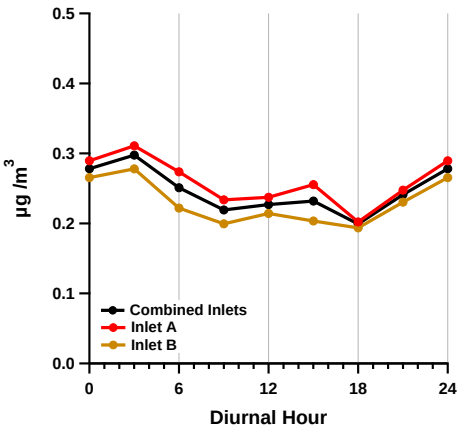

Figure 3.27.: Averaged diurnal variations (LT) of PTR-OA from both inlets and from merged data in 2012. Note that PTR-OA data was pre-averaged to a resolution of 3 hours.

A very high correlation compared to AMS-OA ($R^2 = 0.88$ for 733 data points) is seen in figure 3.28b, with PTR-OA of 14 % of AMS-OA. As mentioned in subsection 2.3.1, a relatively high degradation of the PTR-MS MCP resulted in a low sensitivity for ions with high masses (m/z > 250). Because of the low fragmentation in the PTR-MS, high contributions from larger m/z to PTR-OA mass concentrations are expected. Losing these ions during the measurements may bias total PTR-OA low. This would explain why the TD-PTR-MS measured only approximately 14 % constantly over the whole campaign,

compared to AMS-OA, which is less than half of the percentage seen in 2011 (PTR-OA/AMS-OA = 31 %, subsection 3.1.3). Figure 3.27 shows the 3-hourly averaged diurnal patterns from both inlets separately and from merged data. The highest values were obtained during the night, in addition to a small maximum at around noon-time/early afternoon, which is in agreement with the AMS organic diurnal pattern.

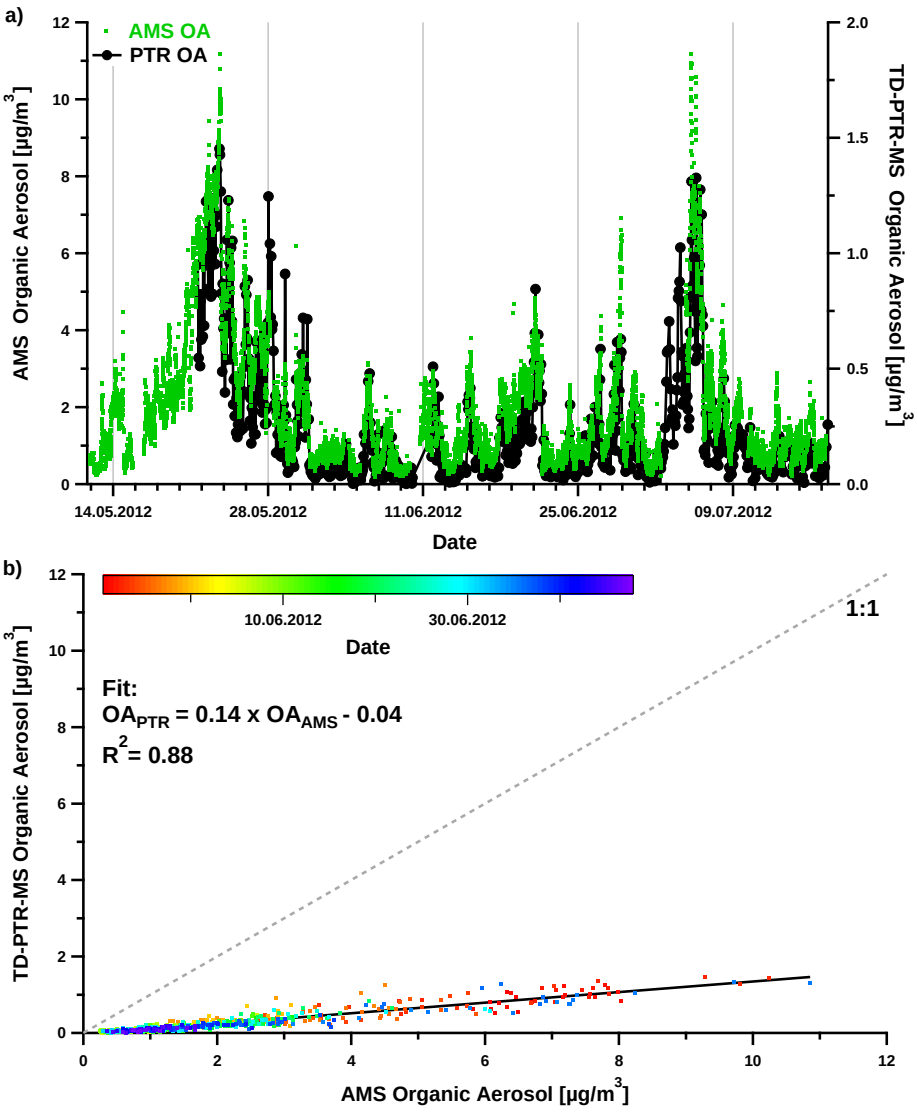

Figure 3.28.: Time series (a) and correlation plot (b) of PTR OA (both inlets combined) and AMS OA mass concentrations in 2012

3.3. ACSM campaign 2012-2013

Figure 3.29 gives an overview of the meteorological conditions during the ACSM campaign at CESAR from 11.07.2012 to 03.06.2013. A separation of the campaign into five time periods was done for practical reasons mentioned below. Moderate wind speeds at around 5 m s^{-1} were seen over the entire year, with long periods of southerly and westerly winds (mostly in the first half of the campaign), alternating with periods of northerly wind directions, like between 21.10. to 25.10.2012 and between 16.01. to 27.01.2013 (highlighted in green).

A clear annual ambient temperature and *RH* cycle can be seen, as expected. Higher daily variations of both parameters were obtained in Spring and Summer (see figure A.15), as also showed by the comparison between Autumn 2011 and Spring 2012 in sections 3.1 and 3.2. Table 3.4 shows an overview of the ambient conditions all of the defined periods and for the whole campaign. The ACSM sample inlet was dried using a Nafion dryer over the whole campaign. Though no measurements of temperature and *RH* were made within the inlet during ambient sampling, a *RH* of maximum 40 % is expected as a result of previous laboratory tests on the efficiency of the dryer.

Table 3.4.: Overview of the ambient temperatures and relative humidities during the ACSM campaign, measured at 2 m height.

	Period	Minimum	Maximum	Average
Temperature [°C]	1 (11.07. - 30.09.2012)	6.7	32.2	16.5
	2 (01.10. - 29.12.2012)	-6.1	21.3	7.7
	3 (08.01. - 15.02.2013)	-12.3	12.4	0.6
	4 (18.02. - 25.04.2013)	-5.1	19.5	3.5
	5 (25.04. - 03.06.2013)	2.9	22.3	10.9
	Entire campaign	-12.3	32.2	9.2
RH [%]	1 (11.07. - 30.09.2012)	35.7	100.6	79.3
	2 (01.10. - 29.12.2012)	51.3	102.6	88.6
	3 (08.01. - 15.02.2013)	58.9	102.9	86.2
	4 (18.02. - 25.04.2013)	23.2	101.2	72.5
	5 (26.04. - 03.06.2013)	35.9	100.3	80.2
	Entire campaign	23.2	102.9	82.2

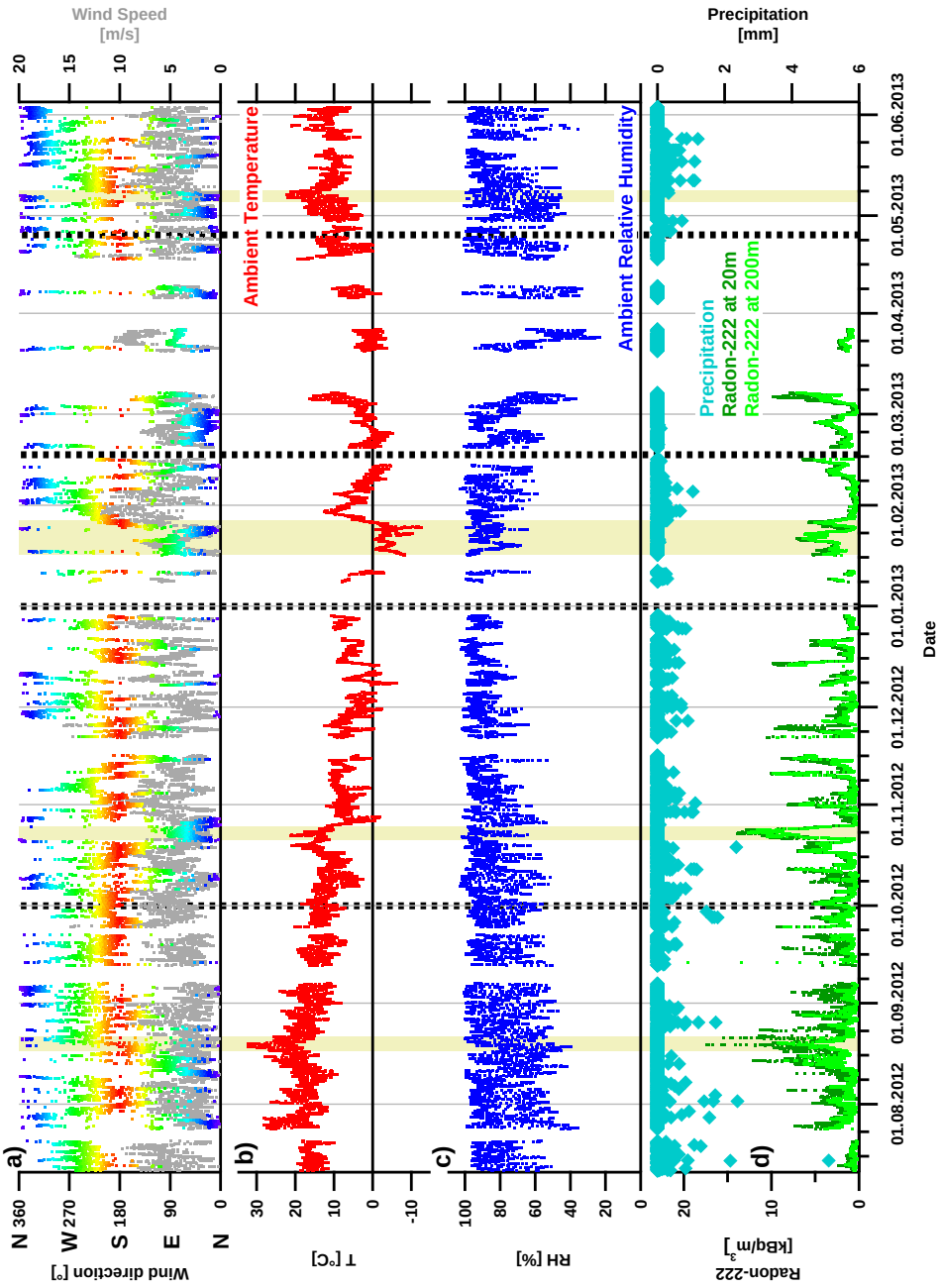

Figure 3.29.: Meteorological overview of the ACSM campaign: a) Wind direction (0°/360°, 90°, 180°, and 270° represent North, East, South, and West, respectively) and wind speed (grey) at 10 m height. b) and c) temperature (red) and relative humidity (blue) at 2 m height. d) Precipitation (turquoise) and Radon-222, measured at 20 m (dark green) and 200 m (light green). High mass periods are indicated by green backgrounds (see below).

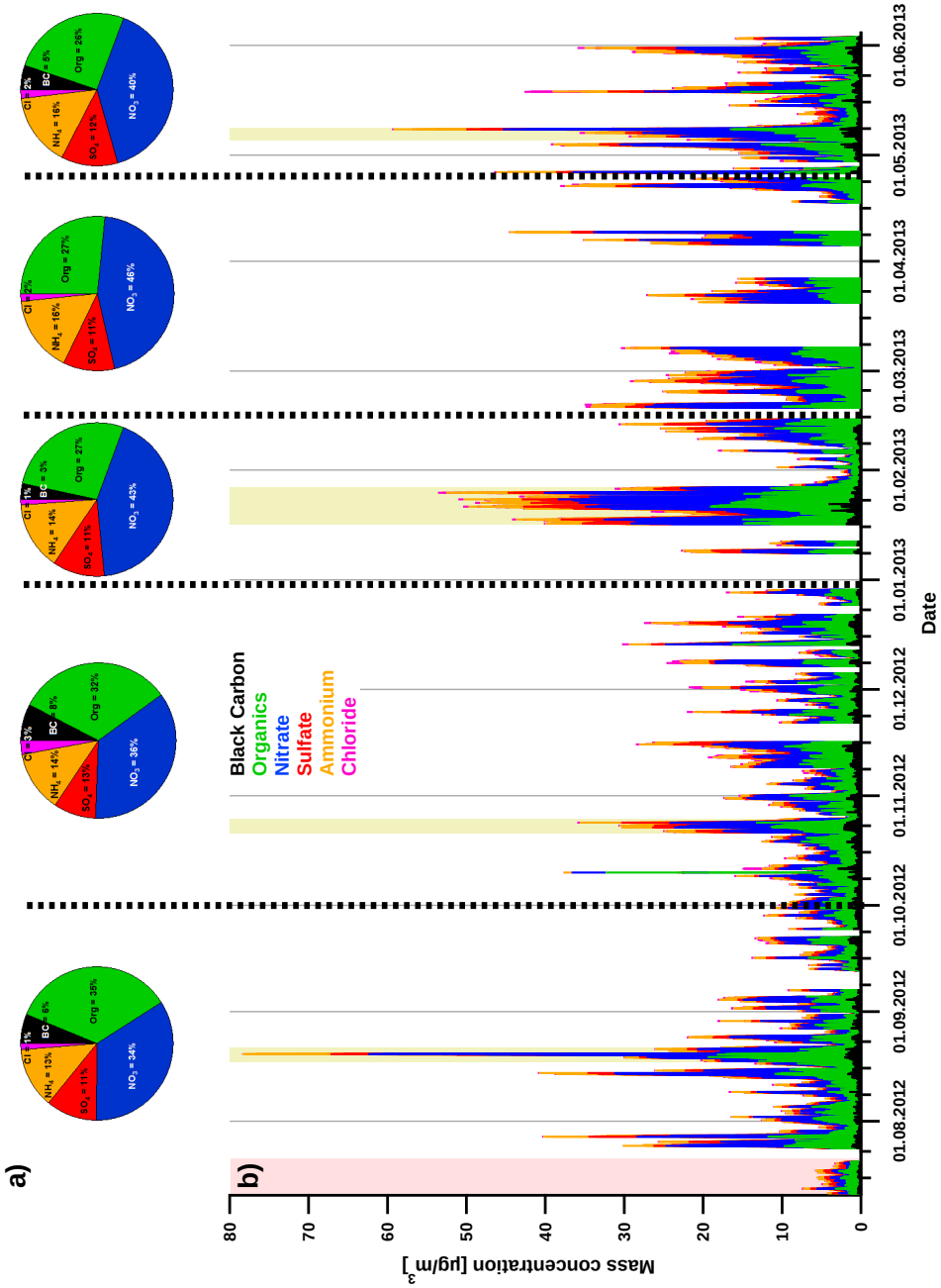

Figure 3.30.: Overview of the ACSM campaign from July 2012 to June 2013. a) Pie charts of average fractional abundances of aerosol species, separated in five periods. b) Stacked time series of mass concentrations of aerosol species. The temporal overlap with the AMS and TD-PTR-MS is highlighted in red. High mass periods are indicated by green backgrounds.

Figure 3.30 shows the average contributions of individual species in form of pie charts in a) and the stacked time series in b). Particulate water could not be calculated or displayed with the ACSM software used in this work. The time period, where the ACSM sampled simultaneously with the AMS and TD-PTR-MS, was from 11.07. to 17.07. and is highlighted in red. A technical problem of the MAAP instrument was responsible for the lag of BC data from 18.02.2013 to 31.02.2013. Because of that, the campaign was not divided strictly season-wise, but into five periods to determine properly average species contributions shown in figure 3.30a. The first two sections represent the summer (July-August-September) and autumn (October-November-December) 2012, while the first half of 2013 was divided into periods with and without BC data.

Larger gaps in ACSM data occurred mainly due to problems with the RGA detector, in addition to minor measurement gaps for maintenance and calibrations. Also for this campaign, BC data was corrected for losses in the 60 m sampling line as mentioned before, while ACSM data was untreated in this regard, since this instrument sampled at 5 m height. The ACSM CE was determined using the algorithm developed by *Mensah et al.* (2012). It had a campaign average of 0.59, its time series is given in the appendix (figure A.16).

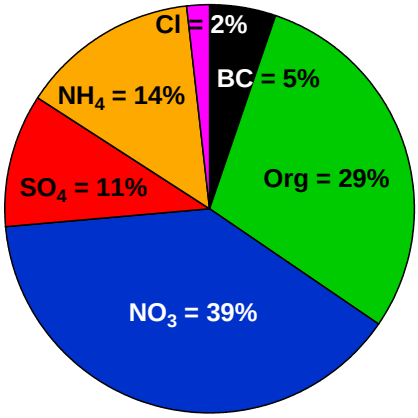

Figure 3.31.: Average contributions of aerosol species from ACSM data over the entire campaign

On average, a total mass concentration of 9.50 µg m^{-3} was measured, with a maximum of 78.4 µg m^{-3} and a minimum of 0.2 µg m^{-3}. The average fractional abundances of individual species over the entire campaign is given in figure 3.31. As mentioned before, NO_3 and organics are the dominant species, representing 39 % and 29 % of the total aerosol, respectively. Both compounds show equal contributions in Summer and Autumn 2012, whereas in Winter (January-February-March) and Spring (April-May-June) the NO_3 fraction increased up to an average of 46 % of the total particulate mass, and the organic and BC fractions decreased. The contributions of the other components show only small variations between the seasons. The most significant high mass periods are highlighted in green in figure 3.30. During the times with high mass concentrations (21.10. to 25.10.2012, 16.01. to 27.01.2013, and 05.05. to 08.05.2013), northerly and north-easterly winds dominated. The second of these periods showed also the coolest temperatures (average: -4°C)

with respect to the whole campaign and a temperature inversion between 2 m and 40 m height in the mornings of 16.01. and 25.01.2013. This fact can be used again as an indicator for the stable boundary layer height (see subsection 3.1.1). On the other hand, no significant temperature inversion seems to be responsible for very high ($> 40\,\mu g\ m^{-3}$) aerosol mass loadings, even in winter times. Many drops of the particulate mass can be either explained by changes in wind directions and/or precipitation events, like in case of the two latter high mass periods (16.01. to 27.01.2013, and 05.05. to 08.05.2013).

No preferred wind direction was seen for most of the species in polar plots in figure 3.32. Chloride showed short distinctive plumes from 225 ° to 0 °.

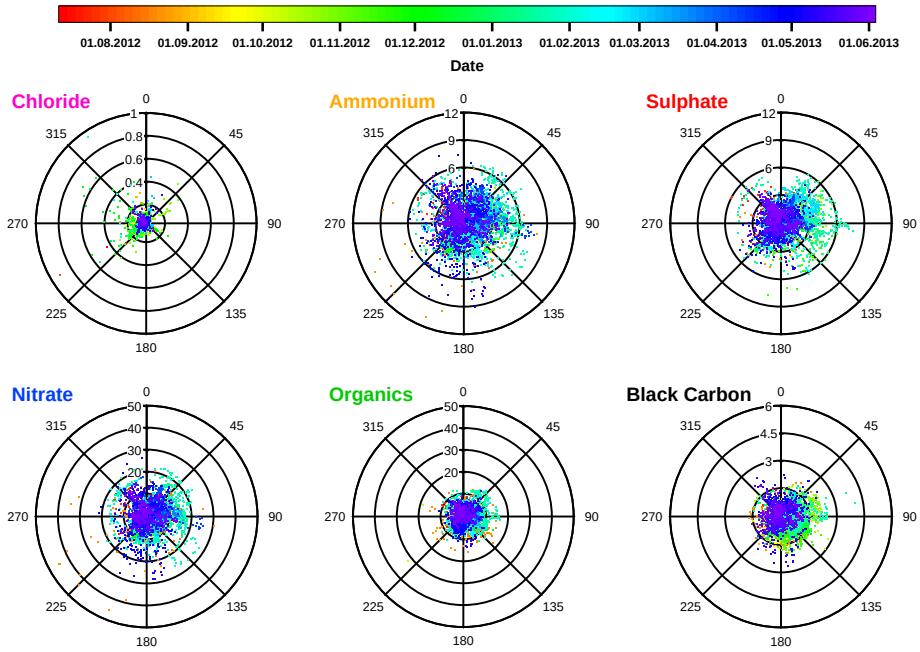

Figure 3.32.: Polar graphs of individual species of ACSM data, colour-coded by time. The radii represent the respective mass concentration in $\mu g\ m^{-3}$, the angles show the cardinal directions, with the tower in the centre of the plots. Attention should be paid on the different radius scales.

Figure 3.33 shows the diurnal patterns of each individual species and the total particulate mass for the whole campaign and separately for the five chosen periods mentioned above (see table 3.4). Overall, NO_3 shows the largest diurnal variations, with a maximum during the night/morning hours and a minimum during the day due to the volatility of NH_4NO_3. Thus NH_4 has a similar pattern. SO_4, which is mainly formed photochemically during the day from gaseous SO_2, has a daytime maximum, although its overall variation

is rather low. BC shows also a maximum during the morning again, while the minimum of the organic fraction is seen during the day. Within period 3, no clear diurnal variation is observed for any compound. This might be a result of the strong influence of the high mass periods with its special meteorological conditions.

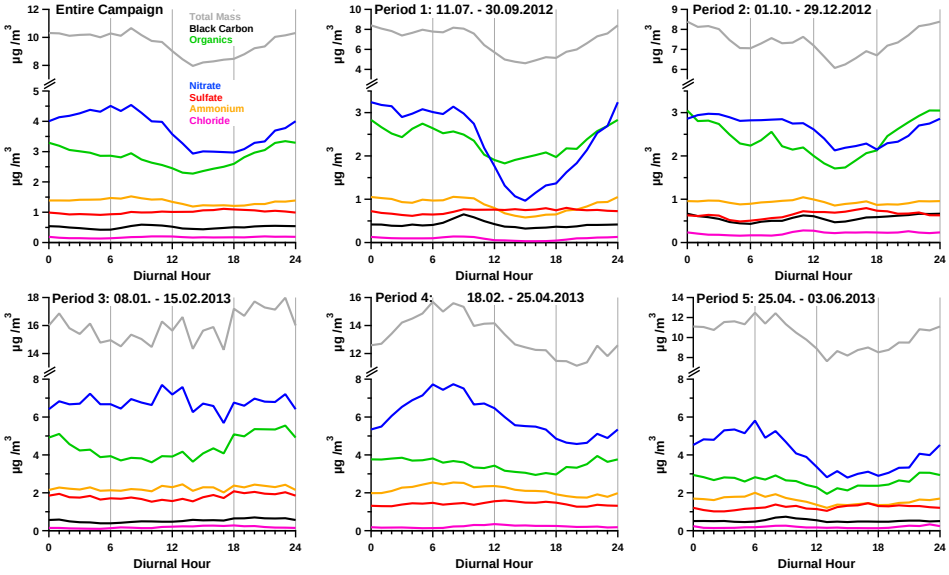

Figure 3.33.: Diurnal variation (LT) of individual species and the total mass, averaged over the whole ACSM campaign and over the five periods, which are explained in table 3.4. Note the different scales of y-axes between the periods.

3.3.0.1. Aerosol ion balance

Plotting the measured NH_4 mass concentration against the predicted NH_4 results in a slope of 0.83 (figure 3.34), which indicates relatively high aerosol acidity during the campaign. In turn, no Excess-NH_4 could be observed. As mentioned in subsection 2.2.1.2, it was not possible to differ the total NO_3, measured by the ACSM, into the organic and inorganic fraction. Therefore, the total NO_3 mass concentration was used to determine the ion balance for the ACSM data set. For the AMS campaign in 2011 (see subsection 3.1.1.2), the use of all nitrate ions to form NH_4NO_3 for the ion balance leads to a similar grade of acidity like presented here. In contrast, Excess-NH_4 was obtained when the inorganic fraction of AMS NO_3 was taken into account only. That means, that uncertainty remains for the acidity observed for the ACSM campaign, when assuming that all nitrate ions are of inorganic origin.

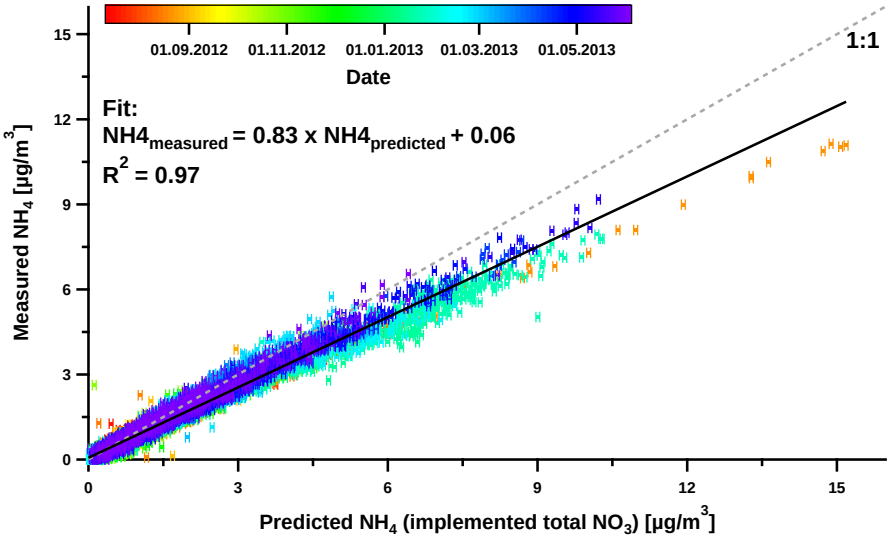

Figure 3.34.: Correlation plot of measured against predicted NH_4 during the ACSM campaign. Error bars represent uncertainties of the NH_4 prediction.

3.3.1. Comparison of measurements of total PM_1 mass

The particle density during the ACSM campaign was determined using the chemical composition data from the ACSM and the MAAP. The time series of the density is given in the appendix (figure A.18). It shows a significant scattering due to the relatively low signal-to-noise ratio of the ACSM, especially during periods with low mass loadings. Therefore, the campaign average of the particle density (1.50 g cm^{-3}) was used to calculate the SMPS total mass concentration from its measured volume concentration throughout the campaign. An average SMPS mass of 11.3 µg m^{-3} (maximum: 55.1 µg m^{-3}, minimum: 0.17 µg m^{-3}) was determined. Figure 3.35 shows the time series of the SMPS mass, together with its correlation with the combined mass concentrations measured by AMS and MAAP. A correction for wall losses within the 60 m sample line was applied to SMPS and MAAP data. Since the ACSM measured at 5 m height, no correction was applied. Using 12275 common data points, a very high qualitative and quantitative agreement over the whole campaign within the expected errors was observed.

In case when only particles of a D_{va} range of 60 nm to 600 nm are considered for the determination of SMPS mass (see subsection 3.1.2 and 3.2.2), the comparison between the data sets shows slightly less qualitative agreement over the whole campaign (R^2 = 0.76; figure 3.36). More important, the SMPS mass concentrations decreased to around 74 % of the total mass, which is obtained when using all particles detected by the SMPS.

In November 2011 and from May to July 2012, the corresponding decrease was higher (about 50 %). That means, that over the entire ACSM campaign the contribution of the excluded particles to the total SMPS mass is less than in the previous campaigns. This explains partly why the quantitative agreement between the SMPS with the ACSM is better than with the AMS in 2011 and 2012.

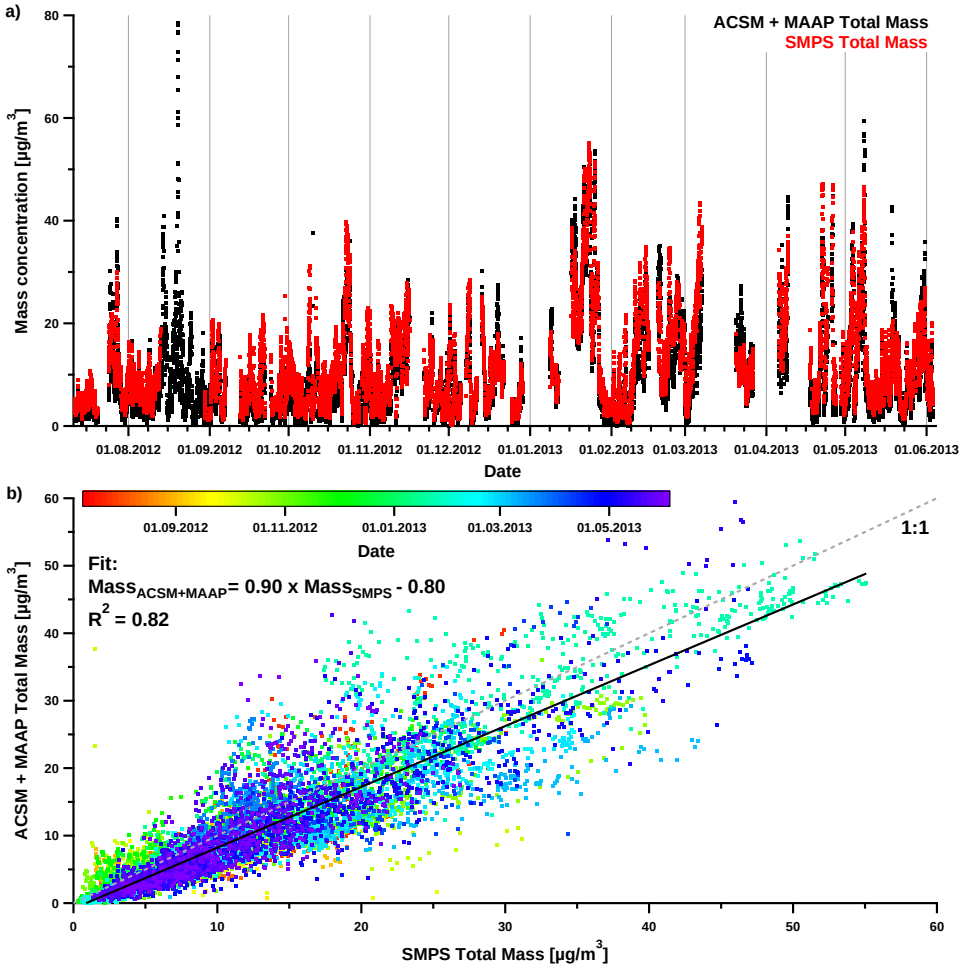

Figure 3.35.: Time series (a) and correlation plot (b) of ACSM+MAAP and SMPS mass concentrations between July 2012 and June 2013

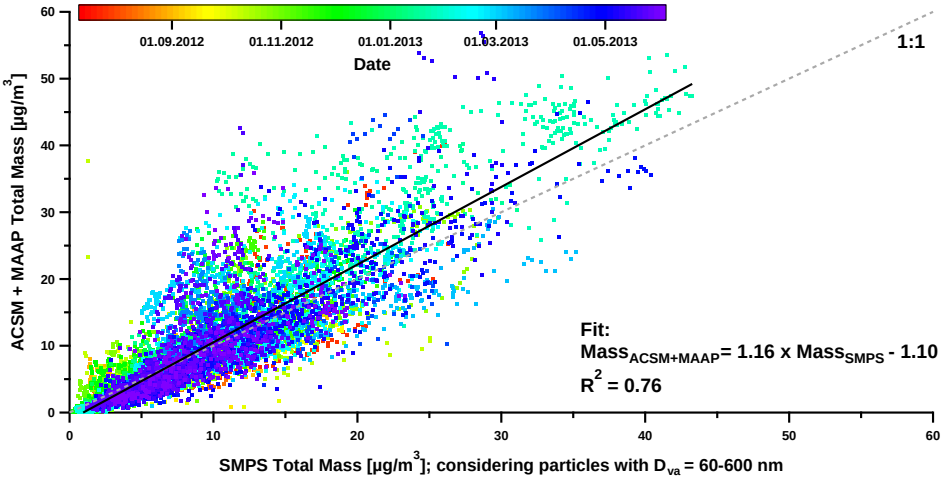

Figure 3.36.: Correlation plot of ACSM+MAAP and SMPS mass concentrations between July 2012 and June 2013. Here, only a D_{va} range of 60 nm to 600 nm was considered for the determination of the SMPS mass.

3.3.2. Comparison of inorganic aerosol mass

Since the MARGA measures routinely the water soluble aerosol compounds, data from ACSM inorganic species can be compared to corresponding MARGA data for the whole year of measurement. Besides smaller gaps one large gap in the MARGA data occurred between 26.09. to 06.11.2012. Figure 3.37 shows the time evolution of particulate PM_1 concentrations of Chl, NH_4, SO_4, and NO_3, measured by the ACSM (coloured dots) and the MARGA (black lines).

The correlation parameters of inorganic aerosol species and the total inorganic masses are given in table 3.5. For every comparison, 1943 data points were used. The corresponding correlation graphs are shown in the appendix (figure A.19).

Table 3.5.: Results of the ACSM to MARGA comparison from four particulate inorganic species and the total inorganic mass (1943 common data points) during 2012-2013

	slope	intercept [µg m^{-3}]	R^2
Chl	0.49	0.11	0.24
NH_4	0.88	0.07	0.93
SO_4	0.63	-0.08	0.86
NO_3	1.23	-0.37	0.96
Total inorganics	1.05	-0.70	0.93

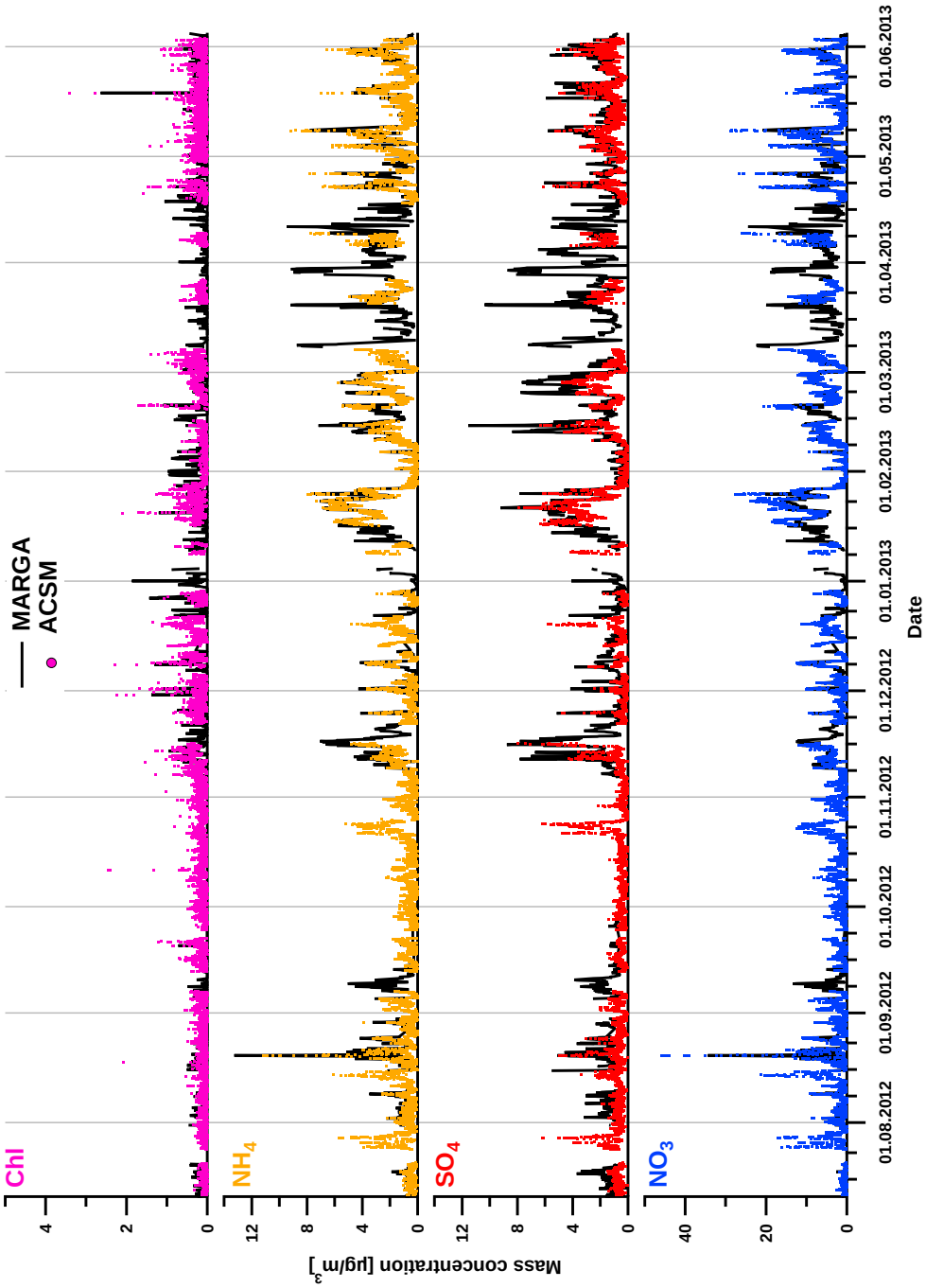

Figure 3.37.: Time series of particulate Chl, NH_4, SO_4, and NO_3, measured by the ACSM (coloured dots) and the MARGA (black lines) between July 2012 and June 2013

Except for chloride, very high qualitative correlation coefficients were achieved. A comparison between the respective sums of all four inorganic species (total inorganics) shows a very high qualitative and quantitative agreement. While the quantitative difference in case of ammonium is rather low, the ACSM underestimates sulphate by 37 % and overestimates nitrate by 23 %, comparing to the MARGA. These discrepancies are within or not far away from the stated ± 30 % accuracy of the ACSM. Similar variations were also found by *Budisulistiorini et al.* (2013) from the comparison between two collocated ACSM's (± 27 %, $R^2 = 0.21$ for Chl, $R^2 > 0.8$ for the other species) and between these ACSM's and a continuous Tapered Element Oscillating Microbalance (TEOM, $PM_{2.5}$) instrument.

The differences in the cases of NO_3 and SO_4 may arise from calibration issues. The mass calibration procedure used in this work was mainly adopted from AMS procedures which may not be directly suitable for the ACSM. As mentioned in subsection 2.2.1, the RIE of sulphate might be overestimated due to high observed background signals during the calibration using $(NH_4)_2SO_4$ particles. An overestimated RIE_{SO_4} results in underestimated mass concentrations. This would in turn explain the low SO_4 mass concentrations comparing to the MARGA. Additionally, the ACSM fragmentation table could not be adjusted for interferences of ions from different aerosol species on the same m/z, but the standard table had to be used. This can also be a reason for discrepancies between the MARGA and the ACSM. It should be noted, that chloride concentrations can originate from particulate organic and inorganic chloride components. For the latter, the ACSM is much less sensitive than the MARGA, which would explain the low agreement between the two instruments in case of Chl.

3.3.3. Comparison of measurements of PM_1 chemical contribution

In this section, ACSM data is compared with data derived from the collocated AMS and TD-PTR-MS during the time from 11.07. to 17.07.2012, which is shown in figure 3.38. As it is shown in figure 3.30 above, this overlap time represents a period with low mass concentrations (average of ACSM total mass: 3.5 µg m^{-3}). Nevertheless and despite the relatively low amount of correlated data points (294), a good agreement is observed between individual species ($R^2 = 0.71$ - 0.89), obtained from the AMS and ACSM, except for chloride. The corresponding correlation parameters are summarized in table 3.6, while the correlation plots can be found in the appendix (figures A.20 and A.21)

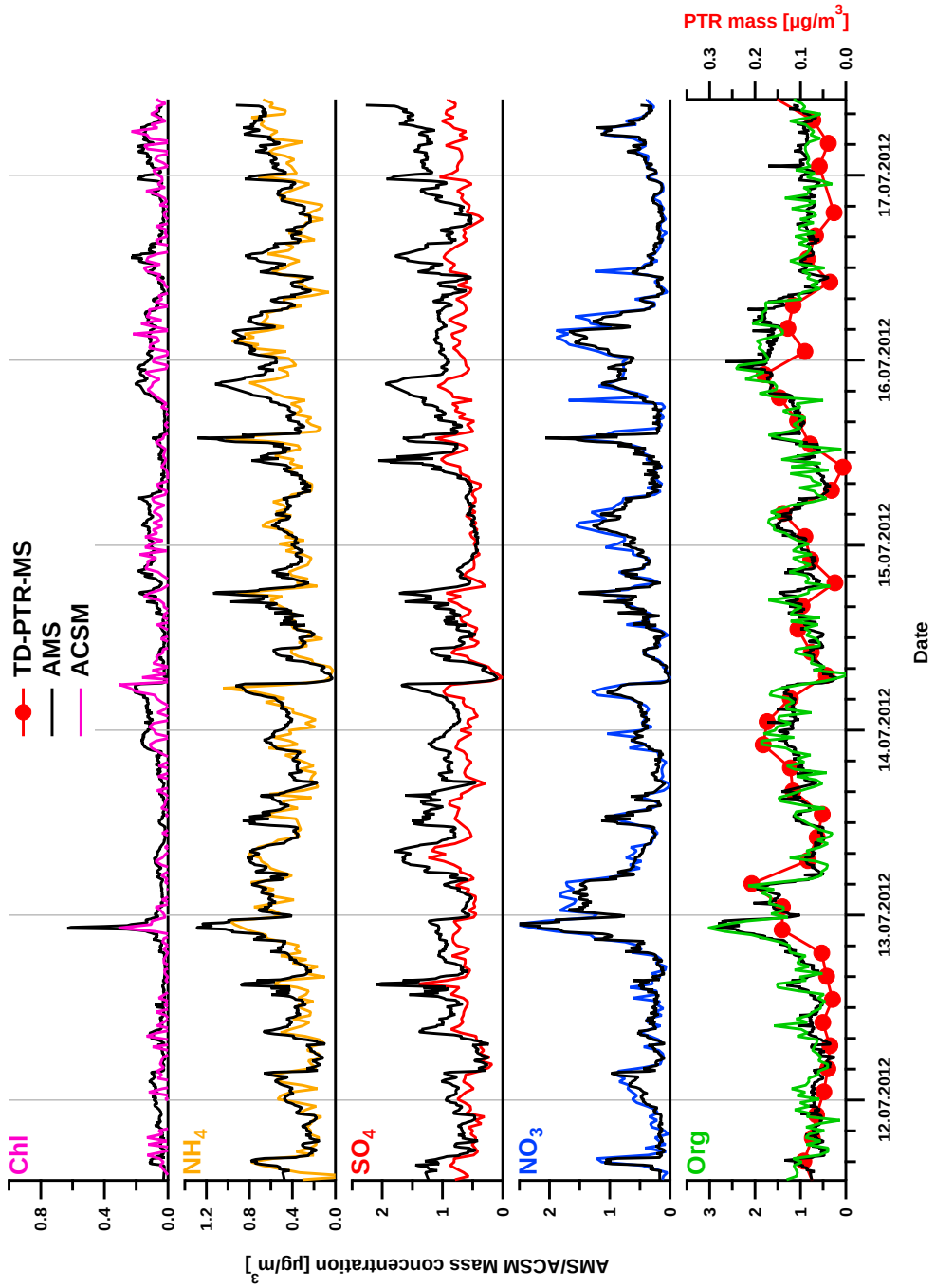

Figure 3.38.: Time series of individual species, measured by the ACSM (coloured lines) and the AMS (black lines) between 11.07. and 17.07.2012. The bottom graph contains also the corresponding PTR-OA (red line with dots).

Similar results were already achieved from the comparison between the ACSM and the MARGA, described in subsection 3.3.2. Again, the quantitative differences between the NO_3 and NH_4 data sets were within the uncertainty, with a slight overestimation of NO_3 (17 %) and underestimation of NH_4 (12 %). Also, a strong underestimation of ACSM-SO_4 is seen comparing to the AMS. Here, the ACSM measures only 49 % of the AMS-SO_4. As explained in subsection 3.3.2, this variation might occur because of an overestimated RIE_{SO_4}. A remarkably high agreement between the ACSM and AMS organic mass concentrations was achieved. Also a visual qualitative agreement of the ACSM-OA to the PTR-OA time series can be seen, while their mathematical correlation results in a low correlation coefficient ($R^2 = 0.37$) and a high intercept (0.61 µg m^{-3}). This is mainly due to the low time resolution of the TD-PTR-MS resulting in few common data points (49), which makes it difficult to get representative correlation results. On the other hand, the low PTR-OA percentage (compared to ACSM-OA: 7 %) is consistent with the comparison between the TD-PTR-MS and the AMS over the entire AMS campaign 2012 (14 %).

Table 3.6.: Results of the ACSM to AMS/TD-PTR-MS comparison from individual species between 11.07. and 17.07.2012

	slope	intercept [µg m^{-3}]	R^2 (common data points)
Chl	0.67	-0.01	0.31 (294)
NH_4	0.82	0.01	0.71 (294)
SO_4	0.49	-0.18	0.76 (294)
NO_3	1.17	-0.02	0.89 (294)
Org (AMS)	1.00	0.07	0.73 (294)
Total (AMS)	0.90	0.02	0.84 (294)
Org (PTR)	5.49	0.61	0.37 (49)

4. Discussion

4.1. Analysis of organic aerosol

The following sections describe the results and solutions obtained by the application of Positive Matrix Factorization (PMF) and Multilinear Engine 2 (ME-2) to the AMS and ACSM data sets, respectively. Since PMF results can be biased by local short term events, AMS data was averaged to hourly data sets prior to PMF analysis to avoid so called spikes in the organic time series. The time resolution of ACSM data was approximately 30 minutes. Thus, an additional averaging was not applied. Note, that the m/z values given here are in UMR and not the exact HR masses.

4.1.1. PMF results for AMS data in 2011

Using the criteria parameters mentioned in subsection 2.5.1 three factors (FPEAK 0.2) were found from PMF calculations of the AMS organic fraction in November 2011: (i) a hydrocarbon-like organic aerosol (HOA) factor, (ii) a biomass burning factor (BBOA), and (iii) an oxygenated organic aerosol (OOA) factor. Figure 4.1 shows the mass spectra (a) and the time series (b) of each factor. The last contains also the time series of important external tracers. The average contributions and diurnal patterns are displayed in figure 4.2.

To assure that the presented solution represents the global minimum of Q/Q_{exp}, a set of 50 PMF seed runs of 3-factor solutions were performed. The variance of the factor mass contributions is shown in the appendix (figure A.22). All factor mass fractions vary within 1 % between the seed runs, with Q/Q_{exp} values varying within 0.005 %. This is clear evidence that the global minimum solution was found. Finally, 100 bootstrapping runs were performed to estimate the uncertainty of the 3-factor solution by terms of each m/z and time series data point. Results are presented in the appendix (figure A.23). There, all values of the final solution are lying within their errors. As discussed in the following, the attribution of the individual factors was performed based on both, the mass spectral features and the correlation of the factor time series with external tracers. A summary of time series correlations is given in the appendix (table A.16).

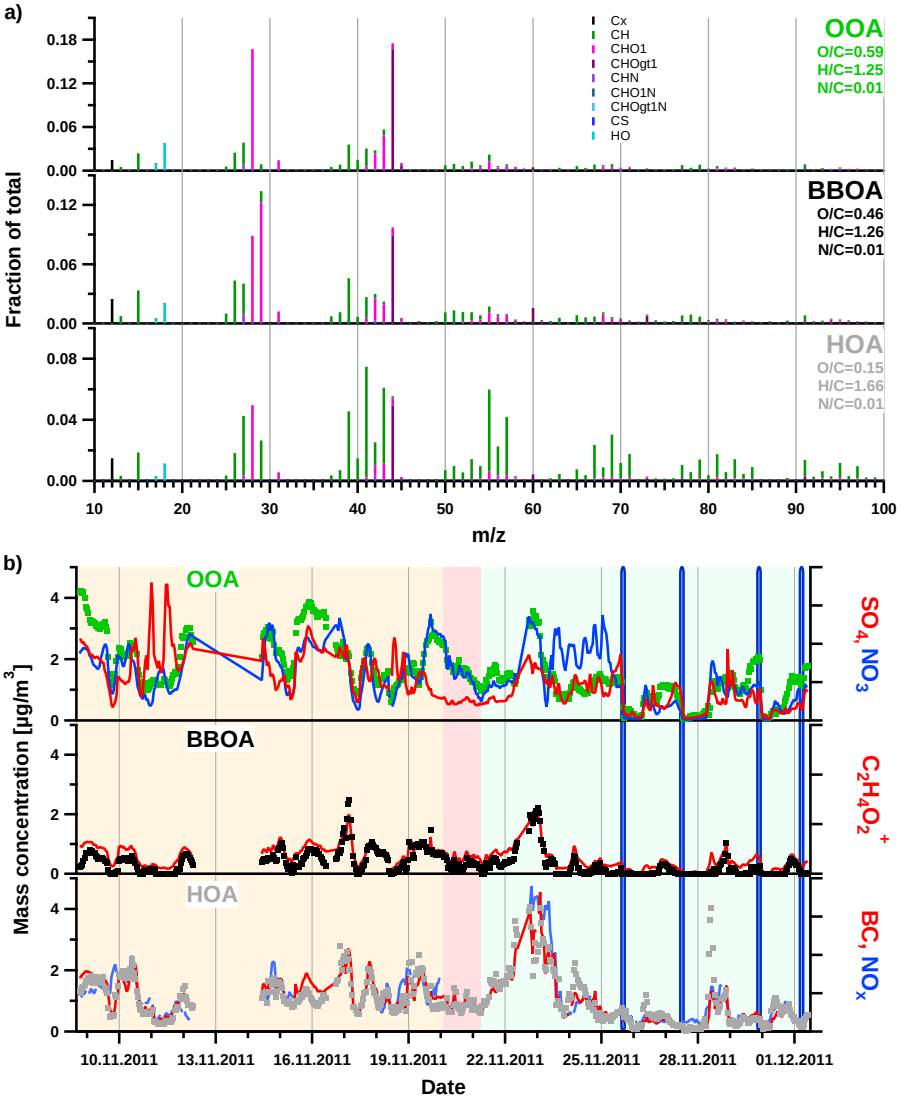

Figure 4.1.: Mass spectra (a) and time series (b) of PMF factors from AMS data and tracers of November 2011. The HR mass peaks in a) are stacked at each unit mass m/z and coloured by their chemical family (gt1 = greater than 1). The time period with southerly and easterly wind directions in b) is highlighted in beige. The time of calm northerly winds is indicated by a red background. The period with southerly and westerly wind directions is illustrated in green. The sharp blue rectangles represent precipitation events. The bottom of each tracer axes is set to zero.

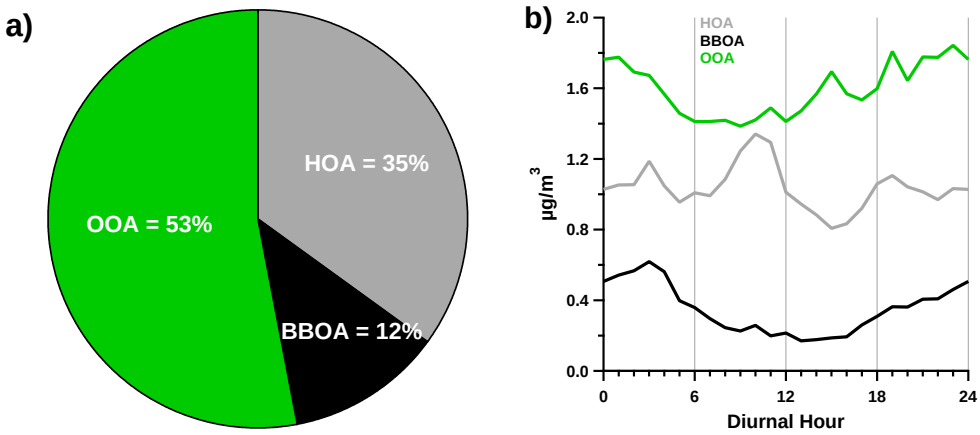

Figure 4.2.: A) Average contributions of AMS PMF factors and b) their diurnal variations (LT) in 2011

The HOA factor contributed about 35 % to the total organic fraction over the entire campaign. Typical for a HOA factor, its mass spectrum (MS) has the highest contributions of ions from the CH-family, which means ions only containing carbon and hydrogen atoms (*Docherty et al.*, 2011; *Mohr et al.*, 2012). The dominant ions from the CH-family are $C_3H_3^+$ (m/z 39), $C_3H_5^+$ (m/z 41), $C_3H_7^+$ (m/z 43), $C_4H_7^+$ (m/z 55), and $C_5H_9^+$ (m/z 57), which are typically seen in spectra of aliphatic hydrocarbons (*Canagaratna et al.*, 2004; *Zhang et al.*, 2005). This is expected for a HOA factor, since it is considered as a primary organic aerosol (POA), which is emitted directly into the atmosphere. Another typical HOA characteristic is the fact, that these m/z are respectively separated by 14 amus (corresponding to the separation of by a CH_2 group), e.g. the ion series m/z 29 ($C_2H_5^+$) to m/z 43 ($C_3H_7^+$) to m/z 57 ($C_5H_9^+$). The biggest difference between HOA reported in the literature and the observed HOA MS is the high signal from the CO_2^+ ion (m/z 44), which is usually attributed to SOA factors. This ion is the main reason of a relatively high O/C ratio (0.15), compared to typical HOA factors (0.02-0.08; *Docherty et al.* (2011); *Mohr et al.* (2012); *Setyan et al.* (2012)). On the other hand, *Aiken et al.* (2009) reported a high O/C ratio (0.16) of the HOA factor, obtained during the MILAGRO campaign in March 2006. Note that the AMS fragmentation table defines the CO^+ (m/z 28) signal equal to the CO_2^+ signal. Therefore, both ions are correlated in every organic MS.

The HOA time series shows the highest correlations with BC ($R^2 = 0.79$), Chl ($R^2 = 0.69$), gaseous NO_x ($R^2 = 0.66$), and CO data ($R^2 = 0.54$). The maxima in the morning and evening hours and the minimum during the day of the HOA diurnal variation lead to the conclusion, that this factor is mainly emitted by traffic during rush hours.

BBOA is another POA factor and contributed on average 12 % of the total organic

mass. Its MS is dominated by CHO^+ (m/z 29) and CO_2^+ (m/z 44), which is characteristic for BBOA factors (*Schneider et al.*, 2006; *Saarikoski et al.*, 2012; *Ng et al.*, 2011a; *Crippa et al.*, 2013b; *Canonaco et al.*, 2013). Note that mass spectra of BBOA factors are known to vary strongly depending on the measurement site (*Crippa et al.*, 2014). In addition, the BBOA MS has high contributions of the ions $C_2H_4O_2^+$ (m/z 60) and $C_3H_5O_2^+$ (m/z 73). These fragments are characteristic of anhydrosugars such as levoglucosan (*Alfarra et al.*, 2007) which are established markers of wood combustion processes (*Simoneit et al.*, 1999; *Simoneit and Elias*, 2001). Therefore, these ions are commonly used as BBOA tracer ions. The high correlations of the time series of both ions ($R^2 = 0.88$ and 0.83, respectively) with the BBOA time series underlines that the main source of this factor is biomass burning. The BBOA diurnal behaviour shows an increase during the late afternoon, consistent with domestic heating activities, as expected especially in cold seasons.

The highest contribution to AMS-OA in 2011 (53 %) was obtained from the OOA factor (O/C = 0.59). Its MS is dominated by the CO_2^+ ion (m/z 44), which results from the thermal decomposition and fragmentation of highly oxygenated species such as organic acids (*Ng et al.*, 2010). Typically high CO_2^+ contributions to OA factor MS are observed for low-volatile oxygenated organic aerosol (LVOOA, *Lanz et al.* (2007)). The OOA MS showed very good correlations with AMS LVOOA factors found by *Mensah* (2011) and *Crippa et al.* (2014) in May 2008 ($R^2 = 0.93$ and 0.97, respectively) at the CESAR tower in Cabauw.

On the other hand, the correlation of the OOA time series with SO_4 is rather low ($R^2 = 0.40$), and the diurnal variation shows no clear day-time maximum (photo-oxidative sources), as it would be expected for a classical LVOOA behaviour. In fact, the diurnal behaviour and the higher correlation to NO_3 ($R^2 = 0.55$) is characteristic for a semi-volatile OOA (SVOOA) factor. In turn, the correlation of OOA to the sum of the secondary inorganic species NO_3 and SO_4 is better ($R^2 = 0.66$), emphasizing that this factor has SOA characteristics. High agreement was also seen between the OOA factor and the time series of $OrgNO_3$ ($R^2 = 0.72$) and Excess-NH_4 ($R^2 = 0.66$, see table A.16).

The polar graphs presented in figure 4.3 show that most of HOA and OOA masses originated from directions between 45° to 225° in respect to the CESAR tower. The highest concentrations of BBOA were observed in a plume coming from south-south-east.

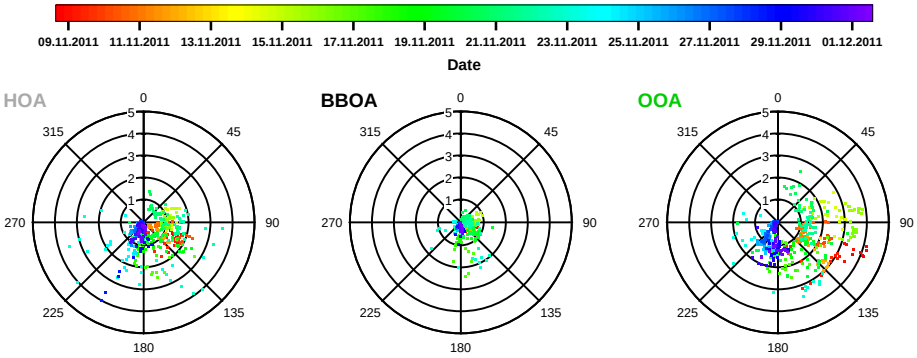

Figure 4.3.: Polar graphs of PMF factors from AMS data of November 2011, colour-coded by time. The radii represent the respective mass concentration in µg m^{-3}, the angles show the cardinal directions, with the tower in the centre of the plots.

4.1.2. PMF results for AMS data in 2012

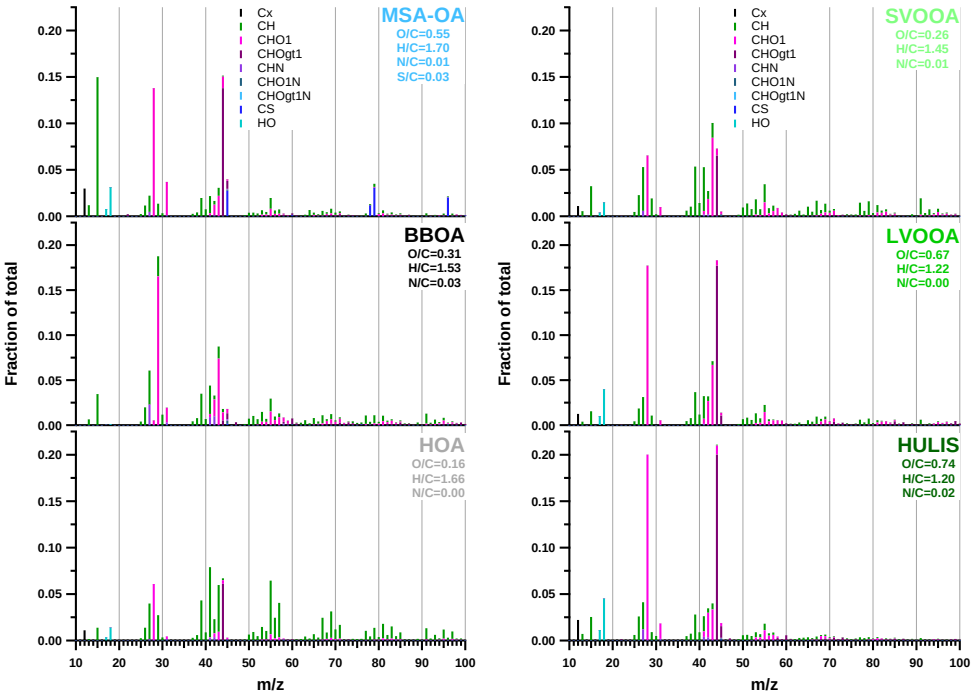

Figure 4.4.: Mass spectra of PMF factors from AMS data from May to July 2012. The HR mass peaks are stacked at each unit mass m/z and coloured by their chemical family (gt1 = greater than 1).

The PMF analysis of the AMS organic fraction in 2012 obtained six factors (FPEAK = 0). Their mass spectra and time series are displayed in figures 4.4 and 4.5, respectively. The latter contains also the time series of important external tracers. Besides the POA factors HOA and BBOA, three more oxidised organic profiles were found with increasing O/C ratios: a SVOOA, a LVOOA and a HULIS factor (see subsection 4.1.1). All SOA factors (SVOOA, LVOOA, HULIS) together contribute 77 % to the total organic fraction. The sixth factor was attributed to methanesulfonic acid (CH_3SO_3H, MSA), thus called MSA-OA. The average contributions and diurnal variations of each factor are displayed in figure 4.6. A summary of time series correlations is given in the appendix (table A.17).

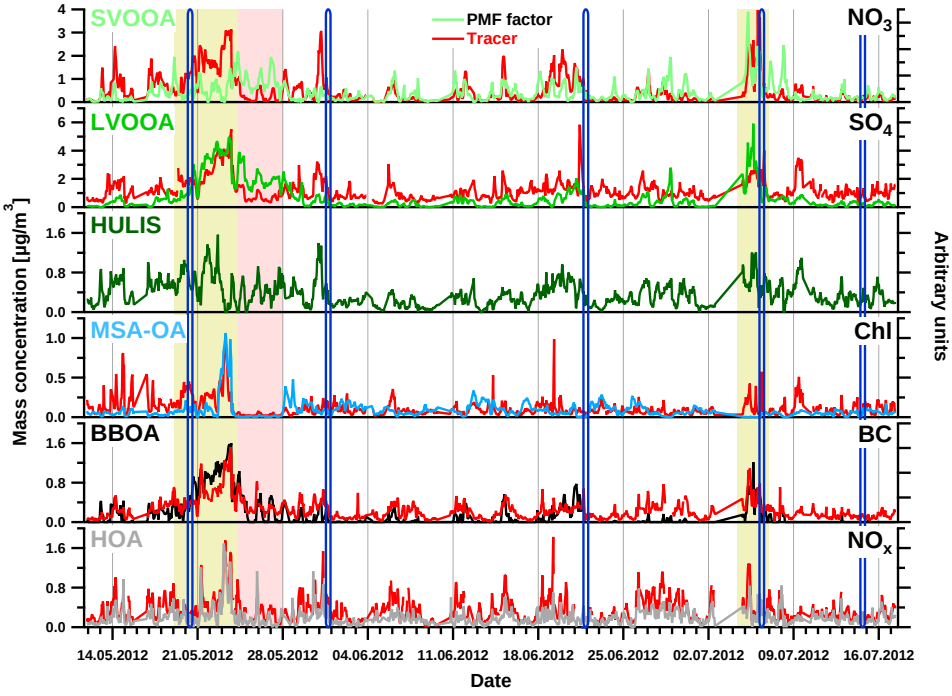

Figure 4.5.: Time series of PMF factors from AMS data and tracers between May and July 2012. High mass periods are indicated by light green backgrounds. The time period with easterly wind directions and high organic contribution is highlighted in red. The sharp blue rectangles indicate main precipitation events. The bottom of the tracer axes is set to zero.

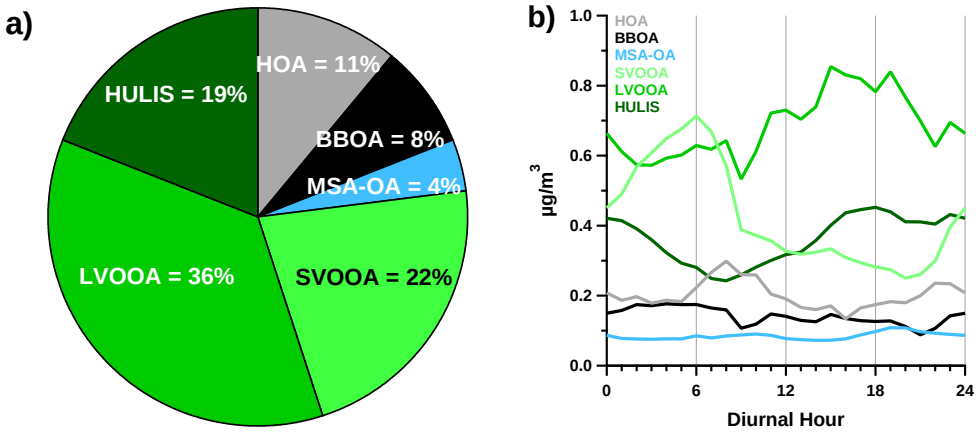

Figure 4.6.: a) Average contributions of AMS PMF factors and b) their diurnal variations (LT) in 2012

The HOA profile is very similar to the HOA factor found in 2011, including the O/C and H/C ratio. Again, a high CO_2^+ (and consequently a high CO^+) signal is seen, which is in contrast to HOA spectra commonly reported in the literature (*Docherty et al.*, 2011; *Mohr et al.*, 2012). The diurnal pattern shows a maximum in the morning, indicating a traffic source, which is emphasized by the good correlation to the time series of the traffic related tracer NO_x ($R^2 = 0.60$). The correlation coefficients (R^2) of the HOA times series with the other POA tracers BC and CO were 0.49 and 0.25, respectively.

The dominant CHO^+ ion of the BBOA MS is characteristic for this factor class. In contrast to 2011, a lower contribution of the CO_2^+ ion was observed, resulting in a lower O/C and a higher H/C ratio than 2011. Together with a higher contribution of the $C_2H_3O^+$ ion (m/z 43), a higher agreement with BBOA reference spectra from *Crippa et al.* (2014) (2011: $R^2 = 0.59$; 2012: $R^2 = 0.85$) was achieved. Better time series correlations of BC and CO were obtained with the BBOA factor ($R^2 = 0.61$ and 0.51, respectively) than with the HOA factor. Furthermore, a high agreement with the biomass burning tracer ions $C_2H_4O_2^+$ (m/z 60, $R^2 = 0.78$) and $C_3H_5O_2^+$ (m/z 73, $R^2 = 0.79$) was achieved. The night-time maximum of this factor matches also the expectations of a biomass burning source.

The mass spectrum of the MSA-OA factor was dominated by the CH_3^+ ion (m/z 15) and had very high contributions from organic sulphate fragments, such as CHS^+ (m/z 45), $CH_2SO_2^+$ (m/z 78), $CH_3SO_2^+$ (m/z 79), and $CH_4SO_3^+$ (m/z 96). This resulted in a very high S/C ratio of 0.03 of this profile, whereas the other factors had S/C ratios of less than 0.001. Note that the determination of the S/C ratio was not investigated and verified by laboratory experiments yet. A potential correction factor for the calculation of the

S/C ratio from AMS data could not be applied here (see subsection 2.1.1.4). Excluding the high signals derived from CO_2^+ and CO^+, the MS of this factor has high qualitative similarity to reference spectra of MSA, measured with an AMS in laboratory experiments (*Phinney et al.* (2006); *Zorn et al.* (2008); MS data not available). As seen in figure 4.5, the MSA-OA factor in the 2012 campaign showed only few high mass concentration events, e.g. from 23.05. to 24.05.2012. That is why this factor contributes little (4 %) to total organics and shows no clear diurnal pattern over the whole campaign. This event is also accompanied by a high mass peak of particulate chloride. Further details are given in chapter 4.1.5.

The SOA factors SVOOA and LVOOA showed mass spectra similar to those observed in a number of AMS campaigns (*Crippa et al.*, 2013b; *Mohr et al.*, 2012; *Docherty et al.*, 2011), including campaigns at the CESAR tower in Cabauw (*Mensah*, 2011; *Paglione et al.*, 2014; *Crippa et al.*, 2014). Achieved MS correlation coefficients (R^2) were 0.86 and 0.82 for SVOOA and 0.94 and 0.95 for LVOOA, compared to *Mensah* (2011) and *Crippa et al.* (2014), respectively.

The SVOOA factor showed the lowest O/C ratio and higher contributions of CH family ions than the other SOA factors. It is further characterized by a maximum during the night-time/morning period and a daytime minimum like the semi-volatile NH_4NO_3 (see figure 3.17). The diurnal pattern of the LVOOA factor is mainly anti-correlated to SVOOA, indicating its photo-oxidative formation during the day similar to the low-volatile particulate SO_4. Though, the corresponding mathematical correlations were rather low ($R^2_{SVOOA-NO_3} = 0.17$; $R^2_{LVOOA-SO_4} = 0.36$). As observed in 2011, Excess-NH_4 correlated well with the LVOOA factor, while $OrgNO_3$ had the best agreement with the SVOOA factor time series.

The so called HULIS factor showed the highest O/C ratio of all factors, mainly resulting from a higher domination of the CO_2^+ ion than e.g. the LVOOA factor. The HULIS factor class was first observed by *Mensah* (2011) in previous AMS campaigns at the CESAR tower in May 2008 and March 2009. These findings were confirmed for 2008 by a re-analysis using ME-2, published by *Crippa et al.* (2014). The identification and characterization of this factor class was done by comparison with data from an ion-exchange chromatographic method for direct quantification of humic-like substances (HULIS) and from water-soluble organic carbon (WSOC) analysed offline on a set of filters collected in parallel (*Paglione et al.*, 2014). Such measurements were not done in the campaigns reported here. A high correlation was found between the HULIS profile observed in 2012 and the reference HULIS spectra ($R^2 = 0.91$ and 0.88, compared to *Mensah* (2011) and *Crippa et al.* (2014), respectively). Similar to the results reported there, no significant time series correlation was found for the HULIS factor in 2012. However, it showed a clear

minimum in the morning hours and maximum during the day, which is in contrast to the literature, where no clear diurnal variation was observed. The correlation of the sum of the secondary inorganic species NO_3 and SO_4 with the sum of the SVOOA, LVOOA, and HULIS time series gives a coefficient of $R^2 = 0.49$ which is slightly higher than with the sum of SVOOA and LVOOA only ($R^2 = 0.44$). This might confirm the SOA character of the HULIS factor.

Figure 4.7 displays the polar graphs of each individual PMF factor. No preferential direction was observed except for the MSA-OA factor. Its plume from 22.05. to 23.05.2012 mentioned above originated from directions between 210° to 315°.

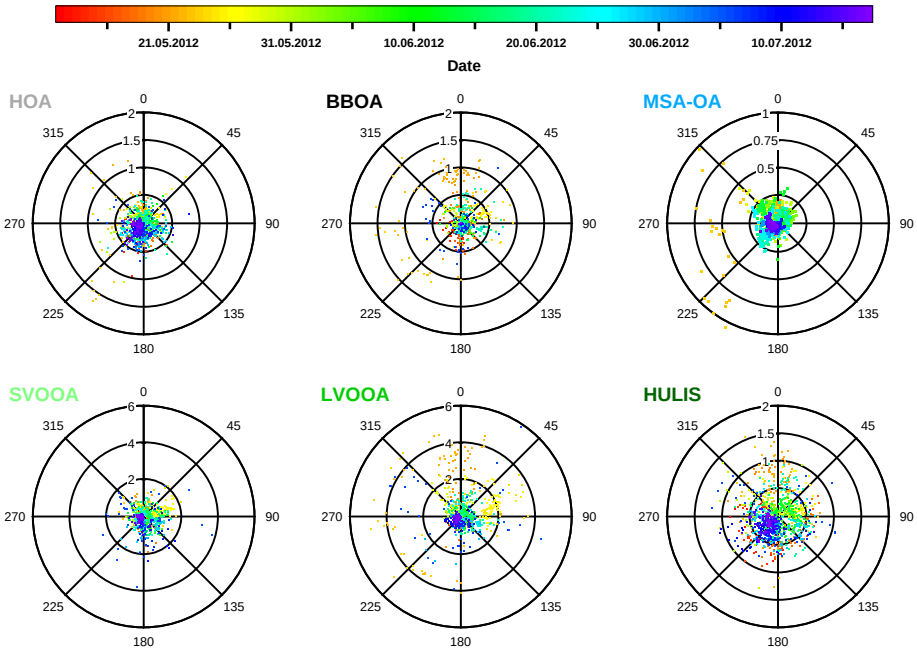

Figure 4.7.: Polar graphs of PMF factors from AMS data in 2012, colour-coded by time. The radii represent the respective mass concentration in µg m^{-3}, the angles show the cardinal directions, with the tower in the centre of the plots. Attention should be paid on the different radius scales.

4.1.3. PMF results for TD-PTR-MS data

This section presents the PMF results from TD-PTR-MS data from the campaigns in 2011 and 2012, using the data matrices summed over all thermal-desorption temperatures (100°C to 300°C).

Although the measured mass concentrations of organic aerosol compounds sampled by both PTR aerosol inlets (A and B) correlated well (see figures A.7 and A.14), slight differences between concentrations measured with both inlets are not avoidable. For example, these differences are responsible for the scattering of the factor time series of the 3-factor PMF solution using the data and error matrices (see figure A.27), merged from both PTR data sets of the PTR aerosol inlets (A and B). Therefore, only PMF data derived from inlet A is considered here for both data sets. The high similarity of the profiles between solutions obtained from inlet A data and merged data, and also to the corresponding PMF solution from data of inlet B (not shown), legitimate this approach.

As mentioned, not every ion measured by the PTR-MS could be attributed to a chemical formula. The mass fraction of all ions not explained by the used mass library was between 0.4 % to 5 % only. Thus the uncertainty of the elemental analysis for the PTR PMF factors is fairly low. The differences between all PTR factors by means of O/C and H/C ratios were smaller than between the AMS factors. On the other hand, the N/C ratios of the PTR factors were much higher (0.02 to 0.15) than those from the AMS (0.006 to 0.012). This was expected, since the TD-PTR-MS is known to be more sensitive for N-containing organic compounds than the AMS (*Holzinger et al.*, 2013).

For TD-PTR-MS data no PMF results were published so far. That means, that reference factor profiles deriving from PTR organic aerosol data are not available at this point to compare with. This limits a precise assignment of a profile to a certain source. *Holzinger et al.* (2013) compared time series of individual ions measured by the TD-PTR-MS with PMF factors obtained by a collocated AMS. However, it is not assured that PTR ions attributed to factor classes by *Holzinger et al.* (2013) can be taken as reference fragments to confirm profiles obtained by a PMF analysis on TD-PTR-MS data itself. Yet a comparison of single ions or PMF factors obtained from a collocated AMS is possible.

In a first approach, the number of factors observable in TD-PTR-MS data was assumed to be the same as for the collocated AMS, using an FPEAK = 0 for both campaigns. In this section therefore solutions for PTR PMF with three and six factors for 2011 and 2012, respectively, are discussed. The use of the AMS PMF results as reference solution for PTR data is reasonable, since the criteria for finding proper PMF solutions are well defined in case of AMS data due to the high level of experience and studies available in the literature.

4.1.3.1. Campaign 2011

Three factors were found by factor analysis of AMS data in 2011. The profiles of the 3-factor solution of TD-PTR-MS data of inlet A are displayed in figure 4.8. Although the PTR-MS detected m/z up to 1143, only m/z $\leq$ 300 are shown, as contributions of larger ions are negligible. Respective factor time series are presented in figure 4.9.

Factor 1 (F1) showed the highest O/C ratio (0.45) with high contributions from ions of the CHOgt1 family, like protonated acetic acid ($C_2H_4O_2H^+$, m/z 61), $C_5H_4O_2H^+$ (m/z 97), $C_4H_2O_3H^+$ (m/z 99), and $C_8H_4O_3H^+$ (m/z 149). Other prominent ions are protonated formaldehyde (CH_2OH^+; m/z 31), methanol (CH_4OH^+, m/z 33), and $CHONH^+$ (m/z 44).

The highest signal of the F2 MS originated from $C_8H_4O_3H^+$ (m/z 149), followed by protonated acetic acid (m/z 61) and $CHONH^+$ (m/z 44). $C_5H_4O_2H^+$ (m/z 97) and $C_4H_2O_3H^+$ (m/z 99) had lower contributions to F2 than to F1, as well as the CHO family ions protonated formaldehyde (CH_2OH^+; m/z 31) and methanol (CH_4OH^+, m/z 33).

The signal of the third factor (F3) was broader distributed over the m/z than the other PTR PMF factors, dominated by $C_5H_4O_2H^+$ (m/z 97). In addition, $C_4H_4O_2H^+$ (m/z 85) showed high signal, which was not seen prominently in the MS of F1 and F2. The F3 MS showed also higher contributions of ions with m/z $>$ 200, where ions of the CHOgt1N family dominate. The mass fraction of these ions to the total F3 MS was 22 % (F1: 3.1 %, F2: 3.5 %). *Holzinger et al.* (2013) showed, that high mass fragments showed the highest agreement with AMS POA factors, whereas lower m/z were rather attributed to LVOOA factors, like in case of F1 and F2 described above. That means, that the occurrence of high mass fragments in the F3 MS indicates that this factor can be rather attributed to a primary organic aerosol. The relatively low O/C and N/C ratios emphasize this assumption.

The mass contributions of each factor to total organic mass and the diurnal variations are presented in figure 4.10. Note, that the TD-PTR-MS data ranged from 02.11. to 01.12.2011. That means the it started to measure 6 days earlier than of the AMS, which started on 08.11.2011. Limiting the PTR data to match the AMS acquisition time did not change the PMF results and the correlations to AMS and supplementary data significantly.

The obtained correlation coefficients (R^2) of the comparison between AMS and PTR-MS factor time series are summarized in table 4.1, the corresponding correlations with most important tracers are given in the appendix (table A.18).

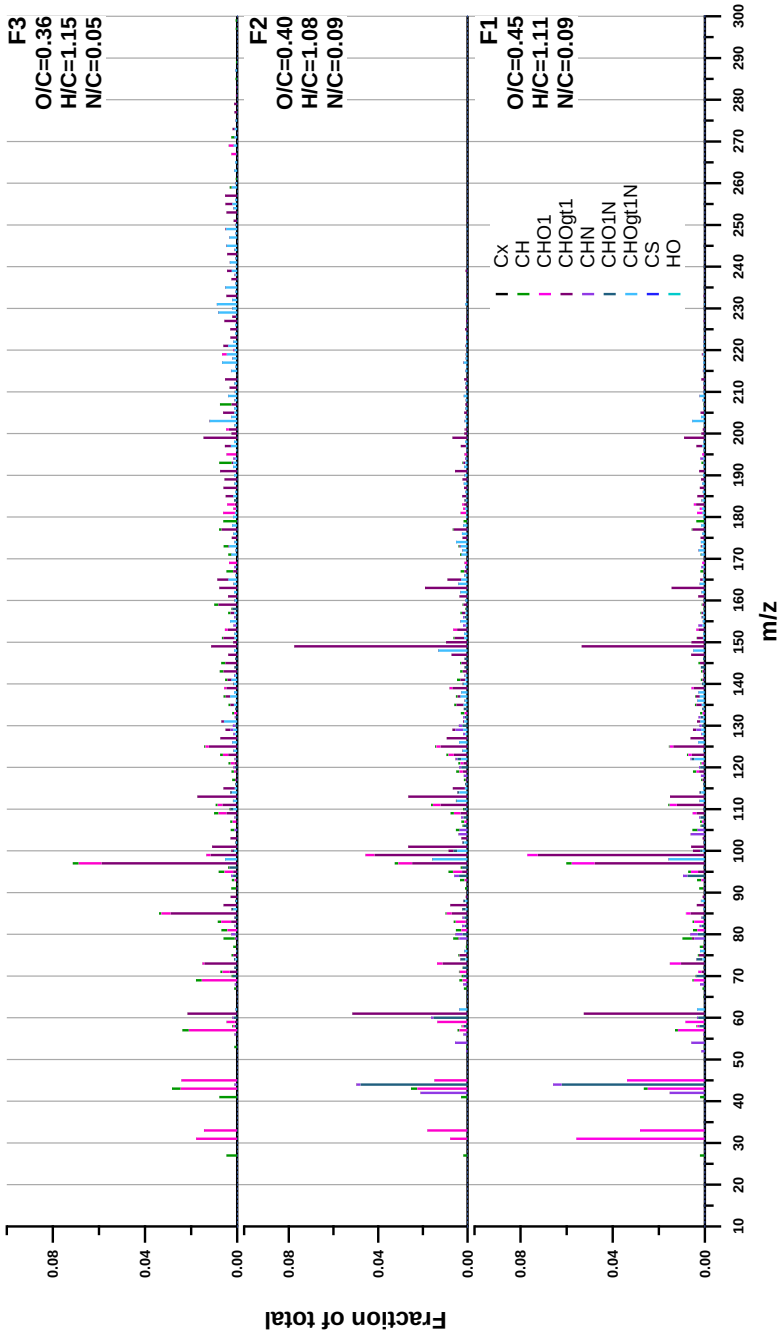

Figure 4.8.: Mass spectra of the 3-factor PMF solution from TD-PTR-MS data (inlet A) in November 2011. The HR mass peaks are stacked at each unit mass m/z and coloured by their chemical family (gt1 = greater than 1).

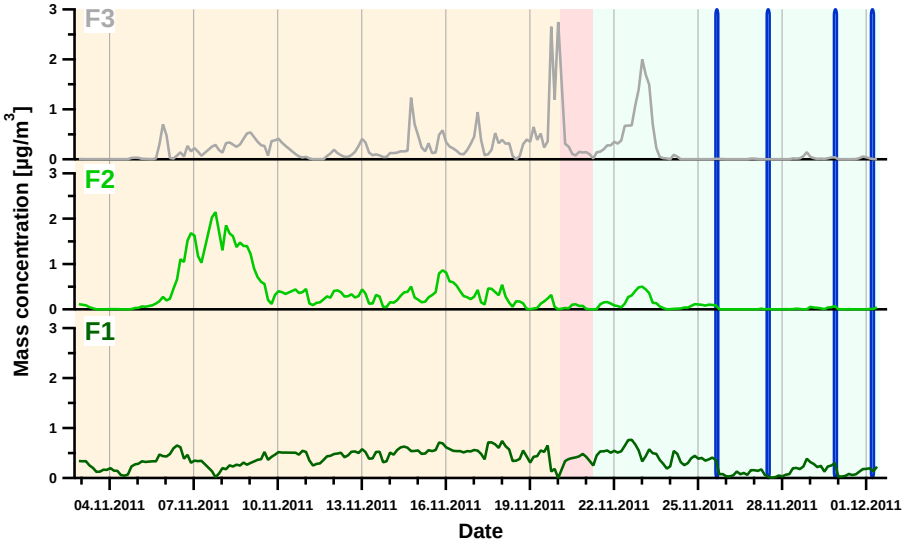

Figure 4.9.: Time series of the 3-factor PMF solution from TD-PTR-MS data (inlet A) in November 2011. The time period with southerly and easterly wind directions is highlighted in beige. The time of calm northerly winds has a red colour. The period with southerly and westerly wind directions is illustrated in green. The sharp blue rectangles represent precipitation events.

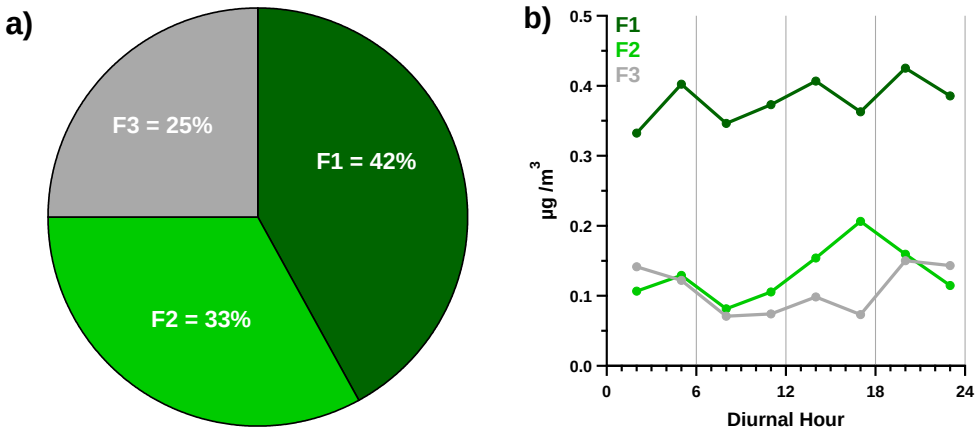

Figure 4.10.: a) Average contributions of TD-PTR-MS PMF factors and b) their diurnal variations (LT) in 2011

Table 4.1.: Correlation coefficients (R^2) of the comparison between AMS and PTR-MS factor time series in 2011

PTR-MS factors	F1	F2	F3
HOA_{AMS}	0.28	0.17	0.21
$BBOA_{AMS}$	0.24	0.17	0.38
OOA_{AMS}	0.35	0.63	0.22

The F1 time series shows a minimum between 07.11. and 09.11. which is in contrast to factor 2 (F2). Another minimum was seen on the 20.11.2011, which is anti-correlated to the time series of factor 3 (F3). The fact that F1 showed no clear diurnal pattern would indicate regionally well mixed aerosol of long atmospheric lifetime. Additionally, F1 showed the highest agreement with the OOA_{AMS} factor, although the achieved coefficient was rather low ($R^2 = 0.35$). Comparing to the most important tracers, F1 correlated best with $OrgNO_3$ ($R^2 = 0.40$).

Factor 2 showed a better correlation with the OOA_{AMS} factor ($R^2 = 0.63$). Its diurnal pattern showed a daytime maximum, which is an indicator for an oxidised LVOOA factor. Likewise the OOA_{AMS} factor, the R^2 value to the AMS SO_4 time series was about 0.4. In contrast to F1, no significant F2 mass concentration was detected after the precipitation event on 25.11.2011.

The diurnal pattern of factor 3 is similar to that of the AMS BBOA. F3 showed also the highest correlation to this AMS factor ($R^2 = 0.38$). The correlation coefficients with BC, gaseous NO_x and CO were 0.37, 0.52, and 0.48, respectively. These are the highest values obtained between all PTR factors and these compounds, which are generally attributed to POA.

Although similarities were found between PTR PMF factors and AMS factors, as well as with a small number of tracer time series, an unambiguous assignment of the PTR PMF factors to aerosol sources could not be achieved. Constraining the factor number corresponding to the number of AMS PMF factors is not based on experience, but on the assumption, that both PMF analyses identified the same number of factors, but with mass spectra deriving from different ionization techniques. This may oversimplify the situation, since the sensitivity of both instruments may well differ for individual aerosol compounds and thus for PMF factor classes. A first exploration of solutions including a higher number of factors up to 15 did not result in an unambiguous attribution of PTR profiles to factor classes. In a next step, factor analysis should be done with PTR data matrices separated by the thermal desorption temperature to distinguish PMF factors by their volatility. This was not part of this work. Nevertheless, PTR profiles observed here can be used as a first reference to compare with other PMF profiles obtained with the TD-PTR-MS.

4.1.3.2. Campaign 2012

Figure 4.11 shows the profiles derived from the 6-factor PMF solution of TD-PTR-MS data in 2012. Due to the degraded MCP inside the TD-PTR-MS in 2012 (see subsection 2.3.1), no significant mass fractions of PMF factors were observed from ions with m/z higher than 200.

The six highest mass peaks within the MS of the first factor (F1) belonged to the CHOgt1 family, dominated by $C_5H_4O_2H^+$ (m/z 97) and $C_4H_2O_3H^+$ (m/z 99). Together, these ions contribute 38.3 % to the total signal of F1. This explains its relatively high O/C and low H/C ratio.

The second factor (F2) is characterized by the highest observed N/C ratio (0.15). That means, that the MS has high contributions from organic N-containing fragments. The most dominant ions are $CHONH^+$ (m/z 44), protonated acetic acid ($C_2H_4O_2H^+$, m/z 61), and $C_4H_2O_3H^+$ (m/z 99). Additionally, a high signal of protonated acetonitril ($C_2H_3NH^+$, m/z 42) was seen. The F2 profile showed qualitative agreement with the F2 factor found in the PMF results of PTR data in 2011.

The mass spectrum of F3 is dominated by $C_4H_2O_3H^+$ (m/z 99), followed by the signal of protonated acetic acid ($C_2H_4O_2H^+$, m/z 61), and protonated acetaldehyde ($C_2H_4OH^+$, m/z 45). Qualitative similarity was observed to the spectrum of factor F1 in 2011.

F4 showed the highest O/C ratio and second highest N/C ratio. Its MS is in parts in agreement with the F3 factor from PTR data in 2011. On exception is that for F4 the contributions from m/z higher than 150 were rather low. This is in contrast to all other PTR PMF factors found in 2012. The F4 factor had the highest contribution from protonated acetaldehyde ($C_2H_4OH^+$, m/z 45), in addition to protonated formaldehyde (CH_2OH^+; m/z 31) and the CHOgt1 ions $C_2H_4O_2H^+$ (m/z 61), $C_5H_4O_2H^+$ (m/z 97), and $C_4H_2O_3H^+$ (m/z 99).

The mass spectra of F5 and F6 were dominated by $C_2H_2OH^+$(m/z 43), $C_2H_4OH^+$ (protonated acetaldehyde, m/z 45), and $C_3H_6OH^+$ (protonated acetone, m/z 61), explaining their low O/C (0.33 and 0.26, respectively) and high H/C ratios (both 1.33). Both N/C ratios (0.02 and 0.04, respectively) were also low comparing to other factors. In addition, the highest mass contribution of the F5 MS was seen from $C_2H_4O_2H^+$ (protonated acetic acid, m/z 61). The mass contributions of each factor to the total organic mass and the diurnal variations are presented in figure 4.10.

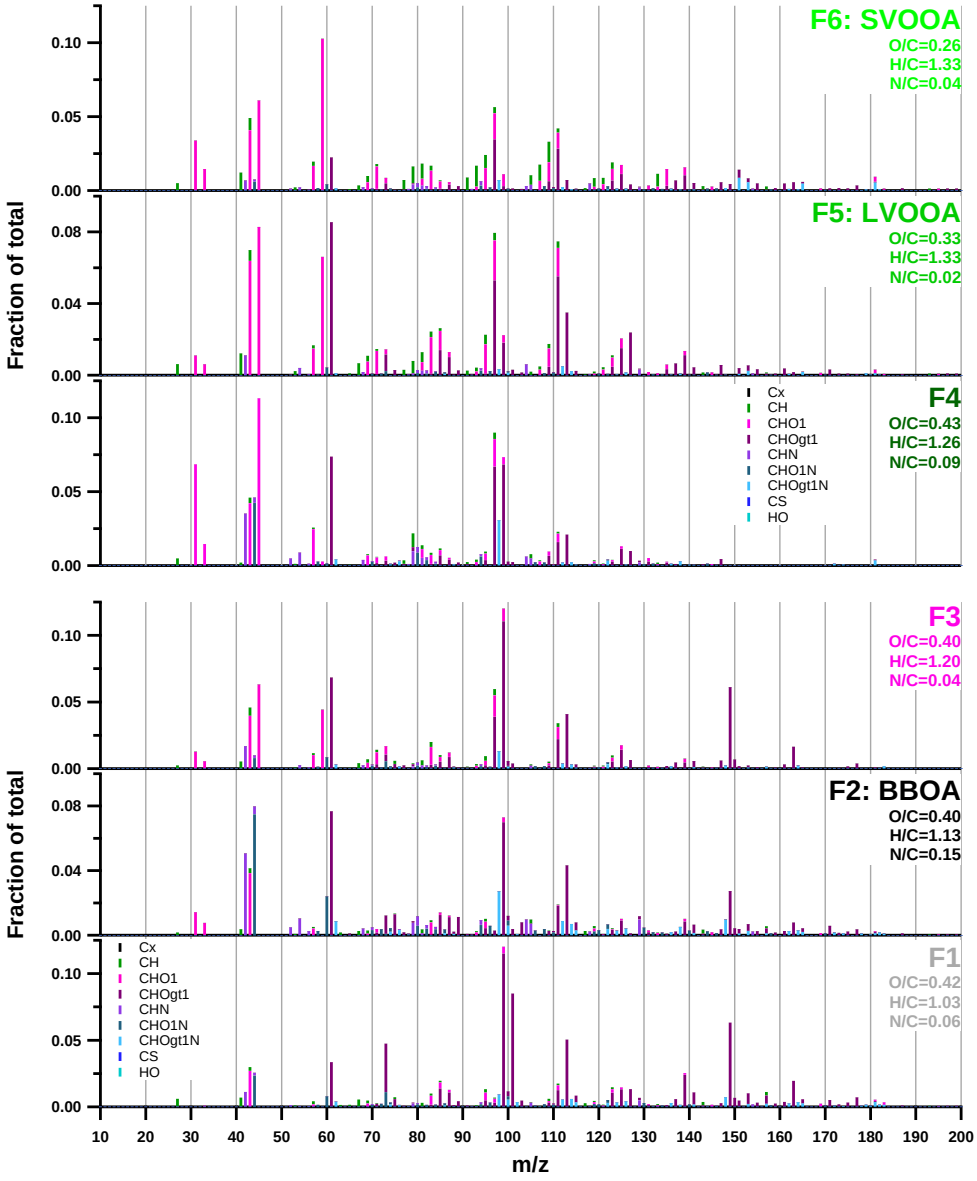

Figure 4.11.: Mass spectra of PMF factors from TD-PTR-MS data from May to July 2012. The HR mass peaks are stacked at each unit mass m/z and coloured by their chemical family (gt1 = greater than 1). The explanation for the denotation is given in the text.

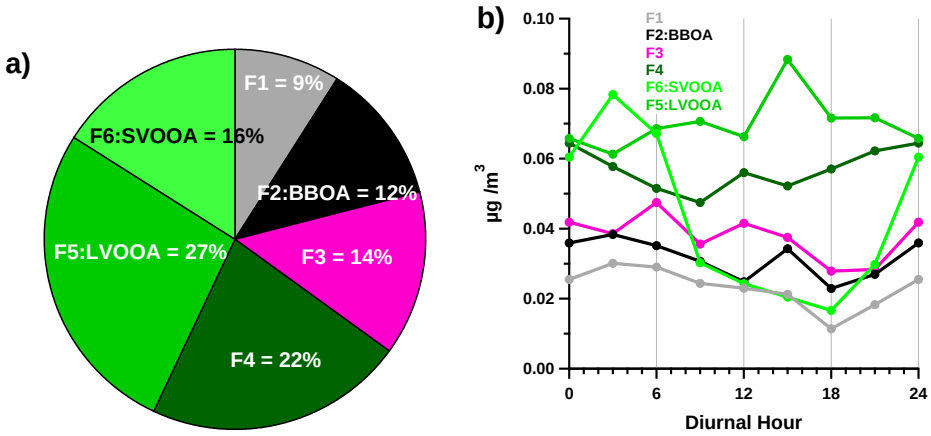

Figure 4.12.: A) Average contributions of TD-PTR-MS PMF factors and b) their diurnal variations (LT) in 2012. The explanation for the denotation is given in the text.

As can be seen in table 4.2, the time series of F2 correlated best with the $BBOA_{AMS}$ (R^2 = 0.82) and the $LVOOA_{AMS}$ factor (R^2 = 0.61) from the AMS PMF solution of 2012 (see subsection 4.1.2). The time series of each PTR factor is presented in figure 4.13, together with a number of correlating AMS factors. The good agreement with the time series of AMS tracer ions $C_2H_4O_2^+$ (R^2 = 0.63) and $C_3H_5O_2^+$ (R^2 = 0.64) and a maximum during the night within its diurnal variations leads to the conclusion, that F2 can be attributed to biomass burning sources. The correlation coefficients (R^2) to the other POA tracers BC and CO were 0.57 and 0.51, respectively. A summary of correlations between PTR PMF factors and tracer time series is given in table A.19.

F1 had similar correlations to AMS factors and most tracers compared to F2. Also its diurnal pattern agreed with the pattern of F2. The time series correlation coefficient (R^2 = 0.84) between F1 and F2 might give evidence, that both factors represent a splitting of one parent factor.

The highest mass concentration of F3 was observed during the high aerosol mass period on 05.06. and 06.06.2011. Its time series correlated best with $SVOOA_{AMS}$, though the coefficient was rather low (R^2 = 0.39). In addition, $OrgNO_3$, determined from AMS data correlated better with F3 (R^2 = 0.45) than with any other PTR factor in 2012. Except for a small minimum in the afternoon, the diurnal pattern of F3 showed no clear trend.

F4 showed only little agreement with AMS factors and external data. The highest by far was the correlation with the $HULIS_{AMS}$ factor (R^2 = 0.36). Both factors show no distintive diurnal pattern and only low correlation with external data. F4 represents the most oxidised PTR profile (O/C = 0.43) in 2012, likewise the $HULIS_{AMS}$ factor during the 2012 AMS campaign.

Factor 5 is attributed LVOOA, since it showed the highest correlation with the $LVOOA_{AMS}$ factor ($R^2 = 0.82$) and less with $BBOA_{AMS}$ ($R^2 = 0.57$). The diurnal maximum of F5 was observed during the day, confirming the assignment to a low-volatile factor. On the other hand, mearly no agreement was seen between this factor and SO_4 ($R^2 = 0.20$), as it would be expected for a LVOOA factor. Excess-NH_4 had the best correlation with this factor ($R^2 = 0.52$), similar to the $LVOOA_{AMS}$ factor (see section 4.4).

The sixth PTR PMF profile (F6) had almost exclusively the highest agreement with the AMS SVOOA factor ($R^2 = 0.67$). The observed strong maximum during the night and morning hours is a key characteristic for a semi-volatile factor, although the highest value was found at 3 am, whereas the highest mass concentration peak of the AMS counterpart was observed 3 hours later (see figure 3.4b).

No similarity was found between the AMS MSA-OA factor and a PTR PMF factor. This is most likely a result of the fact, that the MSA-OA factor showed the highest mass concentrations during a period (23.05 to 24.05.2012), which is not completely covered by the TD-PTR-MS data acquisition.

In summary, three of six factors derived from PMF analysis of TD-PTR-MS data from 2012 could be attributed to certain factor classes: BBOA, LVOOA and SVOOA, explaining together 55 % to PTR total organics. Comparing the absolute mass concentration of these three factors with the respective AMS factors, the TD-PTR-MS detects 22%, 12%, and 10% of the BBOA, LVOOA, and SVOOA respectively. This means, that the sensitivity of the TD-PTR-MS for BBOA is higher than for other factor classes and the total organics (14 % with respect to AMS total organic mass).

However, large uncertainties remain because a number of PTR factors correlate similarly with the same AMS factors. This may indicate that an unique attribution is not possible at this point. Further investigations need to be done by exploring a different number of PTR factors and by applying factor analysis on PTR data matrices separated by the thermal desorption temperatures. Furthermore, laboratory experiments should be performed with the TD-PTR-MS to obtain reference mass spectra (e.g. from pure MSA particles). These PTR-MS spectra can be used to identify and assign observed PTR PMF factors to aerosol sources.

Table 4.2.: Correlation coefficients (R^2) of the comparison between AMS and PTR-MS factor time series in 2012. High values are colored.

PTR-MS factors	F1	F2	F3	F4	F5	F6
HOA_{AMS}	0.25	0.24	0.09	0.04	0.08	0.07
$BBOA_{AMS}$	**0.69**	**0.82**	0.14	0.04	**0.57**	0.34
$MSA\text{-}OA_{AMS}$	0.15	0.15	0.03	0.00	0.04	0.00
$SVOOA_{AMS}$	0.10	0.10	**0.39**	0.01	0.16	**0.67**
$LVOOA_{AMS}$	**0.57**	**0.61**	0.21	0.04	**0.82**	0.33
$HULIS_{AMS}$	0.14	0.20	0.15	**0.36**	0.16	0.01

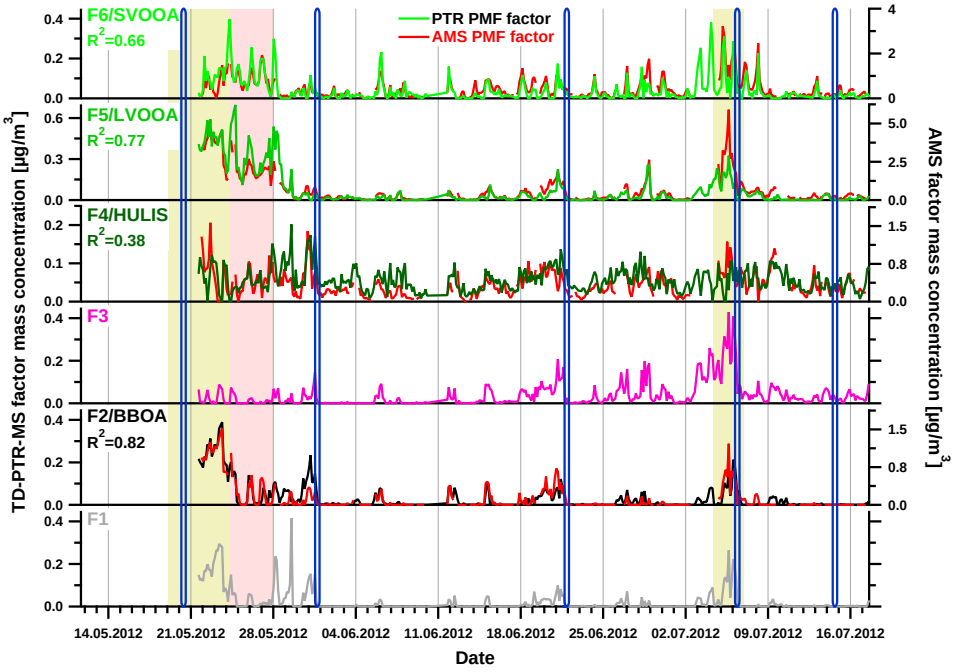

Figure 4.13.: Comparison of time series of PMF factors from PTR and AMS data between May and July 2012. High mass periods are indicated by light green background. The time period with easterly wind directions and high organic contribution is highlighted in red. The sharp blue rectangles indicate main precipitation events.

4.1.4. Factor analysis of ACSM data

The ACSM data set was divided into four seasons prior to the factor analysis of the organic fraction using PMF/ME-2:

(i) July-August-September 2012: Summer 2012

(ii) October-November-December 2012: Autumn 2012

(iii) January-February-March 2013: Winter 2013

(iv) April-May-beginning of June 2013: Spring 2013

This segmentation differs from „classical“ seasons (e.g. June-July-August for Summer terms and so forth), since ACSM data acquisition started in July 2012. Therefore, it was not feasible to combine the „classical“ Summer months July and August from 2012 with June 2013 as one season. Furthermore, the periods were chosen corresponding to the appearance of gaps in the ACSM data set. As PMF/ME-2 is providing factors with periodically occurring sources, long data gaps should be avoided for the application of factor analysis.

Table 4.3 gives an overview about the observed PMF factors for every season. Two POA factors (HOA, BBOA) and two SOA factors (OOA, HULIS) were found over the whole year of data acquisition, except that BBOA was not found significantly in Summer 2012. The SOA factors showed always higher contribution (54 % - 84 %) to total organics compared to POA (16 % - 46 %, see figure 4.14). The POA profiles were constrained within ME-2 using the HOA and BBOA mass spectra found by ME-2 analysis by *Crippa et al.* (2014) at the CESAR tower in Cabauw in March 2009. For the HOA profile, a constant a-value of 0.1 was found to be most suitable for every season. If observed, the BBOA a-value was set to either 0.2 (Autumn 2012) or 0.3 (Winter and Spring 2013).

Table 4.3.: Overview of ACSM PMF factors observed for each season. X means this factor was found. For the constrained profiles HOA and BBOA, the applied a-value is written in brackets.

Season	HOA	BBOA	OOA	HULIS
Summer 2012 (11.07. - 30.09.2012)	X (a = 0.1)	-	X	X
Autumn 2012 (01.10. - 29.12.2012)	X (a = 0.1)	X (a = 0.2)	X	X
Winter 2013 (08.01. - 27.03.2013)	X (a = 0.1)	X (a = 0.3)	X	X
Spring 2013 (05.04. - 03.06.2013)	X (a = 0.1)	X (a = 0.3)	X	X

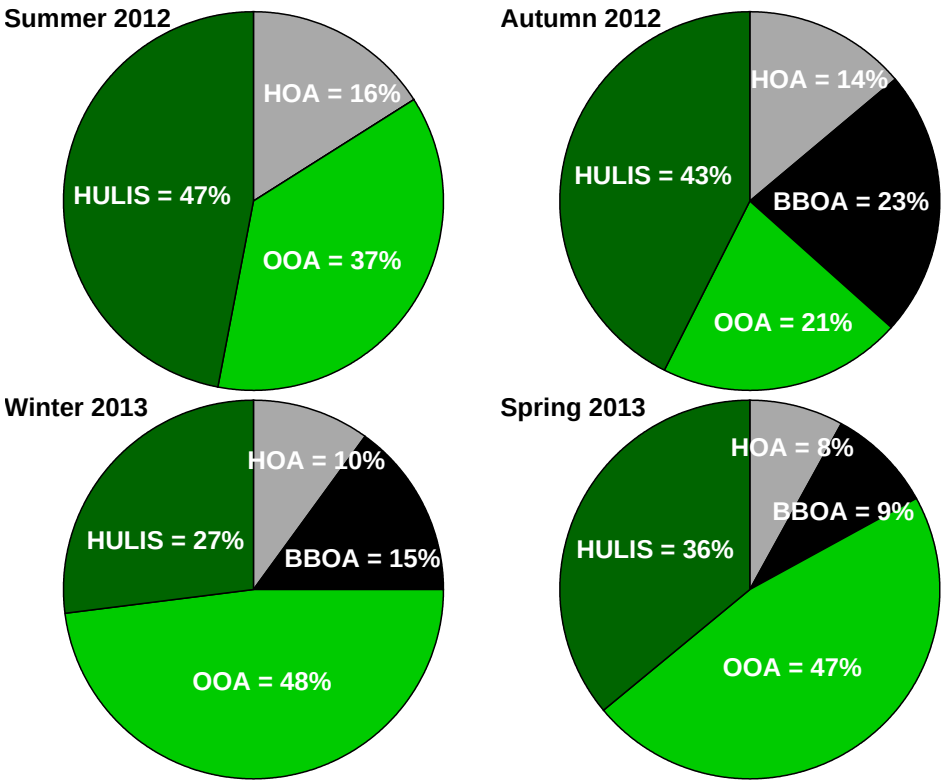

Figure 4.14.: Average contributions of ACSM PMF factors for each observed season

Figure 4.15 shows factor profiles found in each season. As can be seen, the mass spectra of all factor classes vary relatively little between all seasons. The reference profiles for HOA and BBOA which were used as initial constrains are indicated by red bars. In general elemental analysis cannot be performed with UMR spectra. Instead of elemental ratios, the so called f44 and f43 values can be determined. These are the mass fractions of m/z 44 and m/z 43 to the total respective MS. Since m/z 44 is dominated by the CO_2^+ ion and m/z 43 has the highest contributions of $C_3H_7^+$ and $C_2H_3O^+$ ions, these ratios can be used as indicator for the magnitude of oxygen and hydrogen content of the particular profile, comparing to its carbon fraction. In addition, the corresponding f60 value is used as an indicator for BBOA influence, as m/z 60 is largely dominated by the BBOA tracer ion $C_2H_4O_2^+$ (see subsection 4.1.1). *Aiken et al.* (2008) found a correlation between the f44 value and the O/C ratio, using high resolution AMS data from ambient and chamber studies. This justifies the use of f44 as a surrogate for the oxygen content of OA in data sets in which only UMR AMS data are available. Table A.21 in the appendix shows the

estimated O/C ratios of ACSM PMF factors for each season using the equation given by *Aiken et al.* (2008).

The HOA profile varies less than the BBOA factor over the entire year by means of its MS pattern, explaining its lower a-value. As expected for POA, the HOA MS shows a low f44 (0.01 - 0.02) and a high f43 (0.10 - 0.12) comparing to the other factor classes. Although the HOA profile was constrained relatively strict (a-value = 0.1), the estimated O/C ratios of 0.12 - 0.16 are in the range of the corresponding values found by the AMS PMF factors in 2011 and 2012 (0.15 and 0.16, respectively).

The BBOA factors showed a very high m/z 29 signal (10 % - 11 % contribution), using almost the whole freedom of the ME-2 model given by the a-values. This is a typical characteristic for a BBOA factor for this measurement site as also seen within the AMS campaigns (12 % - 17 % contribution). The fraction of m/z 60 in Autumn 2012 (3.7 %) and Winter 2013 (3.2 %) is higher than from the BBOA reference spectrum (2.5 %). The corresponding value in Spring 2013 was 2.4 %. The calculated O/C ratios (0.23 - 0.31) are lower than of the AMS BBOA factors for the previous campaigns in 2011 and 2012 (0.46 and 0.31, respectively).

The OOA profile was also observed in PMF results of the AMS campaign in November 2011, showing a MS pattern as expected for a LVOOA factor. It is dominated by m/z 44, followed by m/z 43 and in most seasons m/z 29, but no significant contribution from m/z higher than 50 (approximately 1 % - 2 %). The estimated O/C ratio varied between 0.81 to 0.96, which is higher than every O/C ratio of a PMF factor found by the AMS. The correlation coefficients (R^2) with the OOA and LVOOA MS given by *Ng et al.* (2011a) are 0.94 and 0.97, respectively. Similar agreement was found compared to the LVOOA factor observed by *Mensah* (2011) and *Crippa et al.* (2014) (R^2 = 0.97 and 0.94, respectively) at the CESAR tower in May 2008. The comparison with the OOA profile found in 2011 resulted in R^2 = 0.94.

The HULIS factor class is described in subsection 4.1.2. HULIS was not only observed in 2012 at the CESAR tower, but also by *Mensah* (2011) and *Crippa et al.* (2014) in May 2008. The HULIS profile found here shows therefore high agreement to spectra from the literature (R^2 = 0.99 for both references), as well as with the findings in 2012 (R^2 = 0.94). It is characterized by a very high f44, increasing from Summer 2012 to Spring 2013 from 0.23 to 0.35, and very low f43 and f60 values, confirming its high oxidised state. In addition, very high O/C ratios (0.96 - 1.42) were obtained by the conversion of the f44 values according to *Aiken et al.* (2008).

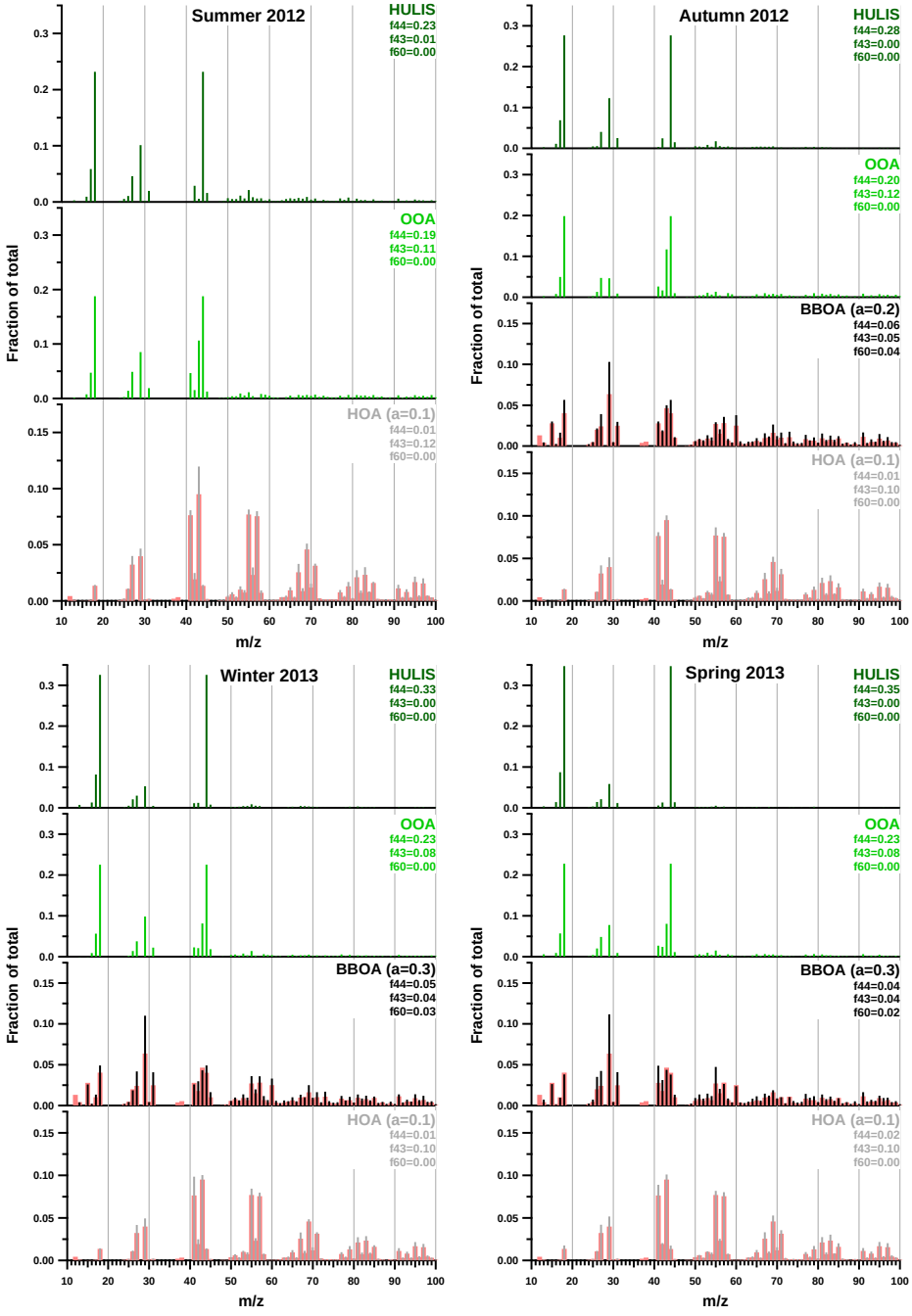

Figure 4.15.: Mass spectra of ACSM PMF factors for each season between 2012 and 2013. For the constrained profiles HOA and BBOA, the applied a-value is written in brackets. Corresponding reference spectra are shown by red bars. F44, f43, and f60 are the mass fractions of m/z 44, m/z 43, and m/z 60 of the particular MS, respectively. Note that the y-axis scales of the POA are zoomed by a factor of 2 comparing to SOA profiles.

In figure 4.16, the time series of PMF factor classes found for all seasons are merged in one graph. Note that in Summer 2012, no significant BBOA influence was seen. Thus, no BBOA time series exists for this season. For all other factors the time series are continuous on 01.10.2012, i.e. analysis of separate data files leads to a consistent result in terms of both factor profiles and concentrations. The diurnal patterns of each factor separated by the seasons are shown in figure 4.17. A summary of time series correlations for the whole year is given in the appendix (table A.20).

The HOA contribution to total organic mass decreased from Summer 2012 to Spring 2013 from 16 % to 8 %. It reached a campaign average of 14 %. Relatively high mass concentrations were seen during two of the highlighted high mass periods (18.08. to 22.08.2012, and 16.01. to 27.01.2013), in addition to two distinctive time periods in the nights of 19.05. and 26.05.2013, where concentrations reached up to 8 µg m^{-3} (average over the whole year: 0.33 µg m^{-3}). The maximum on 19.05. was accompanied by very high concentration peaks of both, particulate Chl and gaseous CO. All HOA diurnal patterns show a maximum at 7 and 11 am (LT) and a slight increase in the evening. In winter 2013, these maxima were less distinctive comparing to the other seasons. HOA showed the highest agreements with the POA tracers BC, NO_x and CO (R^2 = 0.38, 0.47, and 0.47, respectively) over the entire campaign.

The BBOA factor showed its highest contributions in the colder Autumn and Winter seasons. This and the diurnal maximum during the evenings and nights match the expectations for a factor linked with domestic heating activities. The mass fraction of BBOA was higher in Autumn (23 %) than in Winter (15 %), although the ambient temperature was generally lower in Winter 2013 (see figure 3.29). Averaged over the whole campaign, the contribution to total organics was 12 %, including Summer 2012, where its fraction was set to zero. As expected, the BBOA time series agreed very well with the signal of m/z 60 (R^2 = 0.94), measured by the ACSM. Similar to the other POA factor HOA, the highest correlations were observed with BC, NO_x and CO (R^2 = 0.39, 0.36, and 0.49, respectively).

The OOA factor dominated in Winter and Spring 2013 (47 % and 48 % contribution, respectively; 33 % over the whole year). As seen in the AMS campaign in November 2011, the OOA factor observed during the ACSM campaign showed a night-time maximum and a day-time minimum. This is characteristic for a SVOOA behaviour, as well as the high agreement with NO_3 over the whole year (R^2 = 0.63). The correlation to the LVOOA associated compound SO_4 is less (R^2 = 0.48). During the defined high mass periods (highlighted in green in figure 4.16), the increase of the OOA mass concentration (up to 11.8 µg m^{-3}), relative to the campaign average (1.05 µg m^{-3}), is much stronger compared to the other PMF factors, meaning that its mass fraction increases during these periods.

The HULIS factor provided the highest contribution to the total organic mass over the entire campaign (41 %) and was the dominant factor in Summer and Autumn 2012. The diurnal pattern of the HULIS factor showed no distinctive trend, except for a slight night-time maximum in Autumn 2012. Also the comparison to the most important tracers (table A.20) showed no particular preferential attribution, either to a low-volatile (R^2 = 0.41 with SO_4), semi-volatile (R^2 = 0.47 with NO_3) or even to primary organic aerosol (R^2 = 0.47 with BC). These characteristics were also reported for the HULIS factor found at CESAR in Cabauw in May 2008 (*Mensah*, 2011; *Crippa et al.*, 2014) and May to July 2012 (subsection 4.1.2). The correlation of the sum of the secondary inorganic species NO_3 and SO_4 with the sum of the OOA and HULIS time series gives a coefficient of R^2 = 0.70, which is slightly higher than with OOA only (R^2 = 0.67). Again this might speak for the SOA character of the HULIS factor.

For all PMF factors, no preferential wind direction was observed over the entire campaign, as shown in figure 4.18. During the high mass periods mentioned above, OOA originated mostly from the directions between 20° and 180° in respect to the tower. This is not the case for HULIS, which origins vary throughout all directions, also during high mass periods. The distinctive plume of HOA in the nights of 19.05. and 26.05.2013 came from the north east.

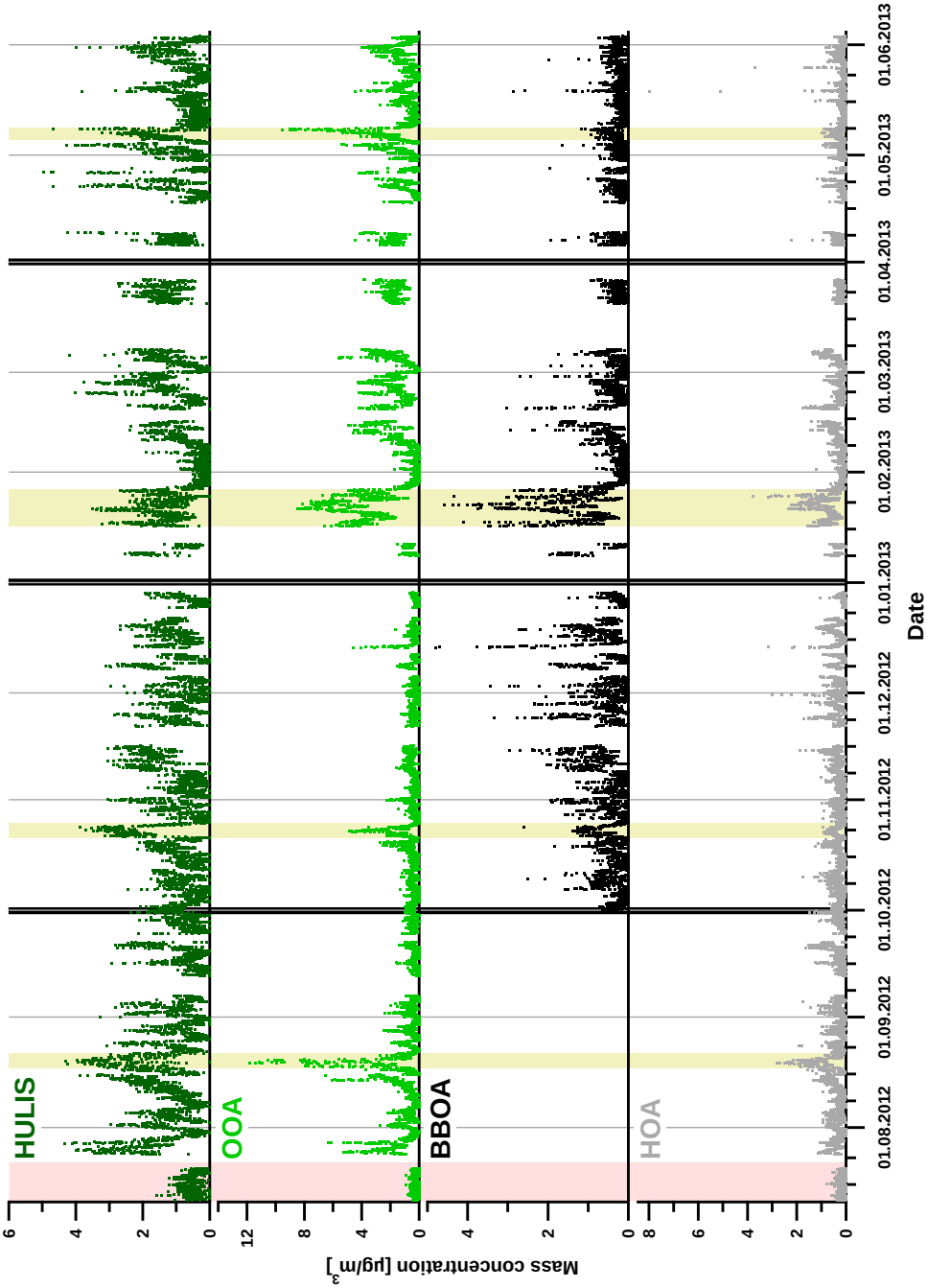

Figure 4.16.: Merged time series of ACSM PMF factors between 2012 and 2013. Note, that these plots were not obtained from one PMF/ME-2 exploration. The temporal overlap with the AMS and TD-PTR-MS is highlighted in red. High mass periods are indicated by green backgrounds, according to figure 3.30. Vertical lines represent the division into the four seasons.

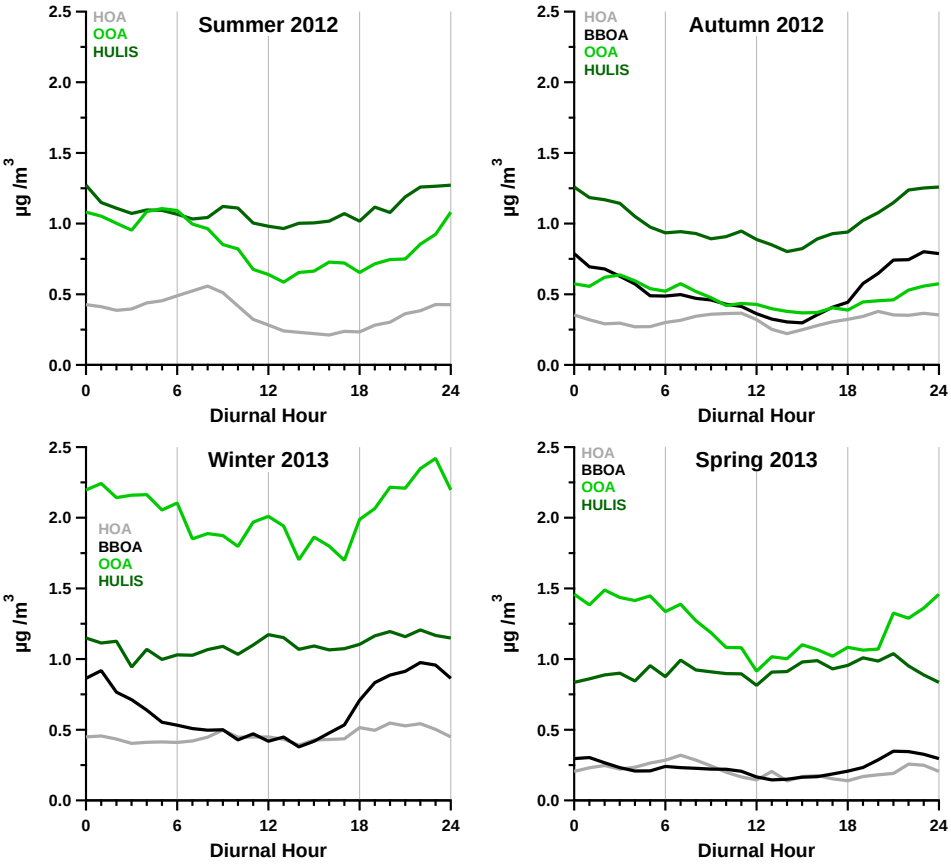

Figure 4.17.: Average diurnal variations (LT) of ACSM PMF factors separated by season

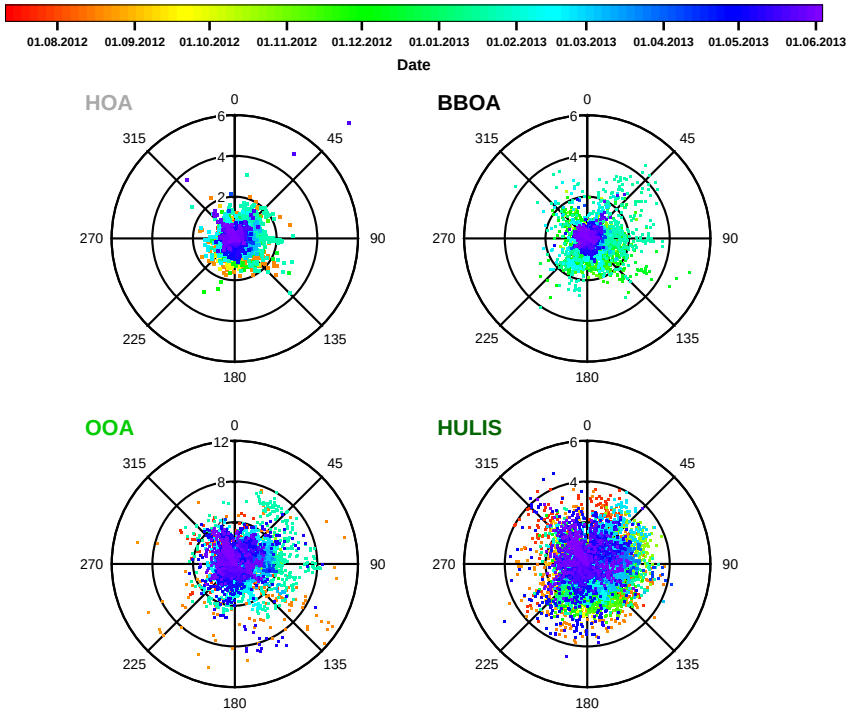

Figure 4.18.: Polar graphs of ACSM PMF factors between 2012 and 2013, colour-coded by time. The radii represent the respective mass concentration in µg m^{-3}, the angles show the cardinal directions, with the tower in the centre of the plots. Attention should be paid on the different radius scales.

4.1.5. Summary and conclusions from organic aerosol analysis

Throughout all AMS/ACSM campaign periods at the CESAR tower in Cabauw, secondary organic aerosol (SOA) dominated the PM_1 organic fraction over primary organic aerosol (POA = HOA + BBOA). Here, SOA is considered as the sum of OOA, SVOOA, LVOOA, and HULIS, depending on which factor classes were observed. Figure 4.19 shows average abundances of particular factors during a number of high mass periods defined in chapter 3.

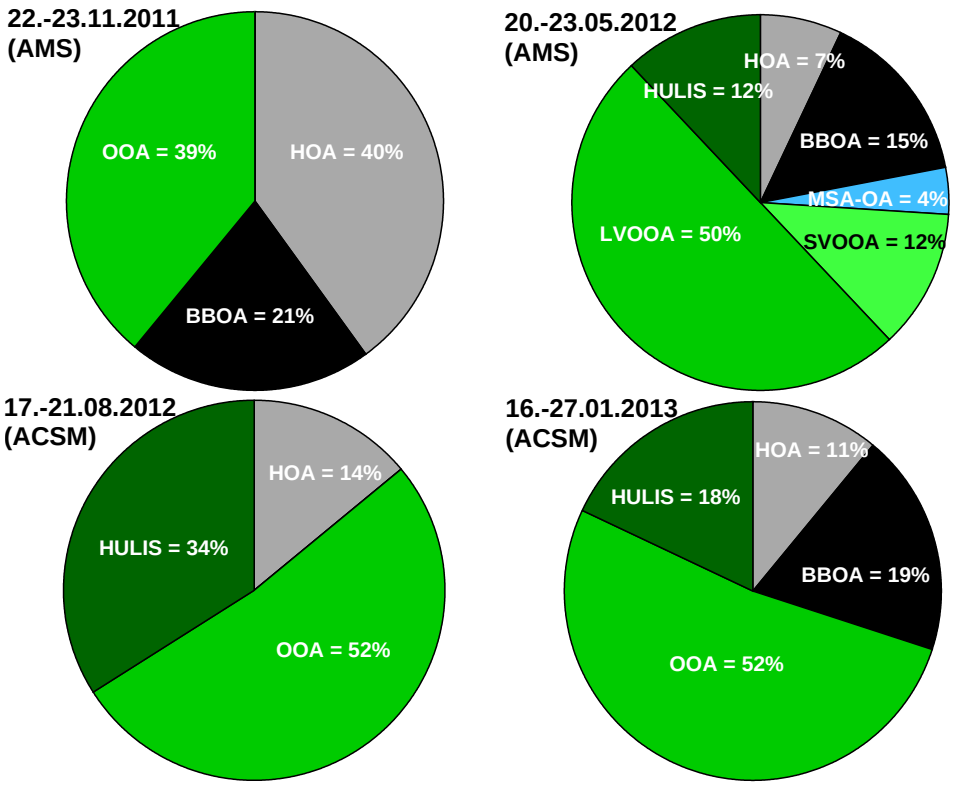

Figure 4.19.: Average contributions of PMF factors during selected high mass periods

HOA showed the highest average mass contributions in November 2011 (35 %). Besides 2011, HOA had less influence, varying between 8 % and 16 % of total organics. The characteristic maxima during the morning and evening rush hours and the relatively high correlation to traffic related tracer compounds CO and NO_x emphasizes that the main source for HOA is attributed to traffic. Black carbon (BC) is related to both POA sources, traffic and biomass burning. Its correlation to both factors is equal on average regarding all campaigns. During the high mass period from 21.11. to 23.11.2011, the HOA fraction increased to 40 %, while the OOA fraction decreased with respect to its campaign average (53 %). As explained in subsection 4.1.1, the AMS was most likely sampling within the stable boundary layer (SBL) in this period. Within the SBL, the AMS measured fresh night-time emissions from the ground, which were not mixed with the upper layers. Thus, high concentrations of POA were detected by the AMS within the SBL, resulting in a high contribution of HOA at this time. This is in contrast to the other periods shown in figure 4.19, where no evidence of such a scenario was seen. Hence, the HOA fraction

was changing only marginally during the last three periods in figure 4.19 relative to the respective seasonal average.

The BBOA factor showed a clear and expected annual variation. Except for the Summer term in 2012, it was found in every campaign period, where it had largest contribution in the colder seasons Autumn and Winter (12 % - 23 %). Together with its diurnal pattern, this is within the expectations for a factor linked with domestic heating sources. The relatively low temperatures during the AMS campaign between May and July 2012 and in Spring 2013 (diurnal minima: 12°C and 7°C, respectively) explain, why this source could also be reasonably seen there, but with lower contribution (8 % and 9 %, respectively). In comparison, the average diurnal minimum temperature in Summer 2012 was 13.5°C. During periods with high total mass concentrations, the BBOA fraction is increased by approximately 4-9 percentage points comparing to the respective seasonal or campaign average.

Major mass contribution of SOA were seen during the seasons with high average temperatures, namely Summer 2012 (84 %) and Spring 2013 (83 %). The average SOA fraction between May and July 2012 was still high (67 %), but less than in Winter 2013 (75 %). In both Autumn periods (November 2011 [AMS] and Autumn 2012 [ACSM]), the lowest contribution were obtained from SOA (53 % and 51 %, respectively), with the remainder of OA attributed to POA sources (HOA, BBOA). These findings are in agreement with PMF/ME-2 results by *Crippa et al.* (2014), where SOA factors contributed 61 % and 70 % to total organics in Cabauw in May 2008 and March 2009, respectively.

The OOA factor found in 2011 and during all seasons during the ACSM campaign was the most dominant OA besides the HULIS factor. As a result of the generally high OA oxidation state seen at the CESAR tower the OOA profile showed a relatively high O/C ratio and a dominance of the CO_2^+ ion (AMS), respectively a high f44 (ACSM). These findings are typical for LVOOA factors presented by *Zhang et al.* (2011) and *Ng et al.* (2011b). On the other hand, the OOA diurnal behaviour, which is anti-correlated with the ambient temperature, and its high correlation with particulate NO_3 links this factor with a semi-volatile character. OOA is the most important factor when mass concentrations increase during periods shown in figure 4.19.

A similar behaviour over time like OOA was observed for the SVOOA factor in 2012. In addition, its profile matches the expectation for a semi-volatile factor (*Zhang et al.*, 2011). During the 2012 high mass period its contribution (12 %) was less than the campaign average (22 %), which underlines that in 2012, the highly oxygenated LVOOA factor had more influence on the total organic fraction than the semi-volatile factor.

The high OA oxidation state in Cabauw is underlined by the prominent abundance of the very highly oxidised HULIS profile, seen both in 2012 and during the ACSM

measurement time. This factor class was also found by *Mensah* (2011) and *Crippa et al.* (2014) at CESAR. Since it had no distinct diurnal variation and preferential wind direction at almost every investigated season, it can be considered as regional background aerosol at this rural site. Additionally, the variation between the seasonal average concentrations of HULIS within the ACSM data set is less than ±10 %, as indicated in figure 4.16. The reason why HULIS was the dominant factor in Summer and Autumn 2012, is due to the lower mass concentrations of the other factors compared to the remaining periods. In turn, OA mass increased during high mass periods mainly due to the increase of the other SOA concentrations, resulting in higher mass fractions of especially OOA and LVOOA. A number of studies are published with different theories on the formation and sources of atmospheric HULIS. *Graber and Rudich* (2006) suggested that the formation of HULIS happens by oligomerization of lighter organic acids in liquid droplets in the atmosphere within time scales of hours to days. This is consistent with the findings reported in this work, that HULIS is an ubiquitous background factor at this measurement site, characterized as regionally well mixed aerosol of long atmospheric lifetime.

The MSA-OA factor is belonging to the SOA fraction, but was exclusively found in the 2012 AMS campaign, mainly at one distinctive plume between 22.05. 4 pm to 23.05.2012 10 pm. The high fraction of organic sulphates to the MSA-OA profile attributes this factor to marine sources. MSA is an oxidation product of dimethyl sulphide ($(CH_3)_2S$, DMS), which is released from the ocean into the atmosphere (*Chasteen and Bentley* (2004), see also chapter 1). Thus, the source of an MSA-OA factor can be attributed to marine air. This factor class was not only observed in marine environments *Zorn et al.* (2008); *Schmale et al.* (2013), but also in the continental mega city of Paris (*Crippa et al.*, 2013b). Furthermore, the organic sulphate ions mentioned above are used as tracer ions for marine aerosols. These organic sulphate ions were exclusively attributed to the MSA-OA factor. As expressed in figure 4.7, MSA-OA originated from directions between 210° to 315°. This is reasonable, keeping in mind that the Dutch sea coast ranges from the north to south western directions with respect to the CESAR tower. At the time of the MSA-OA plume, HULIS is the only factor with decreasing mass concentration (see figure 4.5), showing that HULIS has no marine origin.

Overall, local POA emissions have less importance for the organic fraction comparing to SOA sources throughout all seasons, as expected for this rural site (*Mensah*, 2011; *Crippa et al.*, 2014). The local reduction of organic aerosol mass is therefore challenging, also because the ubiquitous HULIS fraction shows no designated local source.

4.2. Aerosol composition during specific periods

4.2.1. High mass periods

Within this work, PM_1 chemical composition data was obtained by the ACSM at the CESAR tower in Cabauw for a period of almost one year. Several air quality standards for particulate matter have been established so far. Table 4.4 summarizes the air quality standard for $PM_{2.5}$ mass, defined by the WHO air quality guideline (global update 2005, *WHO* (2006)) and the EU Air Quality Directive 2008/50/EC[1], respectively. For both guidelines, a data coverage of 75 % for one day and 90 % for one calendar year, respectively, is mandatory for a proper risk assessment. Although the last requirement could not be achieved with the ACSM between July 2012 and June 2013 (70 % coverage), the average total PM_1 mass of 9.5 µg m^{-3} determined in this time might be an indicator, that the WHO $PM_{2.5}$ annual mean limit was at least approximated.

Table 4.4.: Air quality standards for $PM_{2.5}$, established by the WHO and the EU

Guideline	$PM_{2.5}$ 24h mean	$PM_{2.5}$ annual mean
WHO Air Quality Guideline, 2005	25 µg m^{-3}	10 µg m^{-3}
EU Air Quality Directive 2008/50/EC	-	25 µg m^{-3}

Figure 4.20 shows the time series of the daily mean total mass derived from ACSM and MAAP data, where the required data coverage of 75 % was reached. The WHO $PM_{2.5}$ daily mean limit was exceeded on 12 days, at least one time per season. 7 exceedances were observed during the high mass period from 16.01. to 27.01.2013. In order to investigate which sources have the largest impact on air quality at this rural site, it is important to identify the aerosol components and their origins during these time periods, where the highest mass concentrations were observed.

In subsection 4.1.5, the composition of organic aerosol during several periods, especially with high particulate mass loadings, was discussed. Since the inorganic species dominated the total mass on average throughout all seasons, it is important to investigate the total aerosol composition at these times in order to propose a strategy to reduce particulate mass effectively.

[1] http://eur-lex.europa.eu/LexUriServ/LexUriServ.do?uri=OJ:L:2008:152:0001:0044:EN:PDF

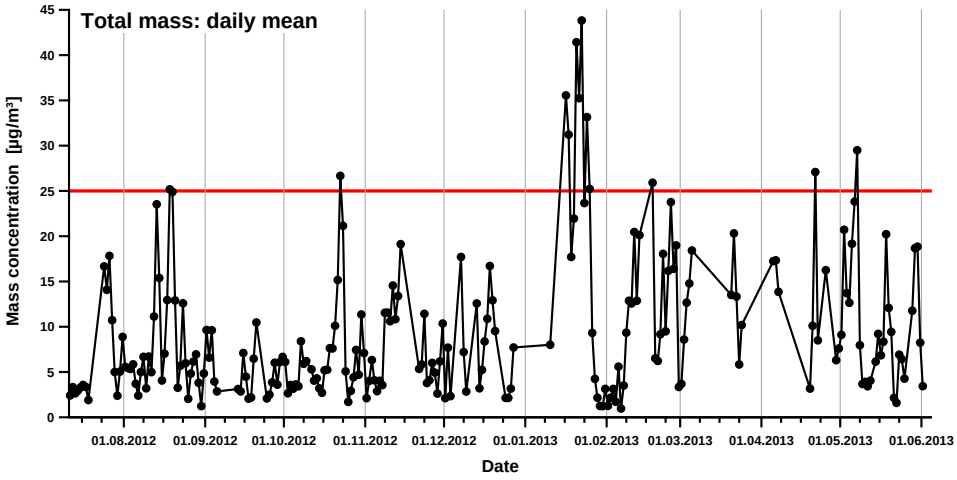

Figure 4.20.: Daily mean time series of ACSM+MAAP total mass between July 2012 and June 2013. The horizontal red line indicates the WHO $PM_{2.5}$ daily mean limit.

Figure 4.21 shows the average fraction of aerosol species observed at the high mass periods corresponding the figure 4.19. Again, the special meteorological situation on 22.11. and 23.11. is clearly seen by the increased contribution of BC (25 %), while the sum of inorganics results in only 40 % of total mass concentration. This is in contrast to all other periods. The AMS was likely sampling within the SBL during the high mass period in 2011. The observations emphasize that BC and POA (see subsection 4.1.5), to which BC is linked, have a much higher influence on the total mass in the SBL than in the upper layers. In the 2011 high mass period, the POA components HOA, BBOA and BC contributed 41 % to total aerosol mass, resulting in a concentration of 9.23 µg m^{-3} on average.

Nevertheless, nitrate and organics remain as the dominant species in all these periods, reaching up to 77 % of total mass in August 2012. Since the inorganic species NO_3 and SO_4 are produced by atmospheric processes, they are considered as secondary aerosols (see chapter 1). Together with the high abundance of SOA during the periods in 2012 and 2013, chemically aged aerosol components have the largest impact on total particulate mass at this rural site at Cabauw.

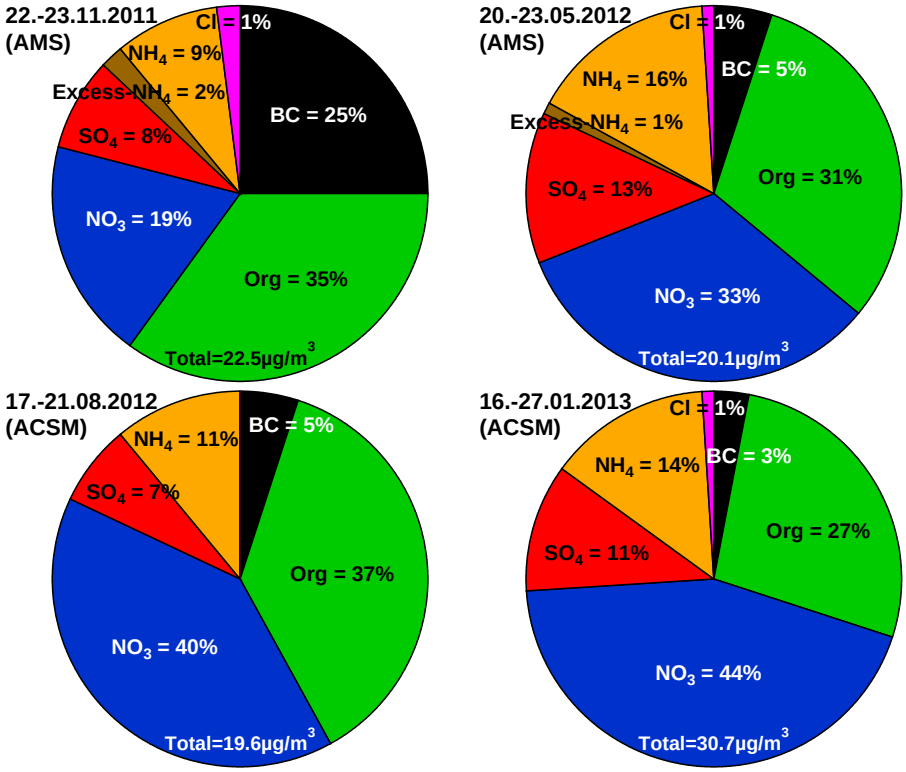

Figure 4.21.: Average contributions of individual aerosol species during selected high mass periods

4.2.2. Precipitation events

An important removal process for atmospheric particles is wet deposition, or in other words aerosols and their gaseous precursors are washed out by precipitation like rain. Due to the equilibrium between the particulate and gas phase, a depletion of gases due to e.g. rain causes a concentration gradient between gas and particles. This results in an evaporation of corresponding particulate compounds. The different physical and chemical properties of compounds like water solubility result in different removal efficiencies.

Figure 4.22 shows the relative decrease of aerosol species (a) and of PMF factors (b), from concentration measurements averaged closely before and after selected precipitation events, in these cases rain or sleet. Figures A.28 and A.29 in the appendix display the corresponding fractional abundances. The following events were chosen:

(i) 25.11.2011: 165 mm rainfall within 2 hours.

(ii) 31.05.2012: 4266 mm rainfall within 3 hours

(ii) 26.01.2013: 117 mm rainfall (sleet) within 3 hours

These events were selected as the total masses changed significantly and the wind direction was not changing. In this way the change in aerosol composition seen can be considered to be mainly due to the varying efficiencies of organic and inorganic components wet removal.

A large decrease of mass concentration was observed for NO_3 at each examined event. Further analysis of the rain events in 2011 and 2012 shows, that the inorganic nitrate ($InOrgNO_3$) fraction was more affected by wet deposition than the organic ($OrgNO_3$) fraction. The ratio of $OrgNO_3$ to total nitrate mass increased from 27 % to 73 % and from 6 % to 27 %, respectively. This is not surprising, because particulate $InOrgNO_3$ consisted largely of NH_4NO_3 at this site, and has therefore a high water solubility (NH_4NO_3: 2089 g L^{-1} at 25°C, *Adams and Gibson* (1932)), whereas the alkyl fragments of $OrgNO_3$ molecules lower the water solubility compared to pure NH_4NO_3 (*Roberts*, 1990). As an example, methyl nitrate (CH_3ONO_2) as the lightest organic nitrate has a water solubility of 1 mg L^{-1} (at 25°C; *Patty et al.* (1982)). Although methyl nitrate is not expected within the particulate phase, it illustrates the large decrease of hygroscopicity by adding one methyl group compared to NH_4NO_3.

Particulate SO_4 also mainly existed as its inorganic ammonium salt $(NH_4)_2SO_4$, as indicated by the presence of Excess-NH_4 in the campaigns in 2011 and 2012. The mass fraction of this compound (water solubility: 754 g L^{-1} at 20°C, *Haynes* (2012)) decreased during the precipitation event on 25.11.2011 and rose during the rain events in 2012 and 2013. This is also a result of the different organic composition (see below). The reduction of NH_4 is likely a result of scavenging of NH_4NO_3 and $(NH_4)_2SO_4$, while Excess-NH_4 was

reduced almost completely. A remarkable low reduction was seen from BC during the precipitation on 25.11.2011. This event is close after the high mass period from 21.11. to 23.11.2011 described above. The low scavenging effect on BC here underlines again the assumption that the stable boundary layer consisted of fresh and less oxidised aerosols This is reflected by their low water solubility, also of compounds contributing to black carbon.

On average, the hygroscopicity of organic compounds is thought to be positively correlated with the O/C ratio, since oxygen atoms increase the polarity and thus the affinity to water (*Jimenez et al.*, 2009). On the other hand, this topic is more complex since other parameters like molecular weight, size and the nature of functional groups influence the water solubility as well (*Pearlman et al.*, 1984). Besides oxygen, the most prominent heteroatoms are sulphur and nitrogen. These elements have likely less impact on the water solubility within the presented data compared to oxygen, because of their relative low abundance as seen by the low N/C ratios and S/C ratios of the AMS PMF factors (both 0.00 - 0.03; O/C = 0.16 - 0.74).

As expressed in figure A.29, HOA provided major contribution to total organics before and after the rain event in 2011, thus the reduction is rather small. Although the HOA profile had a relatively high O/C ratio (0.15, see subsection 4.1.1) it is still considered to contain a high amount of rather hydrophobic hydrocarbons.

The largest decreases were seen for BBOA, especially for the events in 2011 and 2012, although its O/C ratio (0.46 and 0.31, respectively) was lower than the O/C of the OOA, LVOOA, or HULIS factor. This indicates that BBOA had higher contribution of water soluble compounds than these SOA factors. Also LVOOA was more reduced than the highly oxidised HULIS, which shows, that the elemental ratios should not be taken as the only parameters to predict the removal efficiencies for wet deposition. The relatively low efficiency of wet removal of HULIS is in accordance with the following consideration. Atmospheric HULIS is reported to show similarities to terrestrial humic acids (HA) and fulvic acids (FA) due to their (poly-) acidic nature, but with lower molecular weight ($<$ 1000 amu) than HA or FA (*Graber and Rudich*, 2006; *Kiss et al.*, 2003). On the other hand, solid-phase extraction protocols for HULIS associate them with the more hydrophobic fraction of water-soluble aerosols (e.g. *Varga et al.* (2001)).

Note that the mass concentration of MSA-OA was below the detection limit for organics ($0.037\,\mu g\ m^{-3}$) both before and after the precipitation event on 31.05.2012. Thus, its percentaged reduction should be neglected.

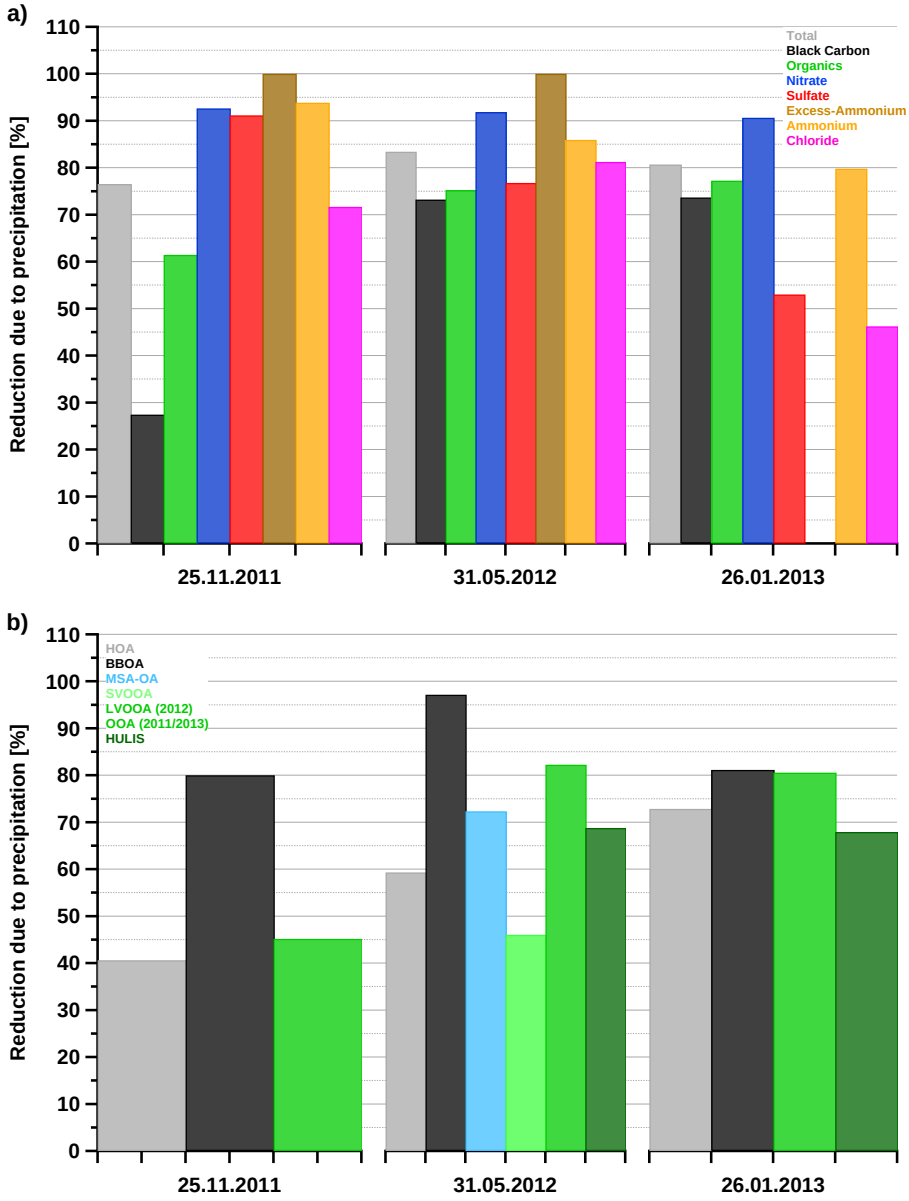

Figure 4.22.: Relative reduction of mass concentrations from individual aerosol species and total mass (a), and from PMF factors (b) due to precipitation events on 25.11.2011 (AMS), 31.05.2012 (AMS) and on 26.01.2013 (ACSM).

4.3. Organic nitrates

As seen in subsections 3.1.1.1 and 3.2.1.1, significant amounts of particulate organic nitrates were observed during the 2011 and 2012 AMS campaigns. There, concentrations of 0.47 µg m^{-3} and 0.22 µg m^{-3} were determined, corresponding to 40.0 % and 13 % to total nitrate mass, respectively. This is in agreement with *Mensah* (2011), where concentrations of 0.52 µg m^{-3} and 0.36 µg m^{-3} in May 2008 and March 2009 could be obtained at CESAR, which resulted in $OrgNO_3$ fractions of 31 % and 27 %, respectively. Within the European Integrated project on Aerosol Cloud Climate and Air Quality Interactions (EUCAARI; *Kulmala et al.* (2011)), organic nitrates were seen at almost all AMS measurement sites across Europe, where the highest mass concentrations were determined in central European sites like San Pietro Capofiume (Italy, average: 1.2 µg m^{-3}) and the lowest in remote areas such as Jungfraujoch (Switzerland, average: 0.03 µg m^{-3}. In addition, only little variations of the $OrgNO_3$ fraction were seen for all sites when comparing the measurement periods May 2008, October 2008, and March 2009 (38 %, 44 %, and 34 %, respectively). A summary is given by *Kiendler-Scharr et al.* [2014, in preparation].

The maxima during the night and at 1 pm (LT) of particulate $OrgNO_3$ in 2011, as seen in figure 3.6, indicate the two different formation processes of organic nitrates: The oxidation of VOC's by OH radicals (only at day-time) and ozone (at day- and night-time; see chapter 1). Since the temperatures were generally low during the 2011 campaign, losses of this aerosol compound class due to evaporation were less important than in 2012. The proposed semi-volatile character of organic nitrates is underlined by the fact, that $OrgNO_3$ correlated best with the semi-volatile OA factors OOA (2011, $R^2 = 0.72$) and SVOOA (2012, $R^2 = 0.47$), as also seen by *Mensah* (2011) and *Kiendler-Scharr et al.* [2014, in preparation].

The prominent presence of $OrgNO_3$ suggests that the oxidation of VOC's with NO_3 radicals plays an important role for the formation of organic aerosols. Furthermore, the findings of this nitrate fraction even in rural sites with less anthropogenic emissions of NO_x leads to the conclusion, that organic nitrates might also serve as a temporary reservoir for NO_x and could transport it into regions without primary emissions, as suggested by *Kiendler-Scharr et al.* [2014, in preparation]. Overall, a potential reduction of the organic nitrate fraction, which contribute significantly to organic aerosols, might be effectively achieved by the control of anthropogenic NO_x emissions.

4.4. Excess ammonium

AMS data from November 2011 and from May to July 2012 showed the presence of Excess-NH_4 (see subsections 3.1.1.2 and 3.2.1.2) with average contributions of 2 % and 1 % to total particulate mass, respectively. In 2011, Excess-NH_4 was found throughout the whole month apart from scavenging events near the end of the campaign, while in 2012 significant concentrations were observed mainly within the high mass periods from 21.05.-24.05. and on 05.07. and 06.07.2012. As described in subsection 2.2.1.2, the fraction of inorganic nitrates to total nitrate could not be determined for ACSM data. Thus, the total nitrate mass was used to determine the aerosol ion balance, which resulted in negative Excess-NH_4 throughout the whole ACSM campaign (subsection 3.3.0.1). Due to the uncertainty by terms of the lag of $InOrgNO_3$ information, it cannot be excluded, that Excess-NH_4 might also be present during July 2012 and June 2013, which is emphasized by high gaseous ammonia concentrations measured by the MARGA (see below).

Excess-NH_4 was also found by *Mensah et al.* (2012) in May 2008 at CESAR with a contribution of 4 %. Parallel to the AMS measurements reported here, another AMS was sampling in the afternoons of 21.05. and 22.05.2012 on-board a Zeppelin airship around the CESAR tower and Cabauw at heights between 50 m and 380 m (*Rubach*, 2013). There, Excess-NH_4 was found with average concentrations of 0.68 µg m^{-3} and a maximum of 1.5 µg m^{-3}, representing 2.1 % and 4.8 % to total mass, respectively. Note, that these findings could not be confirmed by collocated MARGA measurements, where the aerosol ion balance showed long periods with acidic aerosols and some high peaks of Excess-NH_4, which are not in agreement with AMS data.

The precursor for particulate NH_4 is gaseous ammonia (NH_3), which condenses on aerosols in form of ammonium salts with sufficient low saturation vapour pressures. The agricultural sector dominates as an emission source for ammonia, especially in the Netherlands (*van der Hoek*, 1998). It is dominated by animal husbandry with a share in total ammonia emissions in Europe of about 93.6 %[2]. In agriculture, about 82 % of emissions originate from livestock farming. The remaining NH_3 emissions stem from road transport, the waste sector and industrial processes.

Besides its role as an aerosol precursor, ammonia contributes to acid deposition and eutrophication (*Fangmeier et al.* (1994); *Krupa* (2003) and references therein). The subsequent impacts of acid deposition can be significant, including adverse effects on aquatic ecosystems in rivers and lakes, and damage to forests, crops and other vegetation. Eutrophication can lead to severe reduction in water quality with subsequent impacts in-

[2]http://www.eea.europa.eu/data-and-maps/data/national-emissions-reported-to-the-convention-on-long-range-transboundary-air-pollution-lrtap-convention-7

cluding decreased biodiversity, changes in species composition and dominance, and toxicity effects. Therefore, a number of policies have been implemented within Europe that either directly or indirectly act to reduce emissions of NH_3. One is the Gothenburg Protocol[3] (1999) to the United Nations Economic Commission for Europe's (UNECE) Convention on Long-Range Transboundary Air Pollution (LRTAP Convention) to abate acidification, eutrophication and ground-level ozone. There, the Netherlands obligated themselves to reduce ammonia emissions to a level of 120 kt in the year 2020. This goal was already reached in 2009, as well as for almost all EU-countries: the overall ammonia emission within UNECE-Europe (including international shipping) was reported to be 5543 kt (*Kuenen et al.*, 2014), where the contribution of the Netherlands was 115 kt. The reduction between 2003 and 2009 was approximately 4 % and 14 % for Europe and the Netherlands, respectively.

However, local concentrations of ammonia, especially in rural sites in North-West Europe like Cabauw, reach relatively high levels. In May 2008, NH_3 concentrations showed an average of approximately 20 µg m^{-3} (*Derksen et al.*, 2011). During the AMS campaign 2012, the MARGA measured an average of 9.0 µg m^{-3} of ammonia with its PM_1 inlet. Maxima of 53 µg m^{-3} and 34 µg m^{-3} were seen during the high mass periods between 21.-23.05.2012 and 04.-06.07.2012, respectively, where the highest concentrations of Excess-NH_4 were observed by the AMS. The MARGA showed also high ammonia concentrations during the ACSM campaign (average: 7.0 µg m^{-3}), especially in August 2012, where maxima up to 48 µg m^{-3} were obtained. These observations likely result from the high number of animal farms and the use of nitrogen containing fertilizers around the CESAR tower.

By definition, Excess-NH_4 cannot be bound in aerosols via neutralization by measured inorganic ions given by particulate NO_3, SO_4, and Chl. A pathway of NH_3 uptake to particles that does not include inorganic ions is an acid-base reaction of NH_3 with carboxylic acid groups. Carboxylic acid groups are considered to be detected as equal amounts of CO^+ and CO_2^+ ions by the AMS (*Aiken et al.*, 2008). Note that CO_2^+ is also produced from gas phase CO_2 in the AMS. This contribution was accounted for by the filter measurements described in subsection 2.1.1. The CO_2^+ signal deriving from the particulate organic fraction is referred to as Org-CO_2.

[3]http://www.unece.org/env/lrtap/multi_h1.html

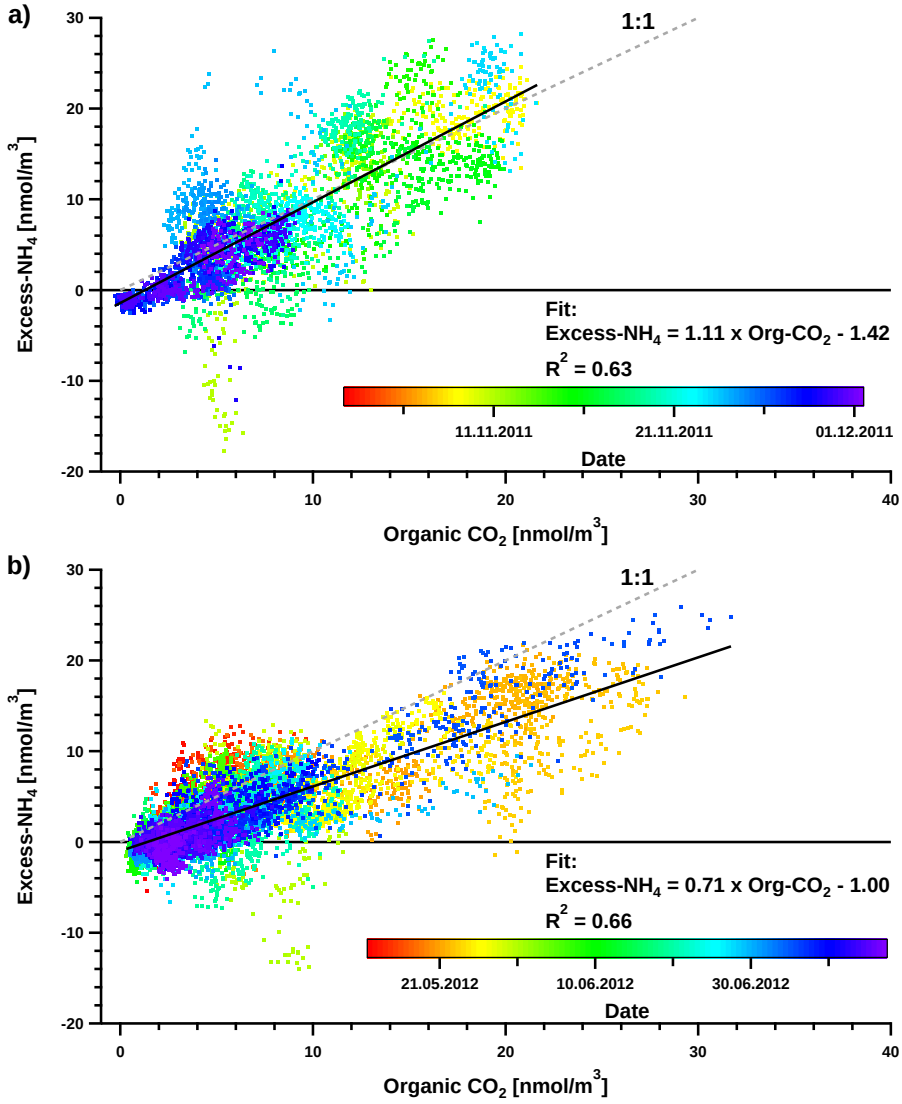

Figure 4.23.: Correlation plots of molar concentrations of Excess-NH_4 and Org-CO_2 from AMS data in 2011 (a) and 2012 (b). Slopes of 1.11 ± 0.01 and 0.71 ± 0.01 were obtained, respectively.

A good correlation was found between the molar concentrations of Excess-NH_4 ($n_{e_{NH_4}}$) and Org-CO_2 ($n_{Org\text{-}CO_2}$) in both AMS campaigns, as seen in figure 4.23. This is in good qualitative agreement with observations by *Rubach* (2013), done partly in parallel with the data presented here. Assuming that each available carboxylic acid group combines with an Excess-NH_4 molecule via an acid-base reaction, a ratio of $n_{e_{NH_4}}$ to $n_{Org\text{-}CO_2}$ of 2

would be expected. This is because a carboxylic acid group is fragmented within the AMS either to a CO^+ or a CO_2^+ ion, with a 50 % chance for each case. The Org-CO_2 concentrations shown here consider the signal of CO_2^+ only. The observed lower slopes of 1.11 ± 0.01 and 0.71 ± 0.01 for 2011 and 2012, respectively, may have the following reasons:

1. Organic acids, whose acid strengths are lower than the one of NH_4^+ ($pK_s(NH_4^+)$ = 9.26; *Bates and Pinching* (1950)) are not able to bind ammonia via an acid-base reaction, but are still contributing to the Org-CO_2 signal.

2. The abundance of Excess-NH_4 might be limited by the available gas phase NH_3, i.e. the organic acids may not be fully neutralized by NH_4. On the other hand, this would only explain the varying $n_{e_{NH_4}}$ concentration, but not the good correlation to organic acid groups. In other words, the theory of the acid-base reaction would not be refuted.

3. Functional groups other than organic acid groups are also fragmented to CO_2^+ ions and contribute to the CO_2^+ signal significantly. However, the good correlation between $n_{e_{NH_4}}$ and $n_{Org\text{-}CO_2}$ would then assume, that particulate molecules with such groups have likely similar time series, or in other words, a similar source like particulate molecules with carboxylic acid groups, or these molecules are even identical.

Since organic aerosols measured in 2011 and 2012 were analysed by PMF (see subsection 4.1.1 and 4.1.2), correlations of different organic factors with Excess-NH_4 can be determined. This may give additional information on the nature of functional groups within the PMF factors. Tables A.16 and A.17 illustrate the correlation coefficients of AMS PMF factors found in 2011 and 2012. The highest correlations were obtained for Excess-NH_4 with the SOA factors OOA in 2011 (R^2 = 0.66) and LVOOA in 2012 (R^2 = 0.64). Additionally, moderate correlations were seen between Excess-NH_4 and the respective BBOA factor (R^2 = 0.29 and 0.49 for 2011 and 2012, respectively). These results can be explained by the relatively high contributions of CO_2^+ to these profiles, expressing a significant amount of carboxylic acid groups within the factors (see figures 4.1 and 4.4).

An exception from this assumption was found by the low agreement between the time series of Excess-NH_4 and the HULIS factor in 2012 (R^2 = 0.36), although its profile was highly dominated by CO_2^+. HULIS is characterized by a poly-acidity, similar to fulvic acid. On the other hand, HULIS shows lower aromaticity, higher H/C molar ratios, and a weaker acidic nature than fulvic acid (*Graber and Rudich* (2006) and references therein). This may explain the apparent disagreement between its acidity and the low correlation with Excess-NH_4.

To quantify the assumption of the acid-base related binding of NH_3, a correlation between the molar concentrations of Excess-NH_4 and SOA-CO_2 has to be determined. Knowing the fractional abundance of CO_2^+ in each factor profile, the time series of the SOA-CO_2 molar concentrations can be determined and correlated to the molar concentration of Excess-NH_4. This was done for the OOA and LVOOA factors, respectively, shown in figure 4.24.

In 2011 and 2012, slopes of 1.61 ± 0.05 and 0.90 ± 0.02 were observed, respectively. These values are still lower than the expected ratio $n_{e_{NH_4}}$ to $n_{Org\text{-}CO_2}$ of 2, but higher than the slopes achieved by the correlation of Excess-NH_4 and the total Org-CO_2. Likely both PMF factors contain components, which do not bind NH_3, but are partly detected as CO_2^+ by the AMS. These groups can derive from e.g. weak organic acids or esters, which are likely detected partly as CO_2^+ by the AMS. A limitation of Excess-NH_4 by ammonia gas phase concentrations is not likely, since very high NH_3 amounts were measured by the MARGA at times with high Excess-NH_4 concentrations (see above). Hence, it can be assumed that the amount of Excess-NH_4 is driven exclusively by the concentration of carboxylic acid groups with sufficient acid strength.

As mentioned, the TD-PTR-MS has a higher sensitivity for nitrogen containing organic aerosols than the AMS. This would lead to the conclusion, that PTR PMF factors (see subsections 4.1.3.1 and 4.1.3.2) with a high N/C ratio should also show a good agreement with either Excess-NH_4 and/or the time series OOA and LVOOA/BBOA factors found by the AMS in 2011 and 2012, respectively. In 2011, the correlation coefficients of the PTR PMF factors F1 and F2 (both N/C = 0.09) with OOA were higher (R^2 = 0.35 and 0.63, respectively) than of F3 (R^2 = 0.22, N/C = 0.05). In 2012, the PTR factors F1 and F2 with high N/C ratios (0.06 and 0.15, respectively) showed also good agreement with Excess-NH_4 (R^2 = 0.42 and 0.43, respectively), as well as with the time series of the AMS LVOOA factor (R^2 = 0.57 and 0.61, respectively) and BBOA factor (R^2 = 0.69 and 0.82, respectively). An exception is the PTR factor F5, which shows also good agreement with Excess-NH_4, $LVOOA_{AMS}$, and $BBOA_{AMS}$ (R^2 = 0.52, 0.82, and 0.57, respectively) but the lowest N/C ratio of 0.03. Despite that the PTR PMF solutions presented in this work are a first approach and need further investigations, the agreements between factors with high nitrogen contributions with AMS Excess-NH_4 is an indicator for already reasonable results.

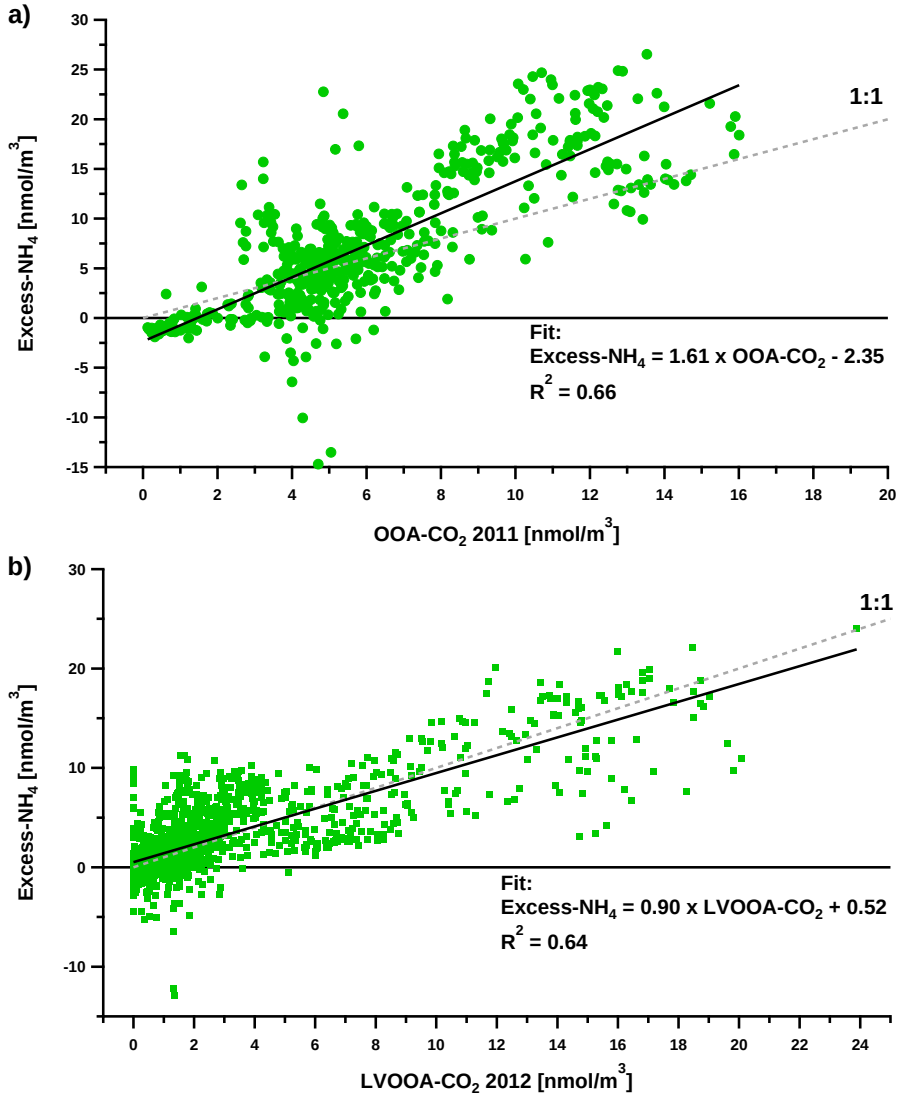

Figure 4.24.: Correlation plots of molar concentrations of Excess-NH_4 and Org-CO_2 fractions of the PMF OOA factor found in 2011 (a) and the PMF LVOOA factor found in 2012 (b). Slopes of 1.61 ± 0.05 and 0.90 ± 0.02 were obtained, respectively. Note that by definition, PMF factors only consist of positive data values.

5. Summary and Outlook

This work provides long term mass spectrometric data of atmospheric aerosols (PM_1) acquired at the CESAR tower in Cabauw, the Netherlands, which is a representative site for North Western Europe. This includes measurements from a High Resolution Time-of-Flight Aerosol Mass Spectrometer (AMS), an Aerosol Chemical Speciation Monitor (ACSM) and a Thermal-Desorption Proton-Transfer-Reaction Time-of-Flight Mass Spectrometer (TD-PTR-MS). Acquisition times ranged from months (AMS, TD-PTR-MS) to almost one year (ACSM). Special focus was laid on the analysis and interpretation of the chemical composition of the aerosol, providing insight into main aerosol sources. Quality assurance of overall mass concentration and aerosol composition was performed using data from collocated SMPS and MARGA instruments, respectively.

It is demonstrated, that the nitrate and organic fraction were the dominant aerosol species throughout almost all campaigns at this rural site. Nitrate showed the highest contributions during Winter and Spring 2013.

The total PM_1 aerosol mass exceeded the WHO $PM_{2.5}$ daily mean limit twelve times in total. An average total mass of $9.50\,\mu g\ m^{-3}$ was obtained during July 2012 and June 2013, close to the the WHO $PM_{2.5}$ annual mean limit of $10\,\mu g\ m^{-3}$. At high mass periods, nitrate was mostly the major fraction, followed by organics, except for individual cases, where organics and black carbon largely dominated. Inorganic nitrates consisted nearly exclusively of ammonium nitrate. In addition, the observation of excess ammonium, bound most likely by carboxylic acid groups within the particulate phase, indicates also the high influence of nitrogen containing precursors such as NH_3 and NO_x on the formation of inorganic (mainly NH_4NO_3 and $(NH_4)_2SO_4$) and organic aerosols (e.g. $OrgNO_3$) at this rural measurement site. Controlling the emissions of anthropogenic nitrogen oxides and ammonia should therefore have a very large effect on the reduction of particulate mass.

Further analysis of the organic aerosol (OA) fraction was performed by applying Positive Matrix Factorization (PMF) and Multilinear Engine 2 (ME-2), respectively, on all data sets. It is shown that secondary organic aerosols (SOA) were the dominant factors throughout all periods, including factors with semi-volatile, low-volatile, and HULIS characteristics. The last is shown to be a highly oxidised regional background aerosol with no designated local source. Major contribution of primary organic aerosols (POA) originate

from traffic related hydrocarbon like (HOA) and biomass burning aerosol (BBOA), which dominated the organic fraction at individual high mass periods. Besides this, primary emissions played a minor role in Cabauw. Removal efficiencies of organic factors by wet deposition are seen to differ largely. While BBOA showed the highest reduction due to precipitation, HULIS is observed to rather remain in the particulate phase, underlining its role as background aerosol. Since chemically aged organic aerosol showed the highest contribution, a potential reduction of this fraction is challenging on a local scale. Hence, the control of primary organic aerosol emissions should be performed together with the reduction of secondary OA precursors.

First PMF analyses were performed with organic aerosol data obtained by the TD-PTR-MS, indicating that especially nitrogen containing components could be identified sensitively. PTR PMF results show reasonable correlations with factors from the collocated AMS. However, further investigations on this topic will be performed to gain the full potential of the TD-PTR-MS system. This includes the exploration of PMF approaches of data sets separated by the thermal desorption temperature. Hence, a pre-separation of factors by their volatility will be achieved and simplify the PMF analysis. Furthermore, reference mass spectra for expected factors (e.g. MSA-OA) need to be obtained with the TD-PTR-MS to compare them with mass spectra found within PMF of ambient measurements. This will help to understand and identify proper PTR-PMF solutions and deepens the understanding of processes involved in organic aerosol mass formation and ageing.

The aerosol composition data sets and results obtained in this work can be used as basis for regional chemical transport models. Using these models quantitative estimations can be achieved on the efficiency of scenarios regarding the reduction of particulate mass.

List of abbreviations

Abbreviation	Meaning
AB	Air Beam
ACSM	Aerosol Chemical Speciation Monitor
AIM	Aerosol Instrument Manager
AMS	Aerosol Mass Spectrometer
$ANMF$	Ammonium Nitrate Mass Fraction
BBOA	Biomass Burning Organic Aerosol
BC	Black Carbon
BS	Bootstrapping
BVOC	Biogenic Volatile Organic Compound
CCN	Cloud Condensation Nuclei
CDCE	Composition Dependent Collection Efficiency
CE	Collection Efficiency
CESAR	Cabauw Experimental Site for Atmospheric Research
Chl	Particulate Chloride
COA	Cooking Organic Aerosol
CPC	Condensation Particle Counter
CTD	Collection Thermal Desorption
DAQ	Data Acquisition software
D_{em}	Electro-Mobility Diameter
DL	Detection Limit
DMA	Differential Mobility Analyser
DMS	Dimethyl Sulphide
D_{va}	Vacuum Aerodynamic Diameter
ECN	Energy research Centre of the Netherlands, The Netherlands
EI	Electron Impact
EU	European Union
EUCAARI	European Integrated project on Aerosol Cloud Climate and Air Quality Interactions
f43	Contribution of m/z 43 to the organic mass spectrum
f44	Contribution of m/z 44 to the organic mass spectrum
f60	Contribution of m/z 60 to the organic mass spectrum
FA	Fulvic Acid

Abbreviation	**Meaning**
FWHM	Full Width at Half Maximum
G	Gain
HA	Humic Acid
HEPA	High Efficiency Particulate Air
HOA	Hydrocarbon-like Organic Aerosol
HR	High Resolution
HR-ToF-AMS	High Resolution Time-of-Flight Aerosol Mass Spectrometer
HULIS	Humic-Like Substances
ID	Inner Diameter
IE	Ionization Efficiency
IMAU	Institute for Marine and Atmospheric research Utrecht, The Netherlands
$InOrgNO_3$	Inorganic Nitrate
KNMI	Royal Netherlands Meteorological Institute, The Netherlands
LiDAR	Light Detection And Ranging
LRTAP	Long-Range Transboundary Air Pollution
LT	Local Time
LVOOA	Low-Volatile Oxidised Organic Aerosol
MAAP	Multi-Angle Absorption Photometer
MARGA	Monitor for Aerosol and Gases
MCP	Multichannel Plate
ME-2	Multilinear Engine 2
MS	Mass Spectrum
MSA	Methanesulfonic Acid
MSA-OA	Methanesulfonic Acid Organic Aerosol
MW	Molecular Weight
N_a	Avogadro Constant
NH_4	Particulate Ammonium
NIST	National Institute for Standards and Technology
NL	The Netherlands
NMHC	Non-Methane Hydrocarbons
NO_x	Nitrogen Oxides
NO_3	Particulate Nitrate
NR	Non-Refractory
NR-PM	Non-Refractory Particulate Matter

Abbreviation	**Meaning**
OA	Organic Aerosol
OOA	Oxidised Organic Aerosol
OM	Organic Matter
Org	Particulate Organics
Org-CO_2	CO_2^+-signal, derived from particulate organics
$OrgNO_3$	Organic Nitrate
PA	Primary Aerosol
PET	Positive Matrix Factorization Evaluation Tool
PILS	Particle-Into-Liquid Sampler
PM	Particulate Matter
PMF	Positive Matrix Factorization
POA	Primary Organic Aerosol
PSL	Polystyrene Latex Spheres
PToF	Particle Time of Flight
PTR	Proton-Transfer-Reaction
PTR-MS	Proton-Transfer-Reaction Mass Spectrometer
Q-AMS	Quadrupole Aerosol Mass Spectrometer
RF	Response Factor
RGA	Residual Gas Analyser
RH	Relative Humidity
RIE	Relative Ionization Efficiency
R	Resolution
SA	Secondary Aerosol
SBL	Stable Boundary Layer
SD	Standard Deviation
SF	Shape Factor
σ_p	Particle Density
SJAC	Steam Jet Aerosol Collector
SM	Summed Matrices
SMPS	Scanning Mobility Particle Sizer
SNR	Signal-to-Noise Ratio
SO_4	Particulate Sulphate
SOA	Secondary Organic Aerosol
SVOOA	Semi-Volatile Oxidised Organic Aerosol
TAG	Thermal-Desorption Aerosol Gas Chromatograph
TD-PTR-(ToF)-MS	Thermal-Desorption Proton-Transfer-Reaction

Abbreviation	Meaning
	Time-of-Flight Mass Spectrometer
TEOM	Tapered Element Oscillating Microbalance
TNO	Netherlands Organisation for Applied Scientific Research, The Netherlands
ToF-MS	Time-of-Flight Mass Spectrometer
UMR	Unit Mass Resolution
UNECE	United Nations Economic Commission for Europe
UTC	Universal Time, Coordinated
VMR	Volume Mixing Ratio
VOC	Volatile Organic Compound
WAD	Wet Annular Denuder
WHO	World Health Organization
WSOC	Water-Soluble Organic Carbon

List of Figures

1.1. Global mean radiative forcings 2
1.2. Overview of the aerosol chemical compositions across the globe 3
1.3. Relationship between O/C and hygroscopicity of OA 7

2.1. Schematic drawing of the HR-ToF-AMS 10
2.2. Schematic drawing of the ACSM 22
2.3. Scheme of the ACSM filter cycle 23
2.4. Resolutions of different AMS types 27
2.5. Schematic drawing of the TD-PTR-MS 29
2.6. Measurement cycle of the TD-PTR-MS 30
2.7. Measurement site and picture of the CESAR tower 34
2.8. Data coverage from aerosol and gas phase instruments deployed at the CESAR tower 37
2.9. Scheme of Positive Matrix Factorization 41

3.1. Meteorological overview of the 2011 campaign 50
3.2. Height profiles of ambient temperatures in 2011 and picture of the tower, made on 22.11.2011, 11 am (LT) 52
3.3. Aerosol composition during the 2011 campaign 53
3.4. Average contributions of aerosol species and their diurnal variations (LT) in 2011 54
3.5. Polar graphs of individual species in 2011 55
3.6. Average diurnal variations (LT) of the AMS organic and inorganic nitrate fraction in 2011 56
3.7. Time series of the AMS organic and inorganic nitrate fraction in 2011 . . . 57
3.8. Average diurnal variation (LT) of the Excess-NH_4 in 2011 57
3.9. Correlation plot of measured against predicted NH_4 and time series of Excess-NH_4 in 2011 58
3.10. Average size distribution of individual species and the total inorganics, measured by the AMS in November 2011 59

3.11. Time series and correlation plot of AMS+MAAP and SMPS mass concentrations in 2011 . . . 61
3.12. Correlation plot of AMS+MAAP and SMPS mass concentrations in 2011. Here, only a D_{va} range of 60 nm to 600 nm was considered for the determination of the SMPS mass . . . 62
3.13. Time series and correlation plot of PTR OA (both inlets combined) and AMS OA mass concentrations in 2011 . . . 63
3.14. Averaged diurnal variations (LT) of PTR-OA from both inlets and from merged data in 2011 . . . 64
3.15. Meteorological overview of the 2012 campaign . . . 66
3.16. Aerosol composition during the 2012 campaign . . . 68
3.17. Average contributions of aerosol species and their diurnal variations (LT) in 2012 . . . 69
3.18. Polar graphs of individual species in 2012 . . . 69
3.19. Time series of the AMS organic and inorganic nitrate fraction in 2012 . . . 70
3.20. Average diurnal variations (LT) of the AMS organic and inorganic nitrate fraction in 2012 . . . 70
3.21. Average diurnal variation (LT) of the Excess-NH_4 in 2012 . . . 71
3.22. Correlation plot of measured against predicted NH_4 and time series of Excess-NH_4 in 2012 . . . 72
3.23. Average size distribution of individual species and the total mass, measured by the AMS from May to July 2012 . . . 73
3.24. Time series and correlation plot of AMS+MAAP and SMPS mass concentrations in 2012 . . . 74
3.25. Correlation plot of AMS+MAAP and SMPS mass concentrations in 2012 . 75
3.26. Time series of particulate Chl, NH_4, SO_4, and NO_3, measured by the AMS and the MARGA between May to July 2012 . . . 76
3.27. Averaged diurnal variations (LT) of PTR-OA from both inlets and from merged data in 2012 . . . 77
3.28. Time series and correlation plot of PTR OA (both inlets combined) and AMS OA mass concentrations in 2012 . . . 78
3.29. Meteorological overview of the ACSM campaign . . . 80
3.30. Overview of the ACSM campaign from July 2012 to June 2013 . . . 81
3.31. Average contributions of aerosol species from ACSM data over the entire campaign . . . 82
3.32. Polar graphs of individual species of ACSM data . . . 83

3.33. Diurnal variation (LT) of individual species and the total mass, averaged over the whole ACSM campaign and over selected periods 84
3.34. Correlation plot of measured against predicted NH_4 during the ACSM campaign 85
3.35. Time series and correlation plot of ACSM+MAAP and SMPS mass concentrations between July 2012 and June 2013 86
3.36. Correlation plot of ACSM+MAAP and SMPS mass concentrations between July 2012 and June 2013. Here, only a D_{va} range of 60 nm to 600 nm was considered for the determination of the SMPS mass. 87
3.37. Time series of particulate Chl, NH_4, SO_4, and NO_3, measured by the ACSM and the MARGA between July 2012 and June 2013 88
3.38. Time series of individual species, measured by the ACSM, AMS and the TD-PTR-MS between 11.07. and 17.07.2012 90

4.1. Mass spectra and time series of PMF factors from AMS data and tracers in 2011 94
4.2. Average contributions of AMS PMF factors and their diurnal variations (LT) in 2011 95
4.3. Polar graphs of PMF factors from AMS data in 2011 97
4.4. Mass spectra of PMF factors from AMS data in 2012 97
4.5. Time series of PMF factors from AMS data and tracers in 2012 98
4.6. Average contributions of AMS PMF factors and their diurnal variations (LT) in 2012 99
4.7. Polar graphs of PMF factors from AMS data in 2012 101
4.8. Mass spectra of the 3-factor PMF solution from TD-PTR-MS data (inlet A) in 2011 104
4.9. Time series of the 3-factor PMF solution from TD-PTR-MS data (inlet A) in 2011 105
4.10. Average contributions of TD-PTR-MS PMF factors and their diurnal variations (LT) in 2011 105
4.11. Mass spectra of PMF factors from TD-PTR-MS data in 2012 108
4.12. Average contributions of TD-PTR-MS PMF factors and their diurnal variations (LT) in 2012 109
4.13. Comparison of time series of PMF factors from TD-PTR-MS and AMS data in 2012 111
4.14. Average contributions of ACSM PMF factors for each observed season . . . 113

4.15. Mass spectra of ACSM PMF factors for each observed season between 2012 and 2013 . . . 115
4.16. Merged time series of ACSM PMF factors between 2012 and 2013 . . . 118
4.17. Average diurnal variations (LT) of ACSM PMF factors separated by season 119
4.18. Polar graphs of ACSM PMF factors between 2012 and 2013 . . . 120
4.19. Average contributions of PMF factors during selected high mass periods . . 121
4.20. Daily mean time series of ACSM+MAAP total mass between July 2012 and June 2013 . . . 125
4.21. Average contributions of individual aerosol species during selected high mass periods . . . 126
4.22. Relative reduction of mass concentrations from individual aerosol species and total mass, and from PMF factors due to precipitation . . . 129
4.23. Correlation plots of molar concentrations of Excess-NH_4 and Org-CO_2 from AMS data in 2011 and 2012 . . . 133
4.24. Correlation plots of molar concentrations of Excess-NH_4 and Org-CO_2 fractions of the PMF OOA factor found in 2011 and the PMF LVOOA factor found in 2012 . . . 136

A.1. Diurnal variations (LT) of the ambient temperature and the temperature at the manifold of the 60 m sampling line in 2011 . . . 206
A.2. Correlation plot of measured against predicted NH_4 in 2011 using total nitrate concentrations . . . 207
A.3. Average size distribution of individual species and the total inorganics, measured by the AMS in 2011 . . . 207
A.4. Collection efficiency used for AMS data in 2011 . . . 208
A.5. SMPS particle size distribution in 2011 . . . 208
A.6. Particle density, determined from AMS aerosol composition in 2011 . . . 209
A.7. Time series of PTR-OA, measured from aerosol inlet A and B in 2011 . . . 209
A.8. Diurnal variations (LT) of the ambient temperature and the temperature in the AMS inlet in 2012 . . . 210
A.9. Correlation plot of measured against predicted NH_4 in 2012 using total nitrate concentrations . . . 210
A.10. Collection efficiency used for AMS data in 2012 . . . 211
A.11. SMPS particle size distribution from May to July 2012 . . . 211
A.12. Particle density, determined from AMS aerosol composition in 2012 . . . 212
A.13. Correlation graphs of Chl, NH_4, SO_4, NO_3, and total inorganic mass concentration from AMS and MARGA data of 2012 . . . 213

A.14.Time series of PTR-OA, measured from aerosol inlet A and B in 2012 . . . 214
A.15.Diurnal variations (LT) of ambient temperatures at 2 m height from 2012 to 2013 . . . 214
A.16.Collection efficiency used for ACSM data . . . 215
A.17.SMPS particle size distribution from July 2012 to June 2013 . . . 215
A.18.Particle density, determined from ACSM aerosol composition from July 2012 to June 2013 . . . 216
A.19.Correlation graphs of Chl, NH_4, SO_4, NO_3, and total inorganic mass concentration from ACSM and MARGA data from 2012 to 2013 . . . 217
A.20.Correlation graphs of individual species and total mass from ACSM data with AMS data from 11.07. to 17.07.2012 . . . 218
A.21.Correlation graph of the organic fractions from ACSM data with TD-PTR-MS data from 11.07. to 17.07.2012 . . . 219
A.22.Variance of AMS PMF factors and residuals found in 2011 . . . 219
A.23.Bootstrapping results of the AMS PMF 3 factor solution in 2011 . . . 220
A.24.Variance of AMS PMF factors and residuals found in 2012 . . . 221
A.25.Bootstrapping results of the AMS PMF 6 factor solution in 2012: Mass spectra . . . 222
A.26.Bootstrapping results of the AMS PMF 6 factor solution in 2012: Time series . . . 223
A.27.Mass spectra and time series of the 3-factor PMF solution from TD-PTR-MS data (merged from both inlets) in 2011 . . . 224
A.28.Average contributions of individual species before and after precipitation events . . . 227
A.29.Average contributions of PMF factors before and after precipitation events 227

List of Tables

2.1. Summary of averaged calibration results and RIE's used for AMS data . . 17
2.2. Summary of averaged calibration results and RIE's used for ACSM data . 25

3.1. Overview of the temperatures and relative humidities in 2011 50
3.2. Overview of the temperatures and relative humidities in 2012 65
3.3. Results of the AMS to MARGA comparison from four particulate inorganic species and the total inorganic mass in 2012 76
3.4. Overview of the ambient temperatures and relative humidities during the ACSM campaign 79
3.5. Results of the ACSM to MARGA comparison from four particulate inorganic species and the total inorganic mass during 2012-2013 87
3.6. Results of the ACSM to AMS/TD-PTR-MS comparison from individual species between 11.07. and 17.07.2012 91

4.1. Correlation coefficients (R^2) of the comparison between AMS and PTR-MS factor time series in 2011 106
4.2. Correlation coefficients (R^2) of the comparison between AMS and PTR-MS factor time series in 2012 111
4.3. Overview of ACSM PMF factors observed for each season 112
4.4. Air quality standards for $PM_{2.5}$, established by the WHO and the EU . . . 124

A.1. Results from AMS ionization efficiency calibrations of the V-mode during the campaign in Cabauw 2011 171
A.2. Results from AMS ionization efficiency calibrations of the W-mode during the campaign in Cabauw 2011 171
A.3. Results from AMS particle size distribution calibrations during the campaign in Cabauw 2011 171
A.4. Manually set values used for AB correction of V- and W-mode for the 2011 AMS data 172
A.5. Manually set values used for PToF determination for the 2011 AMS data . 173

A.6. Correction factors used in the AMS UMR fragmentation table for the 2011 data . . . 173
A.7. Results from AMS ionization efficiency calibrations for V-mode during the campaign in Cabauw 2012 . . . 174
A.8. Results from AMS ionization efficiency calibrations for W-mode during the campaign in Cabauw 2012 . . . 174
A.9. Results from AMS particle size distribution calibrations during the campaign in Cabauw 2012 . . . 175
A.10. Manually set values used for AB correction of V- and W-mode for the 2012 AMS data . . . 176
A.11. Manually set values used for PToF determination for the 2012 AMS data . 176
A.12. Correction factors used in the AMS UMR fragmentation table for the 2012 data . . . 176
A.13. Overview of the detection limits for each aerosol species from AMS and ACSM . . . 177
A.14. List and basic information of all detected ions used for TD-PTR-MS data analysis in 2011 . . . 178
A.15. List and basic information of all detected ions used for TD-PTR-MS data analysis in 2012 . . . 197
A.16. Correlation coefficients (R^2) of the comparison between AMS PMF factor and tracer time series in 2011 . . . 221
A.17. Correlation coefficients (R^2) of the comparison between AMS PMF factor and tracer time series in 2012 . . . 223
A.18. Correlation coefficients (R^2) of the comparison between TD-PTR-MS PMF factor and tracer time series in 2011 . . . 225
A.19. Correlation coefficients (R^2) of the comparison between TD-PTR-MS PMF factor and tracer time series in 2012 . . . 225
A.20. Correlation coefficients (R^2) of the comparison between ACSM PMF factor and tracer time series between July 2012 to June 2013 . . . 226
A.21. F44 and O/C ratios from PMF profiles of ACSM organic data separated by season . . . 226

Bibliography

Adams, L. H., and R. E. Gibson, Equilibrium in binary systems under pressure. III. The influence of pressure on the solubility of ammonium nitrate in water at 25°C, *Journal of the American Chemical Society*, *54*(12), 4520–4537, doi:10.1021/ja01351a008, 1932.

Aiken, A. C., P. F. DeCarlo, and J. L. Jimenez, Elemental analysis of organic species with electron ionization high-resolution mass spectrometry, *Analytical Chemistry*, *79*(21), 8350–8358, doi:10.1021/ac071150w, 2007.

Aiken, A. C., P. F. DeCarlo, J. H. Kroll, D. R. Worsnop, J. A. Huffman, K. S. Docherty, I. M. Ulbrich, C. Mohr, J. R. Kimmel, D. Sueper, Y. Sun, Q. Zhang, A. Trimborn, M. Northway, P. J. Ziemann, M. R. Canagaratna, T. B. Onasch, M. R. Alfarra, A. S. H. Prevot, J. Dommen, J. Duplissy, A. Metzger, U. Baltensperger, and J. L. Jimenez, O/C and OM/OC ratios of primary, secondary, and ambient organic aerosols with high-resolution time-of-flight aerosol mass spectrometry, *Environmental Science & Technology*, *42*(12), 4478–4485, doi:10.1021/es703009q, 2008.

Aiken, A. C., D. Salcedo, M. J. Cubison, J. A. Huffman, P. F. DeCarlo, I. M. Ulbrich, K. S. Docherty, D. Sueper, J. R. Kimmel, D. R. Worsnop, A. Trimborn, M. Northway, E. A. Stone, J. J. Schauer, R. M. Volkamer, E. Fortner, B. de Foy, J. Wang, A. Laskin, V. Shutthanandan, J. Zheng, R. Zhang, J. Gaffney, N. A. Marley, G. Paredes-Miranda, W. P. Arnott, L. T. Molina, G. Sosa, and J. L. Jimenez, Mexico City aerosol analysis during MILAGRO using high resolution aerosol mass spectrometry at the urban supersite (T0) Part 1: Fine particle composition and organic source apportionment, *Atmospheric Chemistry and Physics*, *9*(17), 6633–6653, doi:10.5194/acp-9-6633-2009, 2009.

Aiken, A. C., B. de Foy, C. Wiedinmyer, P. F. DeCarlo, I. M. Ulbrich, M. N. Wehrli, S. Szidat, A. S. H. Prevot, J. Noda, L. Wacker, R. Volkamer, E. Fortner, J. Wang, A. Laskin, V. Shutthanandan, J. Zheng, R. Zhang, G. Paredes-Miranda, W. P. Arnott, L. T. Molina, G. Sosa, X. Querol, and J. L. Jimenez, Mexico City aerosol analysis during MILAGRO using high resolution aerosol mass spectrometry at the urban supersite (T0) Part

2: Analysis of the biomass burning contribution and the non-fossil carbon fraction, *Atmospheric Chemistry and Physics*, *10*(12), 5315–5341, doi:10.5194/acp-10-5315-2010, 2010.

Albrecht, B. A., Aerosols, cloud microphysics, and fractional cloudiness, *Science*, *245*(4923), 1227–1230, doi:10.1126/science.245.4923.1227, 1989.

Alfarra, M. R., Insights into atmospheric organic aerosols using an Aerosol Mass Spectrometer, Ph.D. thesis, University of Manchester Institute of Science and Technology, 2004.

Alfarra, M. R., H. Coe, J. D. Allan, K. N. Bower, H. Boudries, M. R. Canagaratna, J. L. Jimenez, J. T. Jayne, A. A. Garforth, S.-M. Li, and D. R. Worsnop, Characterization of urban and rural organic particulate in the Lower Fraser Valley using two Aerodyne Aerosol Mass Spectrometers, *Atmospheric Environment*, *38*(34), 5745–5758, doi:10.1016/j.atmosenv.2004.01.054, 2004.

Alfarra, M. R., A. S. H. Prevot, S. Szidat, J. Sandradewi, S. Weimer, V. A. Lanz, D. Schreiber, M. Mohr, and U. Baltensperger, Identification of the mass spectral signature of organic aerosols from wood burning emissions, *Environmental Science & Technology*, *41*(16), 5770–5777, doi:10.1021/es062289b, 2007.

Allan, J. D., J. L. Jimenez, P. I. Williams, M. R. Alfarra, K. N. Bower, J. T. Jayne, H. Coe, and D. R. Worsnop, Quantitative sampling using an Aerodyne Aerosol Mass Spectrometer 1. Techniques of data interpretation and error analysis, *Journal of Geophysical Research-Atmospheres*, *108*(D3 4090), doi:10.1029/2002JD002358, 2003.

Allan, J. D., A. E. Delia, H. Coe, K. N. Bower, M. R. Alfarra, J. L. Jimenez, A. M. Middlebrook, F. Drewnick, T. B. Onasch, M. R. Canagaratna, J. T. Jayne, and D. R. Worsnop, A generalised method for the extraction of chemically resolved mass spectra from Aerodyne Aerosol Mass Spectrometer data, *Journal of Aerosol Science*, *35*(7), 909–922, doi:10.1016/j.jaerosci.2004.02.007, 2004.

Bates, R. G., and G. D. Pinching, Dissociation constant of aqueous ammonia at 0 to 50°C from E. m. f. studies of the ammonium salt of a weak acid, *Journal of the American Chemical Society*, *72*(3), 1393–1396, doi:10.1021/ja01159a087, 1950.

Berndt, T., T. Jokinen, M. Sipilä, R. L. Mauldin, III, H. Herrmann, F. Stratmann, H. Junninen, and M. Kulmala, H2SO4 formation from the gas-phase reaction of stabilized Criegee Intermediates with SO2: Influence of water vapour content and temperature, *Atmospheric Environment*, *89*, 603–612, doi:10.1016/j.atmosenv.2014.02.062, 2014.

Bolton, D., The computation of equivalent potential temperature, *Monthly Weather Review*, *108*(7), 1046–1053, doi:10.1175/1520-0493(1980)108<1046:Tcoept>2.0.Co;2, 1980.

Budisulistiorini, S. H., M. R. Canagaratna, P. L. Croteau, K. Baumann, E. S. Edgerton, M. S. Kollman, N. L. Ng, V. Verma, S. L. Shaw, E. M. Knipping, D. R. Worsnop, J. T. Jayne, R. J. Weber, and J. D. Surratt, Intercomparison of an Aerosol Chemical Speciation Monitor (ACSM) with ambient fine aerosol measurements in Downtown Atlanta, Georgia, *Atmospheric Measurement Techniques Discussions*, *6*(6), 11,181–11,213, doi:10.5194/amtd-6-11181-2013, 2013.

Canagaratna, M. R., J. T. Jayne, D. A. Ghertner, S. Herndon, Q. Shi, J. L. Jimenez, P. J. Silva, P. Williams, T. Lanni, F. Drewnick, K. L. Demerjian, C. E. Kolb, and D. R. Worsnop, Case studies of particulate emissions from in-use New York City vehicles, *Aerosol Science and Technology*, *38*(6), 555–573, doi:10.1080/02786820490465504, 2004.

Canagaratna, M. R., J. T. Jayne, J. L. Jimenez, J. D. Allan, M. R. Alfarra, Q. Zhang, T. B. Onasch, F. Drewnick, H. Coe, A. Middlebrook, A. Delia, L. R. Williams, A. M. Trimborn, M. J. Northway, P. F. DeCarlo, C. E. Kolb, P. Davidovits, and D. R. Worsnop, Chemical and microphysical characterization of ambient aerosols with the Aerodyne Aerosol Mass Spectrometer, *Mass Spectrometry Reviews*, *26*(2), 185–222, doi:10.1002/mas.20115, 2007.

Canonaco, F., M. Crippa, J. G. Slowik, U. Baltensperger, and A. S. H. Prevot, SoFi, an IGOR-based interface for the efficient use of the generalized Multilinear Engine (ME-2) for the source apportionment: ME-2 application to Aerosol Mass Spectrometer data, *Atmospheric Measurement Techniques*, *6*(12), 3649–3661, doi:10.5194/amt-6-3649-2013, 2013.

Chasteen, T. G., and R. Bentley, Volatile organic sulfur compounds of environmental interest: dimethyl sulfide and methanethiol. An introductory overview, *Journal of Chemical Education*, *81*(10), 1524–1528, doi:10.1021/ed081p1524, 2004.

Chhabra, P. S., R. C. Flagan, and J. H. Seinfeld, Elemental analysis of chamber organic aerosol using an Aerodyne High-Resolution Aerosol Mass Spectrometer, *Atmospheric Chemistry and Physics*, *10*(9), 4111–4131, doi:10.5194/acp-10-4111-2010, 2010.

Craven, J. S., L. D. Yee, N. L. Ng, M. R. Canagaratna, C. L. Loza, K. A. Schilling, R. L. N. Yatavelli, J. A. Thornton, P. J. Ziemann, R. C. Flagan, and J. H. Seinfeld, Analysis of secondary organic aerosol formation and aging using positive matrix factorization of high-resolution aerosol mass spectra: Application to the dodecane

low-nox system, *Atmospheric Chemistry and Physics*, *12*(24), 11,795–11,817, doi: 10.5194/acp-12-11795-2012, 2012.

Crippa, M., F. Canonaco, J. G. Slowik, I. El Haddad, P. F. DeCarlo, C. Mohr, M. F. Heringa, R. Chirico, N. Marchand, B. Temime-Roussel, E. Abidi, L. Poulain, A. Wiedensohler, U. Baltensperger, and A. S. H. Prevot, Primary and secondary organic aerosol origin by combined gas-particle phase source apportionment, *Atmospheric Chemistry and Physics*, *13*(16), 8411–8426, doi:10.5194/acp-13-8411-2013, 2013a.

Crippa, M., P. F. DeCarlo, J. G. Slowik, C. Mohr, M. F. Heringa, R. Chirico, L. Poulain, F. Freutel, J. Sciare, J. Cozic, C. F. Di Marco, M. Elsasser, J. B. Nicolas, N. Marchand, E. Abidi, A. Wiedensohler, F. Drewnick, J. Schneider, S. Borrmann, E. Nemitz, R. Zimmermann, J.-L. Jaffrezo, A. S. H. Prevot, and U. Baltensperger, Wintertime aerosol chemical composition and source apportionment of the organic fraction in the metropolitan area of Paris, *Atmospheric Chemistry and Physics*, *13*(2), 961–981, doi: 10.5194/acp-13-961-2013, 2013b.

Crippa, M., I. El Haddad, J. G. Slowik, P. F. DeCarlo, C. Mohr, M. F. Heringa, R. Chirico, N. Marchand, J. Sciare, U. Baltensperger, and A. S. H. Prevot, Identification of marine and continental aerosol sources in Paris using high resolution aerosol mass spectrometry, *Journal of Geophysical Research-Atmospheres*, *118*(4), 1950–1963, doi:10.1002/jgrd.50151, 2013c.

Crippa, M., F. Canonaco, V. A. Lanz, M. Äijälä, J. D. Allan, S. Carbone, G. Capes, D. Ceburnis, M. Dall'Osto, D. A. Day, P. F. DeCarlo, M. Ehn, A. Eriksson, E. Freney, L. Hildebrandt Ruiz, R. Hillamo, J. L. Jimenez, H. Junninen, A. Kiendler-Scharr, A.-M. Kortelainen, M. Kulmala, A. Laaksonen, A. A. Mensah, C. Mohr, E. Nemitz, C. O'Dowd, J. Ovadnevaite, S. N. Pandis, T. Petäjä, L. Poulain, S. Saarikoski, K. Sellegri, E. Swietlicki, P. Tiitta, D. R. Worsnop, U. Baltensperger, and A. S. H. Prevot, Organic aerosol components derived from 25 AMS data sets across Europe using a consistent ME-2 based source apportionment approach, *Atmospheric Chemistry and Physics*, *14*(12), 6159–6176, doi:10.5194/acp-14-6159-2014, 2014.

Crosier, J., J. D. Allan, H. Coe, K. N. Bower, P. Formenti, and P. I. Williams, Chemical composition of summertime aerosol in the Po Valley (Italy), northern Adriatic and Black Sea, *Quarterly Journal of the Royal Meteorological Society*, *133*(S1), 61–75, doi: 10.1002/qj.88, 2007.

D'Almeida, G. A., P. Koepke, and E. P. Shettle, *Atmospheric aerosols: global climato-*

logy and radiative characteristics (studies in geophysical optics and remote sensing), A. Deepak Publishing, 1991.

DeCarlo, P. F., J. G. Slowik, D. R. Worsnop, P. Davidovits, and J. L. Jimenez, Particle morphology and density characterization by combined mobility and aerodynamic diameter measurements. Part 1: Theory, *Aerosol Science and Technology*, *38*(12), 1185–1205, doi:10.1080/027868290903907, 2004.

DeCarlo, P. F., J. R. Kimmel, A. Trimborn, M. J. Northway, J. T. Jayne, A. C. Aiken, M. Gonin, K. Fuhrer, T. Horvath, K. S. Docherty, D. R. Worsnop, and J. L. Jimenez, Field-deployable, High-Resolution, Time-of-Flight Aerosol Mass Spectrometer, *Analytical Chemistry*, *78*(24), 8281–8289, doi:10.1021/ac061249n, 2006.

Derksen, J., G.-J. Roelofs, R. Otjes, G. de Leeuw, and T. Röckmann, Impact of ammonium nitrate chemistry on the AOT in Cabauw, the Netherlands, *Atmospheric Environment*, *45*(31), 5640–5646, doi:10.1016/j.atmosenv.2011.02.052, 2011.

Diesch, J.-M., F. Drewnick, S. R. Zorn, S.-L. von der Weiden-Reinmüller, M. Martinez, and S. Borrmann, Variability of aerosol, gaseous pollutants and meteorological characteristics associated with changes in air mass origin at the SW Atlantic coast of Iberia, *Atmospheric Chemistry and Physics*, *12*(8), 3761–3782, doi:10.5194/acp-12-3761-2012, 2012.

Docherty, K. S., A. C. Aiken, J. A. Huffman, I. M. Ulbrich, P. F. DeCarlo, D. Sueper, D. R. Worsnop, D. C. Snyder, R. E. Peltier, R. J. Weber, B. D. Grover, D. J. Eatough, B. J. Williams, A. H. Goldstein, P. J. Ziemann, and J. L. Jimenez, The 2005 Study of Organic Aerosols at Riverside (SOAR-1): Instrumental intercomparisons and fine particle composition, *Atmospheric Chemistry and Physics*, *11*(23), 12,387–12,420, doi:10.5194/acp-11-12387-2011, 2011.

Dryahina, K., M. Polasek, and P. Spanel, A selected ion flow tube, SIFT, study of the ion chemistry of H3O+, NO+ and O2+ ions with several nitroalkanes in the presence of water vapour, *International Journal of Mass Spectrometry*, *239*(1), 57–65, doi:10.1016/j.ijms.2004.09.007, 2004.

Fangmeier, A., A. Hadwiger-Fangmeier, L. van der Eerden, and H.-J. Jäger, Effects of atmospheric ammonia on vegetation - A review, *Environmental Pollution*, *86*(1), 43–82, doi:10.1016/0269-7491(94)90008-6, 1994.

Farmer, D. K., A. Matsunaga, K. S. Docherty, J. D. Surratt, J. H. Seinfeld, P. J. Ziemann, and J. L. Jimenez, Response of an Aerosol Mass Spectrometer to organonitrates and

organosulfates and implications for atmospheric chemistry, *Proceedings of the National Academy of Sciences*, *107*(15), 6670–6675, doi:10.1073/pnas.0912340107, 2010.

Finlayson-Pitts, B. J., and J. N. Pitts, *Chemistry of the upper and lower atmosphere - theory, experiments and applications*, Academic Press, 2000.

Fry, J. L., A. Kiendler-Scharr, A. W. Rollins, P. J. Wooldridge, S. S. Brown, H. Fuchs, W. Dubé, A. Mensah, M. Dal Maso, R. Tillmann, H.-P. Dorn, T. Brauers, and R. C. Cohen, Organic nitrate and secondary organic aerosol yield from NO3 oxidation of β-pinene evaluated using a gas-phase kinetics/aerosol partitioning model, *Atmospheric Chemistry and Physics*, *9*, 1431–1449, doi:10.5194/acp-9-1431-2009, 2009.

Fry, J. L., A. Kiendler-Scharr, A. W. Rollins, T. Brauers, S. S. Brown, H.-P. Dorn, W. P. Dubé, H. Fuchs, A. Mensah, F. Rohrer, R. Tillmann, A. Wahner, P. J. Wooldridge, and R. C. Cohen, SOA from limonene: Role of NO3 in its generation and degradation, *Atmospheric Chemistry and Physics*, *11*(8), 3879–3894, doi:10.5194/acp-11-3879-2011, 2011.

Goldstein, A. H., and I. E. Galbally, Known and unexplored organic constituents in the earth's atmosphere, *Environmental Science & Technology*, *41*(5), 1514–1521, doi:10.1021/Es072476p, 2007.

Graber, E. R., and Y. Rudich, Atmospheric HULIS: How humic-like are they? A comprehensive and critical review, *Atmospheric Chemistry and Physics*, *6*(3), 729–753, doi:10.5194/acp-6-729-2006, 2006.

Graus, M., M. Müller, and A. Hansel, High Resolution PTR-TOF: Quantification and formula confirmation of VOC in real time, *Journal of the American Society for Mass Spectrometry*, *21*(6), 1037–1044, doi:10.1016/j.jasms.2010.02.006, 2010.

Guenther, A., C. N. Hewitt, D. Erickson, R. Fall, C. Geron, T. Graedel, P. Harley, L. Klinger, M. Lerdau, W. A. Mckay, T. Pierce, B. Scholes, R. Steinbrecher, R. Tallamraju, J. Taylor, and P. Zimmerman, A global model of natural volatile organic compound emissions, *Journal of Geophysical Research-Atmospheres*, *100*, 8873–8892, doi:10.1029/94JD02950, 1995.

Guenther, A. B., X. Jiang, C. L. Heald, T. Sakulyanontvittaya, T. Duhl, L. K. Emmons, and X. Wang, The Model of Emissions of Gases and Aerosols from Nature version 2.1 (MEGAN2.1): an extended and updated framework for modeling biogenic emissions, *Geoscientific Model Development*, *5*(6), 1471–1492, doi:10.5194/gmd-5-1471-2012, 2012.

Hallquist, M., J. C. Wenger, U. Baltensperger, Y. Rudich, D. Simpson, M. Claeys, J. Dommen, N. M. Donahue, C. George, A. H. Goldstein, J. F. Hamilton, H. Herrmann, T. Hoffmann, Y. Iinuma, M. Jang, M. Jenkin, J. L. Jimenez, A. Kiendler-Scharr, W. Maenhaut, G. McFiggans, T. F. Mentel, A. Monod, A. S. H. Prevot, J. H. Seinfeld, J. D. Surratt, R. Szmigielski, and J. Wildt, The formation, properties and impact of secondary organic aerosol: current and emerging issues, *Atmospheric Chemistry and Physics*, *9*(1), 3555–3762, doi:10.5194/acp-9-5155-2009, 2009.

Hansel, A., A. Jordan, C. Warneke, R. Holzinger, and W. Lindinger, Improved detection limit of the Proton-Transfer Reaction Mass Spectrometer: On-line monitoring of volatile organic compounds at mixing ratios of a few pptv, *Rapid Communications in Mass Spectrometry*, *12*(13), 871–875, doi:10.1002/(SICI)1097-0231(19980715)12:13<871::AID-RCM245>3.0.CO;2-L, 1998.

Haynes, W., *CRC Handbook of Chemistry and Physics, 93rd edition*, Taylor & Francis, 2012.

Hayward, S., C. N. Hewitt, J. H. Sartin, and S. M. Owen, Performance characteristics and applications of a Proton Transfer Reaction Mass Spectrometer for measuring volatile organic compounds in ambient air, *Environmental Science & Technology*, *36*(7), 1554–1560, doi:10.1021/es0102181, 2002.

Hinds, W. C., *Aerosol technology: properties, behavior, and measurement of airborne particles*, Wiley-Interscience, 1999.

Holzinger, R., A. Kasper-Giebl, M. Staudinger, G. Schauer, and T. Röckmann, Analysis of the chemical composition of organic aerosol at the Mt. Sonnblick observatory using a novel high mass resolution thermal-desorption proton-transfer-reaction mass-spectrometer (hr-TD-PTR-MS), *Atmospheric Chemistry and Physics*, *10*(20), 10,111–10,128, doi:10.5194/acp-10-10111-2010, 2010a.

Holzinger, R., J. Williams, F. Herrmann, J. Lelieveld, N. M. Donahue, and T. Roeckmann, Aerosol analysis using a Thermal-Desorption Proton-Transfer-Reaction Mass Spectrometer (TD-PTR-MS): a new approach to study processing of organic aerosols, *Atmospheric Chemistry and Physics*, *10*(5), 2257–2267, doi:10.5194/acp-10-2257-2010, 2010b.

Holzinger, R., A. H. Goldstein, P. L. Hayes, J. L. Jimenez, and J. Timkovsky, Chemical evolution of organic aerosol in Los Angeles during the CalNex 2010 study, *Atmospheric Chemistry and Physics*, *13*(19), 10,125–10,141, doi:10.5194/acp-13-10125-2013, 2013.

Huffman, J. A., J. T. Jayne, F. Drewnick, A. C. Aiken, T. Onasch, D. R. Worsnop, and J. L. Jimenez, Design, modeling, optimization, and experimental tests of a particle beam width probe for the Aerodyne Aerosol Mass Spectrometer, *Aerosol Science and Technology*, *39*(12), 1143–1163, doi:10.1080/02786820500423782, 2005.

Hunter, E. P. L., and S. G. Lias, Evaluated gas phase basicities and proton affinities of molecules: An update, *Journal of Physical and Chemical Reference Data*, *27*(3), 413–656, 1998.

IPCC, *Climate Change 2013: The Physical Science Basis. Contribution of Working Group I to the Fifth Assessment Report of the Intergovernmental Panel on Climate Change*, 1535 pp., Cambridge University Press, Cambridge, United Kingdom and New York, NY, USA, doi:10.1017/CBO9781107415324, 2013.

Jayne, J. T., D. C. Leard, X. F. Zhang, P. Davidovits, K. A. Smith, C. E. Kolb, and D. R. Worsnop, Development of an Aerosol Mass Spectrometer for size and composition analysis of submicron particles, *Aerosol Science and Technology*, *33*(1-2), 49–70, doi: 10.1080/027868200410840, 2000.

Jimenez, J. L., J. T. Jayne, Q. Shi, C. E. Kolb, D. R. Worsnop, I. Yourshaw, J. H. Seinfeld, R. C. Flagan, X. Zhang, K. A. Smith, J. W. Morris, and P. Davidovits, Ambient aerosol sampling using the Aerodyne Aerosol Mass Spectrometer, *Journal of Geophysical Research-Atmospheres*, *108*(D7), doi:10.1029/2001JD001213, 2003.

Jimenez, J. L., M. R. Canagaratna, N. M. Donahue, A. S. H. Prevot, Q. Zhang, J. H. Kroll, P. F. DeCarlo, J. D. Allan, H. Coe, N. L. Ng, A. C. Aiken, K. S. Docherty, I. M. Ulbrich, A. P. Grieshop, A. L. Robinson, J. Duplissy, J. D. Smith, K. R. Wilson, V. A. Lanz, C. Hueglin, Y. L. Sun, J. Tian, A. Laaksonen, T. Raatikainen, J. Rautiainen, P. Vaattovaara, M. Ehn, M. Kulmala, J. M. Tomlinson, D. R. Collins, M. J. Cubison, E. J. Dunlea, J. A. Huffman, T. B. Onasch, M. R. Alfarra, P. I. Williams, K. Bower, Y. Kondo, J. Schneider, F. Drewnick, S. Borrmann, S. Weimer, K. Demerjian, D. Salcedo, L. Cottrell, R. Griffin, A. Takami, T. Miyoshi, S. Hatakeyama, A. Shimono, J. Y. Sun, Y. M. Zhang, K. Dzepina, J. R. Kimmel, D. Sueper, J. T. Jayne, S. C. Herndon, A. M. Trimborn, L. R. Williams, E. C. Wood, A. M. Middlebrook, C. E. Kolb, U. Baltensperger, and D. R. Worsnop, Evolution of organic aerosols in the atmosphere, *Science*, *326*(5959), 1525–1529, doi:10.1126/science.1180353, 2009.

Jordan, A., S. Haidacher, G. Hanel, E. Hartungen, L. Maerk, H. Seehauser, R. Schottkowsky, P. Sulzer, and T. Maerk, A high resolution and high sensitivity Proton-

Transfer-Reaction Time-of-Flight Mass Spectrometer (PTR-TOF-MS), *International Journal of Mass Spectrometry*, *286*(286), 122–128, doi:10.1016/j.ijms.2009.07.005, 2009.

Kanakidou, M., J. H. Seinfeld, S. N. Pandis, I. Barnes, F. J. Dentener, M. C. Facchini, R. van Dingenen, B. Ervens, A. Nenes, C. J. Nielsen, E. Swietlicki, J. P. Putaud, Y. Balkanski, S. Fuzzi, J. Horth, G. K. Moortgat, R. Winterhalter, C. E. L. Myhre, K. Tsigaridis, E. Vignati, E. G. Stephanou, and J. Wilson, Organic aerosol and global climate modelling: A review, *Atmospheric Chemistry and Physics*, *5*, 1053–1123, doi:10.5194/acp-5-1053-2005, 2005.

Kiss, G., E. Tombacz, B. Varga, T. Alsberg, and L. Persson, Estimation of the average molecular weight of humic-like substances isolated from fine atmospheric aerosol, *Atmospheric Environment*, *37*(27), 3783–3794, doi:10.1016/S1352-2310(03)00468-0, 2003.

Krupa, S. V., Effects of atmospheric ammonia (NH3) on terrestrial vegetation: A review, *Environmental Pollution*, *124*(2), 179–221, doi:10.1016/S0269-7491(02)00434-7, 2003.

Kuenen, J. J. P., A. J. H. Visschedijk, M. Jozwicka, and H. A. C. Denier van der Gon, TNO-MACC II emission inventory: a multi-year (2003-2009) consistent high-resolution European emission inventory for air quality modelling, *Atmospheric Chemistry and Physics Discussions*, *14*(5), 5837–5869, doi:10.5194/acpd-14-5837-2014, 2014.

Kulmala, M., A. Asmi, H. K. Lappalainen, U. Baltensperger, J.-L. Brenguier, M. C. Facchini, H.-C. Hansson, O. Hov, C. D. O'Dowd, U. Pöschl, A. Wiedensohler, R. Boers, O. Boucher, G. de Leeuw, H. A. C. Denier van der Gon, J. Feichter, R. Krejci, P. Laj, H. Lihavainen, U. Lohmann, G. McFiggans, T. Mentel, C. Pilinis, I. Riipinen, M. Schulz, A. Stohl, E. Swietlicki, E. Vignati, C. Alves, M. Amann, M. Ammann, S. Arabas, P. Artaxo, H. Baars, D. C. S. Beddows, R. Bergstroem, J. P. Beukes, M. Bilde, J. F. Burkhart, F. Canonaco, S. L. Clegg, H. Coe, S. Crumeyrolle, B. D'Anna, S. Decesari, S. Gilardoni, M. Fischer, A. M. Fjaeraa, C. Fountoukis, C. George, L. Gomes, P. Halloran, T. Hamburger, R. M. Harrison, H. Herrmann, T. Hoffmann, C. Hoose, M. Hu, A. Hyvärinen, U. Horrak, Y. Iinuma, T. Iversen, M. Josipovic, M. Kanakidou, A. Kiendler-Scharr, A. Kirkevag, G. Kiss, Z. Klimont, P. Kolmonen, M. Komppula, J.-E. Kristjaensson, L. Laakso, A. Laaksonen, L. Labonnote, V. A. Lanz, K. E. J. Lehtinen, L. V. Rizzo, R. Makkonen, H. E. Manninen, G. McMeeking, J. Merikanto, A. Minikin, S. Mirme, W. T. Morgan, E. Nemitz, D. O'Donnell, T. S. Panwar, H. Pawlowska, A. Petzold, J. J. Pienaar, C. Pio, C. Plass-Duelmer, A. S. H. Prevot, S. Pryor, C. L. Reddington, G. Roberts, D. Rosenfeld, J. Schwarz, O. Seland, K. Sellegri, X. J. Shen, M. Shiraiwa, H. Siebert, B. Sierau, D. Simpson, J. Y. Sun, D. Topping, P. Tunved,

P. Vaattovaara, V. Vakkari, J. P. Veefkind, A. Visschedijk, H. Vuollekoski, R. Vuolo, B. Wehner, J. Wildt, S. Woodward, D. R. Worsnop, G.-J. van Zadelhoff, A. A. Zardini, K. Zhang, P. G. van Zyl, V.-M. Kerminen, K. S Carslaw, and S. N. Pandis, General overview: European Integrated project on Aerosol Cloud Climate and Air Quality interactions (EUCAARI); integrating aerosol research from nano to global scales, *Atmospheric Chemistry and Physics*, *11*(24), 13,061–13,143, doi:10.5194/acp-11-13061-2011, 2011.

Lanz, V. A., M. R. Alfarra, U. Baltensperger, B. Buchmann, C. Hueglin, and A. S. H. Prevot, Source apportionment of submicron organic aerosols at an urban site by factor analytical modelling of aerosol mass spectra, *Atmospheric Chemistry and Physics*, *7*(6), 1503–1522, doi:10.5194/acp-7-1503-2007, 2007.

Lindinger, W., A. Hansel, and A. Jordan, On-line monitoring of volatile organic compounds at pptv levels by means of proton-transfer-reaction mass spectrometry (PTR-MS) - Medical applications, food control and environmental research, *International Journal of Mass Spectrometry*, *173*(3), 191–241, doi:10.1016/S0168-1176(97)00281-4, 1998.

Liu, P., P. J. Ziemann, D. B. Kittelson, and P. H. McMurry, Generating particle beams of controlled dimensions and divergence. 1. Theory of particle motion in aerodynamic lenses and nozzle expansions, *Aerosol Science and Technology*, *22*(3), 293–313, doi:10.1080/02786829408959748, 1995a.

Liu, P., P. J. Ziemann, D. B. Kittelson, and P. H. McMurry, Generating particle beams of controlled dimensions and divergence. 2. Experimental evaluation of particle motion in aerodynamic lenses and nozzle expansions, *Aerosol Science and Technology*, *22*(3), 314–324, doi:10.1080/02786829408959749, 1995b.

Liu, P. S. K., R. Deng, K. A. Smith, L. R. Williams, J. T. Jayne, M. R. Canagaratna, K. Moore, T. B. Onasch, D. R. Worsnop, and T. Deshler, Transmission efficiency of an aerodynamic focusing lens system: Comparison of model calculations and laboratory measurements for the Aerodyne Aerosol Mass Spectrometer, *Aerosol Science and Technology*, *41*(8), 721–733, doi:10.1080/02786820701422278, 2007.

Matthew, B. M., A. M. Middlebrook, and T. B. Onasch, Collection efficiencies in an Aerodyne Aerosol Mass Spectrometer as a function of particle phase for laboratory generated aerosols, *Aerosol Science and Technology*, *42*(11), 884–898, doi:10.1080/02786820802356797, 2008.

Mensah, A. A., Water and organic nitrate detection in an AMS: Laboratory characterization and application to ambient measurements, Ph.D. thesis, Universität zu Köln, 2011.

Mensah, A. A., A. Buchholz, T. F. Mentel, R. Tillmann, and A. Kiendler-Scharr, Aerosol mass spectrometric measurements of stable crystal hydrates of oxalates and inferred relative ionization efficiency of water, *Journal of Aerosol Science*, *42*(1), 11–19, doi: 10.1016/j.jaerosci.2010.10.003, 2011.

Mensah, A. A., R. Holzinger, R. Otjes, A. Trimborn, T. F. Mentel, H. ten Brink, B. Henzing, and A. Kiendler-Scharr, Aerosol chemical composition at Cabauw, The Netherlands as observed in two intensive periods in May 2008 and March 2009, *Atmospheric Chemistry and Physics*, *12*(10), 4723–4742, doi:10.5194/acp-12-4723-2012, 2012.

Middlebrook, A. M., R. Bahreini, J. L. Jimenez, and M. R. Canagaratna, Evaluation of composition-dependent collection efficiencies for the Aerodyne Aerosol Mass Spectrometer using field data, *Aerosol Science and Technology*, *46*(3), 258–271, doi: 10.1080/02786826.2011.620041, 2012.

Mohr, C., P. F. DeCarlo, M. F. Heringa, R. Chirico, J. G. Slowik, R. Richter, C. Reche, A. Alastuey, X. Querol, R. Seco, J. Penkett, S Auelas, J. L. Jimenez, M. Crippa, R. Zimmermann, U. Baltensperger, and A. S. H. Prevot, Identification and quantification of organic aerosol from cooking and other sources in Barcelona using Aerosol Mass Spectrometer data, *Atmospheric Chemistry and Physics*, *12*(4), 1649–1665, doi: 10.5194/acp-12-1649-2012, 2012.

Monks, P. S., C. Granier, S. Fuzzi, A. Stohl, M. L. Williams, H. Akimoto, M. Amann, A. Baklanov, U. Baltensperger, I. Bey, N. Blake, R. S. Blake, K. Carslaw, O. R. Cooper, F. Dentener, D. Fowler, E. Fragkou, G. J. Frost, S. Generoso, P. Ginoux, V. Grewe, A. Guenther, H. C. Hansson, S. Henne, J. Hjorth, A. Hofzumahaus, H. Huntrieser, I. S. A. Isaksen, M. Jenkin, J. Kaiser, M. Kanakidou, Z. Klimont, M. Kulmala, P. Laj, M. G. Lawrence, J. D. Lee, C. Liousse, M. Maione, G. McFiggans, A. Metzger, A. Mieville, N. Moussiopoulos, J. J. Orlando, C. D. O'Dowd, P. I. Palmer, D. D. Parrish, A. Petzold, U. Platt, U. Pöschl, A. S. H. Prevot, C. E. Reeves, S. Reimann, Y. Rudich, K. Sellegri, R. Steinbrecher, D. Simpson, H. ten Brink, J. Theloke, G. R. van der Werf, R. Vautard, V. Vestreng, C. Vlachokostas, and R. von Glasow, Atmospheric composition change - global and regional air quality, *Atmospheric Environment*, *43*(33), 5268–5350, doi:10.1016/j.atmosenv.2009.08.021, 2009.

Morgan, W. T., J. D. Allan, K. N. Bower, M. Esselborn, B. Harris, J. S. Henzing, E. J. Highwood, A. Kiendler-Scharr, G. R. McMeeking, A. A. Mensah, M. J. Northway, S. Osborne, P. I. Williams, R. Krejci, and H. Coe, Enhancement of the aerosol direct radiative effect by semi-volatile aerosol components: Airborne measurements in North-Western Europe, *Atmospheric Chemistry and Physics*, *10*(17), 8151–8171, doi:10.5194/acp-10-8151-2010, 2010.

Neff, J., E. Holland, F. Dentener, W. McDowell, and K. Russell, The origin, composition and rates of organic nitrogen deposition: A missing piece of the nitrogen cycle?, *Biogeochemistry*, *57-58*(1), 99–136, doi:10.1023/A:1015791622742, 2002.

Ng, N. L., M. R. Canagaratna, Q. Zhang, J. L. Jimenez, J. Tian, I. M. Ulbrich, J. H. Kroll, K. S. Docherty, P. S. Chhabra, R. Bahreini, S. M. Murphy, J. H. Seinfeld, L. Hildebrandt, N. M. Donahue, P. F. DeCarlo, V. A. Lanz, A. S. H. Prevot, E. Dinar, Y. Rudich, and D. R. Worsnop, Organic aerosol components observed in northern hemispheric datasets from aerosol mass spectrometry, *Atmospheric Chemistry and Physics*, *10*(10), 4625–4641, doi:10.5194/acp-10-4625-2010, 2010.

Ng, N. L., M. R. Canagaratna, J. L. Jimenez, Q. Zhang, I. M. Ulbrich, and D. R. Worsnop, Real-time methods for estimating organic component mass concentrations from Aerosol Mass Spectrometer data., *Environmental Science & Technology*, *45*(3), 910–916, doi:10.1021/es102951k, 2011a.

Ng, N. L., S. C. Herndon, A. Trimborn, M. R. Canagaratna, P. L. Croteau, T. B. Onasch, D. Sueper, D. R. Worsnop, Q. Zhang, Y. L. Sun, and J. T. Jayne, An Aerosol Chemical Speciation Monitor (ACSM) for routine monitoring of the composition and mass concentrations of ambient aerosol, *Aerosol Science and Technology*, *45*(7), 780–794, doi:10.1080/02786826.2011.560211, 2011b.

Paatero, P., Least squares formulation of robust non-negative factor analysis, *Chemometrics and Intelligent Laboratory Systems*, *37*(1), 23–35, doi:10.1016/S0169-7439(96)00044-5, 1997.

Paatero, P., The Multilinear Engine - A table-driven, least squares program for solving multilinear problems, including the n-way parallel factor analysis model, *Journal of Computational and Graphical Statictics*, *8*(4), 854–888, doi:10.2307/1390831, 1999.

Paatero, P., and P. K. Hopke, Discarding or downweighting high-noise variables in factor analytic models, *Analytica Chimica Acta*, *490*(1-2), 277–289, doi:10.1016/S0003-2670(02)01643-4, 2003.

Paatero, P., and P. K. Hopke, Rotational tools for factor analytic models, *Journal of Chemometrics*, *23*(2), 91–100, doi:10.1002/cem.1197, 2009.

Paatero, P., and U. Tapper, Positive Matrix Factorization - a non-negative factor model with optimal utilization of error-estimates of data values, *Environmetrics*, *5*(2), 111–126, doi:10.1002/env.3170050203, 1994.

Paatero, P., P. K. Hopke, X.-H. Song, and Z. Ramadan, Understanding and controlling rotations in factor analytic models, *Chemometrics and Intelligent Laboratory Systems*, *60*(12), 253–264, doi:10.1016/S0169-7439(01)00200-3, 2002.

Paglione, M., A. Kiendler-Scharr, A. A. Mensah, E. Finessi, L. Giulianelli, S. Sandrini, M. C. Facchini, S. Fuzzi, P. Schlag, A. Piazzalunga, E. Tagliavini, J. S. Henzing, and S. Decesari, Identification of humic-like substances (HULIS) in oxygenated organic aerosols using NMR and AMS factor analyses and liquid chromatographic techniques, *Atmospheric Chemistry and Physics*, *14*(1), 25–45, doi:10.5194/acp-14-25-2014, 2014.

Patty, F., G. Clayton, and F. Clayton, *Patty's industrial hygiene and toxicology*, Wiley, doi:10.1002/0471435139, 1982.

Pearlman, R. S., S. H. Yalkowsky, and S. Banerjee, Water solubilities of polynuclear aromatic and heteroaromatic compounds, *Journal of Physical and Chemical Reference Data*, *13*(2), 555–562, doi:10.1063/1.555712, 1984.

Perring, A. E., S. E. Pusede, and R. C. Cohen, An observational perspective on the atmospheric impacts of alkyl and multifunctional nitrates on ozone and secondary organic aerosol, *Chemical Reviews*, *113*(8), 5848–5870, doi:10.1021/cr300520x, 2013.

Petzold, A., and M. Schönlinner, Multi-angle absorption photometry: A new method for the measurement of aerosol light absorption and atmospheric black carbon, *Journal of Aerosol Science*, *35*(4), 421–441, doi:10.1016/j.jaerosci.2003.09.005, 2004.

Petzold, A., H. Schloesser, P. J. Sheridan, W. P. Arnott, J. A. Ogren, and A. Virkkula, Evaluation of multiangle absorption photometry for measuring aerosol light absorption, *Aerosol Science and Technology*, *39*(1), 40–51, doi:10.1080/027868290901945, 2005.

Petzold, A., J. A. Ogren, M. Fiebig, P. Laj, S.-M. Li, U. Baltensperger, T. Holzer-Popp, S. Kinne, G. Pappalardo, N. Sugimoto, C. Wehrli, A. Wiedensohler, and X.-Y. Zhang, Recommendations for reporting "black carbon" measurements, *Atmospheric Chemistry and Physics*, *13*(16), 8365–8379, doi:10.5194/acp-13-8365-2013, 2013.

Phinney, L., W. Richard Leaitch, U. Lohmann, H. Boudries, D. R. Worsnop, J. T. Jayne, D. Toom-Sauntry, M. Wadleigh, S. Sharma, and N. Shantz, Characterization of the aerosol over the sub-arctic north east Pacific Ocean, *Deep Sea Research Part II: Topical Studies in Oceanography*, *53*(20-22), 2410–2433, doi:10.1016/j.dsr2.2006.05.044, 2006.

Pope, I. C., R. T. Burnett, and M. J. Thun, Lung cancer, cardiopulmonary mortality, and long-term exposure to fine particulate air pollution, *Journal of the American Medical Association*, *287*(9), 1132–1141, doi:10.1001/jama.287.9.1132, 2002.

Quinn P. K., Bates T. S., Coffman D., Onasch T. B., Worsnop D., Baynard T., de Gouw J. A., Goldan P. D., Kuster W.C., Williams E., Roberts J. M., Lerner B., Stohl A., Pettersson A., and E. R. Lovejoy, Impacts of sources and aging on submicrometer aerosol properties in the marine boundary layer across the Gulf of Maine, *Journal of Geophysical Research-Atmospheres*, *111*(D23S36), doi:10.1029/2006JD007582, 2006.

Ramanathan, V., F. Li, M. V. Ramana, P. S. Praveen, D. Kim, C. E. Corrigan, H. Nguyen, E. A. Stone, J. J. Schauer, G. R. Carmichael, B. Adhikary, and S. C. Yoon, Atmospheric brown clouds: Hemispherical and regional variations in long-range transport, absorption, and radiative forcing, *Journal of Geophysical Research-Atmospheres*, *112*(D22), doi:10.1029/2006JD008124, 2007.

Reff, A., S. I. Eberly, and P. V. Bhave, Receptor modeling of ambient particulate matter data using Positive Matrix Factorization: Review of existing methods., *Journal of the Air & Waste Management Association*, *57*(2), 146–154, doi:10.1080/10473289.2007.10465319, 2007.

Roberts, J. M., The atmospheric chemistry of organic nitrates, *Atmospheric Environment*, *24*(2), 243–287, doi:10.1016/0960-1686(90)90108-Y, 1990.

Rogge, W. F., M. A. Mazurek, L. M. Hildemann, G. R. Cass, and B. R. T. Simoneit, Quantification of urban organic aerosols at a molecular-level - identification, abundance and seasonal-variation, *Atmospheric Environment Part A-General Topics*, *27*(8), 1309–1330, doi:10.1016/0960-1686(93)90257-Y, 1993.

Romanou, A., B. Liepert, G. A. Schmidt, W. B. Rossow, R. A. Ruedy, and Y. Zhang, 20th century changes in surface solar irradiance in simulations and observations, *Geophysical Research Letters*, *34*(L05713), doi:10.1029/2006GL028356, 2007.

Rubach, F., Aerosol processes in the planetary boundary layer: High resolution aerosol mass spectrometry on a Zeppelin NT airship, Ph.D. thesis, Bergische Universität Wuppertal, 2013.

Russchenberg, H., F. Bosveld, D. Swart, H. ten Brink, G. de Leeuw, R. Uijlenhoet, B. Arbesser-Rastburg, H. van der Marel, L. Ligthart, R. Boers, and A. Apituley, Ground-based atmospheric remote sensing in the Netherlands: European outlook, *IEICE Transactions on Communications*, *E88B*(6), 2252–2258, doi:10.1093/ietcom/e88-b.6.2252, 2005.

Saarikoski, S., S. Carbone, S. Decesari, L. Giulianelli, F. Angelini, M. Canagaratna, N. L. Ng, A. Trimborn, M. C. Facchini, S. Fuzzi, R. Hillamo, and D. R. Worsnop, Chemical characterization of springtime submicrometer aerosol in Po Valley, Italy, *Atmospheric Chemistry and Physics*, *12*(18), 8401–8421, doi:10.5194/acp-12-8401-2012, 2012.

Sarwar, G., K. Fahey, R. Kwok, R. C. Gilliam, S. J. Roselle, R. Mathur, J. Xue, J. Yu, and W. P. L. Carter, Potential impacts of two SO2 oxidation pathways on regional sulfate concentrations: Aqueous-phase oxidation by NO2 and gas-phase oxidation by Stabilized Criegee Intermediates, *Atmospheric Environment*, *68*, 186–197, doi:10.1016/j.atmosenv.2012.11.036, 2013.

Sarwar, G., H. Simon, K. Fahey, R. Mathur, W. S. Goliff, and W. R. Stockwell, Impact of sulfur dioxide oxidation by Stabilized Criegee Intermediate on sulfate, *Atmospheric Environment*, *85*, 204–214, doi:10.1016/j.atmosenv.2013.12.013, 2014.

Schaap, M., R. P. Otjes, and E. P. Weijers, Illustrating the benefit of using hourly monitoring data on secondary inorganic aerosol and its precursors for model evaluation, *Atmospheric Chemistry and Physics*, *11*(21), 11,041–11,053, doi:10.5194/acp-11-11041-2011, 2011.

Schmale, J., J. Schneider, E. Nemitz, Y. S. Tang, U. Dragosits, T. D. Blackall, P. N. Trathan, G. J. Phillips, M. Sutton, and C. F. Braban, Sub-Antarctic marine aerosol: dominant contributions from biogenic sources, *Atmospheric Chemistry and Physics*, *13*(17), 8669–8694, doi:10.5194/acp-13-8669-2013, 2013.

Schneider, J., S. Weimer, F. Drewnick, S. Borrmann, G. Helas, P. Gwaze, O. Schmid, M. Andreae, and U. Kärcher, Mass spectrometric analysis and aerodynamic properties of various types of combustion-related aerosol particles, *International Journal of Mass Spectrometry*, *258*(13), 37–49, doi:10.1016/j.ijms.2006.07.008, 2006.

Seibert, P., F. Beyrich, S.-E. Gryning, S. Joffre, A. Rasmussen, and P. Tercier, Review and intercomparison of operational methods for the determination of the mixing height, *Atmospheric Environment*, *34*(7), 1001–1027, doi:10.1016/S1352-2310(99)00349-0, 2000.

Seinfeld, J. H., and S. N. Pandis, *Atmospheric chemistry and physics: From air pollution to climate change*, Wiley-Interscience, 2006.

Setyan, A., Q. Zhang, M. Merkel, W. B. Knighton, Y. Sun, C. Song, J. E. Shilling, T. B. Onasch, S. C. Herndon, D. R. Worsnop, J. D. Fast, R. A. Zaveri, L. K. Berg, A. Wiedensohler, B. A. Flowers, M. K. Dubey, and R. Subramanian, Characterization of submicron particles influenced by mixed biogenic and anthropogenic emissions using high-resolution aerosol mass spectrometry: results from CARES, *Atmospheric Chemistry and Physics*, *12*(17), 8131–8156, doi:10.5194/acp-12-8131-2012, 2012.

Simoneit, B. R. T., and V. O. Elias, Detecting organic tracers from biomass burning in the atmosphere, *Marine Pollution Bulletin*, *42*(10), 805–810, doi:10.1016/S0025-326X(01)00094-7, 2001.

Simoneit, B. R. T., J. J. Schauer, C. G. Nolte, D. R. Oros, V. O. Elias, M. P. Fraser, W. F. Rogge, and G. R. Cass, Levoglucosan, a tracer for cellulose in biomass burning and atmospheric particles, *Atmospheric Environment*, *33*(2), 173–182, doi:10.1016/S1352-2310(98)00145-9, 1999.

Slowik, J. G., A. Vlasenko, M. McGuire, G. J. Evans, and J. P. D. Abbatt, Simultaneous factor analysis of organic particle and gas mass spectra: AMS and PTR-MS measurements at an urban site, *Atmospheric Chemistry and Physics*, *10*(4), 1969–1988, doi:10.5194/acp-10-1969-2010, 2010.

Spanel, P., J. M. Van Doren, and D. Smith, A selected ion flow tube study of the reactions of H3O+, NO+, and O2+ with saturated and unsaturated aldehydes and subsequent hydration of the product ions, *International Journal of Mass Spectrometry*, *213*(23), 163–176, doi:10.1016/S1387-3806(01)00531-0, 2002a.

Spanel, P., T. Wang, and D. Smith, A selected ion flow tube, SIFT, study of the reactions of H3O+, NO+ and O2+ ions with a series of diols, *International Journal of Mass Spectrometry*, *218*(3), 227–236, doi:10.1016/S1387-3806(02)00724-8, 2002b.

Stull, R., *An introduction to boundary layer meteorology*, Atmospheric sciences library, Kluwer Academic Publishers, 1988.

Subramanian, R., A. Y. Khlystov, J. C. Cabada, and A. L. Robinson, Positive and negative artifacts in particulate organic carbon measurements with denuded and undenuded sampler configurations special issue of aerosol science and technology on findings from the fine particulate matter supersites program, *Aerosol Science and Technology*, *38*(sup1), 27–48, doi:10.1080/02786820390229354, 2004.

Sun, Y., Z. Wang, H. Dong, T. Yang, J. Li, X. Pan, P. Chen, and J. T. Jayne, Characterization of summer organic and inorganic aerosols in Beijing, China with an Aerosol Chemical Speciation Monitor, *Atmospheric Environment*, *51*, 250–259, doi: 10.1016/j.atmosenv.2012.01.013, 2012.

Sun, Y. L., Q. Zhang, J. J. Schwab, K. L. Demerjian, W.-N. Chen, M.-S. Bae, H.-M. Hung, O. Hogrefe, B. Frank, O. V. Rattigan, and Y.-C. Lin, Characterization of the sources and processes of organic and inorganic aerosols in New York city with a High-Resolution Time-of-Flight Aerosol Mass Spectrometer, *Atmospheric Chemistry and Physics*, *11*(4), 1581–1602, doi:10.5194/acp-11-1581-2011, 2011.

Sun, Y. L., Z. F. Wang, P. Q. Fu, T. Yang, Q. Jiang, H. B. Dong, J. Li, and J. J. Jia, Aerosol composition, sources and processes during wintertime in Beijing, China, *Atmospheric Chemistry and Physics*, *13*(9), 4577–4592, doi:10.5194/acp-13-4577-2013, 2013.

Todd, J. F., Recommendations for nomenclature and symbolism for mass spectroscopy, *International Journal of Mass Spectrometry and Ion Processes*, *142*(3), 209–240, doi: 10.1016/0168-1176(95)93811-F, 1995.

Trebs, I., F. X. Meixner, J. Slanina, R. Otjes, P. Jongejan, and M. O. Andreae, Real-time measurements of ammonia, acidic trace gases and water-soluble inorganic aerosol species at a rural site in the Amazon Basin, *Atmospheric Chemistry and Physics*, *4*(4), 967–987, doi:10.5194/acp-4-967-2004, 2004.

Ulbrich, I. M., M. R. Canagaratna, Q. Zhang, D. R. Worsnop, and J. L. Jimenez, Interpretation of organic components from Positive Matrix Factorization of aerosol mass spectrometric data, *Atmospheric Chemistry and Physics*, *9*(9), 2891–2918, doi: 10.5194/acp-9-2891-2009, 2009.

Ulden, A. P., and J. Wieringa, Atmospheric boundary layer research at Cabauw, *Boundary-Layer Meteorology*, *78*(1-2), 39–69, doi:10.1007/BF00122486, 1996.

van der Hoek, K. W., Estimating ammonia emission factors in Europe: Summary of the work of the UNECE ammonia expert panel, *Atmospheric Environment*, *32*(3), 315–316, doi:10.1016/S1352-2310(97)00168-4, 1998.

Varga, B., G. Kiss, I. Ganszky, A. Gelencsar, and Z. Krivacsy, Isolation of water-soluble organic matter from atmospheric aerosol, *Talanta*, *55*(3), 561–572, doi:10.1016/S0039-9140(01)00446-5, 2001.

Vermeulen, A. T., A. Hensen, M. E. Popa, W. C. M. van den Bulk, and P. A. C. Jongejan, Greenhouse gas observations from Cabauw Tall Tower (1992-2010), *Atmospheric Measurement Techniques*, *4*(3), 617–644, doi:10.5194/amt-4-617-2011, 2011.

Vestreng, V., G. Myhre, H. Fagerli, S. Reis, and L. Tarrason, Twenty-five years of continuous sulphur dioxide emission reduction in Europe, *Atmospheric Chemistry and Physics*, *7*(13), 3663–3681, doi:10.5194/acp-7-3663-2007, 2007.

Viana, M., X. Chi, W. Maenhaut, J. Cafmeyer, X. Querol, A. Alastuey, P. Mikuska, and Z. Vecera, Influence of sampling artefacts on measured PM, OC, and EC Levels in carbonaceous aerosols in an urban area, *Aerosol Science and Technology*, *40*(2), 107–117, doi:10.1080/02786820500484388, 2006.

Viana, M., W. Maenhaut, H. M. ten Brink, X. Chi, E. Weijers, X. Querol, A. Alastuey, P. Mikuska, and Z. Vecera, Comparative analysis of organic and elemental carbon concentrations in carbonaceous aerosols in three European cities, *Atmospheric Environment*, *41*(28), 5972–5983, doi:10.1016/j.atmosenv.2007.03.035, 2007.

Wallace, J. M., and P. V. Hobbs, *Atmospheric science: An introductory survey*, International geophysics series, v. 92, Elsevier, 2006.

WHO, WHO Air quality guidelines for particulate matter, ozone, nitrogen dioxide and sulfur dioxide, *Tech. Rep. WHO/SDE/PHE/OEH/06.02*, World Health Organization, 20 Avenue Appia, 1211 Geneva 27, Switzerland, 2006.

Williams, A. G., W. Zahorowski, S. Chambers, A. Griffiths, J. M. Hacker, A. Element, and S. Werczynski, The vertical distribution of radon in clear and cloudy daytime terrestrial boundary layers, *Journal of the Atmospheric Sciences*, *68*(1), 155–174, doi:10.1175/2010JAS3576.1, 2010a.

Williams, B. J., A. H. Goldstein, D. B. Millet, R. Holzinger, N. M. Kreisberg, S. V. Hering, A. B. White, D. R. Worsnop, J. D. Allan, and J. L. Jimenez, Chemical speciation of organic aerosol during the International Consortium for Atmospheric Research on Transport and Transformation 2004: Results from in situ measurements, *Journal of Geophysical Research-Atmospheres*, *112*(D10S26), doi:10.1029/2006JD007601, 2007.

Williams, B. J., A. H. Goldstein, N. M. Kreisberg, S. V. Hering, D. R. Worsnop, I. M. Ulbrich, K. S. Docherty, and J. L. Jimenez, Major components of atmospheric organic aerosol in southern California as determined by hourly measurements of source marker compounds, *Atmospheric Chemistry and Physics*, *10*(23), 11,577–11,603, doi:10.5194/acp-10-11577-2010, 2010b.

Zhang, Q., M. R. Alfarra, D. R. Worsnop, J. D. Allan, H. Coe, M. R. Canagaratna, and J. L. Jimenez, Deconvolution and quantification of hydrocarbon-like and oxygenated organic aerosols based on aerosol mass spectrometry, *Environmental Science & Technology*, *39*(13), 4938–4952, doi:10.1021/es048568l, 2005.

Zhang, Q., J. L. Jimenez, M. R. Canagaratna, J. D. Allan, H. Coe, I. Ulbrich, M. R. Alfarra, A. Takami, A. M. Middlebrook, Y. L. Sun, K. Dzepina, E. Dunlea, K. Docherty, P. F. DeCarlo, D. Salcedo, T. Onasch, J. T. Jayne, T. Miyoshi, A. Shimono, S. Hatakeyama, N. Takegawa, Y. Kondo, J. Schneider, F. Drewnick, S. Borrmann, S. Weimer, K. Demerjian, P. Williams, K. Bower, R. Bahreini, L. Cottrell, R. J. Griffin, J. Rautiainen, J. Y. Sun, Y. M. Zhang, and D. R. Worsnop, Ubiquity and dominance of oxygenated species in organic aerosols in anthropogenically-influenced Northern Hemisphere midlatitudes, *Geophysical Research Letters*, *34*(L13801), doi:10.1029/2007GL029979, 2007.

Zhang, Q., J. L. Jimenez, M. R. Canagaratna, I. M. Ulbrich, N. L. Ng, D. R. Worsnop, and Y. Sun, Understanding atmospheric organic aerosols via factor analysis of aerosol mass spectrometry: A review, *Analytical and bioanalytical chemistry*, *401*(10), 3045–3067, doi:10.1007/s00216-011-5355-y, 2011.

Zhao, J., and R. Zhang, Proton transfer reaction rate constants between hydronium ion (H3O+) and volatile organic compounds, *Atmospheric Environment*, *38*(14), 2177–2185, doi:10.1016/j.atmosenv.2004.01.019, 2004.

Zorn, S. R., F. Drewnick, M. Schott, T. Hoffmann, and S. Borrmann, Characterization of the South Atlantic marine boundary layer aerosol using an Aerodyne Aerosol Mass Spectrometer, *Atmospheric Chemistry and Physics*, *8*(16), 4711–4728, doi:10.5194/acp-8-4711-2008, 2008.

A. Appendix

A.1. AMS calibration results and data analysis: November 2011

A.1.1. Calibration results

Table A.1.: Results from AMS Ionization Efficiency (IE) calibrations of the V-mode during the campaign in Cabauw 2011

Calibration date	Mode	IE_V	Ratio IE_V to AB	RIE_{NH_4}
08.11.2011	V	$0.95 \cdot 10^{-7}$	$5.29 \cdot 10^{-13}$	4.8
16.11.2011	V	$1.19 \cdot 10^{-7}$	$6.35 \cdot 10^{-13}$	4.8
22.11.2011	V	$1.11 \cdot 10^{-7}$	$5.93 \cdot 10^{-13}$	4.7
01.12.2011	V	$1.14 \cdot 10^{-7}$	$5.98 \cdot 10^{-13}$	4.4

Table A.2.: Results from AMS Ionization Efficiency (IE) calibrations of the W-mode during the campaign in Cabauw 2011

Calibration date	Mode	IE_W	Ratio IE_W to AB	RIE_{NH_4}
08.11.2011	W	$2.11 \cdot 10^{-9}$	$5.30 \cdot 10^{-13}$	4.8
16.11.2011	W	$3.13 \cdot 10^{-9}$	$6.35 \cdot 10^{-13}$	4.8
22.11.2011	W	$3.11 \cdot 10^{-9}$	$5.93 \cdot 10^{-13}$	4.7
01.12.2011	W	$3.57 \cdot 10^{-9}$	$5.98 \cdot 10^{-13}$	4.4

Table A.3.: Results from AMS particle size distribution calibrations during the campaign in Cabauw 2011; Here, PSL's with diameters of 81, 97, 151, 220, 269, 350, 498, and 596 nm were used. n.m.: not measured.

Calibration date	v_l	v_g	$D*$	b
08.11.2011	n.m.	n.m.	n.m.	n.m.
16.11.2011	10	300	57.17	0.49
22.11.2011	10	300	56.77	0.49
01.12.2011	n.m.	n.m.	n.m.	n.m.

A.1.2. Data analysis

m/z fitting

- List of masses (Diff spectra) used for m/z fitting in V-mode: C^+, OH^+, H_2O^+, O_2^+ Ar^+, CO_2^+, SO^+, SO_2^+, $^{182}W^+$, $^{184}W^+$, $^{186}W^+$
- List of masses (Diff spectra) used for m/z fitting in W-mode: OH^+, H_2O^+, O_2^+, Ar^+, CO_2^+, $^{182}W^+$, $^{184}W^+$

Baseline

- Mass defect wave set to CH
- Added the following m/z regions to default stick integration region:
  - m/z 40-40.2
  - m/z 41-41.2
  - m/z 80-80.3
  - m/z 81-81.3
  - m/z 98-98.3

DC Marker

- Added m/z 30 to Region 2 only channel list
- Added m/z 33 to Region 2 only channel list

Air Beam (AB) correction

- Used N_2 as MS AB reference
- Set manual values, determined of the average values from all ionization efficiency calibrations:

Table A.4.: Manually set values used for AB correction of V- and W-mode for the 2011 AMS data

Mode	MS AB	IE	Flow rate
V	187000	$1.1{\cdot}10^{-7}$	1.33
W	5030	$3.0{\cdot}10^{-9}$	1.33

PToF determination

Set manual values, determined of the average values from all particle size distribution calibrations:

Table A.5.: Manually set values used for PToF determination for the 2011 AMS data

v_l	v_g	$D*$	b
10	300	56.97	0.49

UMR fragmentation table

Table A.6.: Correction factors used in the AMS UMR fragmentation table for the 2011 data

m/z	frag_air	frag_CO2	frag_O16	frag_RH	frag_organic	frag_K
16			0.9			
18				0.015·RH		
29	0.9					
39					39	0
40	1.17				40,-frag_air[40]	

High resolution fitting

- V-mode:
  - Peak width fitting on C^+, CH^+, N^+, OH^+, H_2O^+, C_2H^+, N_2^+, O_2^+, Ar^+, CO_2^+, SO^+, $C_4H_2^+$, SO_2^+, $^{182}W^+$, $^{184}W^+$, $^{186}W^+$
  - Peak shape: O_2^+, CO_2^+, SO_2^+ (left wing); C^+, CH^+, OH^+, H_2O^+, O_2^+, Ar^+, $C_4H_2^+$(right wing)
- W-mode:
  - Peak width fitting on N^+, OH^+, H_2O^+, N_2^+, O_2^+, Ar^+, CO_2^+, $^{182}W^+$, $^{184}W^+$, $^{186}W^+$
  - Peak shape: OH^+, H_2O^+, O_2^+ (left and right wing)

HR fragmentation table

Correction factor for HR_frag_air[H2O]: 0.015·RH

A.2. AMS calibration results and data analysis: May to July 2012

A.2.1. Calibration results

Table A.7.: Results from AMS Ionization Efficiency (IE) calibrations for V-mode during the campaign in Cabauw 2012

Calibration date	Mode	IE_V	Ratio IE_V to AB-signal	RIE_{NH_4}
09.05.2012	V	$9.74 \cdot 10^{-8}$	$5.44 \cdot 10^{-13}$	4.5
16.05.2012	V	$9.78 \cdot 10^{-8}$	$5.15 \cdot 10^{-13}$	4.2
24.05.2012	V	$8.39 \cdot 10^{-8}$	$4.66 \cdot 10^{-13}$	4.1
28.05.2012	V	$8.96 \cdot 10^{-8}$	$4.98 \cdot 10^{-13}$	4.3
05.06.2012	V	$8.71 \cdot 10^{-8}$	$5.12 \cdot 10^{-13}$	4.3
12.06.2012	V	$8.45 \cdot 10^{-8}$	$4.69 \cdot 10^{-13}$	4.3
19.06.2012	V	$8.25 \cdot 10^{-8}$	$4.58 \cdot 10^{-13}$	4.3
26.06.2012	V	$9.37 \cdot 10^{-8}$	$5.21 \cdot 10^{-13}$	4.1
04.07.2012	V	$8.40 \cdot 10^{-8}$	$5.60 \cdot 10^{-13}$	4.3
11.07.2012	V	$9.53 \cdot 10^{-8}$	$5.61 \cdot 10^{-13}$	4.3
17.07.2012	V	$11.2 \cdot 10^{-8}$	$6.22 \cdot 10^{-13}$	4.0

Table A.8.: Results from AMS Ionization Efficiency (IE) calibrations for W-mode during the campaign in Cabauw 2012

Calibration date	Mode	IE_W	Ratio IE_W to AB-signal	RIE_{NH_4}
09.05.2012	W	$4.35 \cdot 10^{-9}$	$5.72 \cdot 10^{-13}$	4.5
16.05.2012	W	$4.48 \cdot 10^{-9}$	$5.15 \cdot 10^{-13}$	4.2
24.05.2012	W	$4.38 \cdot 10^{-9}$	$4.66 \cdot 10^{-13}$	4.1
28.05.2012	W	$4.98 \cdot 10^{-9}$	$4.98 \cdot 10^{-13}$	4.3
05.06.2012	W	$4.97 \cdot 10^{-9}$	$5.12 \cdot 10^{-13}$	4.3
12.06.2012	W	$5.41 \cdot 10^{-9}$	$4.92 \cdot 10^{-13}$	4.3
19.06.2012	W	$5.04 \cdot 10^{-9}$	$4.58 \cdot 10^{-13}$	4.3
26.06.2012	W	$3.90 \cdot 10^{-9}$	$5.20 \cdot 10^{-13}$	4.1
04.07.2012	W	$4.59 \cdot 10^{-9}$	$5.60 \cdot 10^{-13}$	4.3
11.07.2012	W	$5.61 \cdot 10^{-9}$	$5.61 \cdot 10^{-13}$	4.3
17.07.2012	W	$6.82 \cdot 10^{-9}$	$6.20 \cdot 10^{-13}$	4.0

Table A.9.: Results from AMS particle size distribution calibrations during the campaign in Cabauw 2012; Here, PSL's with diameters of 81, 97, 151, 220, 269, 350, 498, and 596 nm were used. n.m.: not measured.

Calibration date	v_l	v_g	$D*$	b
09.05.2012	10	300	54.46	0.48
16.05.2012	10	300	51.64	0.48
24.05.2012	10	300	51.64	0.48
28.05.2012	10	300	48.70	0.48
05.06.2012	10	300	51.08	0.48
12.06.2012	10	300	49.57	0.48
19.06.2012	10	300	51.58	0.48
26.06.2012	10	300	51.58	0.48
04.07.2012	10	300	51.92	0.47
11.07.2012	n.m.	n.m.	n.m.	n.m.
17.07.2012	n.m.	n.m.	n.m.	n.m.

A.2.2. Data analysis

m/z fitting

- List of masses (Diff spectra) used for m/z fitting in V-mode: OH^+, H_2O^+, N_2^+, O_2^+, Ar^+, CO_2^+, SO^+, SO_2^+, $^{182}W^+$, $^{184}W^+$, $^{186}W^+$
- List of masses (Diff spectra) used for m/z fitting in W-mode: OH^+, H_2O^+, N_2^+, O_2^+, Ar^+, CO_2^+, SO^+, $^{182}W^+$, $^{184}W^+$, $^{186}W^+$

Baseline

- Mass defect wave set to CH
- Added the following m/z regions to default stick integration region:
  - m/z 41-41.2
  - m/z 80-80.3
  - m/z 81-81.3
  - m/z 98-98.3

DC Marker

- Added m/z 30 to Region 2 only channel list
- Added m/z 33 to Region 2 only channel list

Air Beam (AB) correction

- Used N_2 as MS AB reference
- Set manual values, determined from the average values of all ionization efficiency calibrations:

Table A.10.: Manually set values used for AB correction of V- and W-mode for the 2012 AMS data

Mode	MS AB	IE	Flow rate
V	176000	$9.2{\cdot}10^{-7}$	1.39
W	9460	$5.0{\cdot}10^{-9}$	1.39

PToF determination

Set manual values, determined from the average values of all particle size distribution calibrations:

Table A.11.: Manually set values used for PToF determination for the 2012 AMS data

v_l	v_g	$D*$	b
10	300	51.35	0.48

UMR fragmentation table

Table A.12.: Correction factors used in the AMS UMR fragmentation table for the 2012 data

m/z	frag_air	frag_CO2	frag_O16	frag_RH	frag_organic	frag_nitrate	frag_K
16			0.9				
18				0.019·RH			
29	0.905						
30						1.7*frag_organic[62]	
33	0.8				33,-frag_air[33]		
34	1.03				34,-frag_air[34]		
39					39		0
40	1.17				40,-frag_air[40]		
44		0.9					

High resolution fitting

- V-mode:
  - Peak width fitting on C^+, N^+, OH^+, H_2O^+, C_2H^+, N_2^+, O_2^+, Ar^+, CO_2^+, SO^+, $C_4H_2^+$, $C_4H_9^+$, SO_2^+, $^{182}W^+$, $^{184}W^+$, $^{186}W^+$
  - Peak shape: C_2H^+, O_2^+ , Ar^+ , CO_2^+, SO^+, SO_2^+, $^{184}W^+$ (left wing); C^+, N^+, OH^+, H_2O^+, O_2^+ (right wing)
- W-mode:
  - Peak width fitting on C^+, N^+, OH^+, H_2O^+, N_2^+, O_2^+, Ar^+, CO_2^+, SO^+, SO_2^+,$^{182}W^+$, $^{184}W^+$, $^{186}W^+$
  - Peak shape: O_2^+ Ar^+, CO_2^+, SO^+, SO_2^+ (left wing); OH^+, H_2O^+, N_2^+, O_2^+, Ar^+ (right wing)

HR fragmentation table

- Correction factor for HR_frag_air[H2O]: 0.021·RH
- Correction factor for HR_frag_air[CO2]: 0.93

A.3. Detection limits of the AMS and the ACSM

Table A.13.: Overview of the detection limits (DL, 3σ) for each aerosol species from AMS (time resolution: 7 minutes) and ACSM (time resolution: 30 minutes). The DL for the AMS were determined using the standard deviation (σ) of all mass concentrations measured from particle free sample air. For the ACSM, values were taken from (*Ng et al.*, 2011b).

Aerosol species	DL_{AMS} (2011)	DL_{AMS} (2012)	DL_{ACSM} (*Ng et al.*, 2011b)
Org	0.078 µg m^{-3}	0.037 µg m^{-3}	0.148 µg m^{-3}
NO_3	0.006 µg m^{-3}	0.004 µg m^{-3}	0.012 µg m^{-3}
NH_4	0.002 µg m^{-3}	0.006 µg m^{-3}	0.284 µg m^{-3}
SO_4	0.011 µg m^{-3}	0.010 µg m^{-3}	0.024 µg m^{-3}
Chl	0.006 µg m^{-3}	0.004 µg m^{-3}	0.011 µg m^{-3}

A.4. TD-PTR-MS data analysis

Table A.14.: List and basic information of all detected ions used for TD-PTR-MS data analysis in 2011. The detection limit (DL) is calculated using the standard deviations (SD) of all background measurements. The SD's were combined over all thermal desorption temperatures and both inlets via error propagation.

Measured mass [Da]	Attributed empirical sum formula	Deviation of the exact mass from measured mass [mDa]	LOD [ng m^{-3}]
27.023	C2H2H+	-0.05	6.986
28.039			1.806
31.017	CH2OH+	0.84	19.191
33.032	CH4OH+	1.49	7.090
40.026			0.136
40.97			0.071
41.003			0.189
41.039	C3H4H+	-0.41	9.117
41.067			0.585
42.008			1.126
42.033	C2H3NH+	0.8	4.904
43.018	C2H2OH+	-0.13	5.583
43.054	C3H6H+	0.22	7.303
44.012	CHONH+	1.06	90.410
44.047	C2H5NH+	2.47	2.097
44.997			0.666
45.033	C2H4OH+	0.45	20.264
47.966			0.069
47.996	18OON+	0.58	0.261
48.985			0.104
49.017			0.073
49.995			0.031
50.981			0.045
51.04			0.077
51.939			0.164
51.994			0.101
52.018	C3HNH+	0.16	0.828
53.039	C4H4H+	-0.42	0.283
53.938			0.060
53.991			0.041
54.033	C3H3NH+	0.81	1.191

Table A.14.: continued

Measured mass [Da]	Attributed empirical sum formula	Deviation of the exact mass from measured mass [mDa]	LOD [ng m^{-3}]
55.934			0.701
56.021	C2HONH+	-7.9	0.041
56.051	C3H5NH+	-1.51	0.269
57.033	C3H4OH+	0.46	3.407
57.07	C4H8H+	-0.11	4.543
57.935			0.060
58.029	C2H3ONH+	-0.23	0.935
58.04	13CC2H4OH+	-3.13	0.479
58.069	13CC3H8H+	4.18	0.243
59.015	C2H2O2H+	-2.24	0.323
59.048	C3H6OH+	1.12	19.237
60.045	C2H5ONH+	-0.6	0.836
60.079	C3H9NH+	1.74	0.150
60.984			0.100
61.027	C2H4O2H+	1.4	6.118
61.979			0.280
62.025	CH3O2NH+	-1.3	1.856
63.982			0.204
64.969			0.048
65.02	CH4O3H+	3.32	0.049
65.038	C5H4H+	0.52	0.046
66.035	C4H3NH+	-1.12	0.030
67.027	C4H2OH+	-9.12	0.048
67.055	C5H6H+	-0.74	0.453
68.019	C3HONH+	-5.85	0.027
68.049	C4H5NH+	0.41	0.211
68.996			1.901
69.033	C4H4OH+	0.48	0.796
69.071	C5H8H+	-1.11	4.266
69.999			0.074
70.029	C3H3ONH+	-0.21	0.197
70.07	13CC4H8H+	3.22	0.247
70.942			0.034
71.014	C3H2O2H+	-1.21	0.220

Table A.14.: continued

Measured mass [Da]	Attributed empirical sum formula	Deviation of the exact mass from measured mass [mDa]	LOD [ng m^{-3}]
71.048	C4H6OH+	1.14	3.180
71.087	C5H10H+	-1.42	1.703
71.931			0.017
71.949			0.025
72.01	C2HO2NH+	-1.94	0.028
72.046	C3H5ONH+	-1.59	0.178
72.089	13CC4H10H+	-0.07	0.106
72.938			0.346
73.028	C3H4O2H+	0.37	1.324
73.064	C4H8OH+	0.73	7.706
73.946			0.227
74.026	C2H3O2NH+	-2.29	0.090
74.061	C3H7ONH+	-0.89	0.531
74.944			0.020
75.028	C6H2H+	-5.03	0.921
75.042	C3H6O2H+	2.03	0.627
75.945			0.050
75.994	CHO3NH+	8.89	0.336
76.038	C2H5O2NH+	1.29	0.310
77.023	C2H4O3H+	0.31	1.477
77.038	C6H4H+	0.54	1.086
77.941			0.026
77.992			0.115
78.025	CH3O3NH+	-6.4	0.124
78.042	13CC5H4H+	0	0.109
78.995	CH2O4H+	7.58	0.169
79.028	C4H2N2H+	1.03	0.933
79.054	C6H6H+	0.16	2.446
80.015	C4HONH+	-1.84	0.413
80.05	C5H5NH+	-0.48	0.585
80.993			0.061
81.035	C5H4OH+	-1.46	0.915
81.07	C6H8H+	-0.08	1.036
82.03	C4H3ONH+	-1.23	0.203

Table A.14.: continued

Measured mass [Da]	Attributed empirical sum formula	Deviation of the exact mass from measured mass [mDa]	LOD [ng m^{-3}]
82.066	C5H7NH+	-0.82	0.136
82.944			0.023
83.014	C4H2O2H+	-1.16	0.069
83.049	C5H6OH+	0.08	0.487
83.086	C6H10H+	-0.42	1.269
83.931			0.021
84.045	C4H5ONH+	-0.59	0.079
84.082	C5H9NH+	-1.18	0.103
84.938			0.023
85.028	C4H4O2H+	0.34	0.473
85.064	C5H8OH+	0.77	0.318
85.103	C6H12H+	-1.79	1.008
85.946			0.057
86.027	C3H3O2NH+	-3.27	0.053
86.06	C4H7ONH+	0	0.093
87.008	C3H2O3H+	-0.26	0.170
87.043	C4H6O2H+	1.04	1.094
87.925			0.018
87.995	C2HO3NH+	7.83	0.148
88.043	C3H5O2NH+	-3.61	0.067
88.075	C4H9ONH+	0.62	0.041
88.95			0.030
89.023	C3H4O3H+	0.27	0.309
89.058	C4H8O2H+	1.69	7.220
89.94			0.056
89.992			0.046
90.015	C2H3O3NH+	3.51	0.063
90.061	13CC3H8O2H+	1.98	0.348
90.946			0.201
90.995	C2H2O4H+	7.55	0.163
91.055	C7H6H+	-0.73	1.281
91.947			0.021
92.058	13CC6H6H+	-0.37	0.135
93.009	C2H4O4H+	9.21	0.141

Table A.14.: continued

Measured mass [Da]	Attributed empirical sum formula	Deviation of the exact mass from measured mass [mDa]	LOD [ng m^{-3}]
93.037	C6H4OH+	-3.44	0.238
93.07	C7H8H+	-0.09	1.132
93.953			0.014
94.029	C5H3ONH+	-0.19	0.654
94.065	C6H7NH+	0.09	0.234
95.026	C2H6O4H+	7.89	0.481
95.048	C6H6OH+	1.14	1.011
95.086	C7H10H+	-0.38	1.162
96.045	C5H5ONH+	-0.58	0.284
96.086	13CC6H10H+	2.88	0.123
97.027	C5H4O2H+	1.36	2.703
97.062	C6H8OH+	2.72	0.649
97.102	C7H12H+	-0.78	1.069
98.024	C4H3O2NH+	-0.29	1.621
99.007	C4H2O3H+	0.59	6.684
99.076	C6H10OH+	4.36	0.347
99.945			0.013
100.011	13CC3H2O3H+	0	0.282
100.037	C4H5O2NH+	2.3	0.162
100.075	C5H9ONH+	0.6	0.759
100.934			0.016
101.022	C4H4O3H+	1.31	0.387
101.057	C5H8O2H+	2.63	0.252
101.94			0.039
102.021	C3H3O3NH+	-2.35	0.045
102.09	C5H11ONH+	1.33	0.041
102.939			0.016
102.999	C3H2O4H+	3.5	0.048
103.039	C4H6O3H+	0	0.269
103.072	C5H10O2H+	3.3	0.426
103.948			0.053
104.049	C7H5NH+	0.42	3.102
105.044	C6H4N2H+	0.63	1.110
105.069	C8H8H+	0.84	1.428

Table A.14.: continued

Measured mass [Da]	Attributed empirical sum formula	Deviation of the exact mass from measured mass [mDa]	LOD [ng m^{-3}]
105.933			0.217
106.039	C6H3ONH+	-10.18	0.340
106.072	13CC7H8H+	1.17	0.176
106.935			0.018
106.99	C2H2O5H+	7.49	0.061
107.048	C7H6OH+	1.07	1.616
107.084	C8H10H+	1.5	1.119
107.928			0.165
107.947			0.059
108.047	C6H5ONH+	-2.59	0.182
108.082	C7H9NH+	-1.19	0.152
109.028	C6H4O2H+	0.33	0.584
109.064	C7H8OH+	0.76	0.399
109.101	C8H12H+	0.11	1.137
110.029	C5H3O2NH+	-5.28	0.089
110.06	C6H7ONH+	0	0.094
110.103	13CC7H12H+	1.43	0.119
111.003	C5H2O3H+	4.66	0.194
111.043	C6H6O2H+	1	0.616
111.077	C7H10OH+	3.33	0.348
111.118	C8H14H+	-1.11	2.311
112.04	C5H5O2NH+	-0.67	0.241
112.121	13CC7H14H+	-0.78	0.220
113.022	C5H4O3H+	1.24	0.555
113.056	C6H8O2H+	3.62	0.252
114.018	C4H3O3NH+	0.57	0.148
114.054	C5H7O2NH+	0.91	0.086
114.09	C6H11ONH+	1.25	0.226
115.013	C3H2O3N2H+	0.81	0.213
115.036	C5H6O3H+	2.88	0.115
115.072	C6H10O2H+	3.34	0.140
116.01	C7HONH+	3.02	0.047
116.034	C4H5O3NH+	0.12	0.031
116.105	C6H13ONH+	1.97	0.024

Table A.14.: continued

Measured mass [Da]	Attributed empirical sum formula	Deviation of the exact mass from measured mass [mDa]	LOD [ng m^{-3}]
116.905			0.012
117.016	C4H4O4H+	2.22	0.063
117.072	C9H8H+	-2.11	0.670
118.065	C8H7NH+	0.12	0.176
118.902			0.010
118.941			0.013
118.989	C3H2O5H+	8.45	0.029
119.026	C4H6O4H+	7.86	0.212
119.051	C8H6OH+	-1.79	0.223
119.085	C9H10H+	0.48	0.827
119.946			0.053
120.044	C7H5ONH+	0.36	0.364
120.084	C8H9NH+	-3.12	0.125
121.036	C7H4O2H+	-7.5	0.165
121.063	C8H8OH+	1.69	0.312
121.099	C9H12H+	2.18	0.653
121.945			0.055
122.023	C6H3O2NH+	0.61	0.328
122.059	C7H7ONH+	0.98	0.118
122.097	C8H11NH+	-0.49	0.097
122.943			0.026
123.042	C7H6O2H+	1.97	1.720
123.078	C8H10OH+	2.34	0.445
123.117	C9H14H+	-0.12	0.497
123.94			0.012
124.041	C6H5O2NH+	-1.61	0.228
124.943			0.022
125.022	C6H4O3H+	1.25	0.338
125.057	C7H8O2H+	2.63	0.266
125.093	C8H12OH+	3	0.209
125.134	C9H16H+	-1.5	0.302
126.02	C5H3O3NH+	-1.39	0.124
126.054	C6H7O2NH+	0.88	0.067
126.903			0.015

Table A.14.: continued

Measured mass [Da]	Attributed empirical sum formula	Deviation of the exact mass from measured mass [mDa]	LOD [ng m^{-3}]
127.001	C5H2O4H+	1.52	0.207
127.038	C6H6O3H+	0.89	0.154
127.071	C7H10O2H+	4.32	0.159
127.991	C4HO4NH+	6.78	0.107
128.036	C5H5O3NH+	-1.66	0.054
128.062	C9H5NH+	-12.42	0.200
129.013	C5H4O4H+	5.16	0.411
129.046	C8H4N2H+	-1.16	1.185
129.067	C5H8O2N2H+	-1.03	1.712
130.034	C8H3ONH+	-5.2	0.545
130.064	C9H7NH+	1.04	0.364
130.991	C4H2O5H+	6.42	0.916
131.045	C4H6O3N2H+	0	0.322
131.986	C3HO5NH+	6.73	0.083
132.045	C8H5ONH+	-0.53	0.099
132.078	C9H9NH+	2.77	0.093
132.974			0.129
133.063	C9H8OH+	1.73	0.195
133.1	C10H12H+	1.06	0.412
133.981			0.035
134.026	C7H3O2NH+	-2.28	0.050
134.06	C8H7ONH+	0	0.068
134.965			0.044
135.044	C8H6O2H+	0	0.431
135.076	C4H10O3N2H+	0.41	0.257
135.115	C10H14H+	1.76	0.361
136.023	C3H5O5NH+	0.95	1.715
137.026	C7H4O3H+	-2.6	0.196
137.057	C3H8O4N2H+	-1.23	0.269
137.132	C10H16H+	0.41	0.349
138.011	C6H3O3NH+	7.45	1.026
138.053	C7H7O2NH+	1.93	0.213
139.01	C6H2O4H+	-7.37	0.159
139.038	C7H6O3H+	0.97	0.137

Table A.14.: continued

Measured mass [Da]	Attributed empirical sum formula	Deviation of the exact mass from measured mass [mDa]	LOD [ng m^{-3}]
139.073	C8H10O2H+	2.36	0.204
139.107	C9H14OH+	4.73	0.192
140.008	C9HONH+	5.04	0.295
140.031	C6H5O3NH+	3.08	0.145
141.014	CH4O6N2H+	0.14	0.109
141.054	C7H8O3H+	0.56	0.099
141.086	C11H8H+	-16.08	0.264
142.012	C5H3O4NH+	1.42	0.029
142.051	C6H7O3NH+	-0.99	0.028
142.078	C10H7NH+	-12.79	0.101
142.991	C5H2O5H+	6.43	0.098
143.034	C6H6O4H+	0	0.116
143.085	C11H10H+	0.43	0.872
144.043	C9H5ONH+	1.3	0.265
144.913			0.013
144.965			0.065
145.006	C5H4O5H+	7.11	0.092
145.057	C6H8O4H+	-7.4	0.290
145.116	C11H12H+	-14.8	0.567
145.97			0.052
146.058	C9H7ONH+	2.04	0.093
146.976	C4H2O6H+	16.31	0.307
147.043	C9H6O2H+	1.03	0.786
147.973	C3HO6NH+	14.5	0.084
148.038	C8H5O2NH+	1.18	1.901
149.022	C8H4O3H+	1.19	10.324
150.026	13CC7H4O3H+	0.6	1.039
150.969	C3H2O7H+	18.27	0.048
151.037	C8H6O3H+	1.96	0.193
151.072	C9H10O2H+	3.32	0.140
151.108	C5H14O3N2H+	-0.15	0.138
151.147	C11H18H+	1.06	0.215
152.033	C7H5O3NH+	1.06	0.046
152.068	C8H9O2NH+	2.59	0.054

Table A.14.: continued

Measured mass [Da]	Attributed empirical sum formula	Deviation of the exact mass from measured mass [mDa]	LOD [ng m^{-3}]
153.02	C7H4O4H+	-1.68	0.099
153.057	C8H8O3H+	-2.3	0.572
153.123	C10H16OH+	4.29	0.324
153.913			0.362
154.009	C6H3O4NH+	4.47	0.170
154.064	C11H7NH+	1.08	0.490
155.078	C7H10O2N2H+	3.41	0.873
155.995	C9HO2NH+	12.95	0.070
156.042	C10H5ONH+	2.34	0.083
156.087	C11H9NH+	-6.09	0.167
157.006	CH4O7N2H+	2.98	0.111
157.054	C7H8O4H+	-4.4	0.155
157.099	C12H12H+	2.04	0.842
158.057	C10H7ONH+	3	0.056
158.101	13CC11H12H+	3.48	0.124
158.984	C5H2O6H+	8.27	0.068
159.042	C10H6O2H+	1.91	0.191
159.13	C12H14H+	-13.05	0.368
160.043	C9H5O2NH+	-3.68	0.056
161.058	C10H8O2H+	1.61	0.284
161.955			0.030
162.054	C9H7O2NH+	0.81	0.174
163.038	C9H6O3H+	0.82	0.916
164.037	C8H5O3NH+	-2.79	0.198
164.959			0.073
165.017	C8H4O4H+	1.16	0.412
165.085	C5H12O4N2H+	1.98	0.198
166.017	C7H3O4NH+	-3.49	0.085
166.95			0.028
167.033	C8H6O4H+	0.84	0.077
167.086	C13H10H+	-0.33	0.484
168.028	C7H5O4NH+	1.01	0.045
168.08	C12H9NH+	0.67	0.148
169.063	C12H8OH+	1.69	1.406

Table A.14.: continued

Measured mass [Da]	Attributed empirical sum formula	Deviation of the exact mass from measured mass [mDa]	LOD [ng m^{-3}]
169.984	C2H3O8NH+	9.01	0.129
170.063			0.219
171.059	C3H10O6N2H+	2.05	0.230
171.115	C13H14H+	1.71	0.583
171.97	CHO9NH+	2.41	0.560
172.039	C10H5O2NH+	0.17	0.184
172.967	C2H4O9H+	25.77	0.071
173.054	C6H8O4N2H+	1.56	0.252
173.137	C13H16H+	-4.5	0.158
173.967	CH3O9NH+	21.05	0.336
174.019	C9H3O3NH+	-0.35	0.210
174.053	C10H7O2NH+	1.91	0.099
174.966	CH2O10H+	5.95	0.132
175.039	C10H6O3H+	0	0.125
175.069			0.165
175.965	C4HO7NH+	17.42	0.067
176.036	C9H5O3NH+	-1.76	0.069
176.068	C10H9O2NH+	2.46	0.064
176.961			0.090
177.053	C10H8O3H+	1.59	1.211
177.162	C13H20H+	1.59	0.218
178.008	C8H3O4NH+	5.34	0.100
178.074	C6H11O5NH+	-2.85	0.268
179.084	C14H10H+	1.43	3.439
180.086	C6H13O5NH+	0.54	0.586
180.936			0.211
181.006	C3H4O7N2H+	3.08	0.161
181.064	C13H8OH+	0.72	0.963
181.936			0.063
182	C7H3O5NH+	8.37	0.183
182.066	13CC12H8OH+	2	0.187
182.933			0.189
182.984	C3H2O9H+	-6.77	0.465
183.079	C13H10OH+	1.28	0.795

Table A.14.: continued

Measured mass [Da]	Attributed empirical sum formula	Deviation of the exact mass from measured mass [mDa]	LOD [ng m^{-3}]
183.993	C6HO6NH+	-5.15	0.134
184.078	C12H9ONH+	-2.21	0.137
184.932			0.066
184.982	C3H4O9H+	10.73	0.161
185.049	C8H8O5H+	-4.44	0.253
185.129	C9H16O2N2H+	-0.37	0.298
185.986	C2H3O9NH+	2.05	0.026
186.054	C11H7O2NH+	0.93	0.056
187.048	C4H10O8H+	-2.99	0.182
187.969	CHO10NH+	-1.5	0.039
188.033	C10H5O3NH+	1.13	0.106
189.043	C7H8O6H+	-3.59	0.224
190.018	C2H7O9NH+	1.33	0.052
190.046	C10H7O3NH+	3.8	0.048
190.964	CH2O11H+	2.86	0.077
191.036	C10H6O4H+	-2.1	0.078
191.069	C11H10O3H+	1.15	0.162
191.969	C4HO8NH+	8.45	0.019
192.032	C9H5O4NH+	-2.69	0.028
192.069	C10H9O3NH+	-3.46	0.050
192.962	CH4O11H+	20.45	0.048
193.01	C4H4O7N2H+	-0.77	0.080
193.099	C15H12H+	2.12	0.591
194.062	C9H7O4NH+	-17.08	0.075
194.095	C14H11NH+	1.36	0.108
194.961	C4H2O9H+	15.99	0.025
195.08	C14H10OH+	0.39	0.297
196.029	C8H5O5NH+	-4.9	0.033
196.079			0.069
196.997	C4H4O9H+	-4.14	0.091
197.061	C13H8O2H+	-1.18	0.219
197.09	C9H12O3N2H+	1.97	0.593
198.057	C12H7O2NH+	-1.98	0.128
199.037	C12H6O3H+	1.79	0.569

Table A.14.: continued

Measured mass [Da]	Attributed empirical sum formula	Deviation of the exact mass from measured mass [mDa]	LOD [ng m^{-3}]
199.166	C12H22O2H+	3.19	0.290
200.04	13CC11H6O3H+	2.2	0.107
201.055	C12H8O3H+	-0.2	0.094
201.179	C15H2OH+	-15.09	0.497
202.064	C8H11O5NH+	6.87	0.051
203.083	C11H10O2N2H+	-1.42	1.822
203.176	C10H22O2N2H+	-0.41	0.316
204.086	C8H13O5NH+	0.61	0.358
205.09	C12H12O3H+	-3.9	0.419
205.192	C10H24O2N2H+	-0.82	0.246
205.931			0.165
206.06	C10H7O4NH+	-15.04	0.106
207.035	C10H6O5H+	-6	0.311
207.115	C16H14H+	1.66	0.256
207.928			0.160
208.036	C9H5O5NH+	-11.86	0.061
208.071	C10H9O4NH+	-10.4	0.058
209.057	C9H8O4N2H+	-1.25	0.791
209.926			0.054
210.06	C6H11O7NH+	0.63	0.138
211.073	C14H10O2H+	2.32	0.231
211.964	C3HO10NH+	3.18	0.038
212.069	C13H9O2NH+	1.48	0.071
213.054	C13H8O3H+	0.43	0.169
213.966	C3H3O10NH+	16.9	0.026
214.053			0.050
214.897			0.053
214.965	C3H2O11H+	1.93	0.045
215.028	C7H6O6N2H+	1.72	0.124
215.958	C2HO11NH+	4.1	0.054
216.03	C11H5O4NH+	-0.86	0.051
216.894			0.064
216.949			0.065
217.023	C10H4O4N2H+	1.3	0.116

Table A.14.: continued

Measured mass [Da]	Attributed empirical sum formula	Deviation of the exact mass from measured mass [mDa]	LOD [ng m^{-3}]
217.097	C12H12O2N2H+	0	0.124
217.919			0.047
217.955	C2H3O11NH+	22.67	0.027
218.01	C10H3O5NH+	-1.53	0.040
218.097	C12H11O3NH+	-15.7	0.042
218.891			0.032
218.944	C2H2O12H+	17.73	0.041
219.075	C11H10O3N2H+	1.31	0.229
219.173	C15H22OH+	1.32	0.570
220.076	C11H9O4NH+	-15.41	0.055
220.175	13CC14H22OH+	2.64	0.103
221.059	C10H8O4N2H+	-3.09	0.147
221.153	C14H20O2H+	0.44	0.658
221.989	C5H3O9NH+	-0.89	0.041
222.057	13CC9H8O4N2H+	2	0.054
222.152	C13H19O2NH+	-3.11	0.110
223.065	C11H10O5H+	-4.68	0.206
224.063	C10H9O5NH+	-7.62	0.076
225.055	C7H12O8H+	5.4	0.116
226.056	C6H11O8NH+	-0.23	0.034
226.935	C4H2O11H+	32	0.029
227.073	C14H10O3H+	-2.72	0.118
228.023	C8H5O7NH+	-9.12	0.024
228.079	13CC13H10O3H+	-5.25	0.044
228.93			0.022
229.098	C13H12O2N2H+	-0.69	0.133
230.1	C10H15O5NH+	2.07	0.043
231.022	C7H6O7N2H+	2.77	0.061
231.079	C5H14O8N2H+	3.24	0.210
232.024	C11H5O5NH+	0	0.024
232.081	C9H13O6NH+	0.46	0.052
233.004	C11H4O6H+	3.96	0.055
233.097	C10H16O6H+	4.9	0.095
234.053	C8H11O7NH+	7.72	0.032

Table A.14.: continued

Measured mass [Da]	Attributed empirical sum formula	Deviation of the exact mass from measured mass [mDa]	LOD [ng m^{-3}]
235.07	C11H10O4N2H+	1.18	0.063
235.202	C11H26O3N2H+	-0.24	0.340
236.07	C11H9O5NH+	-14.64	0.022
237.057	C8H12O8H+	3.32	0.066
238.05	C7H11O8NH+	5.71	0.030
238.251	C16H31NH+	1.91	0.092
239.035	C7H10O9H+	4.54	0.088
239.137	C12H18O3N2H+	1.91	0.102
239.891			0.034
240.03	C6H9O9NH+	4.8	0.035
241.08	C10H12O5N2H+	1.69	0.101
241.888			0.043
242.041	C9H7O7NH+	-11.38	0.028
243.022	C9H6O8H+	-8.26	0.031
243.102	C15H14O3H+	-0.24	0.060
244.074	C10H13O6NH+	7.57	0.027
245.091	C13H12O3N2H+	0.98	0.089
245.221	C13H28O2N2H+	1.23	0.127
247.074	C5H14O9N2H+	2.96	0.069
247.236	C13H30O2N2H+	1.98	0.132
248.071	C9H13O7NH+	5.46	0.026
248.985	C7H4O10H+	2.74	0.039
249.053	C4H12O10N2H+	3.49	0.143
249.159	C14H20O2N2H+	0.75	0.054
250.054	C8H11O8NH+	1.5	0.043
250.983	C10H2O8H+	-0.5	0.026
251.038	C8H10O9H+	1.76	0.048
253.098	C9H16O8H+	-6.07	0.308
254.1	C12H15O5NH+	2.29	0.078
255.083	C12H14O6H+	3.32	0.174
255.204	C14H26O2N2H+	2.55	0.076
256.082	C11H13O6NH+	-0.26	0.048
256.964	CH4O15H+	-1.54	0.107
257.092	C8H16O9H+	-5.14	0.068

Table A.14.: continued

Measured mass [Da]	Attributed empirical sum formula	Deviation of the exact mass from measured mass [mDa]	LOD [ng m^{-3}]
257.245	C16H32O2H+	2.32	0.282
257.959	C4H3O12NH+	13.67	0.031
258.962	C4H2O13H+	-5.18	0.098
259.074	C6H14O9N2H+	3.11	0.074
259.236	C19H30H+	5.96	0.147
260.076	C10H13O7NH+	0.26	0.022
260.957	C4H4O13H+	15.4	0.036
261.252	C19H32H+	5.49	0.123
263.069	C12H10O5N2H+	-2.63	0.043
265.047	C11H8O6N2H+	-1.33	0.043
266.97	C5H2O11N2H+	2.94	0.026
267.17	C19H22OH+	4.27	0.057
269.098	C8H16O8N2H+	0	0.059
269.188	C19H24OH+	1.88	0.060
271.076	C7H14O9N2H+	1.08	0.058
271.242	C20H30H+	0	0.142
273.058	C11H12O8H+	2.46	0.053
273.253	C15H32O2N2H+	0.55	0.200
274.255	C19H31NH+	-1.92	0.046
275.267	C15H34O2N2H+	2.2	0.108
277.097	C11H16O8H+	-4.99	0.069
279.111	C11H18O8H+	-3.35	0.057
281.051	C9H12O10H+	-0.56	0.278
282.051			0.081
283.047	C12H10O8H+	-1.98	0.072
284.044	C11H9O8NH+	-3.69	0.019
285.023	C11H8O9H+	0.86	0.027
285.264	C21H32H+	-6.28	0.420
287.267	C16H34O2N2H+	2.01	0.119
289.282	C21H36H+	6.94	0.086
290.925	C4H2O15H+	21.53	0.109
292.922	C4H4O15H+	40.13	0.142
294.918	C3H2O16H+	23.3	0.070
297.077	C10H16O10H+	4.46	0.028

Table A.14.: continued

Measured mass [Da]	Attributed empirical sum formula	Deviation of the exact mass from measured mass [mDa]	LOD [ng m^{-3}]
297.252	C22H32H+	5.35	0.040
299.269	C22H34H+	4.19	0.058
301.285	C17H36O2N2H+	0	0.090
303.3	C22H38H+	4.55	0.059
307.143	C13H22O8H+	-3.99	0.023
311.258	C19H34O3H+	0	0.028
313.283	C18H36O2N2H+	1.88	0.041
315.299	C18H38O2N2H+	1.26	0.061
316.302	C22H37NH+	-1.9	0.018
317.315	C23H40H+	5.08	0.043
325.281	C20H36O3H+	-7.16	0.021
326.88			0.020
326.999	C12H6O11H+	-0.65	0.081
327.3	C19H38O2N2H+	0.33	0.030
329.315	C19H40O2N2H+	0.99	0.041
331.329	C24H42H+	6.63	0.030
339.299	C20H38O2N2H+	1.36	0.015
341.013	C13H8O11H+	0.68	0.025
341.315	C25H40H+	5.12	0.022
343.006	C11H6O11N2H+	-1.37	0.120
343.329	C20H42O2N2H+	2.75	0.026
345.345	C20H44O2N2H+	2.42	0.020
345.999	C11H7O12NH+	4.84	0.006
355.066	C15H14O10H+	0	1.714
356.066	C14H13O10NH+	-4.63	0.622
357.063	C11H16O13H+	3.21	0.412
357.345	C21H44O2N2H+	2.5	0.036
358.062	C10H15O13NH+	-0.36	0.109
359.05	C10H14O14H+	-4.31	0.041
359.359	C21H46O2N2H+	3.95	0.014
365.011	C10H8O13N2H+	-0.73	0.276
367.326	C23H42O3H+	-5.14	0.010
369.346	C27H44H+	5.54	0.012
371.093	C11H18O12N2H+	0	0.173

Table A.14.: continued

Measured mass [Da]	Attributed empirical sum formula	Deviation of the exact mass from measured mass [mDa]	LOD [ng m^{-3}]
371.36	C22H46O2N2H+	2.97	0.019
372.094	C15H17O10NH+	-1.12	0.065
373.089	C14H16O10N2H+	-1.12	0.043
373.376	C22H48O2N2H+	2.61	0.010
382.985	C9H6O15N2H+	-0.77	0.050
383.363	C23H46O2N2H+	0	0.010
385.376	C23H48O2N2H+	2.7	0.010
387.389	C24H50O3H+	-5.42	0.007
391.028	C12H10O13N2H+	-2.35	0.083
392.998	C12H8O15H+	-4.32	0.045
395.99	C11H9O15NH+	14.26	0.005
397.374	C25H48O3H+	-6.36	0.008
399.391	C24H50O2N2H+	3.2	0.009
400.395	C28H49NH+	-1.2	0.006
401.406	C24H52O2N2H+	4.01	0.006
409.032			0.053
409.372	C26H48O3H+	-4.09	0.008
411.389	C26H50O3H+	-5.76	0.009
413.405	C26H52O3H+	-5.79	0.007
415.028	C12H14O16H+	7.06	0.013
424.987	C11H8O16N2H+	7.65	0.039
425.401	C27H52O3H+	-1.7	0.011
426.988	C11H10O16N2H+	22.2	0.200
429.079	C16H16O12N2H+	-1.29	0.591
430.08	C13H19O15NH+	2.58	0.258
431.076	C17H18O13H+	6.04	0.179
432.077	C16H17O13NH+	0	0.057
433.069	C15H16O13N2H+	3.46	0.022
442.98	C12H14O16N2H+	61.57	0.243
443.981			0.028
445.107	C17H20O12N2H+	1.78	0.124
446.107	C17H19O13NH+	-13.83	0.054
447.103	C14H22O16H+	-4.92	0.038
464.999	C14H12O16N2H+	26.5	0.762

Table A.14.: continued

Measured mass [Da]	Attributed empirical sum formula	Deviation of the exact mass from measured mass [mDa]	LOD [ng m^{-3}]
466.001	C15H15O16NH+	45.2	0.083
478.94			0.014
482.995			0.059
489.031	C19H20O15H+	56.24	0.012
491.015	C18H18O16H+	51.56	0.100
492.014	C17H17O16NH+	47.73	0.015
492.989	C16H16O16N2H+	68.03	0.080
495.972			0.005
503.091	C20H22O15H+	12.07	0.181
504.091	C19H21O15NH+	7.06	0.093
505.086	C19H20O16H+	-3.54	0.070
506.086	13CC18H20O16H+	0	0.026
507.003	C17H18O16N2H+	69.46	0.028
509.017	C17H20O16N2H+	71.26	0.069
510.019			0.010
519.117	C19H22O15N2H+	-7.27	0.077
520.117	C20H25O15NH+	12.48	0.040
521.112	C20H24O16H+	1.56	0.036
526.977			0.077
542.96			0.077
564.983			0.261
565.986			0.034
577.097	C22H28O16N2H+	53.67	0.050
578.096	C23H31O16NH+	75.15	0.030
579.091	C22H30O16N2H+	75.28	0.026
582.978			0.029
590.995			0.009
592.97			0.023
593.122	C23H32O16N2H+	59.91	0.029
594.905			0.022
608.999			0.006
644.892			0.015
664.965			0.027
760.868			0.046

Table A.14.: continued

Measured mass [Da]	Attributed empirical sum formula	Deviation of the exact mass from measured mass [mDa]	LOD [ng m^{-3}]
926.821			0.024
1070.77			0.035
1092.78			0.441
1093.77			0.111
1142.76			0.126

Table A.15.: List and basic information of all detected ions used for TD-PTR-MS data analysis in 2012. The detection limit (DL) is calculated using the standard deviations (SD) of all background measurements. The SD's were combined over all thermal desorption temperatures and both inlets via error propagation.

Measured mass [Da]	Attributed empirical sum formula	Deviation of the exact mass from measured mass [mDa]	LOD [ng m^{-3}]
27.022	C2H2H+	0.92	7.966
28.031			1.775
31.017	CH2OH+	0.84	19.687
33.032	CH4OH+	1.49	26.231
40.026			0.374
40.97			0.520
41.038	C3H4H+	0.57	17.506
42.008			0.498
42.034	C2H3NH+	-0.17	2.891
42.938			0.357
43.018	C2H2OH+	-0.13	11.738
43.054	C3H6H+	0.22	9.637
43.917			0.119
44			2.018
44.012	CHONH+	1.06	17.683
44.048	C2H5NH+	1.45	0.748
44.949			0.719
44.997			0.860
45.014			1.975
45.033	C2H4OH+	0.45	23.151

Table A.15.: continued

Measured mass [Da]	Attributed empirical sum formula	Deviation of the exact mass from measured mass [mDa]	LOD [ng m^{-3}]
51.041			0.352
51.94			0.438
51.994			0.227
52.018	C3HNH+	0.16	0.641
52.939			0.089
53.038	C4H4H+	0.53	0.487
53.939			0.142
53.991			0.104
54.034	C3H3NH+	-0.16	0.451
55.935			1.456
56.049	C3H5NH+	0.45	0.292
56.933			0.140
57.034	C3H4OH+	-0.46	3.848
57.07	C4H8H+	-0.11	6.519
57.935			0.145
58.03	C2H3ONH+	-1.22	0.309
58.931			0.527
59.049	C3H6OH+	0.12	33.900
60.05	C2H5ONH+	-5.58	1.244
61.028	C2H4O2H+	0.37	8.741
62.028	CH3O2NH+	-4.34	0.515
63.025	C5H2H+	-2.02	0.438
65.022	CH4O3H+	1.3	0.048
65.038	C5H4H+	0.52	0.089
67.054	C5H6H+	0.2	0.976
68.05	C4H5NH+	-0.48	0.119
68.997			0.840
69.034	C4H4OH+	-0.48	0.972
69.07	C5H8H+	-0.07	7.965
69.949			0.063
70.029	C3H3ONH+	-0.21	0.111
70.067	C4H7NH+	-1.82	0.431
70.943			0.094
71.013	C3H2O2H+	-0.21	0.397

Table A.15.: continued

Measured mass [Da]	Attributed empirical sum formula	Deviation of the exact mass from measured mass [mDa]	LOD [ng m^{-3}]
71.049	C4H6OH+	0.14	3.000
71.085	C5H10H+	0.5	2.089
71.93			0.050
71.949			0.061
72.049	C3H5ONH+	-4.61	0.176
72.938			0.499
73.029	C3H4O2H+	-0.58	3.794
73.047	C2H4ON2H+	-7.3	18.048
73.064	C4H8OH+	0.73	9.329
73.945			0.462
74.026	C2H3O2NH+	-2.29	0.299
74.048			1.454
74.062	C3H7ONH+	-1.93	0.780
74.944			0.293
75.027	C6H2H+	-4.05	16.580
75.043	C3H6O2H+	1.05	6.284
75.946			0.135
75.995	CHO3NH+	7.9	0.209
76.027	C5HNH+	-8.82	1.070
76.039	C2H5O2NH+	0.3	0.579
77.023	C2H4O3H+	0.31	13.432
77.037	C6H4H+	1.54	4.916
77.941			0.076
77.992			0.197
78.022	CH3O3NH+	-3.43	0.969
78.04	C5H3NH+	-6.17	0.374
79.002	CH2O4H+	0.55	0.897
79.029	C4H2N2H+	0	0.741
79.054	C6H6H+	0.16	1.769
80.013	C4HONH+	0.08	0.231
80.05	C5H5NH+	-0.48	0.301
81.034	C5H4OH+	-0.49	1.191
81.044	C4H4N2H+	0.65	2.022
81.069	C6H8H+	0.81	1.663

Table A.15.: continued

Measured mass [Da]	Attributed empirical sum formula	Deviation of the exact mass from measured mass [mDa]	LOD [ng m^{-3}]
82.03	C4H3ONH+	-1.23	0.190
82.066	C5H7NH+	-0.82	0.185
83.014	C4H2O2H+	-1.16	0.118
83.049	C5H6OH+	0.08	0.890
83.085	C6H10H+	0.5	1.188
83.93			0.045
84.047	C4H5ONH+	-2.52	0.084
84.081	C5H9NH+	-0.17	0.142
84.937			0.050
85.029	C4H4O2H+	-0.51	0.330
85.064	C5H8OH+	0.77	0.604
85.101	C6H12H+	0.17	0.983
85.945			0.101
86.029	C3H3O2NH+	-5.33	0.054
86.062	C4H7ONH+	-1.89	0.071
86.948			0.045
87.009	C3H2O3H+	-1.31	0.180
87.044	C4H6O2H+	0	1.330
87.078	C5H10OH+	2.44	0.426
87.925			0.049
87.996	C2HO3NH+	6.86	0.068
88.045	13CC3H6O2H+	2.38	0.088
88.951			0.121
89.023	C3H4O3H+	0.27	0.862
89.06	C4H8O2H+	-0.27	10.254
89.94			0.071
90.948			0.344
90.996	C2H2O4H+	6.55	0.134
91.054	C7H6H+	0.18	2.006
91.949			0.059
92.057	C6H5NH+	-7.46	0.188
93.036	C6H4OH+	-2.42	1.462
93.07	C7H8H+	-0.09	0.724
93.954			0.043

Table A.15.: continued

Measured mass [Da]	Attributed empirical sum formula	Deviation of the exact mass from measured mass [mDa]	LOD [ng m^{-3}]
94.029	C5H3ONH+	-0.19	0.291
94.066	C6H7NH+	-0.85	0.152
95.018	C5H2O2H+	-5.23	2.069
95.049	C6H6OH+	0.1	3.656
95.085	C7H10H+	0.48	1.761
96.047	C5H5ONH+	-2.59	0.367
97.028	C5H4O2H+	0.39	2.719
97.063	C6H8OH+	1.75	0.991
97.1	C7H12H+	1.17	0.744
98.025	C4H3O2NH+	-1.27	0.695
99.007	C4H2O3H+	0.59	5.660
99.043	C5H6O2H+	0.99	1.399
99.079	C6H10OH+	1.39	0.447
99.946			0.037
100.011	13CC3H2O3H+	0	0.255
100.04	C4H5O2NH+	-0.6	0.106
100.075	C5H9ONH+	0.6	0.103
100.934			0.032
101.023	C4H4O3H+	0.3	0.174
101.059	C5H8O2H+	0.71	0.218
101.941			0.082
102.02	C3H3O3NH+	-1.33	0.044
102.942			0.034
103.04	C4H6O3H+	-0.93	0.213
103.074	C5H10O2H+	1.34	0.258
103.953			0.098
104.049	C7H5NH+	0.42	1.061
105.045	C6H4N2H+	-0.21	0.329
105.068	C8H8H+	1.79	0.601
105.935			0.090
106.039	C6H3ONH+	-10.18	0.092
106.937			0.042
107.049	C7H6OH+	0.11	0.753
107.084	C8H10H+	1.5	0.422

Table A.15.: continued

Measured mass [Da]	Attributed empirical sum formula	Deviation of the exact mass from measured mass [mDa]	LOD [ng m^{-3}]
107.95			0.043
108.046	C6H5ONH+	-1.51	0.104
108.952			0.062
109.029	C6H4O2H+	-0.55	0.547
109.064	C7H8OH+	0.76	0.543
109.1	C8H12H+	1.09	2.586
110.032	13CC5H4O2H+	-0.22	0.065
110.063	C6H7ONH+	-2.86	0.071
111.002	C5H2O3H+	5.66	0.134
111.044	C6H6O2H+	0	0.677
111.079	C7H10OH+	1.33	0.675
111.116	C8H14H+	0.78	2.560
112.042	C5H5O2NH+	-2.69	0.135
113.023	C5H4O3H+	0.23	0.352
113.058	C6H8O2H+	1.7	0.296
114.017	C4H3O3NH+	1.48	0.083
114.059	C5H7O2NH+	-3.99	0.073
115.011	C3H2O3N2H+	2.76	0.177
115.074	C6H10O2H+	1.27	0.153
117.07	C9H8H+	-0.12	0.187
118.065	C8H7NH+	0.12	0.052
118.942			0.032
119.025	C6H2ON2H+	-0.95	0.075
119.051	C8H6OH+	-1.79	0.135
119.084	C9H10H+	1.43	0.465
119.95			0.037
120.045	C7H5ONH+	-0.6	0.088
121.064	C8H8OH+	0.73	0.470
121.1	C9H12H+	1.09	0.238
121.963			0.039
122.024	C6H3O2NH+	-0.24	0.098
122.061	C7H7ONH+	-0.85	0.079
123.044	C7H6O2H+	0	0.467
123.079	C8H10OH+	1.35	0.291

Table A.15.: continued

Measured mass [Da]	Attributed empirical sum formula	Deviation of the exact mass from measured mass [mDa]	LOD [ng m^{-3}]
123.115	C9H14H+	1.72	0.359
123.945			0.032
124.043	C6H5O2NH+	-3.6	0.065
125.023	C6H4O3H+	0.25	0.283
125.058	C7H8O2H+	1.63	0.246
125.094	C8H12OH+	2	0.344
126.023	C5H3O3NH+	-4.41	0.039
126.057	C6H7O2NH+	-2.02	0.041
127.039	C6H6O3H+	0	0.109
127.074	C7H10O2H+	1.27	0.206
129.011	C5H4O4H+	7.22	0.251
129.046	C8H4N2H+	-1.16	0.363
130.032	C8H3ONH+	-3.25	0.087
130.991	C4H2O5H+	6.42	0.346
131.048	C9H6OH+	1.05	0.338
132.046	C8H5ONH+	-1.58	0.063
133.065	C9H8OH+	-0.13	0.160
133.1	C10H12H+	1.06	0.176
134.061	C8H7ONH+	-0.94	0.043
135.044	C8H6O2H+	0	0.295
135.079	C9H10OH+	1.35	0.224
136.022	C3H5O5NH+	2.04	0.233
136.039	C7H5O2NH+	0.27	0.155
137.023	C7H4O3H+	0.27	0.125
137.058	C8H8O2H+	1.64	0.252
138.01	C6H3O3NH+	8.56	0.402
139.038	C7H6O3H+	0.97	0.139
139.074	C8H10O2H+	1.25	0.198
139.109	C9H14OH+	2.64	0.198
140.008	C9HONH+	5.04	0.139
141.013	CH4O6N2H+	1.13	0.073
141.054	C7H8O3H+	0.56	0.073
141.088	C8H12O2H+	2.96	0.148
142.991	C5H2O5H+	6.43	0.105

Table A.15.: continued

Measured mass [Da]	Attributed empirical sum formula	Deviation of the exact mass from measured mass [mDa]	LOD [ng m^{-3}]
143.084	C11H10H+	1.43	0.285
144.044	C9H5ONH+	0.29	0.158
145.063	C10H8OH+	1.74	0.150
146.061	C9H7ONH+	-0.88	0.038
146.975	C4H2O6H+	17.34	0.151
147.043	C9H6O2H+	1.03	0.521
148.04	C8H5O2NH+	-0.59	0.145
148.973			1.023
149.023	C8H4O3H+	0.3	8.850
150.026	13CC7H4O3H+	0.6	0.862
151.038	C8H6O3H+	0.91	0.253
151.074	C9H10O2H+	1.21	0.140
151.109	C5H14O3N2H+	-1.21	0.132
153.019	C7H4O4H+	-0.61	0.124
153.055	C8H8O3H+	-0.31	0.103
153.088	C4H12O4N2H+	-0.92	0.244
153.914			0.195
154.064	C11H7NH+	1.08	0.097
155.071	C8H10O3H+	-0.62	0.357
157.006	CH4O7N2H+	2.98	0.055
157.049	C7H8O4H+	0.47	0.078
157.099	C12H12H+	2.04	0.330
158.058	C10H7ONH+	1.9	0.035
159.043	C10H6O2H+	0.95	0.133
161.058	C10H8O2H+	1.61	0.420
162.056	C9H7O2NH+	-0.97	0.064
163.038	C9H6O3H+	0.82	0.469
164.037	C8H5O3NH+	-2.79	0.066
165.015	C8H4O4H+	3.14	0.107
165.088	C5H12O4N2H+	-0.99	0.110
169.063	C12H8OH+	1.69	0.264
170.061	C11H7ONH+	-0.85	0.047
171.045	C11H6O2H+	-0.86	0.069
171.064	C8H10O4H+	1.03	0.106

Table A.15.: continued

Measured mass [Da]	Attributed empirical sum formula	Deviation of the exact mass from measured mass [mDa]	LOD [ng m^{-3}]
171.97	CHO9NH+	2.41	0.098
173.058	C11H8O2H+	1.56	0.079
173.967	CH3O9NH+	21.05	0.063
174.969	CH2O10H+	2.97	0.045
175.038	C10H6O3H+	0.88	0.071
177.053	C10H8O3H+	1.59	0.165
178.006	C8H3O4NH+	7.48	0.042
179.083	C9H10O2N2H+	-1.43	0.910
180.085	C6H13O5NH+	1.62	0.149
180.936			0.068
181.004	C4H4O8H+	-5.97	0.082
181.063	C13H8OH+	1.63	0.341
181.118	C6H16O4N2H+	0.18	0.264
182.001	C7H3O5NH+	7.28	0.033
182.066	C5H11O6NH+	0	0.065
182.933			0.059
182.986	C2H2O8N2H+	2.38	0.094
183.078	C13H10OH+	2.38	0.247
187.045	C11H6O3H+	-5.99	0.051
193.099	C15H12H+	2.12	0.159
195.078	C14H10OH+	2.34	0.134
197.059	C13H8O2H+	0.59	0.125
199.039	C12H6O3H+	0	0.095
203.083	C11H10O2N2H+	-1.42	0.229
207.03	C10H6O5H+	-1.04	1.462
208.03	C9H5O5NH+	-5.82	0.320
209.055	C9H8O4N2H+	0.63	0.542
210.059	C6H11O7NH+	1.68	0.087
215.024	C8H6O7H+	-5.16	0.036
217.03	C8H8O7H+	4.12	0.043
219.047	C8H10O7H+	2.85	0.050
219.172	C15H22OH+	2.19	0.322
221.149	C9H20O4N2H+	0.44	0.449
223.064	C11H10O5H+	-3.79	0.788

Table A.15.: continued

Measured mass [Da]	Attributed empirical sum formula	Deviation of the exact mass from measured mass [mDa]	LOD [ng m^{-3}]
225.052	C9H8O5N2H+	-1.35	0.343
281.045	C11H8O7N2H+	-4.5	0.595
282.047	C8H11O10NH+	-1.41	0.173
283.04	C12H10O8H+	4.81	0.131

A.5. Observations

A.5.1. Campaign 2011

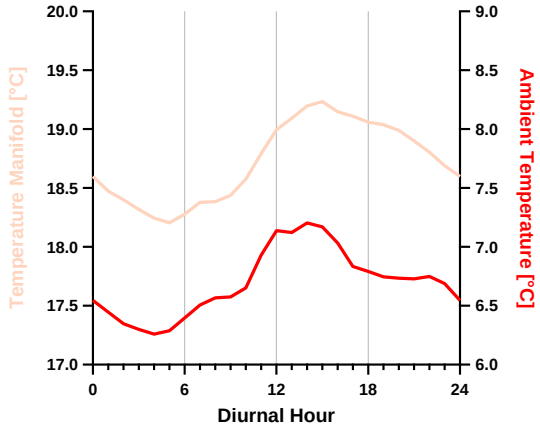

Figure A.1.: Diurnal variations (LT) of the ambient temperature (dark red) and the temperature at the manifold of the 60 m sampling line (light red) in 2011

Aerosol ion balance

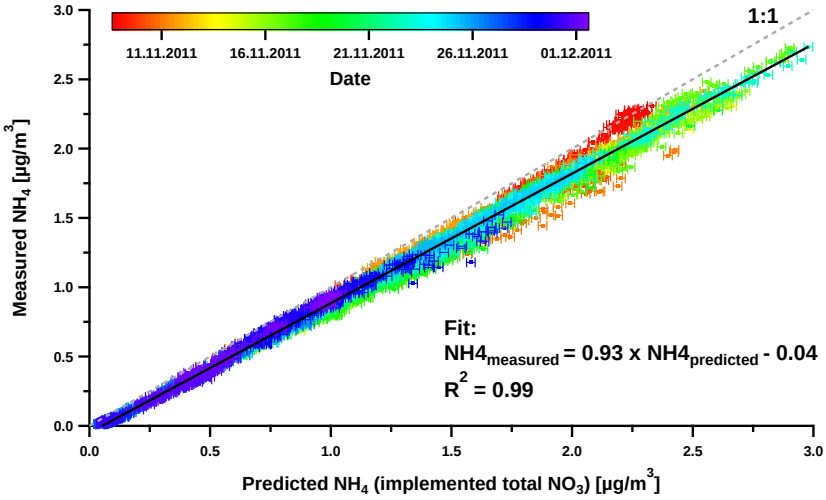

Figure A.2.: Correlation plot of measured against predicted NH_4 in 2011. Here, the total nitrate was used to determine the predicted ammonium concentration. A slope of 0.93 ± 0.00 was determined. Error bars represent uncertainties of the NH_4 prediction.

Size distribution

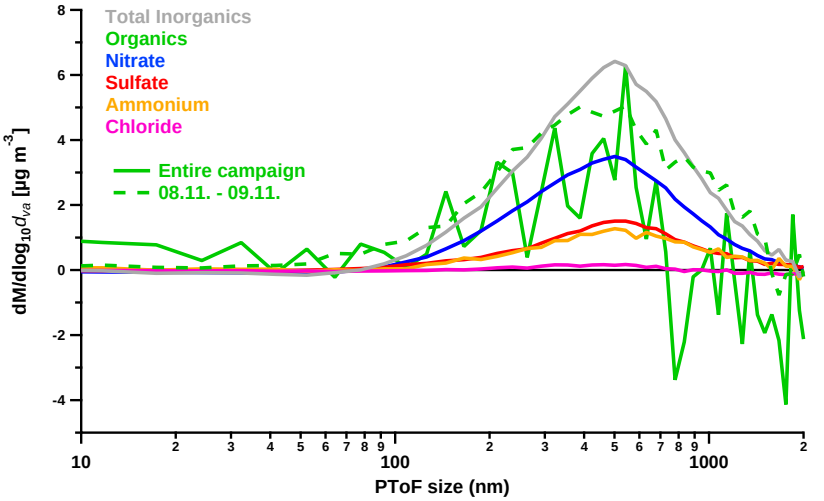

Figure A.3.: Average size distribution of individual species and the total inorganics, measured by the AMS in November 2011. The solid lines represent averages over the whole campaign. The dashed green line represents the average for organics on 08.11. and 09.11.2011.

AMS collection efficiency

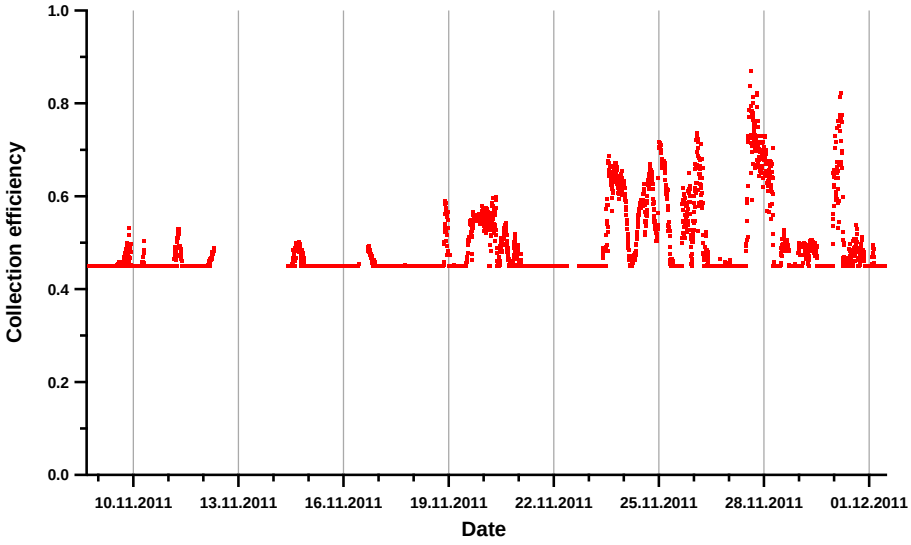

Figure A.4.: Collection efficiency used for AMS data of 2011; Average = 0.49

SMPS particle size distribution

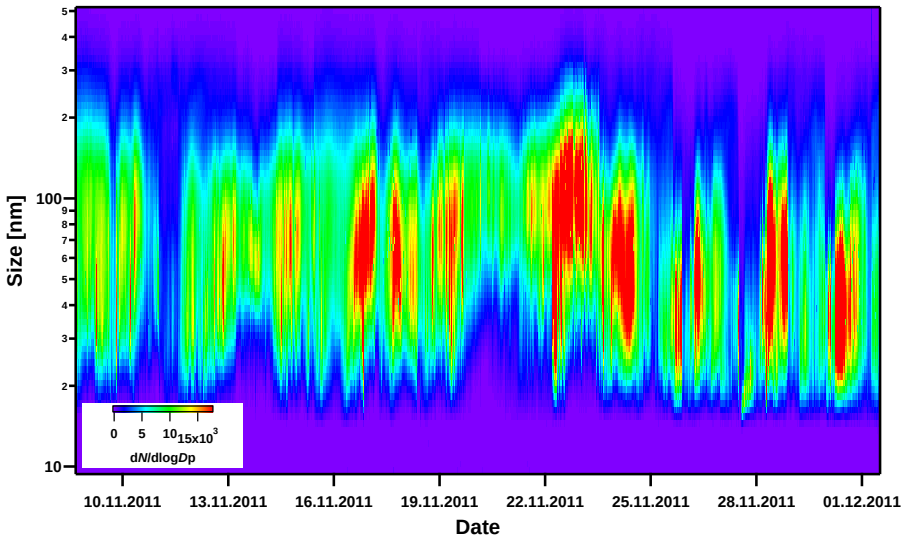

Figure A.5.: SMPS particle size distribution in 2011

Particle density

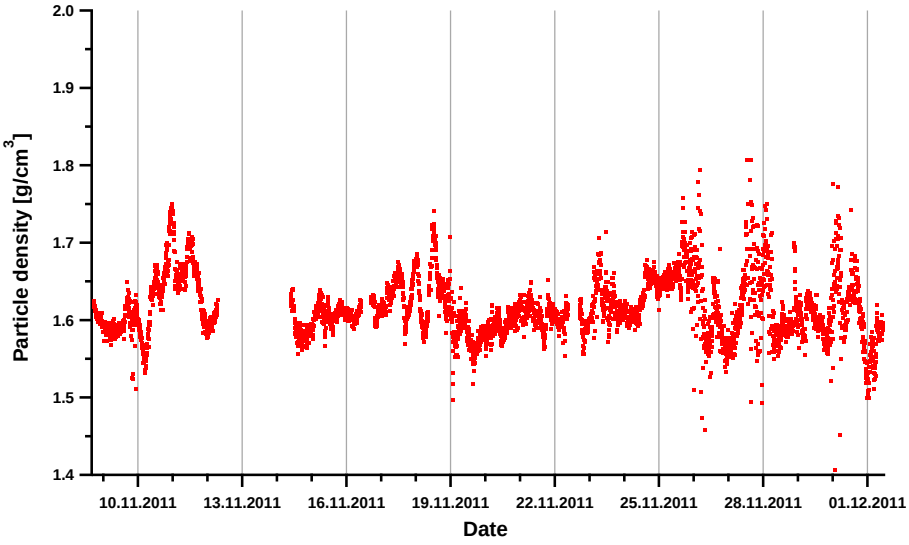

Figure A.6.: Particle density, determined from AMS aerosol composition in November 2011

Organic aerosol mass measured by TD-PTR-MS

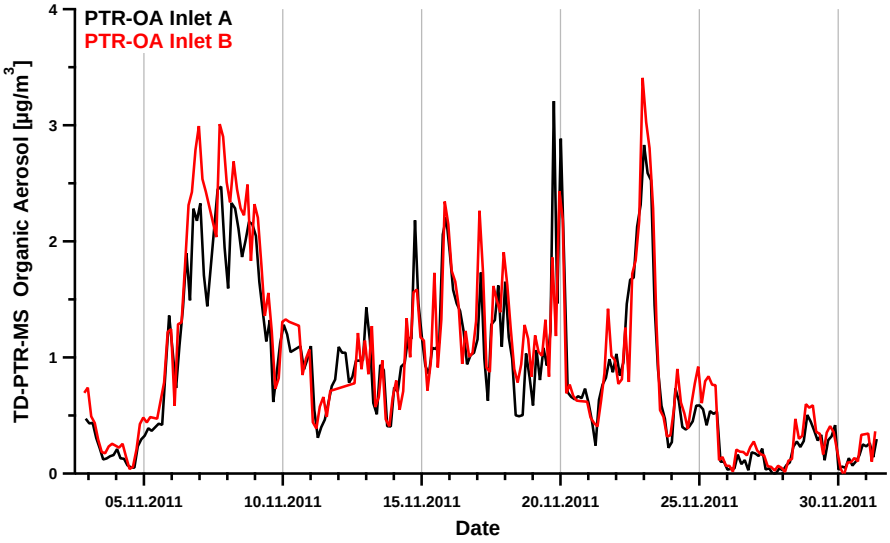

Figure A.7.: Time series of PTR-OA, measured from aerosol inlet A and B in 2011

A.5.2. Campaign 2012

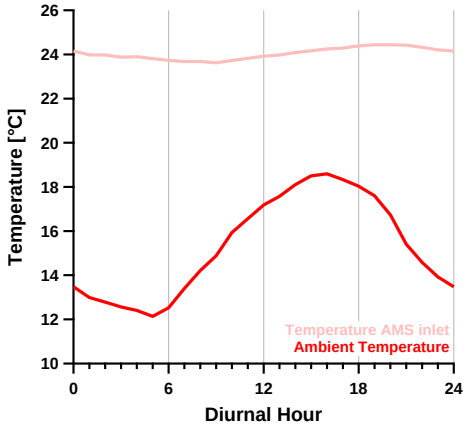

Figure A.8.: Diurnal variations (LT) of the ambient temperature (dark red) and the temperature in the AMS inlet (light red) from May to July 2012

Aerosol ion balance

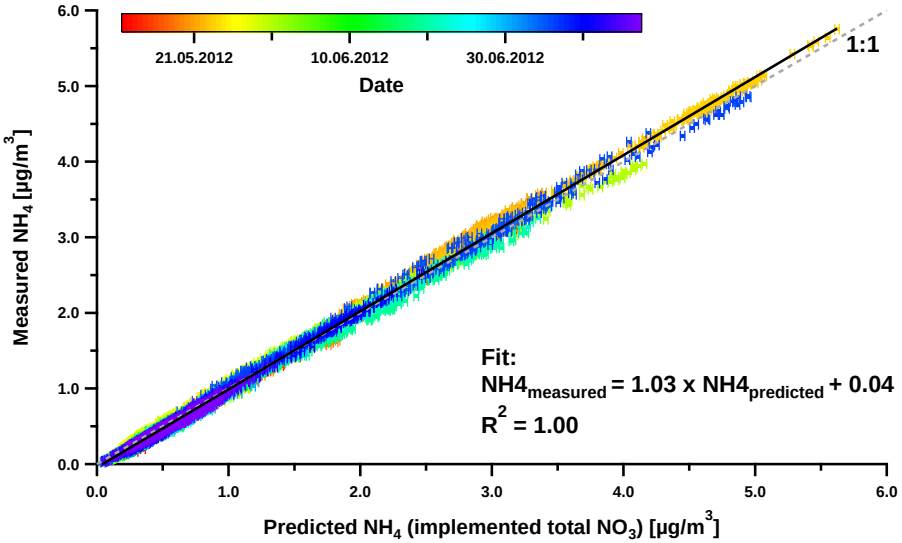

Figure A.9.: Correlation plot of measured against predicted NH_4 in 2012. Here, the total nitrate was used to determine the predicted ammonium concentration. A slope of 1.03 ± 0.00 was determined. Error bars represent uncertainties of the NH_4 prediction.

AMS collection efficiency

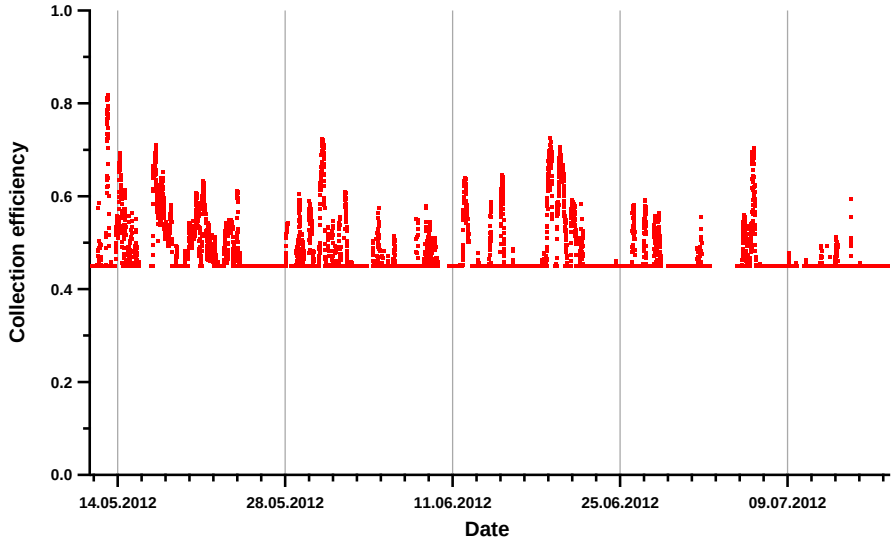

Figure A.10.: Collection efficiency used for AMS data from May to July 2012; Average = 0.48

SMPS particle size distribution

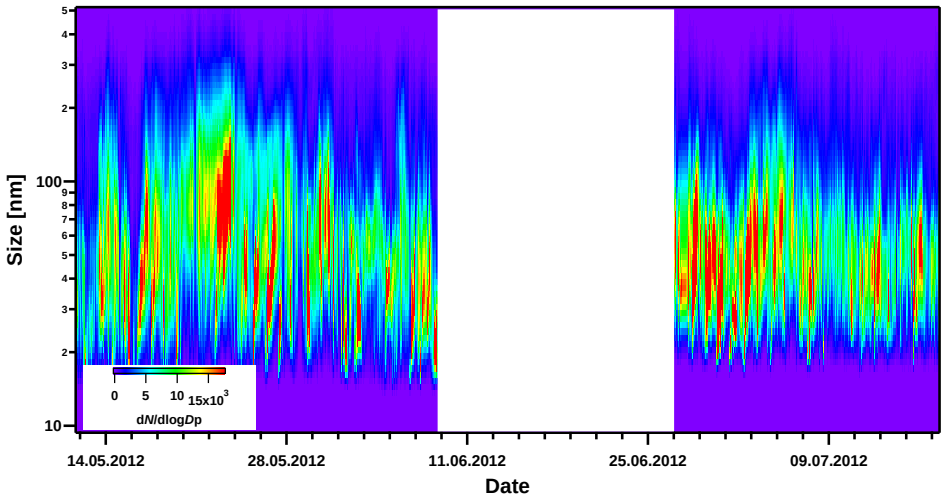

Figure A.11.: SMPS particle size distribution from May to July 2012

Particle density

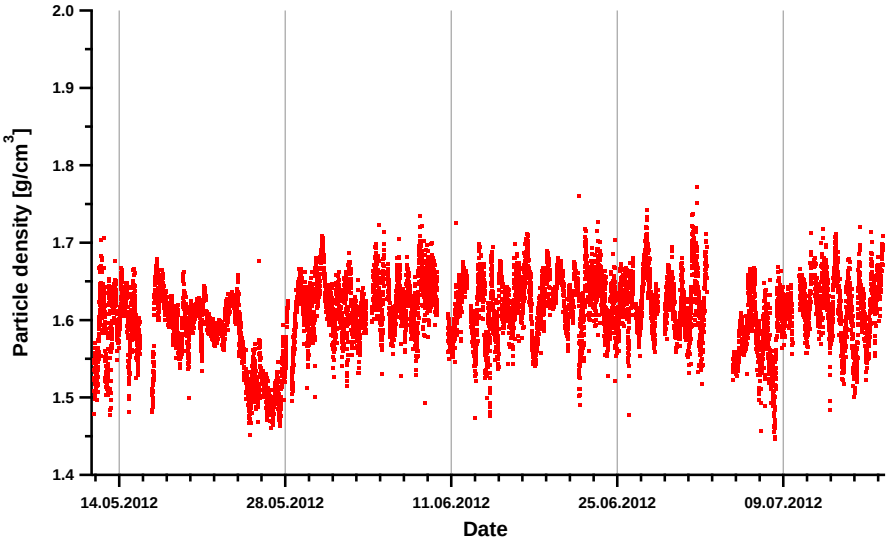

Figure A.12.: Particle density, determined from AMS aerosol composition from May to July 2012

Correlation AMS-MARGA

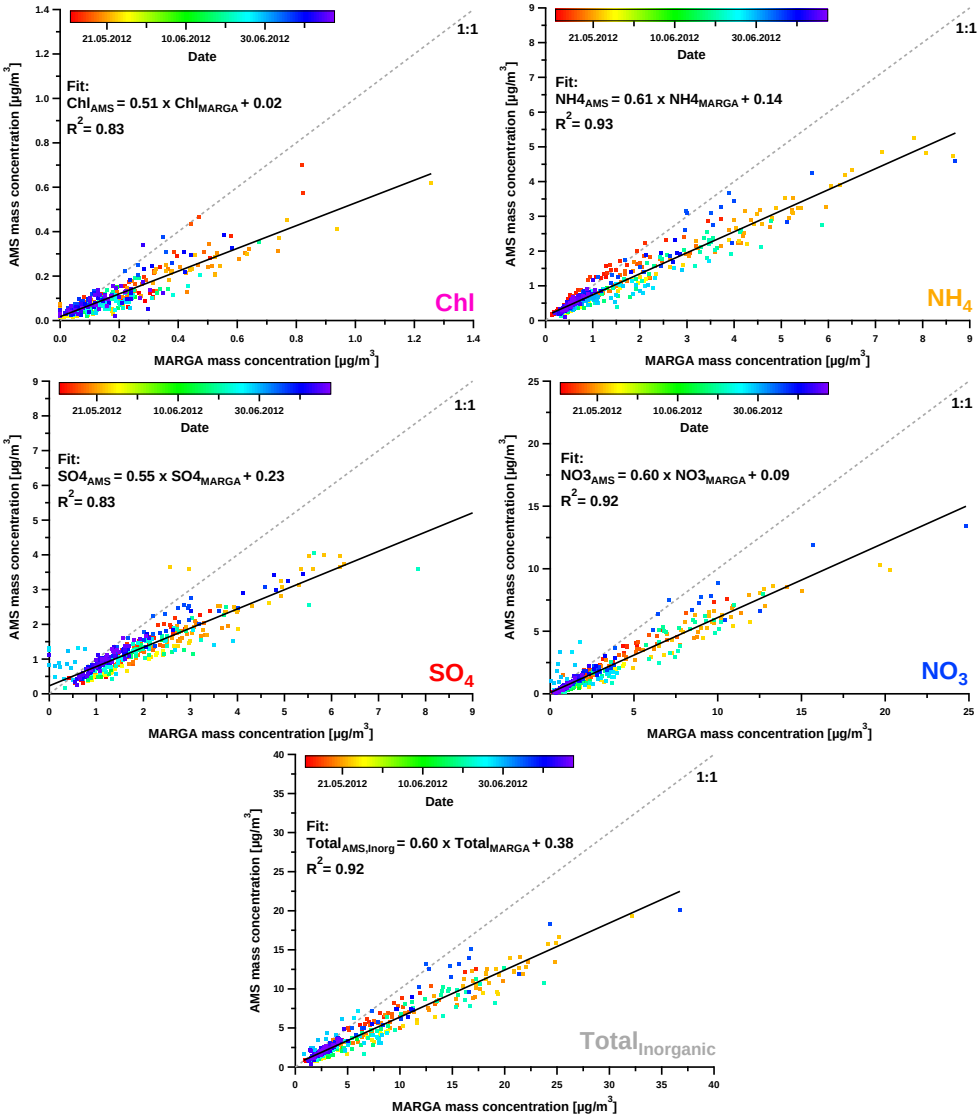

Figure A.13.: Correlation graphs of Chl, NH_4, SO_4, NO_3, and total inorganic mass concentration from AMS and MARGA data from May to July 2012

Organic aerosol mass measured by TD-PTR-MS

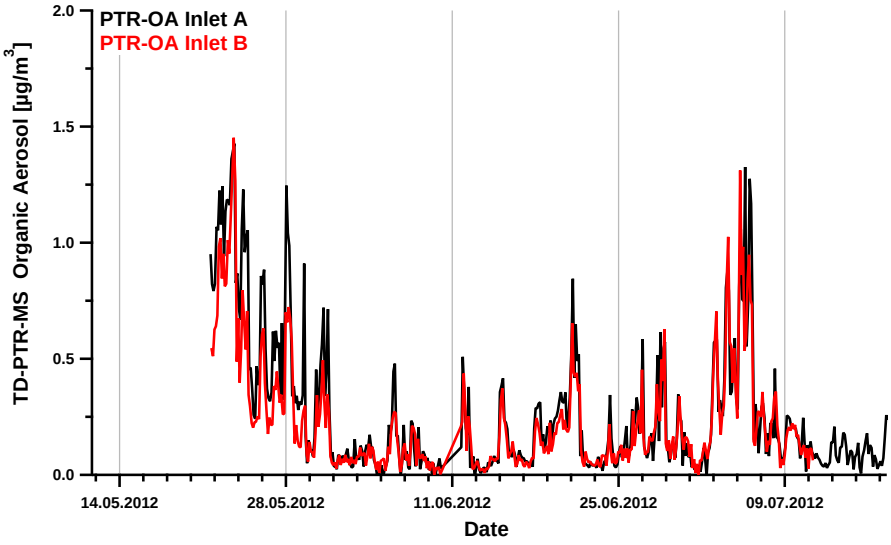

Figure A.14.: Time series of PTR-OA, measured from aerosol inlet A and B in 2012. From 11.07. to 17.07., inlet B showed contaminations. Thus, corresponding data was excluded.

A.5.3. ACSM campaign 2012 - 2013

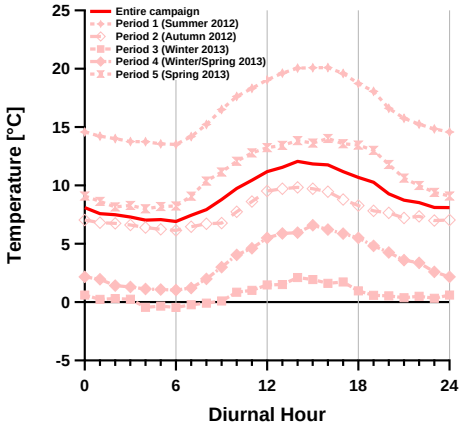

Figure A.15.: Diurnal variations (LT) of ambient temperatures at 2 m height from 2012 to 2013

ACSM collection efficiency

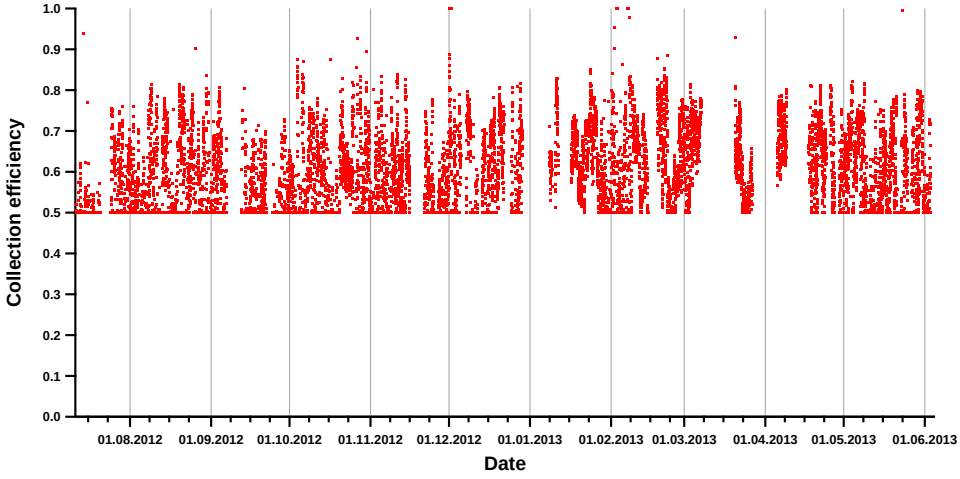

Figure A.16.: Collection efficiency used for ACSM data; Average = 0.59

SMPS particle size distribution

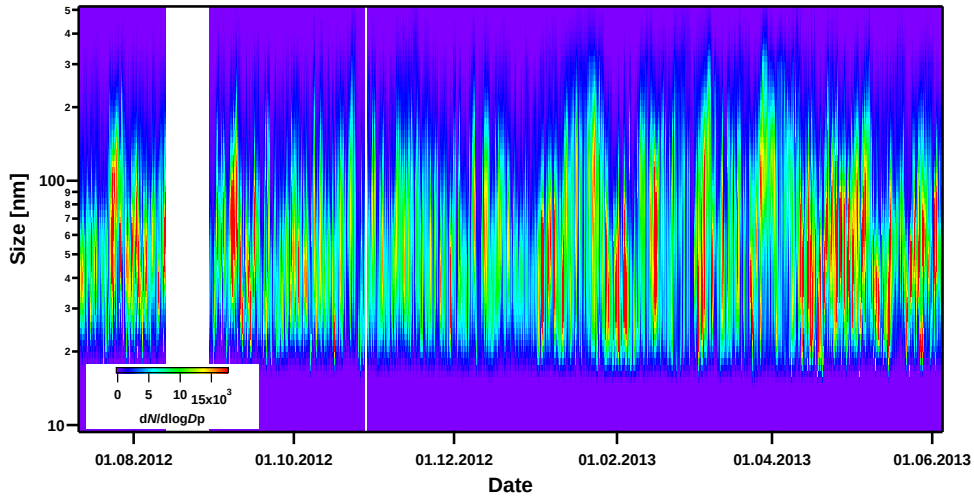

Figure A.17.: SMPS particle size distribution from July 2012 to June 2013

Particle density

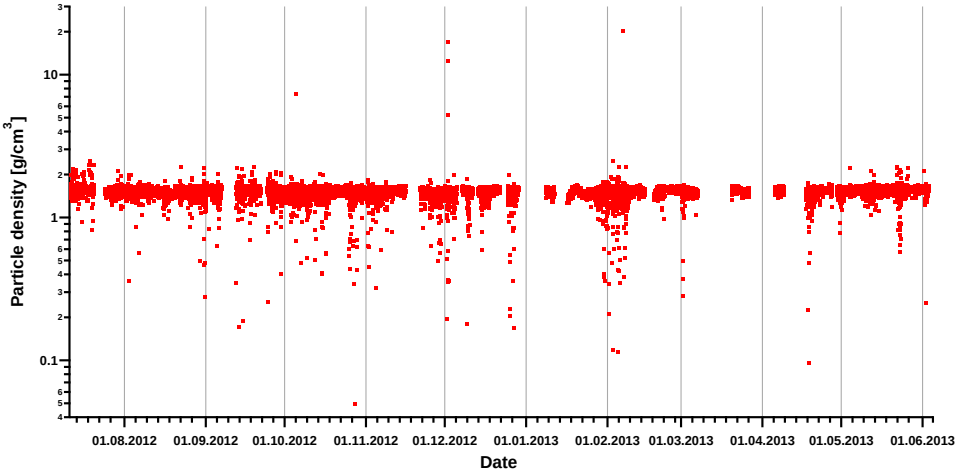

Figure A.18.: Particle density, determined from ACSM aerosol composition from July 2012 to June 2013

Correlation ACSM-MARGA

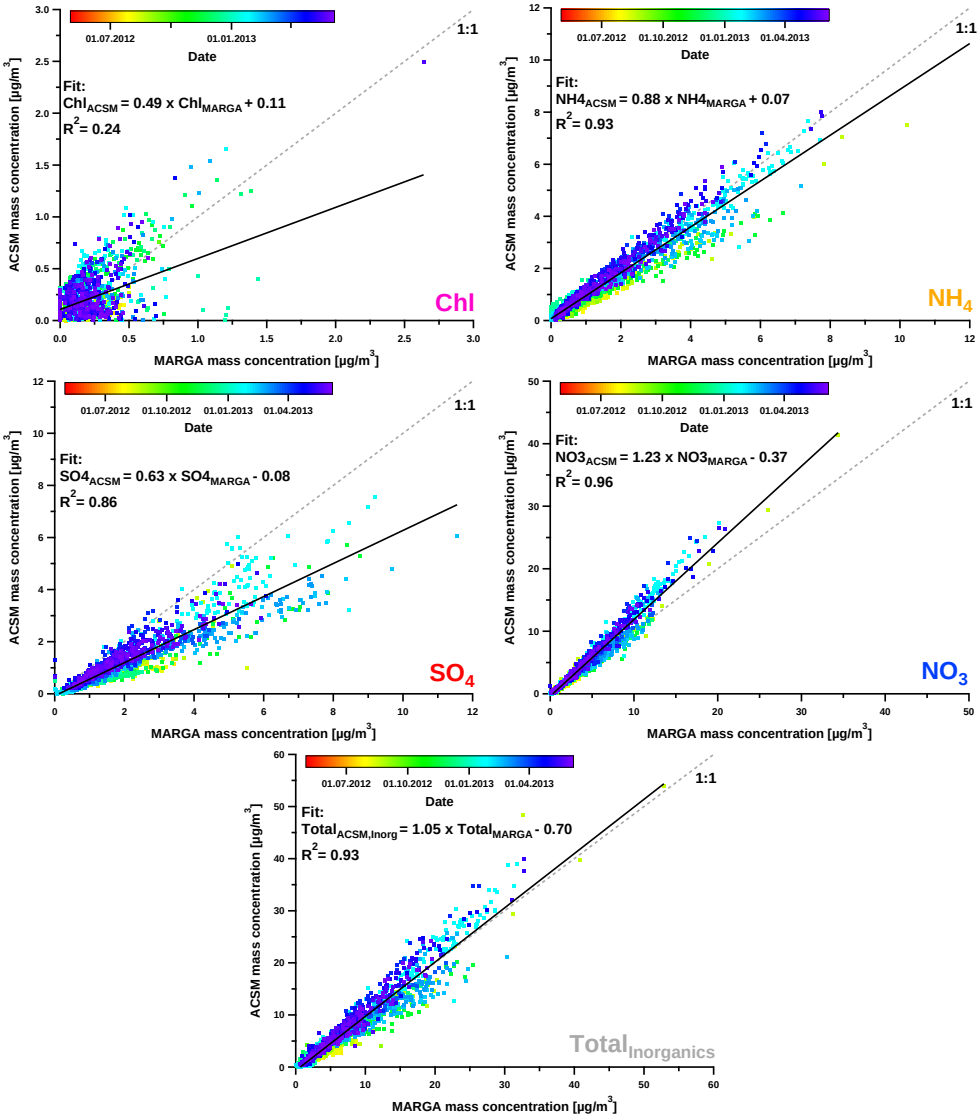

Figure A.19.: Correlation graphs of Chl, NH_4, SO_4, NO_3, and total inorganic mass concentration from ACSM and MARGA data from 2012 to 2013

Instrument comparison: ACSM vs AMS and TD-PTR-MS

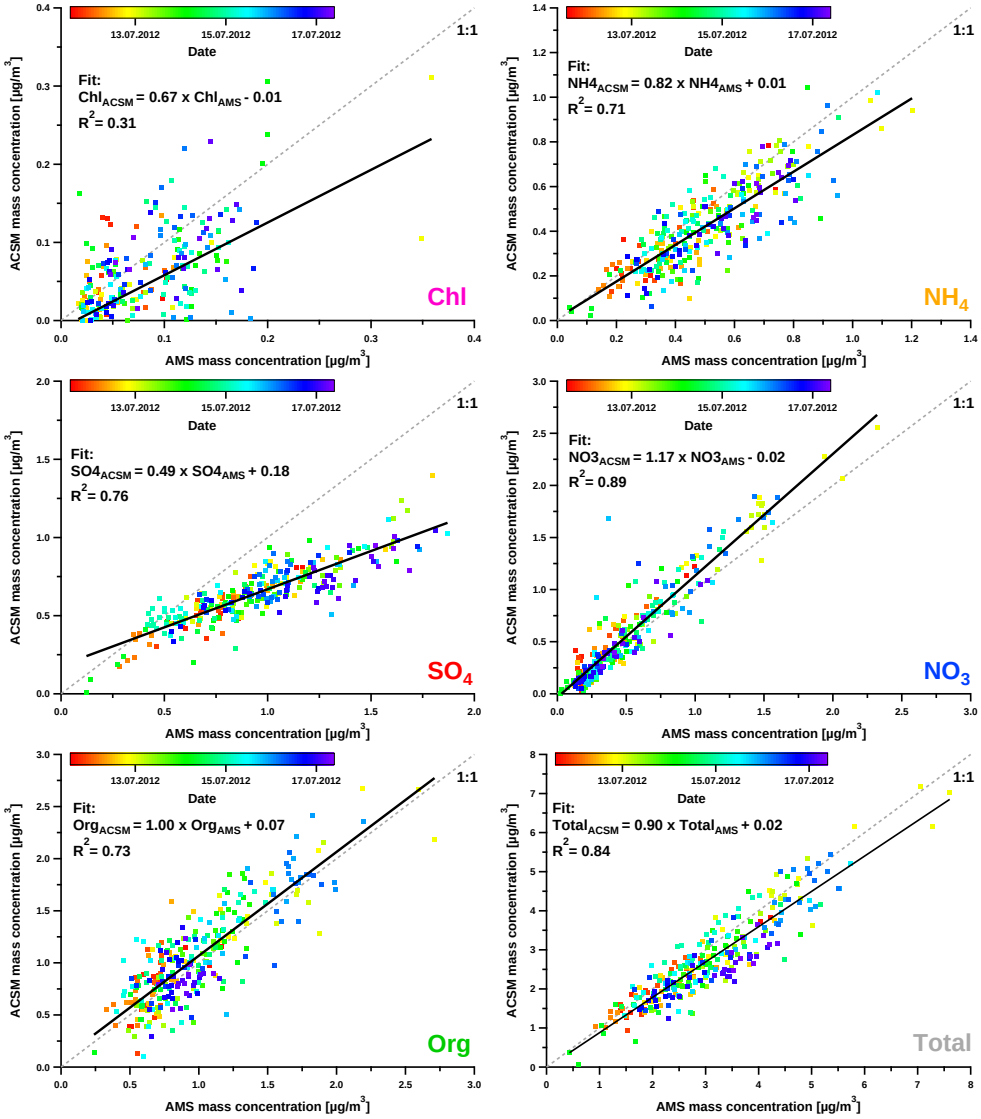

Figure A.20.: Correlation graphs of individual species and total mass from ACSM data with AMS data from 11.07. to 17.07.2012

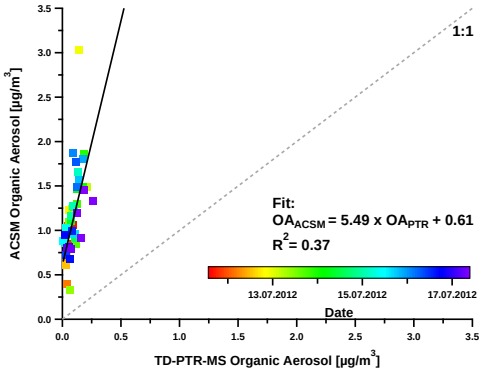

Figure A.21.: Correlation graph of the organic fractions from ACSM data with TD-PTR-MS data from 11.07. to 17.07.2012

A.5.4. PMF results for AMS data in 2011

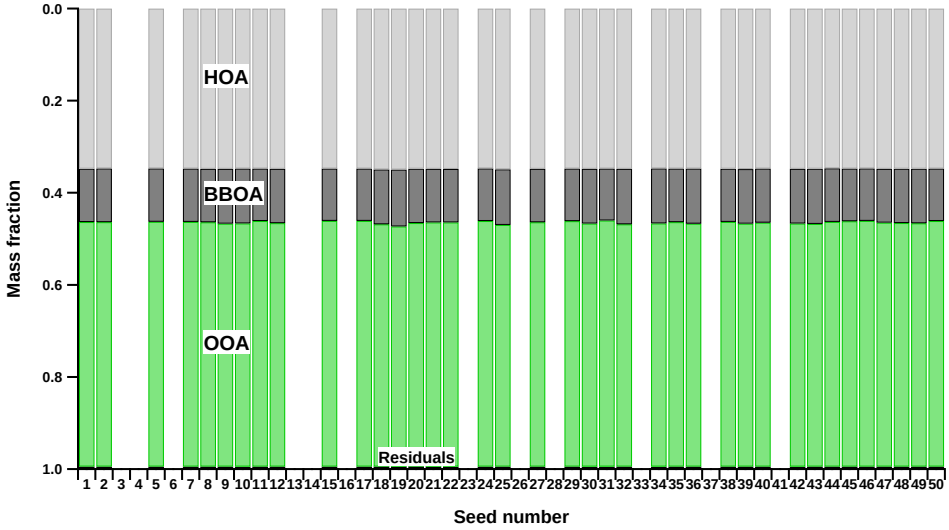

Figure A.22.: Variance of AMS PMF factors and residuals (small black bars at the bottom) found in 2011 throughout 50 seed runs.

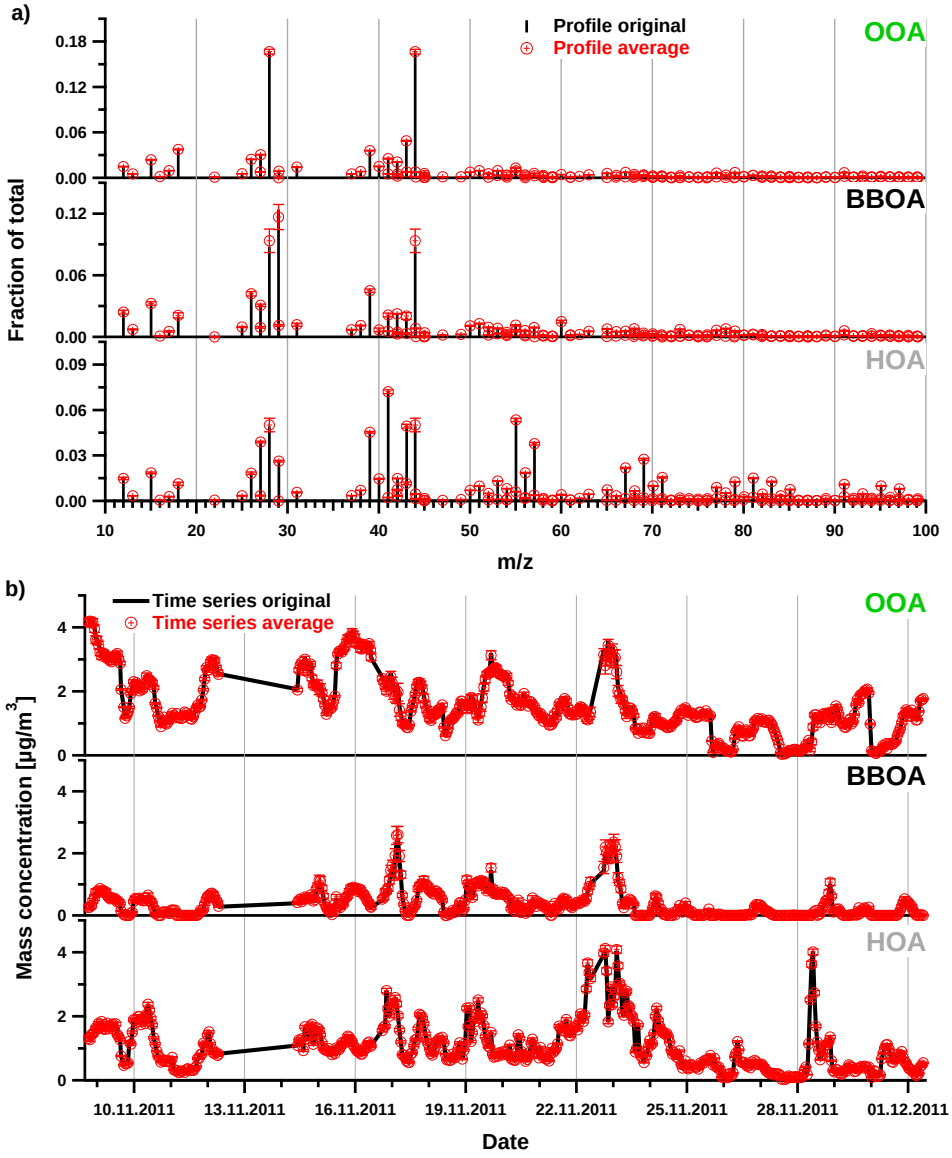

Figure A.23.: Bootstrapping results (100 runs) of the AMS PMF 3 factor solution in 2011: Mass spectra (a) and time series (b). Black lines show original data, red dots and error bars represent the average and 1σ standard deviations, respectively.

Table A.16.: Correlation coefficients (R^2) of the comparison between AMS PMF factor and tracer time series in 2011

	HOA	BBOA	OOA
NO_3	0.25	0.26	0.55
SO_4	0.10	0.12	0.40
NO_3 + SO_4	0.27	0.26	0.66
NH_4	0.26	0.27	0.66
Chl	0.69	0.54	0.29
BC	0.79	0.64	0.44
Excess-NH_4	0.27	0.29	0.66
Organic-NO_3	0.42	0.46	0.72
$C_2H_4O_2^+$ (m/z 60)	0.59	0.88	0.59
$C_3H_5O_2^+$ (m/z 73)	0.57	0.83	0.66
NO_x (gas phase)	0.66	0.51	0.24
CO (gas phase)	0.54	0.43	0.33

A.5.5. PMF results for AMS data in 2012

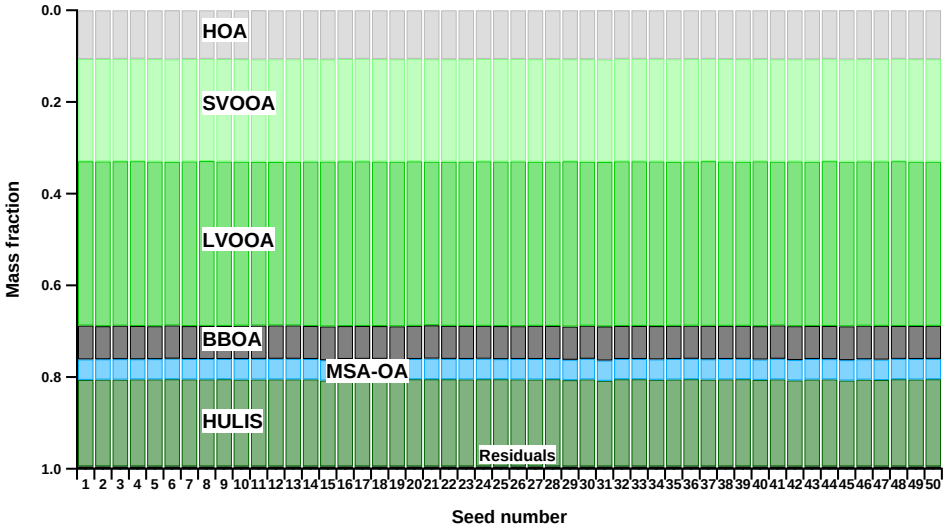

Figure A.24.: Variance of AMS PMF factors and residuals (small black bars at the bottom) found in 2012 throughout 50 seed runs

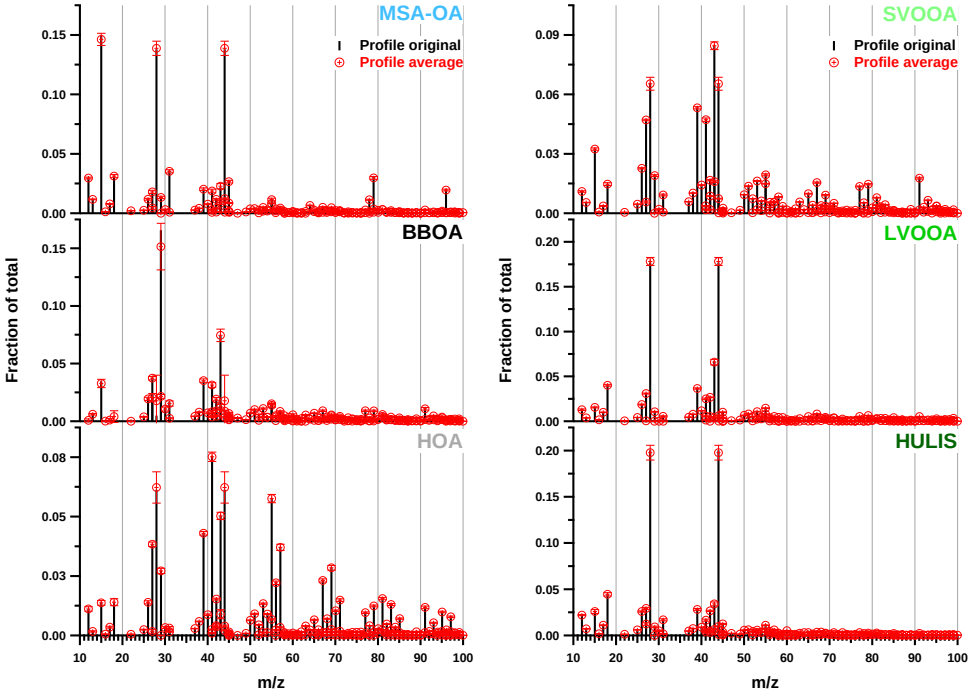

Figure A.25.: Bootstrapping results (100 runs) of the AMS PMF 6 factor solution in 2012: Mass spectra. Black lines show original data, red dots and error bars represent the average and 1σ standard deviations, respectively.

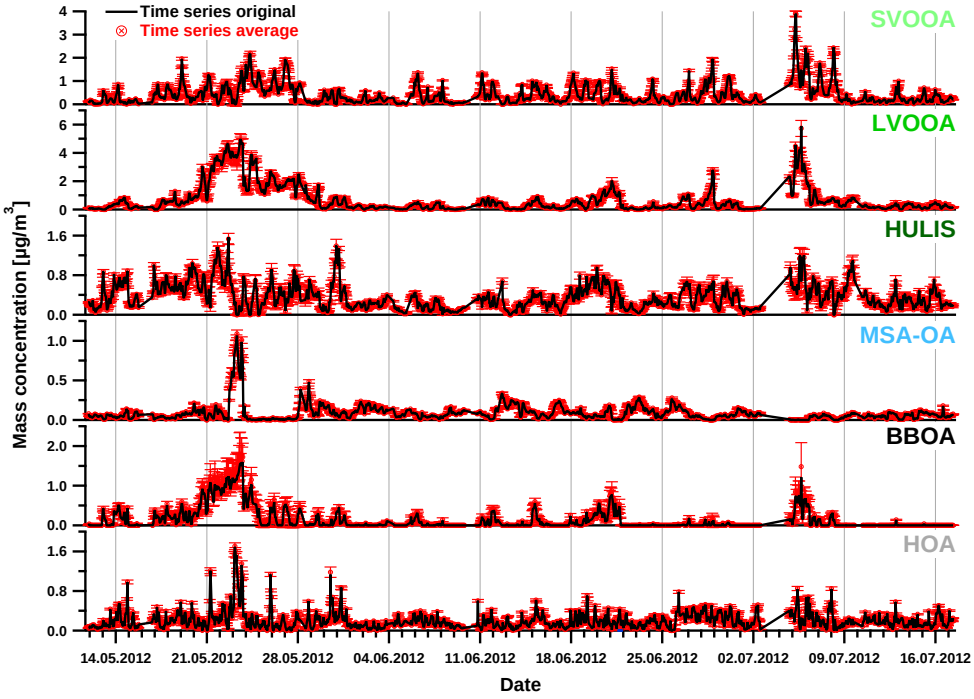

Figure A.26.: Bootstrapping results (100 runs) of AMS PMF 6 factor solution in 2012: Time series. Black lines show original data, red dots and error bars represent the average and 1σ standard deviations, respectively.

Table A.17.: Correlation coefficients (R^2) of the comparison between AMS PMF factor and tracer time series in 2012

	HOA	BBOA	MSA-OA	HULIS	LVOOA	SVOOA
NO_3	0.22	0.69	0.08	0.23	0.42	0.17
SO_4	0.17	0.43	0.16	0.30	0.36	0.02
NO_3 + SO_4	0.24	0.71	0.11	0.29	0.46	0.14
NH_4	0.25	0.72	0.13	0.31	0.49	0.12
Chl	0.22	0.17	0.21	0.07	0.08	0.00
BC	0.49	0.61	0.09	0.13	0.55	0.27
Excess-NH_4	0.10	0.49	0.01	0.36	0.64	0.18
Organic-NO_3	0.10	0.26	0.00	0.17	0.29	0.47
$C_2H_4O_2^+$ (m/z 60)	0.17	0.78	0.04	0.41	0.83	0.34
$C_3H_5O_2^+$ (m/z 73)	0.19	0.79	0.05	0.34	0.92	0.32
$CH_3SO_2^+$ (m/z 79)	0.16	0.15	0.99	0.01	0.08	0.04
NO_x (gas phase)	0.60	0.21	0.06	0.02	0.12	0.16
CO (gas phase)	0.25	0.51	0.01	0.22	0.44	0.20

A.5.6. PMF results for TD-PTR-MS data 2011

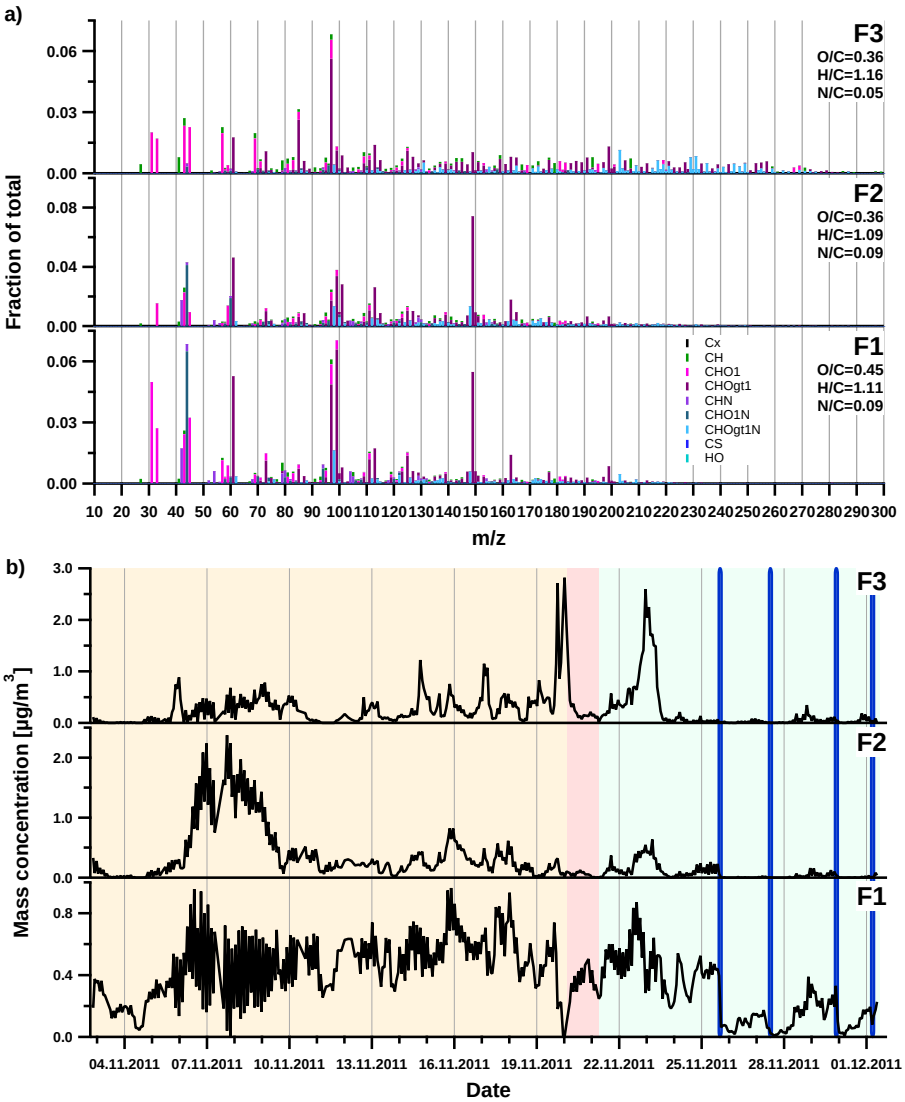

Figure A.27.: Mass spectra (a) and time series (b) of the 3-factor PMF solution from TD-PTR-MS data (merged from both inlets) of November 2011. The HR mass peaks are stacked at each unit mass m/z and coloured by their chemical family (gt1 = greater than 1). The time period with southerly and easterly wind directions is highlighted in beige. The time of calm northerly winds is indicated by a red colour. The period with southerly and westerly wind directions is illustrated in green. The sharp blue rectangles represent precipitation events.

Table A.18.: Correlation coefficients (R^2) of the comparison between TD-PTR-MS PMF factor and tracer time series in 2011

	F1	F2	F3
NO_3	0.29	0.19	0.16
SO_4	0.34	0.46	0.02
NH_4	0.39	0.40	0.13
Chl	0.23	0.10	0.22
BC	0.37	0.11	0.37
Excess-NH_4	0.19	0.30	0.24
Organic-NO_3	0.40	0.31	0.25
$C_2H_4O_2^+$ (m/z 60)	0.37	0.37	0.37
$C_3H_5O_2^+$ (m/z 73)	0.38	0.31	0.35
NO_x (gas phase)	0.21	0.00	0.52
CO (gas phase)	0.35	0.03	0.48

A.5.7. PMF results for TD-PTR-MS data 2012

Table A.19.: Correlation coefficients (R^2) of the comparison between TD-PTR-MS PMF factor and tracer time series in 2012

	F1	F2	F3	F4	F5	F6
NO_3	0.42	0.68	0.34	0.13	0.22	0.27
SO_4	0.44	0.56	0.15	0.16	0.19	0.05
NH_4	0.71	0.75	0.30	0.17	0.26	0.20
Chl	0.19	0.19	0.03	0.02	0.04	0.02
BC	0.53	0.57	0.26	0.08	0.37	0.35
Excess-NH_4	0.42	0.43	0.23	0.10	0.52	0.21
Organic-NO_3	0.26	0.25	0.45	0.03	0.23	0.41
$C_2H_4O_2^+$ (m/z 60)	0.60	0.63	0.27	0.15	0.68	0.35
$C_3H_5O_2^+$ (m/z 73)	0.61	0.64	0.27	0.11	0.73	0.37
$CH_3SO_2^+$ (m/z 79)	0.17	0.18	0.02	0.00	0.05	0.00
NO_x (gas phase)	0.22	0.23	0.18	0.05	0.06	0.21
CO (gas phase)	0.42	0.51	0.22	0.11	0.35	0.25

A.5.8. PMF/ME2 results for ACSM data 2012 - 2013

Table A.20.: Correlation coefficients (R^2) of the comparison between ACSM PMF factor and tracer time series over the entire campaign between July 2012 to June 2013

	HOA	BBOA	OOA	HULIS
NO_3	0.28	0.24	0.63	0.39
SO_4	0.14	0.23	0.48	0.41
NO_3 + SO_4	0.27	0.26	0.67	0.41
NH_4	0.25	0.23	0.63	0.44
Chl	0.14	0.13	0.04	0.10
BC	0.38	0.39	0.34	0.47
m/z 60	0.42	0.94	0.39	0.26
Rn (20 m)	0.30	0.21	0.23	0.34
CO_2 (gas phase, 20 m)	0.24	0.31	0.24	0.21
NO_x (gas phase)	0.47	0.36	0.07	0.10
CO (gas phase)	0.47	0.49	0.37	0.30

Table A.21.: F44 and O/C ratios from PMF profiles of ACSM organic data separated by season. O/C ratios are calculated from f44 values according to *Aiken et al.* (2008)

		f44	O/C (calc.)
Summer 2012	HOA	0.01	0.12
	BBOA	0.19	0.81
	OOA	0.23	0.96
Autumn 2012	HOA	0.01	0.12
	BBOA	0.06	0.31
	OOA	0.20	0.84
	HULIS	0.28	1.15
Winter 2013	HOA	0.01	0.12
	BBOA	0.05	0.27
	OOA	0.23	0.96
	HULIS	0.33	1.34
Spring 2013	HOA	0.02	0.16
	BBOA	0.04	0.23
	OOA	0.23	0.96
	HULIS	0.35	1.42

A.5.9. Aerosol composition during special events

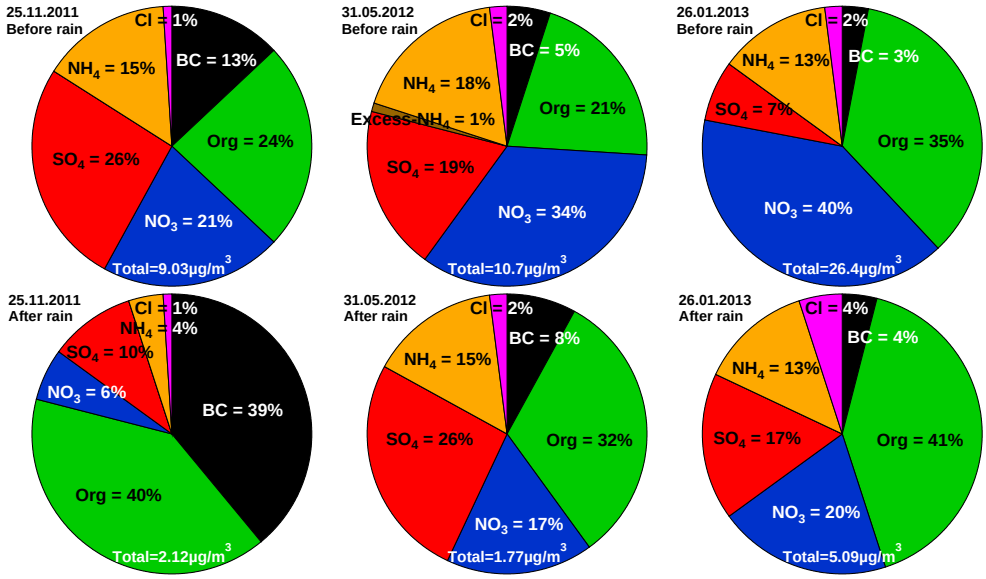

Figure A.28.: Average contributions of individual species before (upper panels) and after (bottom panels) precipitation events.

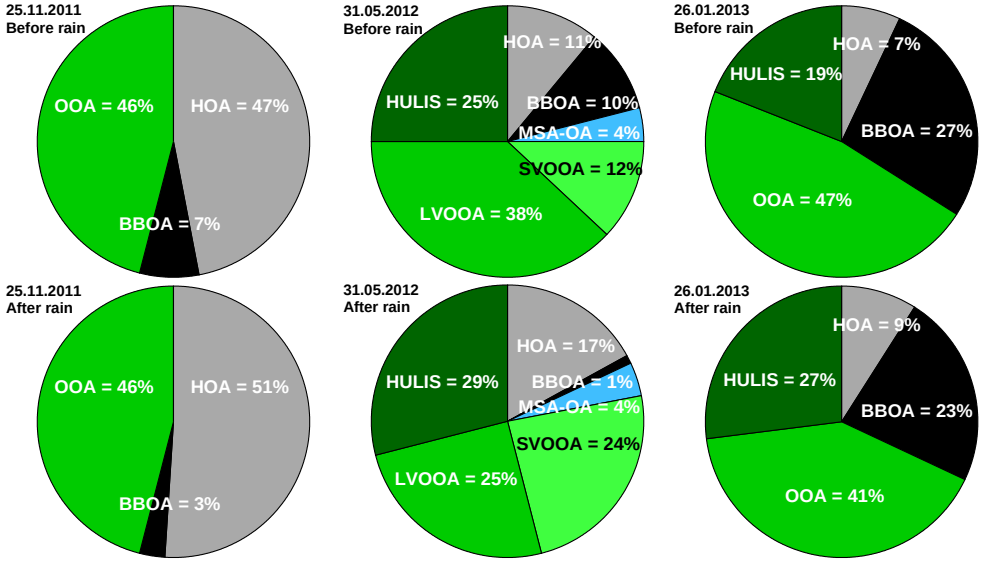

Figure A.29.: Average contributions of PMF factors before (upper panels) and after (bottom panels) precipitation events.

Acknowledgements

An dieser Stelle möchte ich die Gelegenheit nutzen, all den Menschen zu danken, ohne deren Hilfe diese Arbeit so nicht möglich gewesen wäre.

Ein besonders großes Dankeschön geht an Prof. Dr. Astrid Kiendler-Scharr für die überaus gute Betreuung meiner Doktorarbeit, den aufschlussreichen Diskussionen und für die Bereitschaft, diese Arbeit zu begutachten.

Prof. Dr. Andreas Wahner möchte ich für die Möglichkeit, am IEK-8 die hier dargestellten Arbeiten durchzuführen, danken. Außerdem danke ich Prof. Dr. Sanjay Mathur für die Bereitschaft, als Vorsitzender der Prüfungskommission zu fungieren.

Besonders möchte ich mich bei Assistenz-Professor Rupert Holzinger (IMAU) für die schöne Betreuung während meines halbjährigen Aufenthalts an der Universität Utrecht, Niederlande, bedanken. Ein großer Dank geht an Dr. Florian Rubach und Dr. Achim Trimborn für die großartige Zusammenarbeit, vor allem während der Messkampagnen und meiner Einarbeitungsphase in die Tiefen der Aerosol-Massenspektrometrie.

Ich danke Alex Vermeulen, Mark Blom (beide bei ECN, Niederlande), Marcel Moerman und Bas Henzing (beide bei TNO, Niederlande) für die zur Verfügung gestellten Daten ihrer Messinstrumente in Cabauw. Marcel Brinkenberg und Fred Bosveld danke ich sehr herzlich für die tolle Unterstützung während der Feldmesskampagnen in Cabauw.

Ein sehr großes Dankeschön geht an Sebastian Schmitt, Dr. Martin Kaminski und Ismail Acir für das Korrekturlesen dieser Arbeit.

Ich bedanke mich sehr bei den Mitarbeitern des IEK-8 vom Forschungszentrum Jülich und des IMAU der Universität Utrecht für die ganz besonders tolle und angenehme Atmosphäre, die meine Zeit als Doktorand, auch außerhalb der Arbeitszeit, zu einem schönen Erlebnis gemacht haben,

und nicht zuletzt bei meiner Familie und Freunden, die mich während des Studiums und der Promotion immer unterstützt haben.

Band / Volume 238
Development of a highly sensitive and versatile mass spectrometer system for laboratory and atmospheric measurements
S. Albrecht (2014), iv, 171 pp
ISBN: 978-3-95806-009-8

Band / Volume 239
High Temperature Corrosion of Alloys and Coatings in Gas-Turbines Fired with Hydrogen-Rich Syngas Fuels
W. Nowak (2014), 201 pp
ISBN: 978-3-95806-012-8

Band / Volume 240
Einfluss neuer Membranmaterialien auf Herstellung und Betrieb von Direktmethanol-Brennstoffzellen
S. Hürter (2014), V, 164 pp
ISBN: 978-3-95806-013-5

Band / Volume 241
Spannungsinduziertes Versagen in Hochtemperaturschichtsystemen
C. Nordhorn (2014), v, 118 pp
ISBN: 978-3-95806-016-6

Band / Volume 242
Änderungsdetektion digitaler Fernerkundungsdaten mittels objekt-basierter Bildanalyse
C. Listner (2014), 176 pp
ISBN: 978-3-95806-017-3

Band / Volume 243
Räumlich hoch aufgelöste Modellierung des Spaltproduktverhaltens in einem HTR-Core mit kugelförmigen oder prismatischen Brennelementen
A. Xhonneux (2014), viii, 239 pp
ISBN: 978-3-95806-020-3

Band / Volume 244
Effects of Cercospora leaf spot disease on sugar beet genotypes with contrasting disease susceptibility
S. Schmittgen (2015), 121 pp
ISBN: 978-3-95806-021-0

Band / Volume 245
Light scattering and trapping in thin film silicon solar cells with an n-i-p configuration
W. Böttler (2015), 132 pp
ISBN: 978-3-95806-023-4

Band / Volume 246
Nanostructured Si-alloys for silicon solar cells
K. Ding (2015), 210 pp
ISBN: 978-3-95806-024-1

Band / Volume 247
Electrochemical Texturing and Deposition of Transparent Conductive Oxide Layers for the Application in Silicon Thin-Film Solar Cells
J.-P. Becker (2015), ix, 156, XXIV pp
ISBN: 978-3-95806-027-2

Band / Volume 248
Stoffliche Charakterisierung radioaktiver Abfallprodukte durch ein Multi-Element-Analyseverfahren basierend auf der instrumentellen Neutronen-Aktivierungs-Analyse – MEDINA –
A. W. Havenith (2015), 311 pp
ISBN: 978-3-95806-033-3

Band / Volume 249
Quantitative Two-Layer Inversion and Customizable Sensor-Array Instrument for Electromagnetic Induction based Soil Conductivity Estimation
A. T. Mester (2015), viii, 119 pp
ISBN: 978-3-95806-035-7

Band / Volume 250
Partial Neutron Capture Cross Sections of Actinides using Cold Neutron Prompt Gamma Activation Analysis
C. Genreith (2015), vii, 166, XXXII pp
ISBN: 978-3-95806-036-4

Band / Volume 251
Long Term Aerosol Composition Measurements at the CESAR Tower at Cabauw, NL
P. Schlag (2015), iii, 228 pp
ISBN: 978-3-95806-037-1

Energie & Umwelt /
Energy & Environment
Band / Volume 251
ISBN 978-3-95806-037-1

JÜLICH
FORSCHUNGSZENTRUM